UNIVERSITY OF GHANA

DEPARTMENT OF CHEMISTRY

DESIGN, SYNTHESIS, AND BIOLOGICAL STUDIES OF NEW FLUORESCENT ARYLBORONIC ACID CHEMOSENSOR DYES FOR THE DETECTION OF MYCOLACTONE TOWARD THE DIAGNOSIS OF BURULI ULCER

BY

AKOLGO GIDEON ATINGA

(10274146)

This thesis is submitted to the University of Ghana, Legon in partial fulfillment of the requirement for the award of **PhD IN CHEMISTRY DEREE**

DECEMBER 2023

DECLARATION

I, **GIDEON ATINGA AKOLGO**, the author of this thesis hereby declare that the work presented was solely done by me, under supervision, in the Department of Chemistry, University of Ghana, Legon.

Candidate's Signature:  Date: 12-12-2023

Gideon Atinga Akolgo

Principal Supervisor's Signature:  Date: 12-12-2023

Prof. Richard K. Amewu

Co-Supervisor's Signature:  Date: 12-12-2023

Dr. Jerry Joe E. K. Harrison

DEDICATION

This thesis is dedicated to my Late father Akolgo Atayele, my mother Azeyeta Adoona and my sister Azumah Apuriyuure who had no privilege of formal education but saw the value in educating me to the highest level.

ACKNOWLEDGEMENT

First, I express my profound gratitude to my supervisors, Prof. Richard Amewu, and Dr. Jerry Joe Harrison for the scientific direction and encouragement. I am particularly indebted to Prof. Amewu for the opportunity to work in your lab as one of your first students. You exposed me to many things, you held my hand everywhere you went – to conferences, to workshops and you gave me opportunities to present my research findings on various platforms. You taught me scientific writing and I am enormously appreciative of your guidance in writing my thesis and manuscripts.

I am deeply grateful to Dr. Benjamin Partridge and Dr. Tim Craggs of the University of Sheffield. Thank you for the mentorship and direction especially in our monthly progress updates but above all, for providing me the opportunity to work in your labs. I am grateful to have had the opportunity to work on this project with you. I would also want to thank the entire team at the University of Sheffield, especially Deeba Zahoor, who was the Health and Safety Officer during my visit, Dr. Khalid Doudin and the entire NMR laboratory staff for the NMR data, Sharon Spey, and Craig Robertson, thank you for the LCMS analysis. Craig, I am grateful for going the extra mile to determine the X-ray crystal structures for me. Thank you, Luke Duigan Slater, for the FTIR data. Your various contributions made this thesis a reality.

I would want to thank all teaching and non-teaching staff of the Department of Chemistry, UG particularly the Department Secretary, Mr. Solomon Nana Safo, and the technicians Mr. Bob Essien, Mr. Samuel Kwadwo Owusu (aka General), Mr. David Bakomnaah, Mawufemor Babe, my biggest gratitude is to you because, without your collective support, this would not be possible. I cannot forget to mention Mr. Ernest, a non-scientist who made the chemistry possible. God bless you all. To my colleagues at the NMR facility in UG, Mr. Eric Koffie and

Mr. Thomas Mensah, I say God richly bless you for the support all through this journey. Furthermore, I would want to thank all the staff members of the Department of Chemistry, UG.

To all my colleagues in Drug Innovation Group, both past and current, particularly, Henry Akwaffo Onyame (Ph.D.), Justice Akwensi, Patrick Sakyi, Crystal Ade, Fritz Plange, Shaban Mohammed, Stanley Dugbartey, Hagar Afriyie, Deborah Annor, Akua Gyamfuaa Adu-Gyamfi, Magdalene Togoh, Perpetual Anum, Barbara Anibea, Jones Annan, Richard Opoku, I appreciate you all for the pleasant working moments and the many interesting and helpful group meetings and discussions. How can I forget our "waakye" and "kenkey" party moments? It compensated for the frustrating lab sessions and draining mental work – After all, Crystal would say "No matter what you are facing in life, eat first" – it really helped. Sigh! I cannot forget those who directly worked with me on the same project. Thank you, Abass Ibrahim, Millicent Esi Asare, and Zigli Abdulai for our crazy trips to many districts on some of the most terrible roads for sample collection and training.

Thanks to George Rogers, Jasmine Catlow, Fatimah Ibrahim, Rik Sieben, Jenning, Anju Thampan of the Partridge Group, and Mahmoud Addelhamid of the Craggs Group for all the support given to me. You guys collectively made my everyday work in the lab easier and more exciting.

I am grateful to the GNPC Foundation for your financial support. I am equally indebted to Dr. Kinglsey Asiedu and Stéphanie Florence Jourdan of the World Health Organization for your diverse support. God richly bless you both. To Mr. Abass Mohammed and the entire team at Agogo Presby Hospital, your role in this cannot be overlooked. You provided me with clinical samples, without which this dream would not have been realised. I say thank you all.

I would like to pay special appreciation to the entire team at Erasmus+, I am highly indebted to Danielle Bertrand, Siobhan M. Reaney, Olivia Hodson-Barnes, and Dr. Robert Akparibo.

Thank you to Mrs. Selasie E. Agamah and the entire team at ORID-EUDESK, UG. I cannot forget my Erasmus+ cohort members especially Isaac Boadu and Kwame Adjei, the memories at Walkey House will remain forever. Thank you and God bless you.

I am eternally indebted to my parents and the entire family. Your unwavering support and encouragement meant the world to me. To my big sister, Azumah Apuriyuure, you have been my backbone, and I dare say I could not have done this without you. Mpu'esiya!

To my friends, thank you all for believing in me. Let me make special mention of Mr. Sylvester Ayelgum, Atafo Gladys, Mr Saeed Ubeidalah, Mr Abdul Malik Yamba, Hector Kunkpeh, and Torbi Joseph. To Dr. Joseph and Mrs. Lilian Akan-uwe and the kids, Raphael, and Emmanuel, thank you for the love and warmth and for hosting me during my period in Sheffield. God richly bless you.

More importantly, I am extremely indebted to my dear wife, Charity Mbilla, with whom I poured all my frustrations when the chemistry didn't work. Thank you for the sacrifices and compromises all through this very long journey. You are indeed a strong pillar. I love you, Belle – and to my beautiful daughter, Alianna ADELEyine Akolgo, your arrival is a testament that when we lean on God as a family, He will not fail us because His promises for us are Ye and Amen.

All praise belongs to God Almighty.

PUBLICATIONS

In undertaking this thesis, the following articles were published in scientific journals.

1. **Akolgo GA**, Partridge BM, D. Craggs T, Amewu RK. Alternative boronic acids in the detection of Mycolactone A/B using the thin layer chromatography (f-TLC) method for diagnosis of Buruli ulcer. BMC Infectious Diseases. 2023;23(1):495.
2. Amewu RK, **Akolgo GA**, Asare ME, Abdulai Z, Ablordey AS, Asiedu K. Evaluation of the fluorescent-thin layer chromatography (f-TLC) for the diagnosis of Buruli ulcer disease in Ghana. PLOS ONE. 2022;17(8):e0270235.
3. **Akolgo GA**, Ablordey A, Pereko J, Tuffour J, Kotey N. Integrated Management Strategies (Diagnosis, Treatment, and Wound Care Management) for Improved Clinical Outcomes of Buruli Ulcer in Ghana: A Retrospective Case Report in the Ga West Municipal Hospital, Amasaman. Clin Med Rev Case Rep. 2022;9:379.

ABSTRACT

Background: Buruli ulcer (BU) is a devastating neglected tropical skin disease caused by *Mycobacterium ulcerans* (MU). The disease is prevalent in rural areas, accounting for approximately 30% of all ulcer cases that are reported in highly endemic health facilities in Africa. In 2023, 1952 new cases were reported from 12 countries, with 1573 (81%) of the reported cases from the African Region alone and 379 (19%) from the Western Pacific Region. Early and accurate diagnosis of BU is required for appropriate antibiotic therapy. However, the current diagnostic methods including microscopy, culture, histopathology, and PCR are associated with limitations such as not being readily available in endemic areas, low sensitivities and specificities, long turn-around time for results to be obtained, expensive, requiring sophisticated instrumentation, and highly skilled technical expertise. The fluorescent-thin layer chromatography (f-TLC) method which involves the chemical derivatization of mycolactone with a 2-naphthylboronic acid (BA) for its direct detection has been evaluated. The method is rapid and promising; however, it suffers interferences from other co-extracted and co-eluted lipids. In addition, the read-out has not been automated and leads to subjective interpretations of results. This research seeks to provide an improved f-TLC diagnostic method that largely satisfies the **ASSURED** criteria (**A**ffordable and cost-effective, **S**ensitive, **S**pecific, **U**ser-friendly, **R**apid and robust, **E**quipment-free, and **D**elivered to those who need it) for the diagnosis of BU.

Methods: Firstly, the f-TLC method was used to screen a series of 27 commercially available arylboronic acids as potential replacements for the 2-naphthylboronic acid (BA) for mycolactone detection. Secondly, High-Performance Thin Layer Chromatography (HPTLC) was employed for the quantitative detection of mycolactone. Thirdly, considering that fluorescent chemosensors are increasingly becoming relevant in recognition chemistry due to

their great sensitivity, selectivity, fast response time, real-time detection capability, and low cost, a library of fluorescent chemosensors with various signalling moieties (i.e. fluorophores and chromophores with certain beneficial photophysical characteristics) and a recognition moiety (i.e. boronic acid unit) were (i) rationally designed; (ii) synthesized using combinatorial approaches; and (iii) fully characterized using a set of complementary spectrometric and spectroscopic techniques such as NMR, LC-MS, FT-IR, and X-ray crystallography. In addition, a complete set of basic photophysical quantities such as absorption maxima (λ_{abs}^{max}), emission maxima (λ_{em}^{max}), Stokes shift ($\Delta\lambda$), molar extinction coefficient (ε), fluorescence quantum yield (Φ_F), and brightness were determined using UV-vis absorption and fluorescence emission spectroscopy techniques.

Results: Three commercially available boronic acids i.e. BA15, BA18, and BA21 yielded fluorescent bands on TLC with intensities that were superior to BA when coupled to mycolactone. Among the three, BA18 produced the most outstanding TLC profiles, and thus, was validated using clinical samples from patients including five (5) positive and four (4) negative samples that were confirmed by gold standard PCR. These produced bands on TLC plates that were easier to interpret even in the presence of background interference. The automated HPTLC method achieved satisfactory quantification of mycolactone with an R_F value of 0.32. The linear range was 4 – 45 ng for mycolactone with an R^2 = 0.98. The limit of detection (LOD) and limit of quantification (LOQ) were estimated to be 6.6 and 22 ng/spot respectively.

Conclusion: BA18 was found to be a potential alternative to BA from the commercially available aryl boronic acids. A total of 12 fluorescent arylboronic acids were synthesized including aminoacridine, aminoquinoline, azo, BODIPY, coumarin, fluorescein, and rhodamine variants. After assessing the photophysical properties together with the binding

ability of the dyes to mycolactone on TLC, AAG113 emerged as the best (λ_{abs}^{max} = 456 nm, (λ_{em}^{max} = 590 nm, $\Delta\lambda$ = 134 nm, ε = 52816.1 $M^{-1}cm^{-1}$, Φ_F = 0.78, and brightness = 41196.6 $M^{-1}cm^{-1}$). Preliminary results show that HPTLC offers advantages over conventional f-TLC because a number of the steps are automated giving rise to increased resolution, and more accurate quantitative measurements of mycolactone.

TABLE OF CONTENTS

LIST OF FIGURES

LIST OF TABLES

LIST OF SCHEMES

APPENDICES

Appendix 1: ^{1}H, ^{13}C, and ^{11}B NMR spectra Data

LIST OF ABBREVIATIONS

λ_{abs}^{max}	Maximum absorption wavelength
λ_{em}^{max}	Maximum emission wavelength
$\Delta\lambda$	Stokes shift
^{13}C NMR	Carbon NMR
^{1}H NMR	Proton NMR
4-MU	4-methylumbelliferone
A	Absorbance
aa	amino acid identity
acetone-*d_6*	Deuterated acetone
AcOH	Acetic acid
AFB	Acid-fast bacilli
AMR	Antimicrobial resistance
aq.	Aqueous
B	Brightness
$B_2(OH)_4$	Tetrahydroxydiboron
B_2cat_2	Bis(catecholato)diboron
B_2gly_2	Bis(glycolato)diboron
B_2hex_2	Bis(hexylene glycolato) diboron
B_2neop_2	Bis(neopentyl glycolato)diboron
B_2OMe_4	Diboron tetramethoxide
B_2Pin_2	Bis(pinacolato) diboron
BA	2-naphthylboronic acid
BA18	9,9-Diphenyl-9H-fluoren-4-yl)boronic acid
BA21	3-(Naphthalen-1-yl)phenyl)boronic acid
BASE	Boron Affinity Saccharide Electrophoresis
BBA	Bis-boronic acid
$BF_3{\cdot}Et_2O$	Boron trifluoride etherate
BNCT	Boron neutron capture therapy
Boc	*tert*-butoxycarbonyl
***Boc*$_2$O**	*di-tert*-butyl dicarbonate
KOAc	Potassium acetate
LAMP	Loop-mediated isothermal amplification
LC–MS	Liquid Chromatography Mass Spectrometry
$LiAlH_4$	Lithium aluminium hydride
LLE	Liquid–liquid extraction
LOD	Limit of detection
LOQ	Limit of quantification
m	Multiplet
m/z	Mass-to-charge ratio
m-CPBA	meta-Chloroperoxybenzoic acid
MeCN	Acetonitrile
$MgSO_4$	Magnesium sulfate
MHz	Megahertz
mL	Millilitre
MPM	Mycolactone-producing mycobacteria
MS	Mass spectrometry
MU	*Mycobacterium ulcerans*
$NaBH(OAc)_3$	Sodium triacetoxyborohydride
$NaBH_3CN$	Sodium cyanoborohydride
$NaIO_4$	Sodium periodate
***n*-BuLi**	n-Butyllithium
NH_4Cl	Ammonium chloride
NMR	Nuclear magnetic resonance
NP	Natural products reagent
nt	nuecleotide identity
NTDs	Neglected tropical diseases
NTM	Non-tuberculous mycobacterium
***p*-chloranil**	2,3,5,6-tetrachloro-p-benzoquinone
PCR	Polymerase chain reaction
Pd(dppf)Cl_2	[1,1'-bis(diphenylphosphino)ferrocene] dichloro palladium(II)

BODIPY	Boron dipyrromethene	**pin**	Pinacol
Bpin-Bdan	Pinacolato-1,8-diaminonaphthalenato diboron	**PKS**	Polyketide synthases
br q	Broad quartet	**POC**	Point-of-care
br s	Broad singlet	**$POCl_3$**	Phosphoryl chloride
BU	Buruli ulcer	**PPh_3**	Triphenylphosphine
$CDCl_3$	Deuterated chloroform	**ppm**	Parts per million
CH_2Cl_2	dichloromethane	***p*-TsOH**	*p*-Toluenesulfonic acid
d	Doublet	**q**	Quartet
DCE	Dichloroethane	**QTOF**	Quadrupole-Time of Flight
DCM	Dichloromethane	**R_F**	retention factor
ddd	Doublet doublet of doublets of doublets	**RIF**	Rifampicin
DDQ	2,3-dichloro-5,6-dicyano-p-benzoquinone	**RNA**	Ribonucleic acid
DMAP	4-dimethylaminopyridine	**s**	Singlet
DMF	Dimethylformamide	**S/N**	Signal-to-noise ratio
DMSO	Dimethyl sulfoxide	**SCXRD**	Single-Crystal X-Ray Diffraction
DMSO-d_6	Deuterated dimethyl sulfoxide	**MTB**	*Mycobacterium tuberculosis*
DNA	Deoxyribonucleic acid	**SD**	Standard deviation
dt	Doublet triplet	**SOPs**	Standard operating procedures
EDC·HCl	1-(3-Dimethylaminopropyl)-3-ethylcarbodiimide hydrochloride	**SPE**	Solid-Phase. Extraction
ESI	Electrospray ionization	**STR**	Streptomycin
Et_3N	Triethylamine	**TB**	Tuberculosis
EtOAc	Ethyl acetate	**TBAF**	Tetra-*n*-butylammonium fluoride
FNA	Fine-needle aspirates	**TBS**	Tert-butyldimethylsilyl
F-pin$_2$B$_2$	Fluorous bis(pinacolato)diboron	**TBSCl**	*tert*-Butyldimethylsilyl chloride
FT-IR	Fourier-transform infrared	**^{t}BuOK**	Potassium tert-butoxide
f-TLC	fluorescent-thin layer chromatography	**td**	Triplet doublet
H_3BO_3	Boric acid	**TE**	Thioesterase
H_3NSO_3	Sulfamic acid	**TEA**	Triethylamine
HB-Bdan	1,8-naphthalenediaminatoborane	**TEMPO**	2,2,6,6-tetramethylpiperidine 1-oxyl
HBpin	Pinacolborane	**TES**	Triethylsilyl
HNO_2	Nitrous acid	**TFA**	Trifluoroacetic acid
HOBt	Hydroxybenzotriazole	**THF**	Tetrahydrofuran

HPTLC	High-Performance Thin Layer Chromatography	**TLC**	Thin-layer chromatography
HRMS	High-resolution mass spectrometry	**UV-Vis**	Ultraviolet–visible
HWE	Horner–Wadsworth–Emmons	**WHO**	World Health Organization
Hz	Hertz	**δ**	Chemical shift
$^{i}Pr_2NBH_2$	Diisopropylaminoborane	**ε**	Molar extinction coefficient
IS2404	Insertion sequence 2404	**η**	Refractive index
J	Coupling constant	**Φ_F**	Fluorescence Quantum Yield

CHAPTER ONE

1 Introduction

1.1 Background

Buruli ulcer (BU) is a devastating skin infection caused by a toxin-secreting environmental mycobacterium species called *Mycobacterium ulcerans* (MU). MU disease is characterized by necrotizing skin lesions, which can cover up to a third of the entire body surface area of the affected individual. It affects mainly the skin and sometimes bones [1] and thus can lead to irreversible deformity or long-term functional disability when not properly treated [2-6]. *M. ulcerans* disease belongs to the same family as *Mycobacterium tuberculosis* (MTB) and *Mycobacterium leprae* (ML). MU is the third most common mycobacterial disease in humans, after MTB and ML but the most poorly understood of the three [7-9]. However, of the three mycobacterium diseases, MU is unique because it produces a polyketide toxin called mycolactone A/B (herein referred to as "mycolactone") (**Figure 1.1**). The toxin is an important factor in the pathogenesis of Buruli ulcer disease [10-13].

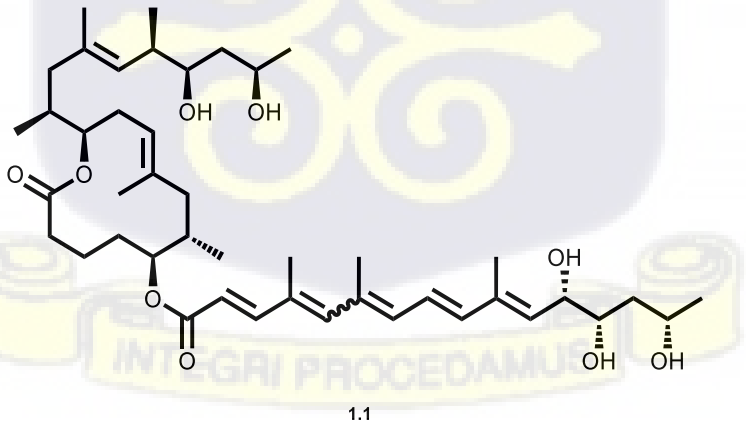

1.1

Figure 1.1. Structure of mycolactone A/B.

Notably, while *M. ulcerans* bacteria rarely disseminate beyond the skin, mycolactone has a body-wide distribution. The bacterial production of mycolactone is mainly required for the virulence and cytotoxicity of the disease [11, 14-16]. At high concentrations, the toxin induces both apoptotic and necrotic changes in various cells [17]. For instance, Krieg et. al. established that *in vitro* cultivation of *M. ulcerans* produced a toxin that, when intradermally inoculated into the skin of guinea pigs caused localized necrosis and inflammation that closely mirrored the skin lesions associated with BU in humans [18]. Also, the injection of purified mycolactone in the dermis of rodent models induced BU-like lesions like those observed in humans [11, 14, 19-22]. It is speculated that mycolactone damages the peripheral nerves, resulting in the painlessness of early lesions, suppress the local immune system and demonstrated to have analgesic properties [23-25].

Buruli ulcer affects all age and sex groups even though children under the age of 15 years are commonly affected particularly in Africa [26, 27]. BU lesions are characterized by minimal pain or painlessness in the initial stages except in instances of secondary infections where pain may be provoked in infected persons [24]. The lack of pain coupled with cultural practices and socio-economic factors often leads patients to underestimate the severity of the disease and thereby delay seeking early medical treatment [28, 29]. The consequence of late reporting is extensive ulcerations that are difficult to manage. Even in instances where there is complete healing, patients sometimes battle with life-long scarring, contractures, and in some cases, long-term disability, and societal stigma, especially among the often-affected children [24, 30] [31, 32] [33]. As such, the disease has been described as an emerging public health problem across endemic regions in rural West and Central Africa because of the deleterious consequences and enormous socio-economic burdens that it poses on patients and their caregivers [34, 35].

1.2 Clinical presentations of BU disease

Buruli ulcer come with variable clinical presentations in different geographical locations. For instance, in the Pacific region particularly in Australia, the early stages of BU start with a papule, which looks like an insect bite whereas in West and Central Africa it may start as a painless nodule without the involvement of subcutaneous tissues [1]. These two forms – papule or nodule gradually progress into a plaque which is defined as a firm, elevated lesion of more than 3 cm in diameter with ill-defined edges. Patients may also present with the oedematous form, which is more diffuse, and ill-defined with non-pitting swelling affecting large areas of the limb or other parts of the body. With oedemas, the skin surrounding the lesion may be reddened or discolouration may be observed [36]. Eventually, the various early clinical forms including papule, nodule, plaque, or oedematous form breakdown into extensive skin ulceration extending into the subcutaneous adipose tissue with the classical, undermined edges and thick necrotic tissue at the wound base which are characteristic features of BU (**Figure 1.2**) [37, 38]. These necrotic lesions are attributed to the cytopathic action of the plasmid-encoded macrolide toxin, mycolactone [11, 19-22] and if untreated, can extend to 15% of a patient's skin surface [39]. Even though lesions are often distributed on the exposed areas of the body including the limbs and the face [33], severe forms of the disease such as osteomyelitis and reactive osteitis also occur. Here, the disease is not only limited to the skin but extends to the bone, causing bone deformities [36].

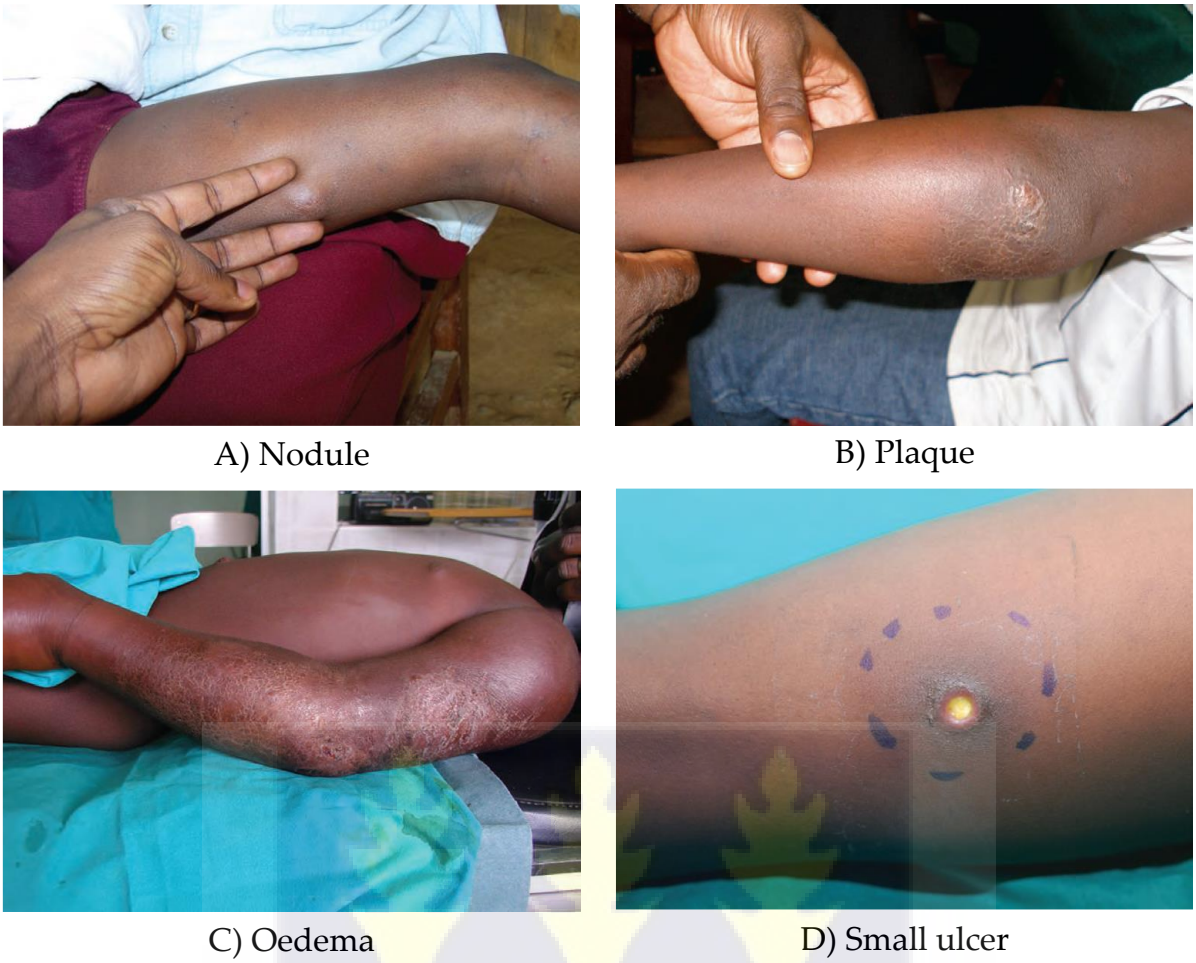

Figure 1.2. Clinical forms of Buruli ulcer. (A) Nodule, (B) Plaque, (C) Oedema, (D) Small ulcer.

1.3 Categories of BU disease

According to the WHO, BU lesions are classified into three categories based on severity: Category I includes a single lesion less than 5 cm in diameter, Category II includes a single lesion 5–15 cm in diameter while Category III includes a single lesion greater than 15 cm in diameter, multiple lesions, critical sites, and osteomyelitis [40, 41].

1.4 Global distribution of BU disease

Since 2002, BU has been reported in 33 countries, mainly in tropical and subtropical climates. The 2019 WHO classification of Neglected Tropical Diseases (NTDs) report ranked Buruli

ulcer as an emerging NTD of global health concern [42-44]. In Africa, the disease is more prevalent in rural areas [45] and more severe among impoverished residents [37]. It accounts for approximately 30% of ulcer cases seen in highly endemic health facilities in Africa, despite significant under-reporting [33]. Efforts by WHO have been aimed at controlling the disease in these two regions over the last decade. However, the following limitations; (i) the scope of the disease is largely unknown in many communities where limited or no activities are being carried out; (ii) within endemic countries where cases are regularly reported, control activities are limited in geographical scope and the data may not reflect the burden at the national level; and (iii) limited knowledge of the disease, its focal distribution, and the fact that it primarily affects impoverished rural communities hamper the efforts. In 2023, 1952 new cases were reported from 12 countries, with 1573 (81%) of the reported cases from the African Region alone and 379 (19%) from the Western Pacific Region (**Figure 1.3**) [46].

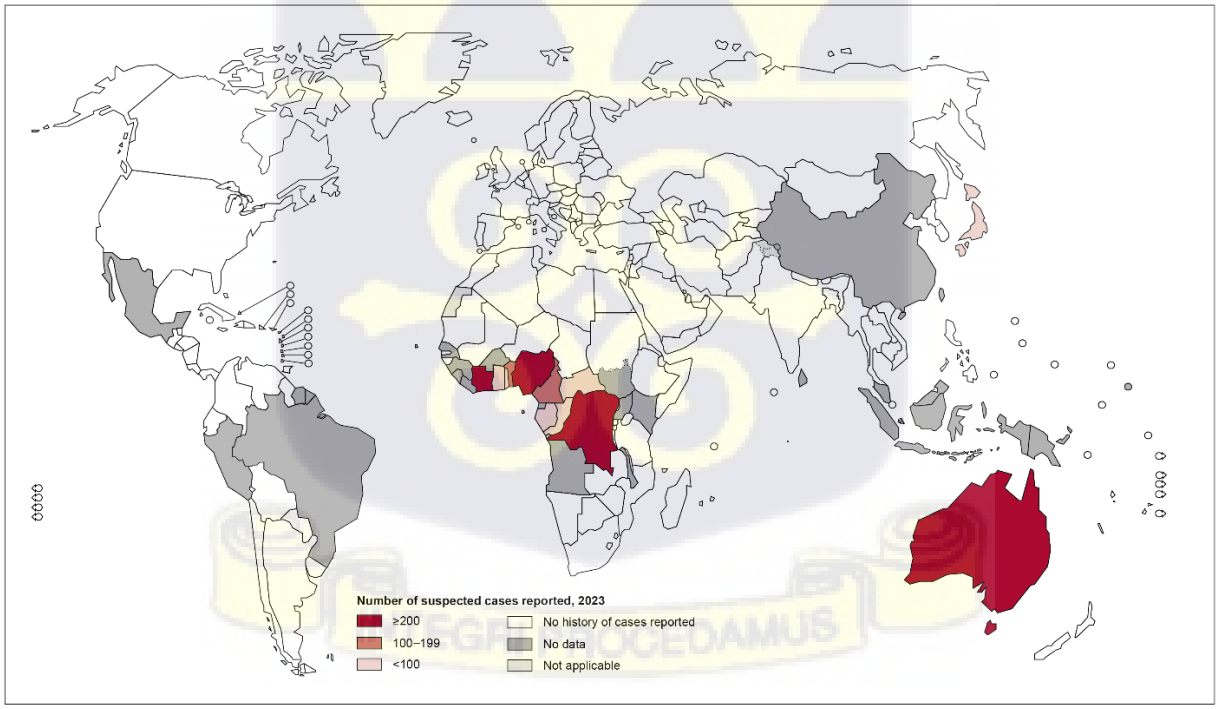

Figure 1.3. Global map showing the distribution of Buruli ulcer disease as of 2023. Data source: World Health Organization. Map production: Control of Neglected Tropical Diseases (NTD), WHO [46]

Between 2010 and 2023, 16 different countries – 14 in the African Region (AFRO) and 3 in the Western Pacific Region (WPRO) – reported 35,502 cases of Buruli ulcer to the WHO. There were 4,906 Buruli ulcer cases reported worldwide in 2010 alone, with 1,923 occurring in AFRO and 294 in WPRO. The annual case burden decreased overall from a peak of 4,906 cases in 2010 to 1,967 cases in 2016. However, the number of cases rose to 2,349 in 2017 (**Table 1.1; Figure 1.4A**), primarily due to a sharp increase in cases from Australia from 219 in 2016 to 311 cases in 2017. The other two WPRO countries of Papua New Guinea and Japan reported very few cases (**Table 1.1; Figure 1.4B**). Reported cases rose to 2,698 in 2018 before starting to decline to 2,271 in 2019, then, sharply declined to 1,459 in 2020 and 1,652 in 2021, respectively. There were 2,119 documented cases in 2022 and 1,952 in 2023. Following a decline in 2020, the number of cases recorded in Australia increased from 2021 to 2023 (**Table 2; Figure 1.4D**). The reported cases for the other WPRO essentially remained constants for the entire period (**Table 2; Figure 1.4D**). The disease is particularly common in Africa, where countries like Ghana, Nigeria, Cameroon, Benin, Côte d'Ivoire, and the Democratic Republic of the Congo have routinely reported more than 200 cases since 2010, a situation known as high burden (**Figure 1.4B**). The Central African Republic, Congo, Gabon, Guinea, Sierra Leone, South Sudan, and Togo are among the other low-burden African countries; their annual case reports range from 20 to 200 (**Figure 1.4B**). Australia has had the highest disease burden in the Western Pacific Region since 2016 whereas the low-burden WPRO countries include Japan and Papua New Guinea [46].

Table 1.1. Buruli ulcer cases reported to the World Health Organization, 2010–2023

	Number of suspected cases of Buruli ulcer reported														Total no. cases
Period	2010	2011	2012	2013	2014	2015	2016	2017	2018	2019	2020	2021	2022	2023	2002-2023
Region and country															
AFRO region															
Benin	572	492	365	378	330	311	312	267	219	240	197	178	166	146	4173
Cote d'Ivoire	2533	1659	1386	1039	827	549	376	344	261	251	231	239	271	207	10173
Cameroon	287	256	160	133	126	133	85	86	155	106	118	168	312	133	2258
CAR	ND	ND	ND	ND	ND	ND	ND	ND	ND	ND	ND	ND	ND	77	77
Congo	107	56	38	6	ND	ND	ND	ND	ND	ND	ND	199	107	83	596
DR Congo	136	209	284	214	192	234	175	120	99	41	334	259	558	332	3187
Gabon	65	59	45	59	47	43	39	45	29	21	24	40	29	24	569
Ghana	1048	971	632	550	443	275	371	538	630	296	127	52	106	81	6120
Guinea	24	59	82	96	46	72	72	98	102	ND	ND	ND	ND	ND	651
Liberia	ND	ND	21	8	ND	105	ND	219	323	ND	1	ND	ND	ND	677
Nigeria	7	4	40	23	65	114	235	259	424	943	150	203	216	482	3165
Sierra Leone	ND	28	ND	ND	ND	ND	ND	ND	ND	ND	ND	ND	ND	ND	28
South Sudan	4	ND	ND	ND	ND	ND	ND	ND	ND	ND	ND	ND	ND	ND	4

Togo	67	52	51	37	67	81	83	62	93	51	51	19	10	8	732
AFRO subtotal	4850	3845	3104	2543	2143	1917	1748	2038	2335	1949	1233	1357	1775	1573	32410
WPRO region															0
Australia	42	143	105	74	89	111	198	297	348	308	221	291	341	376	2944
Japan	9	10	4	10	7	4	2	7	3	3	5	4	3	3	74
Papua New Guinea	5	8	ND	ND	3	9	19	7	12	11	ND	ND	ND	ND	74
WPRO subtotal	56	161	109	84	99	124	219	311	363	322	226	295	344	379	3092
Global total	4906	4006	3213	2627	2242	2041	1967	2349	2698	2271	1459	1652	2119	1952	35502

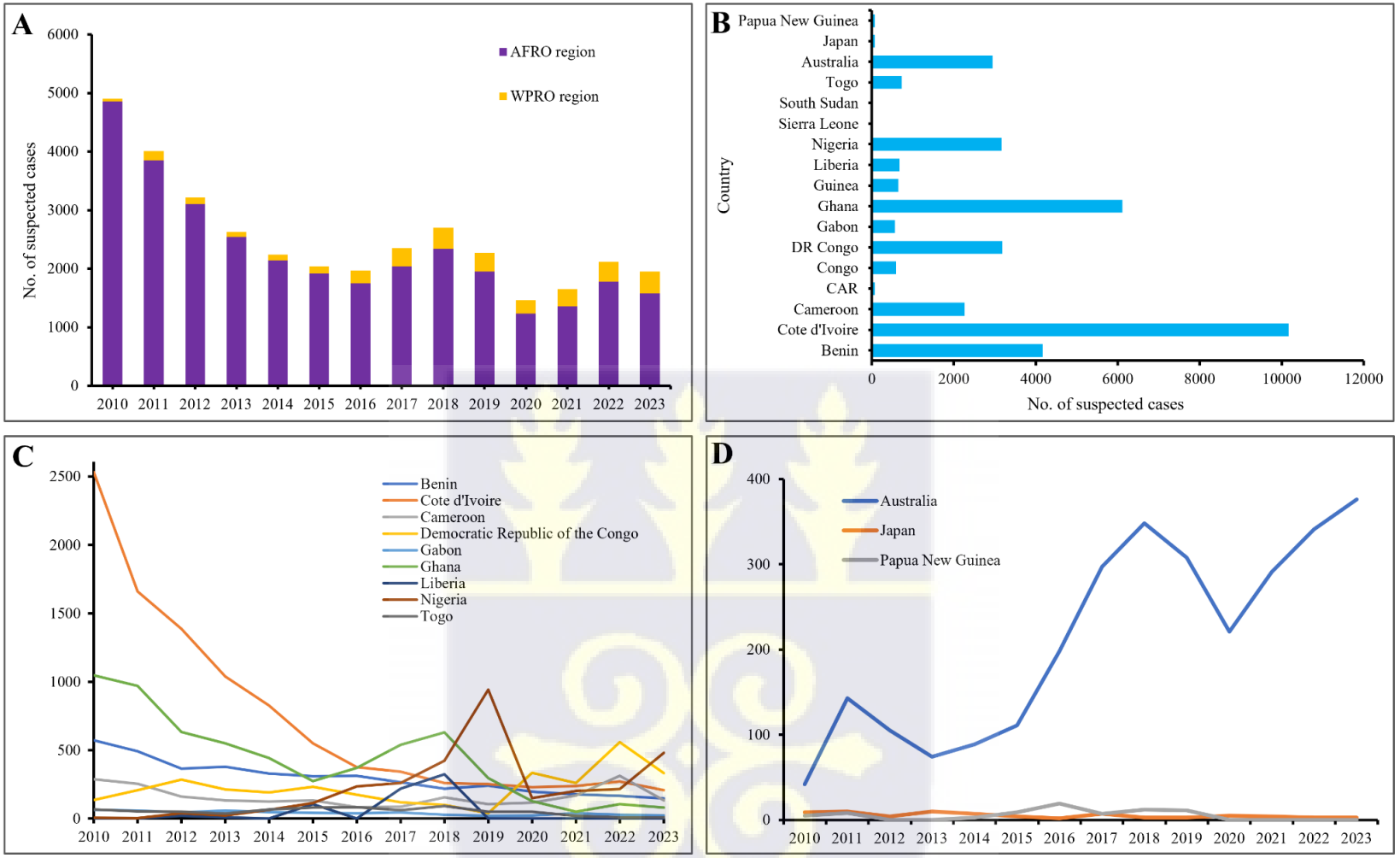

Figure 1.4. Buruli ulcer cases reported to the World Health Organization (WHO) in 2010–2023: A) Cases reported from the African Region and Western Pacific Region; B) Total number of reported cases between 2010 – 2023; C) African Region case trends; D) Western Pacific Region case trends.

1.5 Antibiotic treatment of BU disease

Despite the fact that Buruli ulcer was discovered more than a century ago and has been rapidly spreading since the 1980s, the mode of transmission of the disease remains unknown and poorly understood, making it difficult to implement effective prevention and control strategies [47]. Nonetheless, the effective management and control of BU rely heavily on early case detection especially Category I and II stages, followed by prompt diagnosis and antibiotic treatment [38]. Early diagnosis of Buruli ulcer is crucial in all settings in order to avert severe morbidities, high cost, and long-term disabilities associated with the disease [48].

A combination of antibiotics administered over an eight-week period is the mainstay of BU drug treatment. Rifampicin (RIF) (10 mg/kg once daily, oral tablet) combined with streptomycin (STR) (15 mg/kg once daily, intramuscular injection) is the current World Health Organization (WHO) recommended regimen. For the last four weeks of the eight-week regimen, the injectable STR has recently been replaced with oral clarithromycin for smaller lesions (**Figure 1.5**) [30, 49-51].

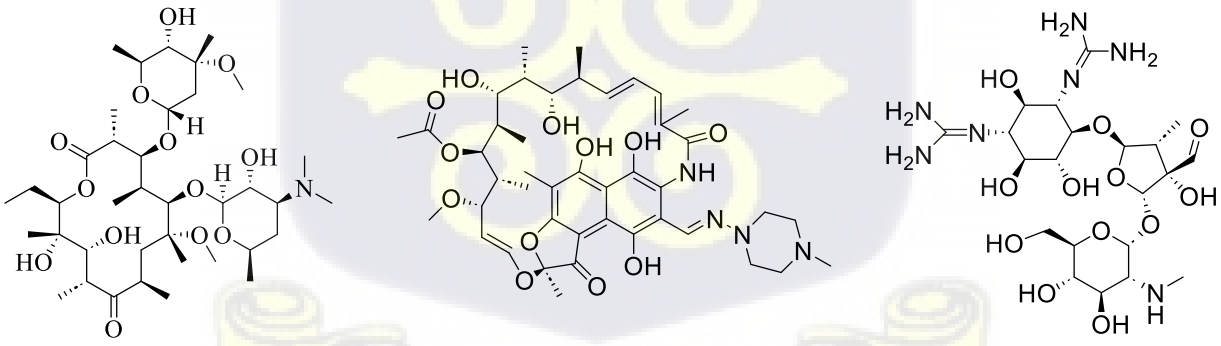

Figure 1.5. Mainstay antibiotic drugs for combination therapy of BU.

1.6 Laboratory Diagnosis of Buruli Ulcer and Associated Challenges

Currently, the diagnosis of BU is based on direct detection of acid-fast bacilli (AFB) by smear microscopy, culture of *M. ulcerans*, histopathology, and Polymerase chain reaction (PCR) targeting the multicopy insertion sequence IS2404 (**Figure 1.6**) [52-54].

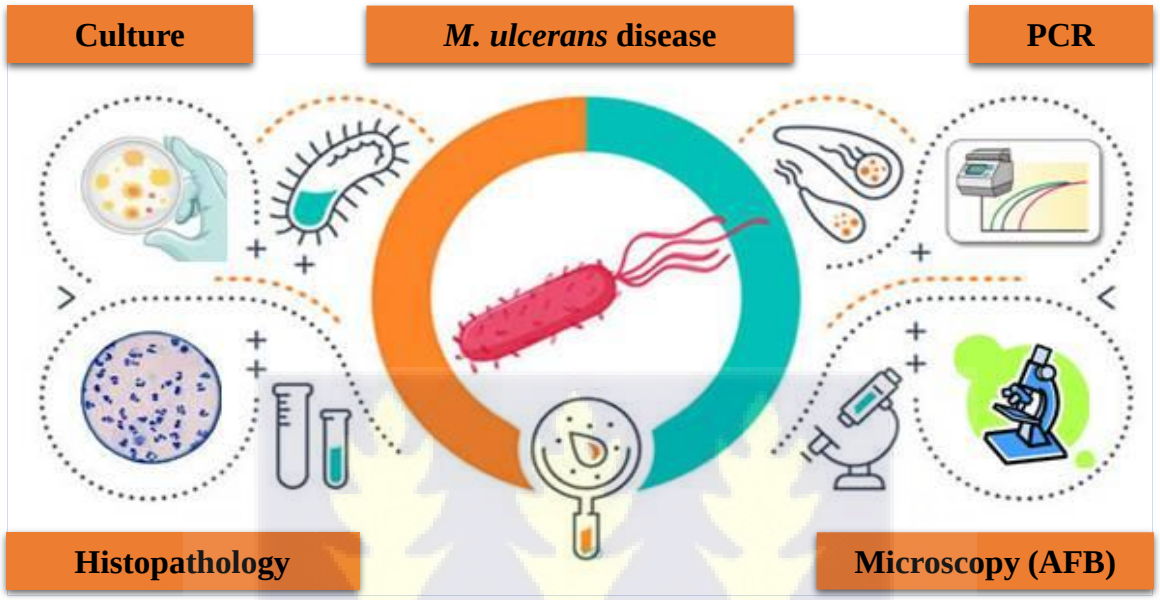

Figure 1.6. Standard diagnostic tools for Buruli ulcer.

The challenge is that all current diagnostic options have major limitations. For instance, culture, histopathology, and PCR are expensive and require sophisticated infrastructure, good laboratory infrastructure and instrumentation, highly skilled and experienced personnel, and strict quality control [40, 55]. In general, diagnostic services for BU are largely restricted to reference centres. Also, MU is an extremely slow-growing mycobacterium that takes several weeks (8 to 12 weeks) to be cultured for primary mycobacterial culture isolates. Therefore, the turn-around time for results to be obtained is too long making culture an impractical pre-treatment or pre-surgical diagnosis tool. Primary cultivation of *M. ulcerans* is therefore carried out primarily for research purposes [48], including the monitoring of the effectiveness of new treatment approaches [51, 56] and the distinction between paradoxical reactions and treatment

failures [57, 58]. In addition, *M. ulcerans* isolates have been used for molecular epidemiological studies [59-61] and are used for the surveillance of the potential emergence of drug resistance.

Microscopy is fast and inexpensive hence, the only test that can be implemented at the district hospital level, however, it has been reported to have relatively low sensitivity. Histopathology and PCR on the other hand offer high sensitivities [40] – the sensitivity of histopathology, for instance, is about 90%, however, it requires invasive procedures such as biopsies [62]. In addition, it is relatively costly and labour-intensive, as such, it is rarely available in most endemic countries such as sub-Saharan Africa [40]. Even in developing countries with reference facilities, a close linkage between the laboratories and peripheral treatment centres does not exist. Thus, testing of specimens in reference centres may not be performed regularly. If histopathology is carried out, the turnaround time for results may be too long to allow a pre-surgical diagnosis. Thus, diagnostic information is available only after the patients have already been treated surgically.

The other highly sensitive PCR technique is equally specific – approaching 100% specificity. As such, it is currently the "gold" standard diagnosis tool in reference laboratories in most endemic countries and is, therefore, widely used for the diagnosis of BU. In resource-poor settings with reference facilities, PCR-based laboratory diagnosis is most often hampered by logistical challenges and high costs. There is also the challenge of delayed transport of clinical specimens to reference laboratories which ultimately results in delayed diagnosis and delayed initiation of treatment for patients thus contributing to morbidity and increased economic hardship [63]. Despite the high sensitivity of PCR, it cannot be used in low-resource rural settings that suffer the greatest disease burden. Owing to these challenges, the diagnosis of BU at remote health facilities in endemic developing African countries still relies primarily on

clinical judgment [48]. There are similarities between ulcerative BU lesions and some important diseases including tropical phagedenic ulcers, chronic lower leg ulcers, diabetic ulcers, cutaneous leishmaniasis, and extensive yaws. Also, early nodular lesions of BU are occasionally confused with boils, lipomas, ganglions, lymph node tuberculosis, and onchocerciasis nodules [42]. Therefore, over the years, differential diagnosis relying on the experience of local health professionals has become challenging because of the possibility of misdiagnosis. Therefore, the World Health Organization (WHO) prioritizes an urgent need for a sensitive, specific, simple, cheap, and rapid point-of-care (POC) diagnostic test for BU, which can suitably be applied for in-field use [64]. In addition, the diagnostic test should be able to return a laboratory confirmation of at least 70% of the cases [65].

1.7 Motivation and Research Goal

The pathogenesis of Buruli ulcer is closely related to the production of mycolactone which is understood to be responsible for the cytotoxicity, painlessness, tissue necrosis, and immunosuppressive properties associated with the disease [11, 14-16, 23, 66]. *M. ulcerans* is the only mycobacterium among the human pathogens that produce mycolactone, a distinctly unique toxin that has been demonstrated to be more widely distributed within infected lesions than the bacilli itself [11, 39, 67]. For these reasons, mycolactone has become an attractive target molecule and a potential biomarker for disease diagnosis as well as for treatment monitoring. Thus, any useful tool developed for the detection of mycolactone could have an impact on clinical diagnosis with the potential to improve the outcome of BU management.

Although mycolactone has not been fully incorporated into diagnostic tools, several techniques have been established to identify and quantify it; these techniques include cytotoxicity assays [14-16], mass spectrometry [16, 68, 69], and thin-layer chromatography (TLC) [11, 70]. Other methods including RNA aptamer binding [71], loop-mediated isothermal amplification

(LAMP) [65, 72], and liquid chromatography mass spectrometry (LC-MS) [16, 73] have also been investigated for the identification of mycolactone from patient biopsy samples. As with the existing standard diagnostic methods including PCR, histopathology, microscopy, and culture, most of these approaches are expensive, unsuitable for use in the field, and require extensive sample preparation by qualified professionals. Kishi and co-workers developed the fluorescent-thin layer chromatography (f-TLC) method that focused on the direct detection of mycolactone as a biomarker using 2-naphthylboronic acid as a stain. This technique addressed most of the concerns of previous tools such as low sensitivity for microscopy and culture, long turn-around time for culture, requirement of sophisticated laboratory and well-trained personnel with specific equipment for PCR and histopathology – plus, it is operationally simple, rapid, and cost-effective [74-77].

Inspired by the successes of using a boronic acid as the reporting unit in the f-TLC technique, the ability of the boronic acid functional group to couple to the 1,3-diol moieties in mycolactone, their stability, environmental friendliness, generally non-toxic and relatively inexpensive nature, my goal was to explore these properties to develop colourimetric or fluorescent arylboronic acid-based chemosensor dyes that can recognize the 1,3-diol moieties of mycolactone with higher affinity, selectivity, and sensitivity taking advantage of the boronic acid unit. The competitive advantage of fluorescent and colourimetric chemosensors is that they provide an attractive alternative by conferring a high degree of selectivity and sensitivity towards diols. They could potentially yield a diagnostic tool that fulfils the requirement of being sufficiently rapid and unambiguous taking advantage of a colour change that could be discerned with the naked eye, and thus, fit-for-purpose for non-specialist use. Above all, it could be used in the field by a non-expert user (e.g. a village resident, non-literate) and requires no electrical supply or specialist equipment.

Therefore, the main goal of the research described in this thesis is to develop an improved method based on molecular recognition of the 1,3-diols moieties of mycolactone that largely satisfy the REASSURED criteria (Real-time connectivity, Ease of specimen collection, Affordable and cost-effective, Sensitive, Specific, User-friendly, Rapid and robust, Equipment-free, and Delivered to those who need it) [78].

1.8 Thesis objectives

Boronic acids have been known for decades to form cyclic boronate esters with both *cis*-1,2- and 1,3-diols through covalent bonding [79-82]. Consequently, boronic acids have attracted considerable interest in molecular recognition taking advantage of this unique intrinsic affinity for 1,2-cis and/or 1,3-cis diols.

The latest diagnostic method that utilizes the derivatization of diol motifs of mycolactone using a 2-naphthylboronic acid forms six-membered cyclic boronate esters (**Figure 1.7**) [74, 77, 83]. Accordingly, 2-naphthylboronic acid and mycolactone proved to successfully work as an acceptor–donor FRET pair. The boronic acid unit reacts selectively with 1,3-diol(s) moieties of mycolactone to form boronate esters which significantly enhances fluorescent intensity. The proposed general mechanism of involves the FRET process, where a donor, in this case the pentaenoate chromophore of mycolactone is excited at a defined wavelength (365 nm), and the energy is transferred, via non-radiative dipole–dipole interactions, to a properly selected acceptor (the 2-naphthylboronic acid), which emits through radiative relaxation. The free 2-naphthylboronic acid with the lowest (n–p*) excited singlet state (S1) has the lower absorptivity and so it is non- or weakly fluorescent. On the other hand, the hybridization of boronic atom plays a secondary role in affecting fluorescence intensity. Therefore, binding with mycolactone at the right temperature results in the formation of the cyclic boronate in which

the hybridization of boron atom changes from sp^2 to sp^3 has the lowest (p–p*) excited singlet state and should resulting in large enhancement of fluorescence emission (**Figure 1.6).**

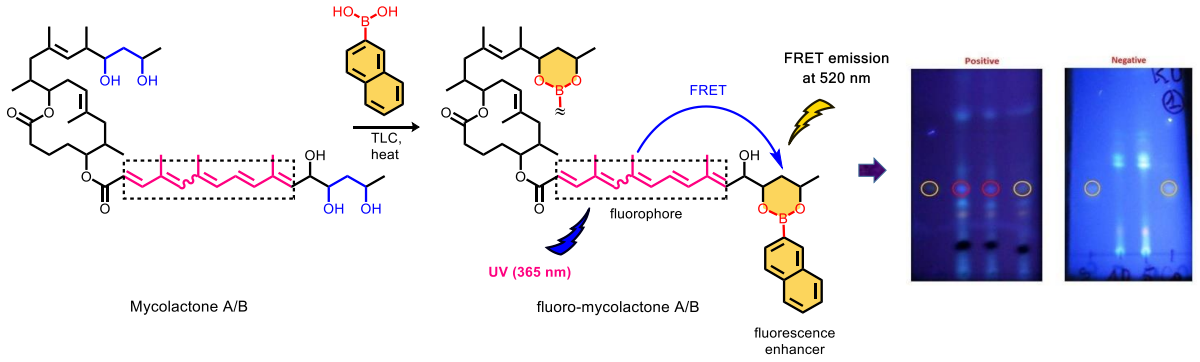

Figure 1.7. A schematic representation of the proposed mechanism of fluorescence of mycolactone and 2-naphthylboronic acid as observed on TLC.

There is also the proposed mechanism of fluorescence where the 2-naphthyl functional group also acts as an excellent fluorescent enhancer. The 2-naphthyl group stimulated the polarization of C–B bond due to its extended π-conjugation and induced the production of rapid signal because of the highly polar C–B bond along with the corresponding boronate unit (Figure 1.6). Though the use of 2-naphthylboronic acid enhances the fluorescence resulting in easier detection of mycolactone, evaluation of the method using clinical samples showed that the fluorescence was generally weak [76]. I hypothesized in this work that boronic acids with extended conjugations could be combined with mycolactone A/B in a similar manner as 2-naphthylboronic acid to form cyclic boronates with improved fluorescence. Therefore, I would attempt to address this by:

Objective 1: Searching for boronic acids with extended conjugations that offer improved fluorescence intensity when coupled to mycolactone as an alternative to the original 2-naphthylboronic acid by screening commercially available boronic acids.

The pathogenesis of *M. ulcerans* disease is widely dependent on the activity of the unique toxin called mycolactone [11]. The other more important and notable characteristic of the mycolactone is that it is only produced by *Mycobacterium ulcerans*, therefore, any method that accurately detects this biomolecule could potentially have an impact on the clinical diagnosis of Buruli ulcer disease. As a result, Kishi and colleagues developed a sensitive and practical f-TLC technique for the detection of the toxin. Here, 2-naphthylboronic acid is coupled to mycolactone A/B and can be detected on a TLC plate as a adduct. The method holds great promise because it is relatively cheaper, simple-to-use, and rapid [74]. Although the method has been successfully evaluated using clinical samples [75, 76], it is hampered by the fact that it is non-quantitative. There are also concerns of interferences from other co-extracted and co-eluted lipids which make reading the results of method subjective [76]. There is a need to improve upon the low detection and quantification rates as well as discriminate the mycolactone from other autofluorescent co-extracted human tissues. In this project, I sought to address these principal challenges associated with the f-TLC technique for the diagnosis of Buruli ulcer by the following strategy:

> **Objective 2:** Explore the potential of High-Performance Thin Layer Chromatography (HPTLC) for the detection and quantitative assessment of mycolactone A/B in patient samples.

Boronic acid-based fluorescent chemosensors have shown great promise for the detection of various species in real-world situations [84]. They have become popular as sensors for monosaccharides and in particular glucose [85], various polysaccharides, dopamine, glycoproteins and glycated haemoglobin [86-92], ionic compounds [93-95], water traces in solvents [96, 97], hydrogen peroxide (H_2O_2) [98, 99] and catecholamines [100]. Boronic acids have also been employed as biochemical tools for a variety of applications, including but not

limited to enzyme inhibitors [101], cell delivery methods [102], whole-body diagnostic imaging [103], and tumour cell imaging [104, 105]. Considering the broad application of boron-based fluorescence sensors, I sought to incorporate the boronic acid motif into various fluorescent dyes as chemosensors for mycolactone by:

> **Objective 3:** Rational design and synthesis of a library of new fluorescent arylboronic acid chemosensor dyes to assess their potential to recognize mycolactone with improved selectivity, high affinity, specificity, and sensitivity.
>
> **Objective 4:** Full characterization of all synthesized fluorescent arylboronic acid chemosensor dyes using a set of complementary techniques and laboratory equipment within organic and synthetic chemistry comprising: NMR, LC-MS, FT-IR, and X-ray crystallography.

Neutral boronic acids are electrophilic because of the vacant p-orbital on the boron, and thus, are highly reactive toward nucleophiles, such as diols [106]. The interaction between a boronic acid and a diol is one of the most powerful functional group interactions [107]. My expectations were twofold: first, like the simple boronic acids and diols, I expect the newly synthesized chemosensors that incorporate a boronic acid motif on various dyes with an empty sp^2 hybridized *p*-orbital of the boron centre with O−B−O bond angle of ~120° to readily bind covalently to 1,3-diols moieties of mycolactone and adopt sp^3 hybridization in the cyclic boronate ester product with the boron adopting a tetrahedral configuration with O−B−O ~109.5° as those in literature [106]. Secondly, I anticipate this to trigger a change in the spectroscopic properties because of significant perturbation of the π system. Therefore, following the successful synthesis and characterization of various fluorescent arylboronic acid chemosensor dyes, I shall:

Objective 5: Perform binding studies of the newly synthesized arylboronic acid chemosensor dyes for the 1,3-diols of mycolactone by monitoring the colourimetric and fluorescence intensity changes using UV-Vis and fluorescence spectrophotometry tools with the view to investigating the affinity and selectivity.

CHAPTER TWO

2 Literature Review

2.1 Background

Buruli ulcer (BU) is a destructive mycobacterial disease of the subcutaneous tissue caused by *Mycobacterium ulcerans (MU). M. ulcerans* is related to the family of acid-fast bacilli mycobacterial diseases such as *Mycobacterium tuberculosis* and *Mycobacterium leprae* that cause tuberculosis and leprosy respectively [8, 9]. Unlike TB and leprosy, it is the least prevalent globally and human-to-human spread of BU is rare [7]. BU has been reported to be endemic in at least 33 tropical and subtropical countries globally with the highest prevalence and incidence occurring in West and Central African countries including Benin, Côte d'Ivoire, the Democratic Republic of Congo, and Ghana [1, 108]**.** The disease affects predominantly children under the age of 5 and 15 years particularly in Africa, unlike Australia where the reverse is true [109].

The natural history of BU usually begins as a small painless subcutaneous nodule, or other pre-ulcerative forms such as papules, plaques, and oedema that progress into large necrotic skin ulcerations with characteristic undermined edges that may cover 15% of a patient's skin, if left untreated [15, 110, 111]. Extreme forms of the disease such as osteomyelitis extend to the bones of infected persons. Large and severe ulcers result in protracted healing which leads to significant cosmetic and functional deformities and disabilities, particularly in children, who if healed, leave behind scarring, disfigurement, and joint contractures [1]. As a result of the devastating consequences presented by the disease, the World Health Organization (WHO) has listed BU as a top-ranking and emerging neglected tropical disease (NTD) [42-44].

2.2 Etymology of Buruli ulcer

Historically, there is an intriguing connection between Buruli ulcer and Nile mythology. Early in the 1860s, the Royal Geographical Society of London organized an expedition and in October of the same year, Captains John Hanning Speke and James Augustus Grant set out from Zanzibar "with the view to discover, if possible, the sources of the Nile" [112]. Their expedition confirmed that the White Nile does indeed originate in Lake Victoria (previously Lake Nyanza) and more precisely the Ripon Falls at the Lake's northern end. Captain James Augustus Grant wrote about their expedition in search of the White Nile's source. Sadly, Grant contracted a mystery disease in December 1861 and was bedridden for five months, so he was not on the shores in July 1862 when Lake Victoria was named as the source of the Nile. From Grant's intriguing narrative of these explorations which was published in 1864 titled, "A walk across Africa or domestic scenes from my Nile journal", he described how the infection that he contracted in December 1861 kept him from joining Speke on the shore of Lake Victoria in July 1862 [113]. In the detailed first-person narrative of his ailment, he wrote: "*The right leg, from above the knee, became deformed with inflammation, and remained for a month in this unaccountable state, giving intense pain, which was relieved temporarily by a deep incision and copious discharge. For three months, fresh abscesses formed, and other incisions were made; my strength was prostrated; the knee stiff and alarmingly bent, and walking was impracticable*" [114]. Captain Grant might have described what is regarded today as the first account of the earliest reported case of Buruli ulcer. This vivid description showed similar indications of the oedematous form of Buruli ulcer that occurs in Western and Central Africa [115].

In 1897, a British missionary physician Sir Ruskin Albert discovered Buruli ulcer at Mengo Hospital in Kampala, Uganda and provided the first clinical description of the disease. In his

case report, Cook detailed uncommon ulcers from Kampala Hospital in Uganda with admission diagnosis of "tubercular ulceration of arms and legs" [116-118]. Later, from 1920 – 1935, Kleinschmidt, another missionary physician in north-east Zaire (now Democratic Republic of the Congo), also indicated the presence of the disease in Uganda and northeast Zaire. Kleinschmidt observed ulcers with large numbers of acid-fast bacilli and undermining skin [67].

As early as 1937, the disease was identified in Bairnsdale in Victoria, South-East Australia by two medical physicians, Alsop and Searls. An epidermic that was later confirmed as BU disease broke out in 1939 following catastrophic rainfalls in the State of Victoria in 1935 [119]. However, it was only in 1948 that Australian pathologist Peter MacCallum and colleagues who were caring for patients at Bairnsdale hospital provided the first thorough description of BU disease. In a seminal report, they described in detail the histopathological characteristics of six Australian patients from rural riverine regions who each had an unidentified single ulcerative lesion with undermined edges on an arm or a leg. The histopathologic findings included extensive necrosis and a large number of acid-fast bacilli without the formation of granulomas [8, 120]. Although there was no evidence of tuberculosis, the ulcers had undermined edges, but with no other signs of tuberculosis except one patient who had a positive tuberculin skin test result. Acid-fast bacilli were present in histological specimens [121]. Initial attempts to cultivate the bacterium with different types of media, atmospheres, and temperatures failed but were finally achieved serendipitously with the inadvertent use of a faulty incubator delivering a controlled 33 °C [118]. It was therefore realized that in contrast to *M. tuberculosis* which can be grown at 37 °C, *M. ulcerans* requires optimal temperatures above 25 °C, but below 37 °C (ideally 30–33 °C) for growth although this growth is quite slow with a doubling time between thirty-six and eighty hours [8, 122]. This optimum temperature is consistent with the primary localization of the microorganisms in the subcutaneous tissue and lower dermis of infected

humans, as suggested by Buckle and Tolhurst in the original 1948 report [122] and later confirmed by Fenner in 1956 [123]. Additionally, it was later demonstrated that low oxygen levels were crucial for cultivating this extremely slow-growing mycobacterium [124].

Since the establishment of the aetiology of the disease by MacCallum and co-workers among a small group of 6 patients in the Bairnsdale region of Victoria, Australia, the mycobacterium was tentatively dubbed "Bairnsdale ulcer", after the region where five of the six patients resided [8]. A few years after they were first described, *M. ulcerans* cases were also observed in Uganda [125-127] and the modern day Democratic Republic of Congo [128]. The name Buruli ulcer was proposed after the Buruli County in Mengo district (today Nakasongola district) near Lake Kyoga in Uganda, a semi-arid area where large numbers of cases were reported in the 1960s [129, 130]. The term "Buruli ulcer" was thus first proposed in 1972 by Clancey, Dodge, and Lunn in Uganda following outbreaks in other African countries [125, 129]. Searls ulcer or Daintree ulcer are other names of Buruli ulcer. Chronologically, despite WHO approving the name Buruli ulcer, Bairnsdale ulcer would also have been historically a correct denomination [131].

Buruli ulcer have a history in Africa that can be traced to pre 1980 and after 1980. Before 1980, several African nations, including Cameroon, the Democratic Republic of Congo, Gabon, Ghana, Nigeria, and Uganda, published significant works on the occurrence of the disease. Cases were suspected but never verified in the United Republic of Tanzania, Kenya, Sudan, a nd the Central African Republic [1]. The most significant prevalence came from the Democratic Republic of the Congo and Uganda [129]. West Africa saw the emergence of new Buruli ulcer foci after 1980. In many West African nations, particularly Benin, Côte d'Ivoire, Ghana, and more recently, Angola, Burkina Faso, Guinea, and Togo, there has been a sharp rise in the incidence of disease [1, 132, 133].

2.3 *Mycobacterium ulcerans* and its unique toxin mycolactone

2.3.1 *Mycobacterium ulcerans*

Mycobacterium ulcerans, first identified in 1947 is a pathogenic non-tuberculous mycobacterium (NTM) responsible for causing Buruli ulcer [36]. *M. ulcerans* is a bacterial pathogen that is acquired from the natural environment. It has long been associated with aquatic and swampy environments, particularly proximity to stagnant or slow-flowing watercourses [134]. *M. ulcerans* is known to adapt to certain ecological niches and is believed to reside in natural environments where oxygen, pH, and availability of nutrients are likely to modulate its proliferation and production of mycolactone [124, 135-137]. There is evidence that it can also be hosted and transmitted by living organisms such as aquatic insects [138], mosquitoes [139], fish, and amphibians [140]. Despite the long-known association of *M. ulcerans* with riverine areas and wetlands as natural reservoirs [127, 141], the disease is sometimes referred to as the "mysterious disease" because its route of transmission is still elusive and remains obscure although several hypotheses have been proposed [142-144].

2.3.2 Mycolactone: The unique toxin behind *Mycobacterium ulcerans*

Even though most pathogenic bacteria produce toxins that play an important role(s) in pathogenicity, there has been no evidence thus far to suggest toxin production among the two other most-recognized pathogenic members of the genus Mycobacterium: *Mycobacterium tuberculosis* and *Mycobacterium leprae.* Therefore, *Mycobacterium ulcerans* is unique among human pathogens in its capacity as the only mycobacterium species among the mycobacteria family to produce and secrete a potent cytotoxin [145]. In 1965, Connor and colleagues suggested that *Mycobacterium ulcerans* played a key role in producing the exotoxin [3]. Later, in 1974, two follow-up reports by Conner and colleagues supported this hypothesis by showing that injecting culture filtrates of various *M. ulcerans* strains into mouse footpads and guinea

pig epidermis had effects that were similar to those generated by inoculation of animals with the actual organism [14, 146]. However, it was not until 1998 that the true nature of the toxin was identified by Small and co-workers [11]. The toxin was successfully isolated and purified from the acetone-soluble lipid extracts of *M. ulcerans* and characterized initially by thin-layer chromatography and mass spectrometry (MS). The toxin was identified as a light-yellow band on TLC with a retention factor (R_F) of 0.23 using chloroform : methanol : water (90:10:1) as the solvent system [11]. MS analysis of the toxin under electrospray ionization in positive ion mode showed an abundant sodium adduct $[M + Na]^+$ of mycolactone signal at *m/z* 765.5. Subsequently, the complete chemical structure of the toxin was resolved to be a 12-membered polyketide macrolide called mycolactone (**Figure 2.1**) [10, 11, 147].

The toxin is an essential virulence factor of *Mycobacterium ulcerans* and plays a central role in pathogenesis hence appropriately classified as the causative toxin of Buruli ulcer [70, 148]. The toxin has been reported to be responsible for tissue necrosis, painlessness, and immunosuppressive properties [11, 23, 66, 83, 149]. This has been demonstrated in animal models where studies have shown that intradermal inoculation of the purified mycolactones into guinea pigs produced characteristic lesions similar to that of Buruli ulcer in humans [70]. In mice, mycolactones are associated with vacuolar nerve tissue injury, which might account for the painlessness of BU lesions [150]. Mycolactone has also been demonstrated to induce necrosis and ulceration by its cytotoxic and immunosuppressive properties [149, 151, 152]. Furthermore, mycolactones have been shown to act both *in vivo* and *in vitro* on various mammalian cell types, including fibroblasts,[68, 70, 153-155] adipocytes, [156] keratinocytes, [151] myocytes, [157, 158] macrophages, [17, 159-162] dendritic cells, [163] and T-cells [164, 165]. In all these cells, the effects caused by mycolactones include necrosis or induction of apoptosis in mammalian cells, [166] cytoskeletal rearrangements, impaired cytokine

production and interference with cellular signaling [167] and finally, down-regulates local and systemic immune responses by interfering with the activation of immune cells [153, 168].

Mycolactones are produced and secreted by a group of pathogenic mycobacteria species that are very closely related in their evolution. These mycobacteria are collectively referred to as mycolactone-producing mycobacteria (MPM). They have been assigned a variety of names including, *M. ulcerans*, *M. liflandii*, *M. pseudoshottsii*, and some strains of *M. marinum* [169-171]. Structurally, ten distinct variants of mycolactones encompassing nine naturally occurring members and one genetically engineered *Marinum* strain have been described so far. Remarkably, all known mycolactones amongst different *M. ulcerans* strains appear to contain the same macrolide core composed of an invariant core comprising a 12-membered lactone ring (**Figure 2.1**, **labelled red**) with a C11-linked northern acyl side-chain (**Figure 2.1**, **labelled blue**) but each is attached to a different highly polyunsaturated southern acyl side-chain that is esterified *via* a C5–O linkage (**Figure 2.1**, **labelled black**) [66]. Thus, while the macrolactone core structure together with the upper side chain are fully conserved, mycolactone populations from different *M. ulcerans* sub-lineages vary in the length, the number and localization of hydroxyl groups, and in the number of double bonds of the lower side chain [172]. Further work has revealed that the heterogeneity of the various toxins from different geographical sources with variations in the side chain structures could be traced to specific changes in the biosynthetic pathway [139, 173].

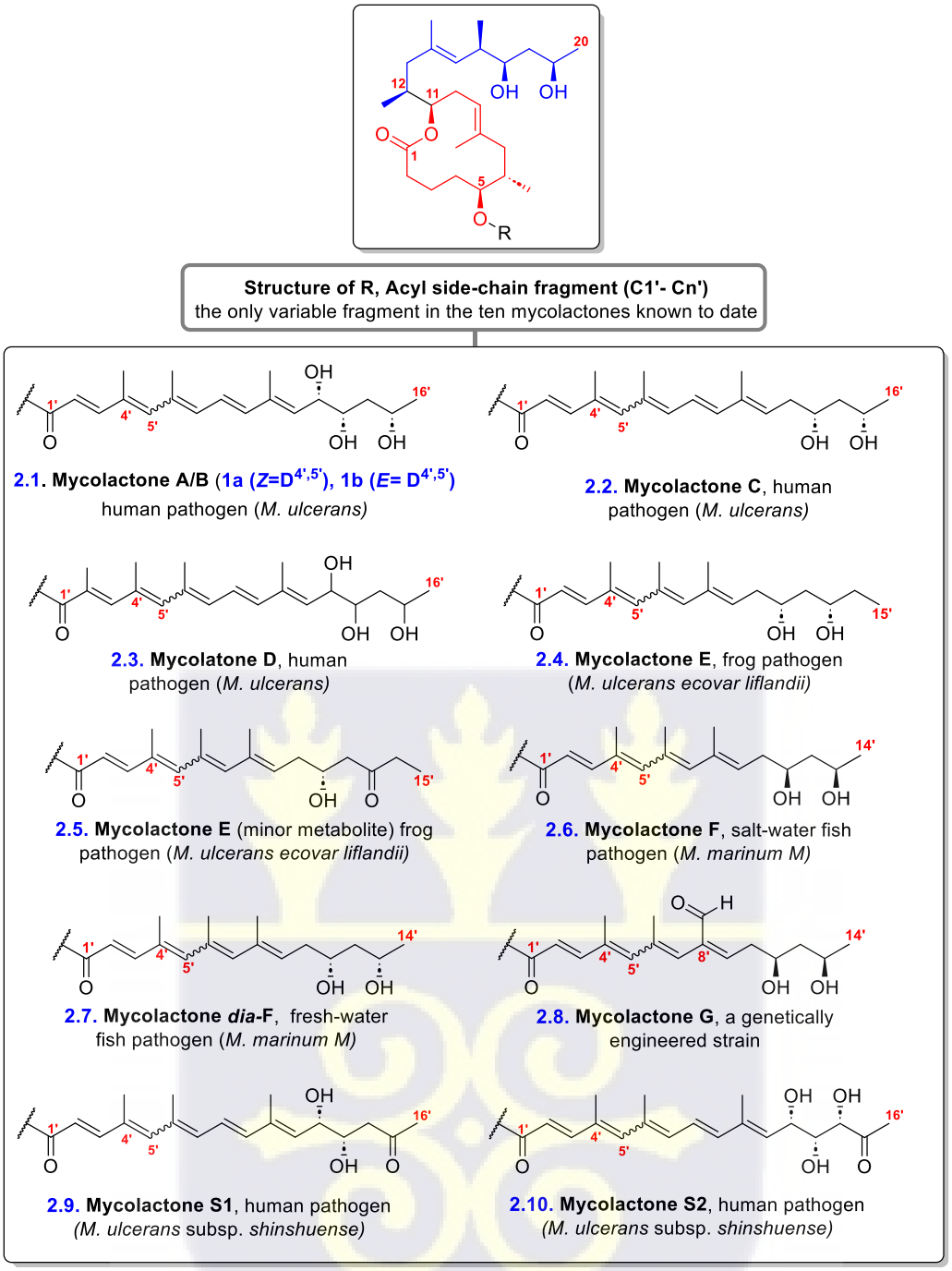

Figure 2.1. Structures of mycolactones A/B[171], C[172], D[174], E[174-176], E (minor metabolite) [174-176], F[155, 177], *dia*-F[178, 179], G[180], S1[181] and S2[181]. The macrolactone core is highlighted in red, the C-linked C12–C20 side chain is coloured in blue, and the polyunsaturated fatty acid side chain is shown in black.

All mycolactones have been shown to have cytotoxic [66], immunosuppressive [66, 149], and apoptosis-inducing [15, 151] effects. However, it has been noted that the potency levels of various individual structures vary noticeably. For example, a stereoisomeric mixture of mycolactones A and B isolated from the classical *M. ulcerans* lineage from West Africa is thought to be the most potent toxin, with the other mycolactones decreasing in potency as they are listed alphabetically [180]. Also, the highly virulent African and Malaysian strains of *M. ulcerans* produce the largest quantities of mycolactones A and B [172].

2.3.3 Gross molecular structures of mycolactone A/B

The gross structures of mycolactones A and B are composed of three different sectors: a 12-membered macrocyclic lactone core C1–C11 with two laterally attached side chains; a short northern C-linked side chain fragment comprising C12–C20; and a much longer southern C5-O-linked polyunsaturated, or fatty acid C1'–C16' acyl side chain fragment. The C1'–C16' acyl side chain is a sensitive conjugated pentaenoic acid ester possessing three stereogenic centres at C12', C13', and C15'.[167, 182]. The stereochemistry, relative and absolute configurations, and the complete structure of the mycolactone core have been established and confirmed by the combined use of an NMR database and a newly developed universal database concept in chiral solvents respectively by Kishi's group [183-185]. Subsequently, the assigned structure was confirmed by the preparation of model compounds through total synthesis [186, 187]. Importantly, through these efforts, mycolactones A and B are now characterized under standard laboratory conditions, as a mixture of two stereoisomers in an approximately 3:2 rapidly equilibrating mixture of *Z*-$\Delta^{4',5'}$ (mycolactone A) and *E*-$\Delta^{4',5'}$ (mycolactone B) geometric isomers centred around the double bond at C4′ C5′ (indicated by the wavy line) of the unsaturated side-chain having the stereochemistry as shown (**Figure 2.2**) [184, 185].

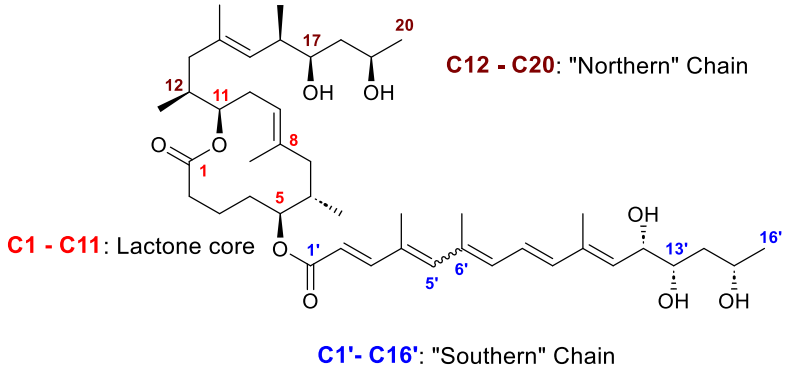

2.1

Figure 2.2. Molecular structure of mycolactone A/B. The chemical structure of mycolactone A/B has a core cyclic lactone ring (C1–C11) and two polyketide-derived highly unsaturated acyl side chains. The upper 'Northern' chain consists of C12–C20 and the longer 'Southern' chain is numbered C1′–C16′. Under common laboratory conditions and light, mycolactone exists as spontaneously forming geometric isomers centred around the double bond at C4′ C5′ (indicated by the wavy line between C5′ and C6′) in a 3:2 ratio.

2.3.4 Biosynthesis of mycolactone

Among the mycobacteria family, *M. ulcerans* are the only species known to produce a unique macrolide toxin called mycolactone, which promotes necrosis of subcutaneous adipose tissue surrounding sites of bacterial colonization [11, 156, 188]. The polyketide synthases (PKS) are responsible for the biosynthesis of polyketide macrolide in *M. ulcerans* and closely related mycobacteria that are encoded on the giant extrachromosomal plasmid of 174-kb called pMUM001 [189-191]. The mycolactone PKS modules and their constituent domains harbour three large genes (mlsA1: 51 kb, mlsA2: 7.2 kb, mlsB: 42 kb) encoding for three Type I PKS of unprecedented size, MLSA1 (1.8 MDa), MLSA2 (0.26 MDa) and MLSB (1.2 MDa) [192]. Each module of the different domains of MLSA and MLSB contains several enzymes (ketosynthase KS, acyltransferase AT, keto-reductase KR, dehydratase DH, and enoyl reductase ER) allowing the synthesis and the functionalization of the polyketidic chains. These genes possess very high DNA sequence identity (**Figure 2.3a**). The PKS has several highly

unusual features that have an important bearing on the structural basis of the specificity of polyketide chain growth on such multienzymes [190, 193, 194]. First, two of the multi-locus sequence PKS proteins; MLSA1 and MLSA2, are composed of a loading module, nine extension modules, and a terminal thioesterase (TE), whilst MLSB consists of one loading module, seven extension modules, and one thioesterase. More surprising still is the extreme mutual sequence similarity between comparable domains in all 16 chain-extension modules suggestive of very recent evolution [192]. The transcription of these PKS is done by a novel SigA-like promoter sequence [192, 195].

The proposed initial steps in the generation of the macrolide toxin involve the process where *mlsA1* and *mlsA2* synthesize the upper side chain and mycolactone core (C1–C20 fragment) of the mycolactones [190, 193, 194] whilst *mlsB* synthesizes its C1′–C16′ acyl side chain [145, 190]. A putative *beta*-ketoacyl transferase encoded by another pMUM gene, mup045, is thought to catalyse the ester linkage between the acyl side chain and the macrolactone core whilst a P450 hydroxylase, encoded by mup053, oxidizes the side chain at C12′ (**Figure 2.3b**) [170, 174, 190, 191]. A third gene, mup038, is predicted to encode a type II thioesterase that might be required for removing aberrant polyketide extension products from the *mls* PKS that form during synthesis. An unusual feature of the mycolactone PKS is the very high level of sequence identity between domains of the same function (98.7–100% nuecleotide (*nt)* identity and 98.3–100% amino acid (*aa)* identity) [145]. This observation suggests that the evolution of the locus may be recent and prone to rearrangements that result in either loss of mycolactone production or production of new mycolactones. These hypotheses have recently gained support from studies that have shown; (i) all mycolactone-producing mycobacteria (which includes *M. ulcerans* and some closely related fish and frog pathogens) have recently evolved from a common *Mycobacterium marinum* ancestor by pMUM plasmid acquisition [170, 196], (ii) laboratory passaging leads to mycolactone negative mutants through spontaneous deletion

of *mls* gene fragments [189], and (iii) natural swapping of particular acyltransferase and ketoreductase domains and loss or gain of entire extension modules in some strains of *M. ulcerans* has led to the production of new mycolactones [171, 174].

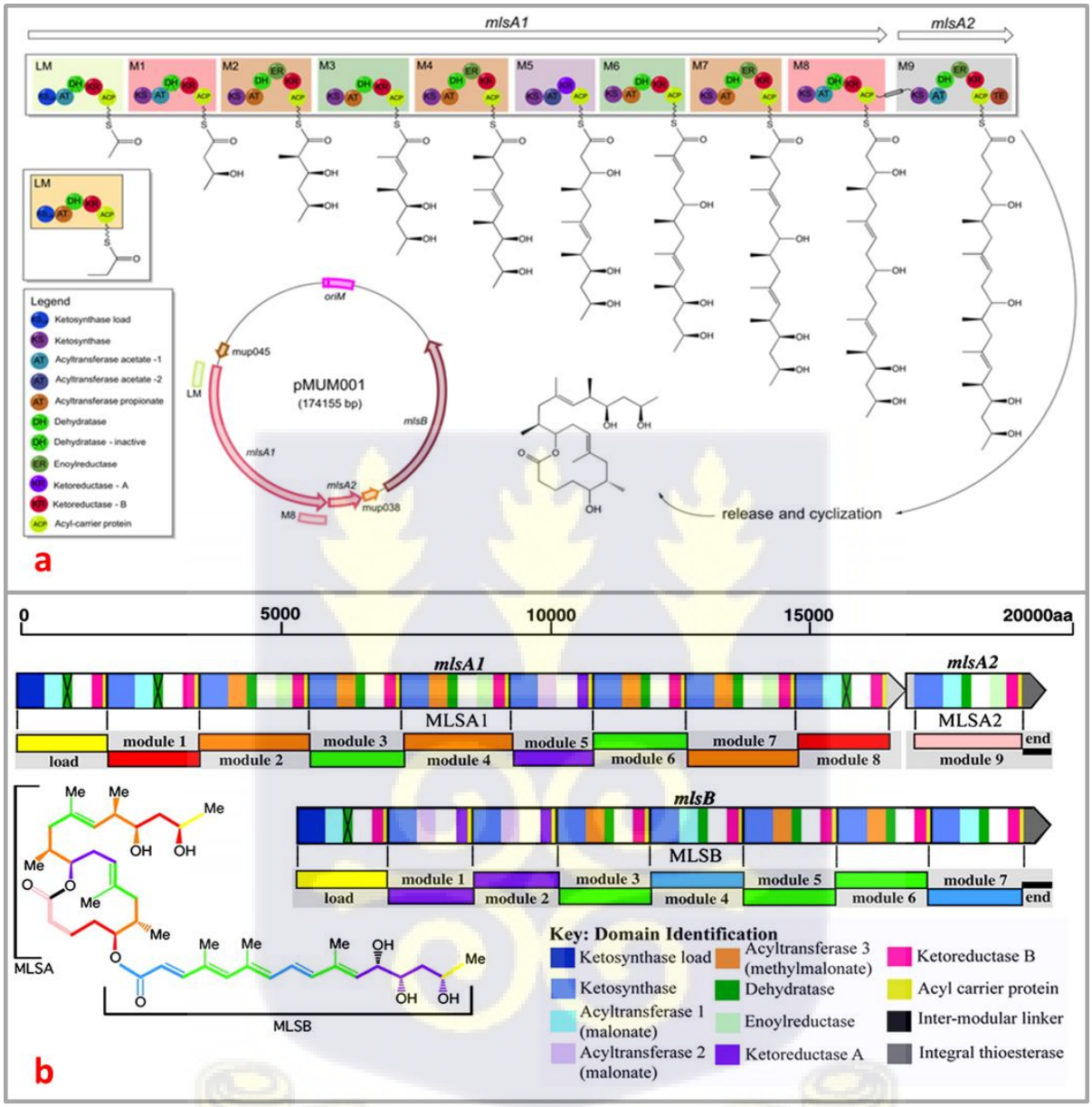

Figure 2.3. Overview of domain and module organization of the mycolactone PKS genes **(a)** *MlsA1* and *MlsA2* from the mycolactone PKS, harboured by the plasmid pMUM001 from *M. ulcerans* Agy99 [197, 198]; (b) Subunits (MLSA1, MLSA2, and MLSB) of different domains are represented by colour block [199].

2.3.5 Chemical synthesis of mycolactone A/B

Several biological studies have provided an early understanding of the role mycolactone plays in Buruli ulcer [17, 24, 153, 159, 161, 163, 200-203]. Studies have shown that increasingly, larger quantities (≥100 mg) of mycolactone A/B are required to help develop an understanding of the mode of action of these polyketides. Unfortunately, investigations of the various mycolactone structures and the explorations of their biological potencies have been seriously hampered by the slow growth of the host mycobacterium and the small (usually microgram) quantities of the toxin available from laboratory-scale culturing efforts respectively [204]. This has further been complicated by the fact that analysis of culture extracts of a typical strain of *M. ulcerans* revealed the presence of minor amounts of additional mycolactones, differing from mycolactone A and B only in the side chain thus, resulting in a clear difference between the *in vivo* and *in vitro* activity of mycolactone A/B [24, 66, 70, 158, 172]. For these reasons, interest from the scientific community on mycolactone is on a record high [205-207]. Even though the total synthesis of mycolactone is an extremely complicated process requiring substantial synthetic expertise, and thus limiting the production of this crucial toxin for research purposes [131, 182], the Kishi group made an outstanding contribution to mycolactone chemistry, synthesis, and research [83, 185-187]. Considering that mycolactone A/B were the first examples of polyketide macrolides to be isolated from a human pathogen, the synthetic work has largely been driven by the desire to afford researchers enough pure toxins as well as their analogues for systematic biological studies for their highly potent biological activity [205-207]. The first total synthesis of mycolactones A and B was achieved by the Kishi group, who also established the relative and absolute configurations and stereostructure of these natural products by chemical synthesis and extensive NMR spectroscopic studies [83, 185-187]. The Kishi group has elaborated first-[185, 187], second-[186], and third generation [208] approaches to the synthesis of mycolactone A/B as well as the syntheses for mycolactone C

[209], E [210], and F [179]. These ground-breaking works have offered efficient synthetic mechanisms of mycolactone A/B [83, 186]. Following these pioneering research, several research groups; Negishi [211], Altman [212], Burkart [207, 213], Gurjar [214], Feringa/Minnaard [205], Blanchard [215], Dai [216] and Aggarwal [217] have reported total and partial syntheses of the various mycolactones. More recently, modular synthetic approaches for the rapid production of diverse analogues of mycolactone A/B have also been described by Saint-Auret and co-workers [182, 215, 218, 219].

2.4 Mycolactone: the immunosuppressor, the analgesic and the cytotoxic toxin

Extensive ulcerative lesions observed in patients suffering from BU can be attributed to the secretion of mycolactone, the toxin produced by *M. ulcerans* [11]. Additionally, the toxin is widely accepted to be responsible for the painlessness that is characteristic of lesions caused by *M. ulcerans* especially in early stages of the disease where there are no concerns of co-infection [34, 111, 220]. Painlessness has been demonstrated in mice models where mycolactone was observed to induce long-lasting hypoesthesia [23, 24]. In recent years, the painless cytotoxin has also been demonstrated to be a natural immunosuppressor in cellular models [163, 165, 221-223]. Considering the role of mycolactone, various researchers have made significant contributions aimed at deciphering the molecular and pathogenic mechanisms underlying the action of mycolactone-mediated ulcerative, immunosuppressive and analgesic properties [19, 147, 222, 224-226].

2.4.1 Cellular targets responsible for the mechanism of action of mycolactone

Several cellular targets have been proposed by various studies to account for the numerous biological effects of mycolactone such as skin ulceration, host immunomodulation and analgesia. A number of internationally acclaimed scientists have studied mycolactone and proposed that its inhibitory mechanisms are accounted for by (i) inhibition of the WASP and

related neural N-WASP [19, 227], (ii) inhibition of Sec61-dependent translocation of proteins into the endoplasmic reticulum [222, 226], and (iii) inhibition of angiotensin II type 2 receptor (AT2R) as illustrated in **Figure 2.4** [23, 147, 228]. There is also the proposition that mycolactone acts as an inhibitor of mechanistic Target of Rapamycin (mTOR) which is attributed to the induction of apoptosis in mammalian cells [229].

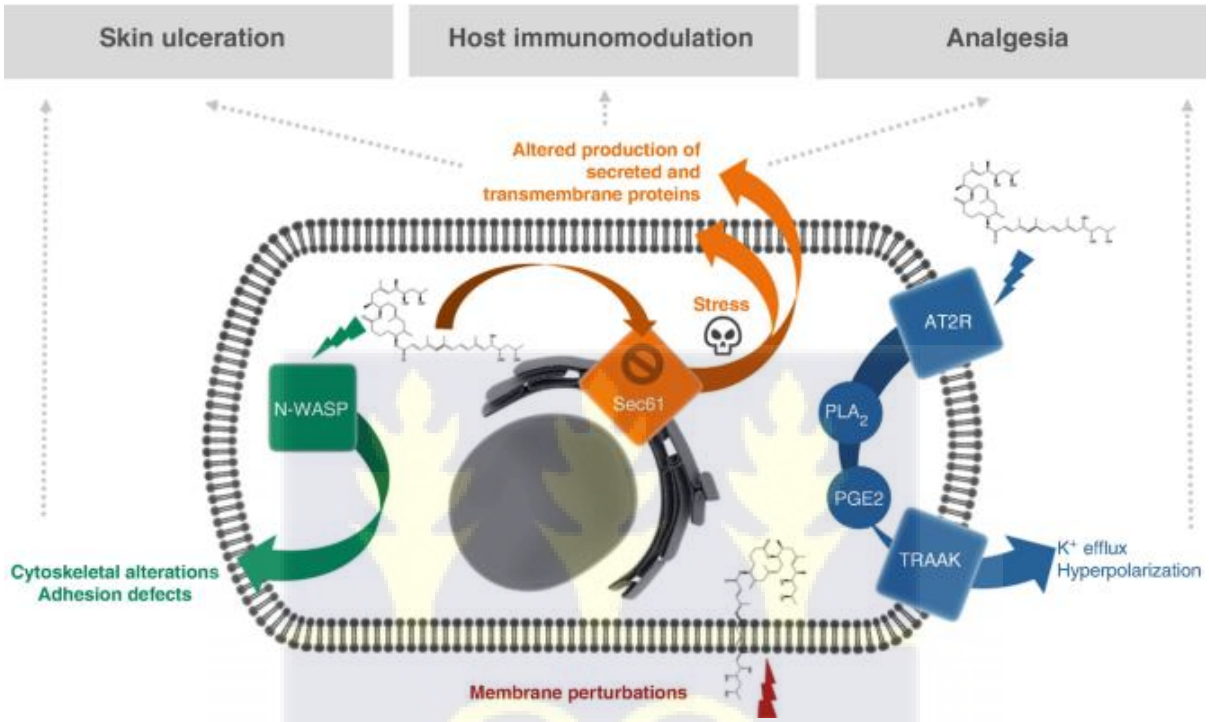

Figure 2.4. Proposed molecular targets and mechanisms of action for mycolactone-mediated ulcerative, immunosuppressive and analgesic properties [147].

2.4.1.1 Wiskott–Aldrich Syndrome protein (WASP) inhibition

The WASP and N-WASP have been identified as molecular targets of mycolactone. The WASP as mycolactone target was first reported by the Demangel group [19, 227]. WASP and N-WASP belong to a family of scaffold proteins that mediate the dynamic remodelling of the actin cytoskeleton [227]. In cell-free assays of actin polymerization, the mechanism involves mycolactone being able to mimic the endogenous GTPase CDC42, and thus able to hijack the WASP and N-WASP. It does so by binding into WASP and N-WASP and activating it with a 100-fold greater affinity than it binds to the natural activator CDC42. This results in alterations

in actin dynamics, leading to defective cell adhesion, uncontrolled directional migration and eventually leading to apoptosis. Thus, the mycolactone-driven destruction of cutaneous tissues and analgesia was attributed to hyperactivation of neural N-WASP (**Figure 2.4**). The neural form (N-WASPs) particularly plays a key role in the ulcerative effects of mycolactone and as a result, it is more expressed than its hematopoietic homolog, the WASP [23, 227].

2.4.1.2 Inhibition of Sec61

Proteins for the endocytic system originate by translation in the cytoplasm, and typically enter the endoplasmic reticulum (ER) cotranslationally. These nascent polypeptides usually enter the ER *via* the Sec61 translocon and engage the glycosylation process [230]. Sec61 translocation is responsible for the transport of about 30 to 50% of all mammalian proteins, including but not limited to circulating inflammatory mediators, immune mediators and proteins involved in lipid metabolism, coagulation, and tissue remodelling [228, 231, 232]. Just as with the N-WASP, the Sec61 translocon was also identified by Simmonds et al. as the second major primary cellular target of mycolactone (**Figure 2.4**). The Sec61 translocon is responsible for the co-translational translocation of newly synthesized proteins through the endoplasmic reticulum (ER) membrane. Therefore, its inhibition is thought to play a critical role in the expression of immune system mediator proteins. Cotransin, decatransin, apratoxin, ipomoeassin, cyclotriazadisulfonamide, and eeyarestatin are a few structurally different natural and synthesized small compounds that bind to Sec61 in a substrate-specific, selective way and prevent protein translocation [233]. Considering that the Sec61 translocon is a primary target of mycolactone, it was hypothesized that cellular effects including cytotoxicity of mycolactone could be attributed to its inhibitory effect on the translocon in the cytosol. Following this, Hall et al. demonstrated the ability of mycolactone to specifically block the Sec61 translocon and hinder protein translocation into the ER, thus causing the ubiquitin–proteasome system to

degrade the proteins in the cytosol. This potentially contributes to tissue damage, immunosuppression, and ultimately, cell death [222, 234]. This is corroborated by the findings of McKenna and colleagues who demonstrated using cell-free experimental assays that mycolactone selectively influences the step of cotranslational translocation of secreted transmembrane proteins (TMPs) into the ER [226]. In another study, Kawashima et al. screened host factors and investigated the mycolactone-induced cell death pathway in human premonocytic THP-1 cells using a genome-scale lenti-CRISPR mutagenesis test. This study was noteworthy since it revealed that SEC61A1, the α-subunit of the Sec61 translocon complex, is a crucial mediator of mycolactone-induced cell death [235]. Despite these findings, the mechanism behind the linkage between mycolactone translocation blockage and apoptosis-induced cell death remained unclear. Gérard et al. used electron cryo-microscopy to analyze translocon and identify the structure of a mycolactone-inhibited mammalian Sec61 in an attempt to better understand the molecular mechanism of action [236]. The first thing they demonstrated was that mycolactone wedges open the cystolic side of the Sec61α lateral gate. This stabilizes a poised and permissive conformation for post-translational translocation, which is remarkably like the conformation stabilized by Sec62/63. Furthermore, they demonstrated that mycolactone concurrently inhibits the path of the signal peptide while holding the translocon in a conformation that is optimal for substrate engagement signals [236]. Given that mycolactone-inhibited Sec61 is unable to transport substrate proteins effectively, it is possible for transmembrane domains and signal peptides to pass through the mycolactone-occupied regions. This reveals novel facets of translocon dynamics and activity and establishes the foundation for understanding the molecular mechanism of Sec61 inhibitors.

Additionally, considering that mycolactone is amphiphilic nature, it allows for significant interactions with lipophilic environments. However, it is unclear how specific these connections are and how membranes contribute to the pathogenicity of the toxin.

Consequently, da Hora and colleagues used enhanced free-energy investigations and molecular dynamics simulations to characterize the association and penetration of mycolactone via the plasma membranes (PMs) and endoplasmic reticulum (ER) of mammals. They demonstrated that lipid content influences both membrane association and mycolactone penetration. The ER membrane keeps its bent c-shape conformation as the two polar tails of the toxin spread across the bilayer in the plasma membranes (PMs). In the PM, this is the most common penetration mechanism [236]. The cause is most likely the cholesterol in the PM, which has a propensity to induce stiffness and thicken the bilayer. This suggests that during penetration, it is nearly hard for the poison to alter the PM while preserving the polar contacts with the water molecules and lipid head groups. Likewise, the free-energy calculations demonstrate that mycolactone has a greater affinity for the ER membrane than PM due to the presence of saturated lipids and cholesterol in the later [237]. On the other hand, investigations using the same molecular dynamics simulations indicate that mycolactone isomer B has a substantial affinity for the ER membrane, which raises the local concentration around Sec61 and may increase the effective affinity for the translocon [238].

2.4.1.3 Inhibition of angiotensin II type 2 receptor (AT2R)

In addition to the inhibition Sec61 by mycolactone, Marsollier et. al. identified angiotensin II type 2 receptor (AT2R) as the main receptor involved in mycolactone-mediated analgesia [23]. They demonstrated the ability of mycolactone to exert an analgesic effect through the inhibition of angiotensin II type 2 receptor (AT2R). Potassium (K^+) channels form a large family of hyperpolarizing channels, as such, they are expressed in every cell of the organisms. They are involved in cellular mechanisms including apoptosis, vasodilation, anaesthesia, pain, neuroprotection and they achieve this by producing background currents that oppose membrane depolarization and cell excitability [239]. Mycolactone therefore is able to bind to angiotensin

II type 2 receptors (AT2Rs) on neurons, leading to potassium-dependent hyperpolarization. Marion et al. were able to show that mycolactone activates AT2R in neurons, with the release of phospholipase A2-mediated arachidonic acid (PLA_2), the generation of prostaglandin E2 from AA by cyclooxygenase-1 (PGE_2) and the subsequent release of potassium through TRAAK channels (**Figure 2.4**) [23]. Notably, drugs known to activate potassium channels display antinociceptive properties as they induce hyperpolarization, thus decreasing neuron sensitization [240]. The sustained hyperpolarization induced in sensory neurons was proposed to mediate the analgesic properties of mycolactone. This has been validated in mice that were inoculated with mycolactone being less sensitive to a pain stimulus using the Hargreaves plantar pain test and that this effect was dependent on the type-2 angiotensin II receptors (AT2R) [241, 242]. In a separate study, Anand and colleagues sought to decipher the mechanisms responsible for mycolactone-induced analgesic effects in rat and human primary dorsal root ganglion (DRG) sensory neurons [224]. They observed significant neurite degeneration in rat and DRG sensory neurons after 24 h of exposure to a 100 nM concentration of mycolactone. These findings are consistent with previous *in vivo* studies by En et. al. using mice models where mycolactone was thought to induce hypoesthesia with an extremely long-lasting effective leading to nerve destruction at late stages of the disease [24, 200, 243]. Additionally, the functional effects of known ligands of AT2R, including agonists or antagonists such as Angiotensin II, C21, and EMA 401 in cultured human and rat DRG neurons were investigated by Anand et. al. It was demonstrated that only mycolactone was able to trigger hyperpolarization of DRG neurons [244, 245]. More interestingly, the AT2R antagonists, EMA 401 or C21 were unable to inhibit hyperpolarization that was triggered by the toxin. This observation confirms the specificity of mycolactone/AT2R interactions and an indication of the lack of involvement of the AT2R in ML-mediated neurotoxicity [224]. Consequently, it has been proposed that the biological mechanisms of mycolactone-induced

cell death entail the hijacking of various signaling pathways. For example, the mTOR pathway and the system requiring Sec61-dependent protein translocation into the ER in which the mycolactone i disrupt the mTOR and Sec61 pathways in DRG neurons [229, 231].

2.4.1.4 Inhibition of mTOR

Mycolactone has been shown by Bieri et al. to bind to and inhibit the mTOR signaling pathway in the body by using L929 fibroblasts as a model [229]. The mTOR forms two structurally and functionally distinct complexes called the mammalian target of rapamycin complex 1 (mTORC1) and mammalian target of rapamycin complex 2 (mTORC2), which together are responsible for the regulation and control of cell growth, metabolism, cell proliferation and survival of several cell processes including apoptosis by participating in multiple signaling pathways in the body [246]. When mTOR (mTORC1 and mTORC2) complexes are exposed to mycolactone, mTORC2 complex is particularly inhibited by the toxin. This prevents phosphorylation of the serine/threonine protein which ultimately inhibits kinase Akt activity. Once Akt is inactivated, it leads to the dephosphorylation and activation of the Akt-targeted transcription factor $FoxO_3$. Subsequent up-regulation of the $FoxO_3$ target gene BCL2L11 (Bim) increases expression of the pro-apoptotic regulator Bim, driving mycolactone treated mammalian cells into apoptosis through the mTORC2-Akt-$FoxO_3$ axis [229]. Signal transduction requires the pro-optotic protein Bim, which is encoded by BCL2L11 gene. It has been demonstrated that experimentally infected Bim mutant animals can inhibit *M. ulcerans* growth and do not form necrotic BU lesions [229]. This conclusion is supported by the observation that human ulcerative forms of Buruli ulcer are linked to genetic variations in BCL2L11, indicating that apoptosis regulation is a critical factor in the disease pathogenicity [247].

2.5 Boron and boronic acid chemistry

2.5.1 The "double discovery" of Boron

The year 1808 referred to as the year of "double discovery" was when boron was first isolated by two independent experiments. It was the time of scientific rivalry between British chemist Sir Humphry Davy and French chemists Joseph Louis Gay-Lussac and his fellow professor at the École Polytechnique Louis Jaques Thénard [248, 249]. Gay-Lussac and Thénard used fused potassium for the decomposition of boric acid (H_3BO_3) and discovered a new element, which was announced on June 21, 1808. They called this element, "bore" which is the name of the element in French today [248]. On June 30, 1808, just within 9 days after the announcement by Gay-Lussac and Thénard, Humphrey Davy submitted to the Royal Society of London an article on the discovery of a new element which he called "boracium" [249]. The name of the element was eventually modified to boron. Pure boron is very rare on Earth and exists mainly as minerals containing boron oxide in various proportions. The principal sources of boron are minerals such as the hydrated sodium borates, borax ($Na_2[B_4O_5(OH)_4]\cdot 8H_2O$) and kernite ($Na_2[B_4O_6(OH)_2]\cdot 3H_2O$); the hydrated calcium borates colemanite ($Ca_2B_6O_{11}.5H_2O$), inyoite ($Ca_2B_6O_{11}\cdot 13H_2O$), and priceite ($Ca_4B_{10}O_{19}\cdot 7H_2O$); and the hydrated magnesium borates szaibelyite ($Mg_2B_2O_5\cdot H_2O$), inderite or kurnakovite ($Mg_2B_6O_{11}\cdot 15H_2O$), and pinnoite ($MgB_2O_4\cdot 3H_2O$). Other sources of boron are the hydrogen borate, sassolite (H_3BO_3), the sodium-calcium borates ulexite ($NaCaB_5O_9.8H_2O$), proberlite ($NaCaB_5O_9\cdot 5H_2O$), and the magnesium-calcium borate, hydroboracite ($CaMgB_6O_{11}\cdot 6H_2O$), and magnesium chloride double salt, boracite ($Mg_3B_7O_{13}Cl$) [250].

2.5.2 Boronic acids

Boron has a unique position in the modern periodic table. Elemental boron is a Group 13 metalloid with three valence electrons and a ground state electronic configuration of $1s^2 2s^2 2p^1$.

Boron is in the same period as carbon but with one fewer electron. As a result, it shares many structural similarities with carbon, making it particularly valuable in organic and medicinal chemistry. The abundance of boron-based reagents in organic synthesis can be attributed to the structural similarity to carbon as compared to other group IIIA elements [251]. Boron typically forms tricoordinate neutral compounds, the most popular being boronic acids, with unique electronic and physicochemical properties that have largely contributed to their extraordinary versatility and utility.

2.5.2.1 Physical Properties

Most boronic acids exist as white crystalline solids that can be handled in the air without any special precautions. Boronic acids are known to be chemically stable under ambient temperatures and most have been proven to have a long shelf life. Boronic acids do not interconvert into their corresponding borinic acid and boric acid even at high temperatures. Boronic acids, on the other hand, tend to form oligomeric anhydrides when dehydrated, complicating their characterization. These anhydrides in turn will initiate the decomposition of boronic acids especially when they are exposed to air. Therefore, it is better to store boronic acids under an inert environment or in a slightly moist state to minimize or avoid oxidation altogether. Commercially available boronic acids sometimes contain a small percentage of water that may help in their long-term preservation. Due to their facile dehydration and the potential of forming anhydrides, boronic acids tend to provide somewhat unreliable values of melting points. Also, boronic acids are partially soluble in both neutral water and polar organic solvents and as a result often makes isolation and purification of boronic acids difficult. For these reasons, it sometimes convenient to use the corresponding boronate esters in which the two hydroxyl groups are protected [82].

2.5.2.2 Chemical Properties

In the boronic acid structure, there are six valence electrons on boron with a vacant *p*-orbital which makes the boron atom sp^2 hybridized, thus adopting a trigonal planar geometry with O−B−O bond angle of ~120°. The boron atom in boronic acid is electron-deficient and isoelectronic with a carbocation due to the vacant p-orbital on the boron atom which is orthogonal to three substituents (**Figure 2.5a).** The electron deficient boron atom always tries to attain the desired octet configuration through overlap with π-donors [252]. They achieve the octet configuration by acting as strong Lewis's acids (behave as electrophiles) that can easily take electrons from Lewis base nucleophiles such as hydroxyl (–OH), amino ($–NH_2$), and carboxylate ($–COO^-$) groups, fluoride (F^-) and cyanide ions (CN^-) ions which resulting in interesting photophysical, and catalytic properties. The Lewis acid-base reaction results ready interconversions of the hybridization of the central boron from sp^2-hybridized trigonal planar neutral boron to sp^3-hybridized tetrahedral anionic boronate species with geometries and isoelectronic structures that are equivalent to those of a neutral sp^3-hybridized carbons [253-257](**Figure 2.5b)**.

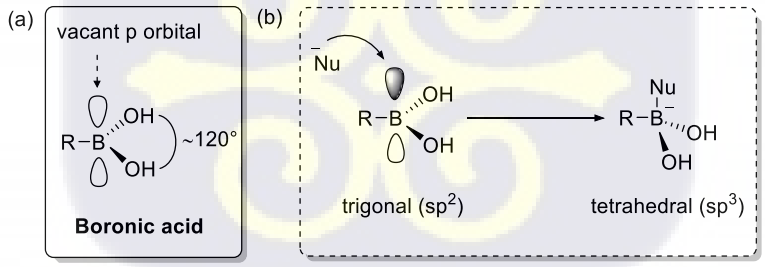

Figure 2.5. (a)Trigonal planar neutral structure of Boronic acid with a vacant p-orbital; (b) Conversion from a neutral and trigonal planar sp^2-hybridized boron to an anionic tetrahedral sp^3-hybridized boron.

Additionally, boronic acids have the unique ability to quickly react covalently with cis 1,2- and/or 1,3-diols in non-aqueous or basic aqueous media to form five- or six-membered cyclic boronate esters. Typically, boronic acids form a boronic ester bond with 1,2 or 1,3-diols in anhydrous organic solvents [252](**Figure 2.6**).

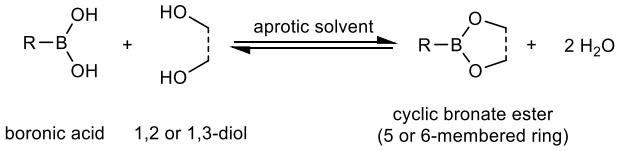

Figure 2.6. Reaction scheme for the ionization of a boronic acid in the presence of a diol using aprotic solvents.

In an aqueous environment, the interaction between a boronic acid and a cis 1,2- and/or 1,3-diol is known to be one of the strongest single-pair reversible functional group interactions (**Figure 2.7**). Under physiological conditions, it is important to note that the Lewis acidity of both the boronic acid (1) and boronic ester (4) is determined by their reaction with a water molecule which results in the formation of the boronate acid (2) and boronate ester (3) respectively with the release of a proton. Therefore, boronic acids and their esters can exist in two different ionization states of the boron atom. The formation of the cyclic boronate esters lead to enhanced pKa of the boronic acid thus making the ‘ester' more acidic than the 'acid'. The enhanced acidity is due to a bond angle compression on formation of a cyclic boronate ester. Boronic acids have a 120° (sp^2) bond angle but in a cyclic ester the bond angle is reduced to 108°. The change in the bond angle from 120° to 108° facilitates the change in hybridization from sp^2 to sp^3 on deprotonation. Thus, the neutral boronic ester constructed from boronic acid in its trigonal form is more unstable than it is before bonding to the diol owing to the ring strain and is therefore easily hydrolysed. Also, boronic and boronate acids (1 and 2) interact reversibly with 1,2- or 1,3 diols to form a boronic and boronate esters (4 and 3) in an aqueous

solution [258]. It is reported that the trivalent planar neutral forms with sp^2-hybridized boron centre are in equilibrium with the anionic forms in which the boron centre is bound to a hydroxide ion, and thus, adopting tetragonal geometry with sp^3-hybridization [259]. The boronate ester (3) and boronic ester (4) are either pentagonal (5-membered) or hexagonal (six-membered) rings depending on whether boronic acid (1) is bound to a cis-type 1,2- or 1,3-diol. It is worth noting that narrowing of the O–B–O bond angle upon complex formation with a diol manifests an increase in boron's Lewis acidity [260].

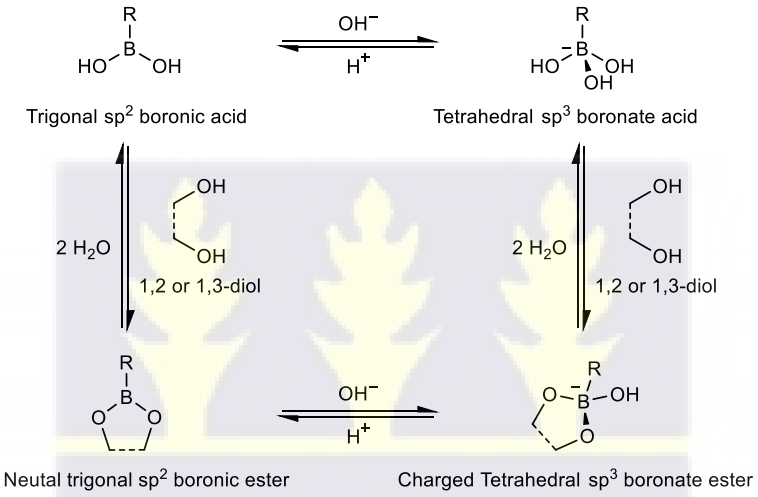

Figure 2.7. Reaction scheme for the ionization of a boronic acid in the presence of a diol in aqueous medium.

2.6 Ultraviolet-visible (UV-Vis) Spectroscopy

Ultraviolet-visible (UV-Vis) spectroscopy is an analytical technique that evaluates the absorption of ultraviolet and visible light of a sample. Due to its versatility, UV-Vis has found use in broad areas of study including chemistry, biochemistry, and environmental science to quantify the concentration of compounds, elucidate molecular structures, and monitor chemical reactions [261]. The technique explores the interaction between matter and light with the potential to cause transitions of electrons in the molecules at different energy levels. The

wavelength range of electromagnetic radiation in the UV-Vis region of the spectrum is roughly 200–700 nm. For routine laboratory analyses, the accessible UV range is 200–350 nm, while the Vis range is 350–700 nm [261]. Light emitted from these regions possess the required energy to excite electrons from the ground state energy level to higher energy levels, which can be quantified in terms of absorption or transmission. Exposing a sample to UV-Vis light, causes some wavelength of the light to be absorbed. The reason behind this that, the energy of the light matches the energy gap between the two energy states of the molecules in the sample. The concentration of the sample and the path length through which the light travels determine the amount of light absorbed. Based on the aforementioned, the relationship between the absorbance of a sample and the concentration of the absorbing species is known as Beer's law which define absorbance as the product of the molar extinction coefficient (ε), optical path-length (l), and concentration (c) [262].

By subtracting the intensity of light before and after passing through the sample, the absorbance is computed. This can then be used to determine the concentration of the sample, making UV-Vis a critical technique for quantitative analysis. The instrumentation of UV-Vis spectrometer consist of light source (spectrum of UV and visible light), monochromator (a prism or diffracting grating for light separation into constituent wavelengths), sample holder (for holding the sample to receive the light), detector (for measuring intensity of light after passing through the sample), and readout device (displace the absorbance spectrum in the form of graph by plotting absorbance against wavelength). Based on the operations of UV-Vis spectroscopy, three types that is absorption, transmission, and reflectance spectroscopy are known. The limitations associated with this instrumentation are limited chromophores, interferences, constant calibration requirement, and path length discrepancies. This notwithstanding, the advances such as non-destructive, high sensitivity and precision, simple and quick, wide range

applications and cost-effective renders UV-Vis spectroscopy an indispensable tool in environmental and life sciences fields of study.

UV-Vis spectroscopy have found applications in various areas. Employing a UV-Vis spectroscopy, the active substances, acetylsalicylic acid, meloxicam, and naproxen in some drugs were determined. The analysis carried out on Perkin-Elmer Lambda 25 spectrophotometer revealed both meloxicam and naproxen were within acceptable limits declared, while the content of acetylsalicylic acid was 89.56% of the declared values falling short of the prescribed values of U.S. Pharmacopoeia [263]. In another study, luteolin, a flavonoid found in most plants and known for its pharmacological activities was interacted with Cu (II) to determine the effect of the of the complex on DNA damage in the copper-catalyzed Fenton reaction. UV-Vis spectroscopy was employed to characterize the interaction between the luteolin and Cu(II) [264]. Similarly, employing UV-Vis and mass spectroscopy, epigenin extracted from the acetone fraction of *Acanthophora spicifera* was structural elucidated [265]. Due to the potential to provide both quantitative and qualitative data efficiently and rapidly, UV-Vis remains one of the accessible and reliable technique for molecular characterization and monitoring [261].

2.7 Fluorescence Spectroscopy

2.7.1 Background and Theory

The phenomenon of fluorescence was known by the middle of the nineteenth century. British scientist Sir George G. Stokes first saw that the mineral fluorspar exhibits fluorescence when illuminated with ultraviolet light, and he coined the word "fluorescence". Stokes interest in the phenomenon was first born out repeated experiments by Sir David Brewster and Sir John Herschel. Sir John Herschel for instance, had discovered that sulphate of quinine appeared colourless and transparent when viewed by transmitted light but exhibited peculiar blue colour

[266]. In 1852, Sir G.G. Stokes in his seminal paper "On the change of refrangibility of light" simply summarized the fundamental property of fluorescence, as when a photon of ultraviolet radiation collides with an electron in a simple atom, exciting and elevating the electron to a higher energy level. Subsequently, the excited electron relaxes to a lower level and emits light in the form of a lower-energy photon (higher wavelength) in the visible light region [262, 267].

Fluorescence is an optical phenomenon where the absorption of light photons by a molecule or material at one wavelength results in emission at another, usually longer wavelength after initial electronic excitation in the light-absorption process [268]. Fluorescence occurs at longer wavelengths compared with excitation. The excitation process can be viewed by recording the absorption spectrum (or the excitation spectrum) of the sensor, recorded by using a UV–vis spectrometer. Fluorescence is usually observed in the case of n → p* or p → p* transition states. The n → p* transition state of an electron from a non-binding ground state to a first excited p-state has a longer lifetime than a pure p → p* transition. Due to their longer lifetime, excited electrons from n → p* transitions are more likely to experience energy dissipation than excited electrons from p → p* transitions [269].

2.7.2 The Fluorescence phenomenon – the Jablonski Diagram

In 1935, Professor Alexander Jablonski, who is regarded as the father of fluorescence spectroscopy devoted his life to the study of the processes that involve the molecular absorbance and emission of light. He interpreted the possible fate of applying photons from the visible spectrum of light to a particular molecule. When a molecule absorbs a photon of appropriate energy, it becomes excited, and releases the absorbed energy through a chain of photophysical events that can be classified to two main type of transition including both non-radiative processes such as vibrational relaxation, internal conversion, intersystem crossing; and radiative processes such as fluorescence and phosphorescence, as demonstrated by the

Jablonski diagram (**Figure 2.8**) [270]. A typical Jablonski diagram is basically an energy diagram arranged with the energy on the vertical axis in which the singlet ground, first, second and third electronic states are depicted by S0, S1, and S2, S3, etc respectively. At each of these electronic energy levels the fluorophores can exist in several vibrational energy levels, depicted by 0, 1, 2, etc.

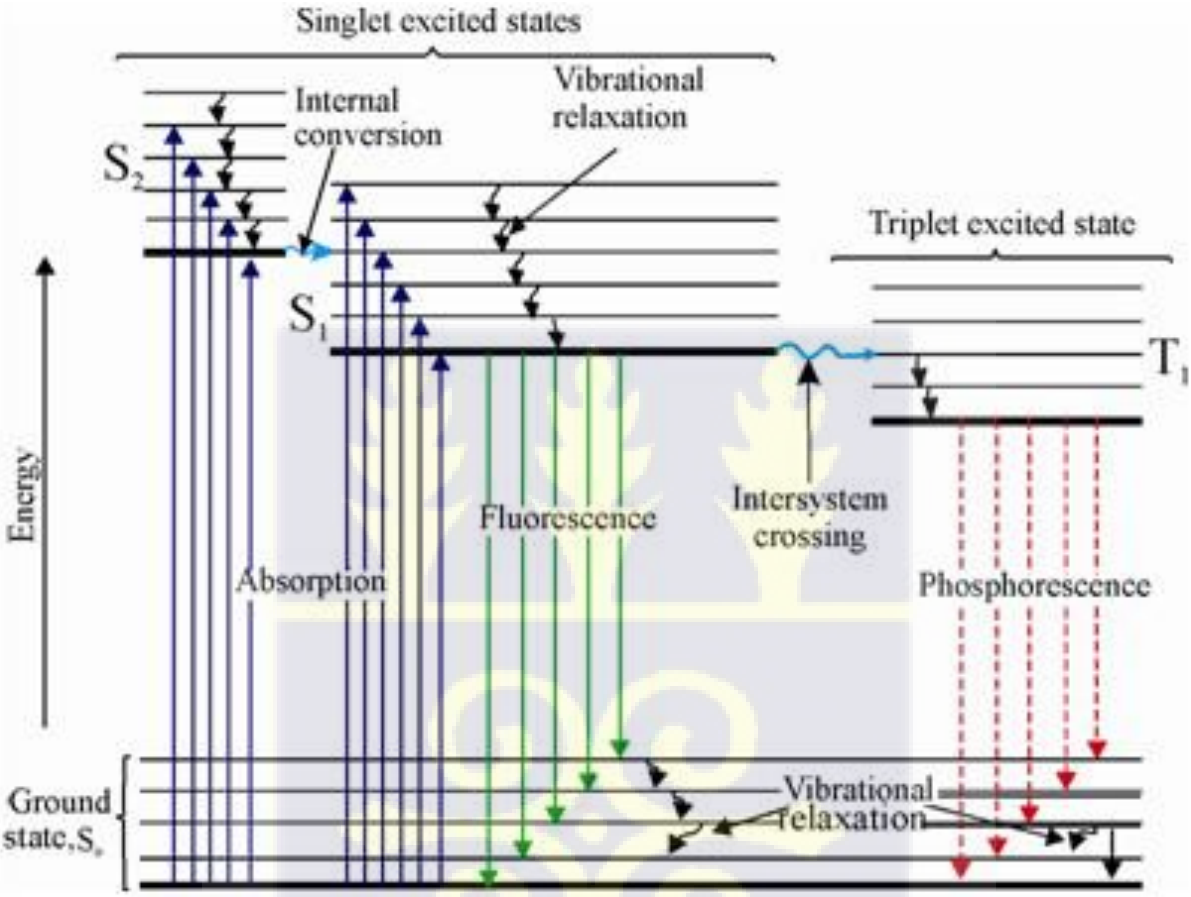

Figure 2.8. Jablonski diagram showing the three stages of the fluorescence process.

In the first transition of the Jablonski diagram, known as absorption, a molecule of interest absorbs light, become excited and the electron promoted from ground electronic state (S0) to an excited state that should possess the same spin multiplicity (such as, S1, S2, S3) thus S0→S1 or S0→S2 or S0→S3. This excludes the triplet excited state (T1, T2) as the final state of

electronic absorption because transitions between states of different multiplicities are improbable "forbidden" (e.g. T→S or S→T) [262]. This absorbance process is fast, usually taking place within 10^{-15} s, and thus the transitions can be justified by a process known as the Franck–Condon principle. The principle states that since the electronic absorption of light occurs in extremely short time ($\sim 10^{-15}$s) during the time scale of absorption, the nuclei are assumed to be frozen, that is that the transitions between various electronic levels are vertical [267, 270].

Following light absorption, several processes involving non-radiative and radiative processes usually occur for energy to be dissipated. Often, the first route to energy dissipation is through the non-radiative relaxation process called vibrational relaxation which involves the rapid relaxation of excited molecules from higher to lowest vibrational level. This process is also very fast, occurring within $\sim 10^{-14}$-10^{-12} s. In a few rare exceptions, excited molecules in condensed phases rapidly relax to the lowest energy singlet excited state, S1 from higher energy excited singlet state such as S2 (S2→S1) in another non-radiative process is called internal conversion. Internal conversion generally occurs within 10^{-12} s or less. Since this is a very fast transition, it is extremely likely to occur immediately following absorbance.

Vibrational relaxation and internal conversion of energy dissipation may be followed by another non-radiative process called intersystem crossing. It involves the relaxation between excited states of different spin multiplicity, thus from a singlet to a triplet state such as S1→T1, and it occurs within a time scale of 10^{-8} s. Intersystem crossing occurs more slowly than internal conversion since it's a less probable process than internal conversion since spin multiplicity is not conserved. It is indicated by a horizontal, curved arrow from one column to another. This is the slowest process in the Jablonski diagram, several orders of magnitude slower than fluorescence.

The other pathways for molecules to deal with energy received from photons is to emit a photon are the two radiative processes namely fluorescence and phosphorescence. Fluorescence refers to the emission of light associated with a radiative transition from an excited electronic state that has the same spin multiplicity as the ground electronic state (S1→S0). Fluorescence is a slow process on the order of 10^{-9} to 10^{-7} s; therefore, it is not a very likely path for an electron to dissipate energy especially at electronic energy states higher than the first excited state. Fluorescence transitions are spin allowed; thus, they occur very rapidly and the average lifetimes of the excited states responsible for fluorescence are typically 10^{-9}-10^{-5} s. On the other hand, phosphorescence is emitted from a triplet state. Phosphorescence refers to the emission of light associated with a radiative transition from an excited electronic state that has a different spin multiplicity from that of the ground electronic state (T1→S0). The excited electron undergoes intersystem crossing to a triplet state, which is blocked from light emission. This is the reason for the large phosphorescence lifetime [269]. Unlike fluorescence, phosphorescence transitions (T1→S0) are spin forbidden; thus, they are less probable than spin allowed transitions and the average lifetimes of the excited states responsible for phosphorescence are typically 10^{-3} s. Therefore, the rate constants for triplet emission are several orders of magnitude smaller than those for fluorescence. [262]. Thus, they usually exhibits significantly longer lifetimes and longer emission wavelengths than do fluorescent processes [271]. Some compounds do not show fluorescence. In this case, the absorbed energy is dissipated by the medium or emitted as phosphorescence, which has a longer lifetime for the excited state.

2.7.3 Stokes Shift

In 1852, when Sir G.G. Stokes studied the same quinine compound that had been used by Herschel, he found out that the emitted (fluorescing) light has longer wavelengths than the excitation (absorbed) light. This phenomenon would later become known as the Stokes shift in

homage to Sir G. G. Stokes who elucidated the process of fluorescence. The energy of the fluorescence emission is generally lower than that of absorption. This is caused by the loss of energy during the internal conversion process because of vibrational relaxation. This energy difference between the absorption and fluorescence spectra is known as "Stokes shift" (**Figure 2.9**) [266, 269].

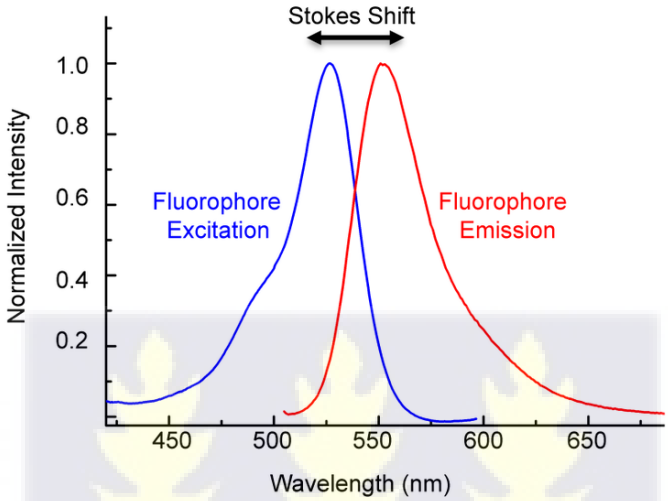

Figure 2.9. Stokes Shift representation showing absorption/excitation (left) and fluorescence emission (right) spectra.

The proper selection of excitation and emission wavelength is important for conducing fluorescence experiments. When a fluorescence spectrum is taken, a fluorescence excitation is nearly identical to an absorption spectrum and is dependent on the same parameters of Beer's Law. It is also depended on the quantum yield of the fluorophore, the power of the source, and the fluorescence collection efficiency of the instrument. The wavelength at which the excitation spectrum displays a maximum intensity is referred to as the $\lambda a = \lambda ex$. The energy differences between λex and λem (Stokes Shift) are an important parameter to consider when choosing fluorophores for chemosensor design to help reduce light scattering. Therefore, excitation and emission wavelength should always be separated and fluorophores with a large Stokes shift are preferred.

2.7.4 Förster Resonance Energy Transfer (FRET)

This mechanism of Förster Resonance Energy Transfer (FRET) was first discovered by the German scientist Theodor Förster in 1948 [272]. FRET is a spectroscopic technique that describes the non-radiative energy transfer between two fluorophores – a donor fluorophore and an acceptor fluorophore. Although "fluorescence resonance energy transfer" is frequently used when both chromophores are fluorescent, the former terminology is preferred because the energy transfer is a non-radiative process that does not include fluorescence [273]. The principle behind FRET operation, is the transfer of excited-state energy from the donor molecule to the acceptor molecule without release of a photon. Shorter wavelength, higher energy light is absorbed by the donor moiety, while longer wavelength, lower energy light is absorbed and emitted by the acceptor. Upon photoexcitation of a donor fluorophore, it transfers energy to an acceptor in proximity, and this allows for the transfer of energy through nonradiative dipole–dipole coupling (**Figure 2.10**).

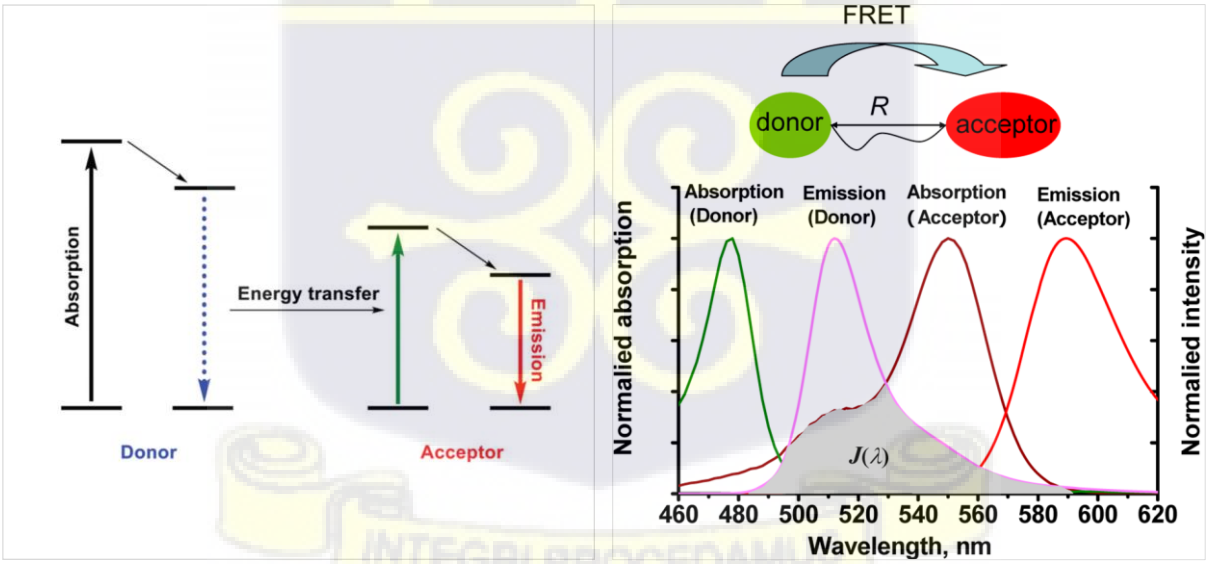

Figure 2.10. Schematic of the Förster Resonance Energy Transfer (FRET) process. R: distance between the energy donor and acceptor, J(l): degree of spectral overlap between the donor emission and the acceptor absorption [274]

In the selection of FRET pairs, it is required that the emission spectrum of the donor overlaps with the absorption/emission spectrum of the acceptor. Secondly, FRET can be particularly effective if the the donor–acceptor pair are in proximity at very short distances (within 10–100 Å of each other). Generally, FRET works best when the donor and acceptor are within the Förster radius (typically 3 – 6 nm) [275]. Lastly, the donor emission moment, acceptor absorption moment, and the separation vector should all be oriented favourably [276].

Because, it involves dipole-dipole interactions, where energy is transferred through space between two molecules, FRET has attracted interest in molecular biology, chemistry, and biophysics to study biomolecular interactions as well as molecular dynamics and cellular processes [277]. The challenges of distance, spectra overlap, orientation dependence and photobleaching has limited the use of FRET. However, advantages such high sensitivity, non-invasive, multiplexing and quantitative capabilities outweighs the limitations thereby making it versatile technique for various fields of study. Some applications of FRET include protein-protein interaction studies, conformational changes in biomolecules, biosensing, nucleic acid studies, cellular imaging and tracking. FRET is therefore a highly valuable and versatile tool used for studying molecular interactions, protein conformation changes, and cellular processes. Interestingly, the sensitivity is in the nanometer-scale distance rendering it a powerful tool in molecular research.

CHAPTER THREE

3 Alternative boronic acids for the detection of Mycolactone A/B using the thin layer Chromatography (f-TLC) method.

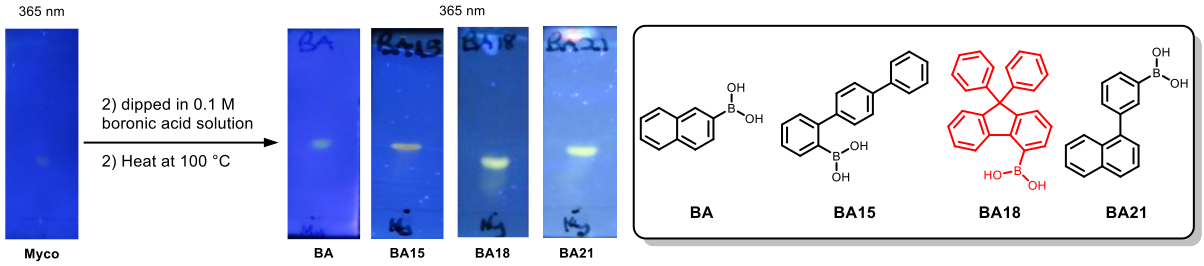

3.1 Background

Mycolactone (ML), the first macrolide cytotoxin known to be produced by a human pathogen *Mycobacterium ulcerans* (MU) is the causative agent of Buruli ulcer (BU) [15, 59]. It is the only macrolide identified in the genus Mycobacterium [10]. In 1965, Connor and co-workers hypothesized that *M. ulcerans* was responsible for the production of the diffusible cytotoxin which was subsequently confirmed using guinea pigs. Injection of mycobacterial culture filtrates into the experimental animal resulted in necrosis like those of human infections [3, 146, 278]. The suspected molecule was later isolated, purified, and characterized from the acetone-soluble portion of lipid extracts of *M. ulcerans* in 1999 by George et al. The chemical structure was subsequently solved as a polyketide named mycolactone (ML) [11, 70]. ML was detected on a thin layer chromatography (TLC) plate as a light yellow, ultraviolet-active lipid band with a retention factor value of 0.23 in chloroform/methanol/water (90:10:1, vol/vol/vol) [11] (**Figure 3.1A**). Electrospray ionization (ESI) mass spectrometry (MS) analysis gave an abundant signal at *m/z* 765.5 that represents the $[M + Na]^+$ adduct of intact mycolactone (**Figure 3.1B**). The core of ML is a 12-membered lactone ring surrounded by a C-linked upper side

chain composed of C12-C20 and a southern C5-O-linked polyunsaturated acyl side chain numbered C1′-C16′. There are variations in the "southern" chain that lead to different congeners of mycolactone, in which the "northern" chain remains constant. Further investigation showed that mycolactone isolated from *M. ulcerans* was a 3:2 mixture of *cis* and *trans* stereoisomers which are distinctive along the double bond between C4′ – C5′ as shown by a wavy line between C5′ and C6′. The two geometric isomers were subsequently designated mycolactones A and B [184, 185] (**Figure 3.1C**).

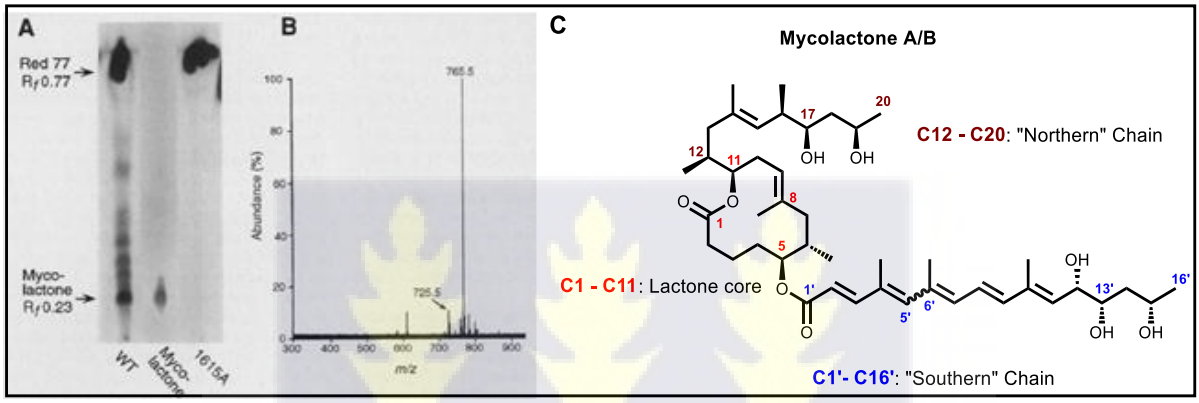

Figure 3.1. TLC profile **(A)**, Mass spectrum **(B)**, and Structure **(C)** of mycolactone A/B from lipid extract of *M. ulcerans.*

The pathogenicity of *Mycobacterium ulcerans* disease is principally dependent on the production of the biologically active polyketide-derived macrolide exotoxin called mycolactone [11]. There are reported evidence to the effect that the toxin is responsible for the immunosuppressive properties, painlessness, and tissue necrosis which characterizes Buruli ulcer disease [23, 66]. Secondly, mycolactone is known to be produced by only *M. ulcerans* and is believed to diffuse from its site of the original infection into lymph organs and peripheral blood thus making it a fascinating biomarker that could be detected in circulating blood [162]. These formed the basis for the development of various methods such as mass spectrometry [16, 68, 69], cytotoxic assays [16], or thin-layer chromatography [11, 70] for the detection of

mycolactone for the diagnosis of Buruli ulcer. Additionally, RNA aptamer binding [71] and LC-MS [16, 73] have recently been used to study mycolactone in patient biopsy samples.

Subsequently, Kishi and colleagues developed a TLC technique that was simple-to-use, less costly, and yet sufficiently sensitive and specific for the detection of mycolactone A/B [74]. In their approach, they took advantage of the selective reaction of 1,3-diols with boronic acids units to couple 2-naphthylboronic acid to mycolactone A/B along its 1,3-diol moieties to form 6-membered cyclic boronates (**Figure 3.2**). The absorption and emission maxima of free mycolactone are 362 nm and 520 nm respectively. This is attributed to the extensive chromophore conjugations between C2′ and C11′ on the polyunsaturated acyl side chain. However, when 2-naphthylboronic acid was coupled to mycolactone A/B along the 1,3-diol motif at C13' and C15' and irradiated at an excitation wavelength of 365 nm, the mycolactone-boronic acid complex was found to exhibit enhanced fluorescence emission at 520 nm. The intense fluorescence which could also be observed on TLC plates was influenced greatly by cyclic boronate esters that was formed [74] (**Figure 3.2**).

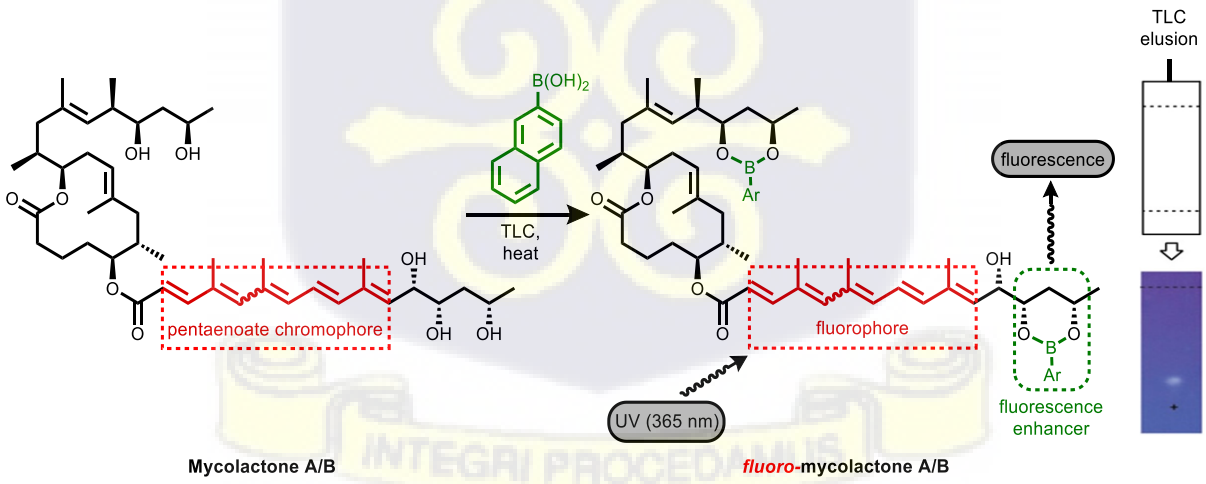

Figure 3.2. Detection of mycolactone A/B on TLC under 365 nm UV light.

In the past, compounds with cis-1,2- and 1,3-diol moieties have been selectively reacted with boronic acids to produce five- or six-membered cyclic esters [79-82]. Boronate esters have

demonstrated to have a significant effect on fluorescence. In 1992, Yoon and Czarnik were the first to publish findings on the usage of a boronic acid as saccharide sensor [279]. Since then, boronic acids and their analogues have been used in a wide range of biomedical applications as sensors leveraging on their unique recognition properties against 1,2- or 1,3-diols [91]. Sensors are essential to the field of diagnostic medicine because they enable fast and accurate analyte resolution. For instance, boronic acids have been demonstrated by Whyte and colleagues to be accurate sensor molecules for a range of polysaccharides, saccharides, glycoproteins, and dopamine [91]. Additionally, ionic compounds [93-95], hydrogen peroxide (H_2O_2) [98, 99], blood glucose levels [88–92], and catecholamines [100] have all been measured using boronic acid sensors. They have also been used as biochemical instruments in many different applications, such as cell transport techniques [102], enzyme inhibitors [101], and tumour cell imaging [104, 105]. These highlight the importance of boron-based fluorescence sensors in ongoing studies.

It has been effectively established that mycolactone can be detected by coupling to BA [74-76, 280]. However, concerns such as background interferences from co-extracted human tissue lipids need to be addressed. The search for a more efficient and fluorescent boronic acid as an alternative to the original BA utilized by Kishi and coworkers is required. To find possible alternatives to BA, several commercially available arylboronic acids were screened using f-TLC. The thin layer chromatography (TLC) of the purchased boronic acids was performed and the profile of their fluorescence band intensities was compared to BA.

3.2 Materials and methods

3.2.1 Reagents and Chemicals

Synthetic mycolactone A/B was kindly donated by Prof Kishi Yoshito (Harvard University) through the World Health Organization (WHO), Geneva, Switzerland. All twenty-six

structurally diverse arylboronic acids were purchased from Sigma-Aldrich. All reagents were of analytical grade and used without further purification. Solvents were of commercial grade and were used as supplied. Fluorescent dye-free TLC silica gel 60 plates (5721-7) were purchased from EMD chemical Inc and were cut into 5 x 2 cm sizes for the development of the plate. The UV lamp used was a benchtop UV transilluminator (UVLM-28 EL Series UV lamp 365/302 nm (8 Watt) purchased from UVP Inc.

3.2.2 Spotting

Solutions of 0.1 M of the various structurally diverse arylboronic acids were prepared by the addition of acetone and used according to the previous report of Kishi and co-workers [74]. Standard mycolactone A/B solution for TLC spotting was prepared from a stock solution of 0.1 mg/mL of mycolactone in 0.5 mL in an ampoule. A 10 ng/µL standard solution of mycolactone A/B was prepared by taking 0.1 mL of the mycolactone stock solution into a glass vial and adding 0.9 mL ethyl acetate to give the required standard. Optimal visualization of mycolactone A/B was accomplished by spotting the standard on the silica-coated glass TLC plates, eluting with a mixture of chloroform/hexane/methanol (5:4:1; v/v/v) and finally, by slow immersion of the eluted plate in the 0.1 M boronic acid solutions, removal, and then heating the plate to a temperature of ~ 100 °C. The glass side of the plate was then wiped clean with an acetone-soaked tissue paper towel and then viewed by illuminating at ~365 nm using a Benchtop UV transilluminator.

3.2.3 Absorption spectroscopy

The absorption spectra were recorded on a Shimadzu UV-1800 Spectrophotometer. All UV-Vis absorption spectra were obtained using quartz cuvettes with a diameter of 1 cm between 200 and 800 nm.

3.2.4 Fluorescence spectroscopy

Two spectrophotometers, a Horiba Jobin Yvon (HJY) Fluoromax-3 and a Shimadzu RF-6000, were used for the fluorometric investigations. The excitation wavelength was set at 365 nm, and the slit widths for excitation and emission were set at 5 nm and 10 nm, respectively. The emission spectra were recorded at room temperature. Using a standard solution of mycolactone A/B (0.1 mg/mL in 0.5 mL EtOAc), as indicated in **Table 3.1** below, different dilutions of the compound (4 to 32 µg/mL) were made and placed in 4 mL amber vials. The final concentrations were achieved by using cyclohexane as the diluent.

Table 3.1. Various concentrations of mycolactone standard solutions in cyclohexane.

No.	0.1 mg/mL mycolactone standard solution (µL)	Diluent (Cyclohexane) (µL)	Final concentration of mycolactone (µg/mL)	Final concentration of mycolactone (µM)
1	160	340	32	43.1
2	140	360	28	37.7
3	120	380	24	32.3
4	100	400	20	26.9
5	80	420	16	21.5
6	60	440	12	16.2
7	40	460	8	10.8
8	20	480	4	5.4
9	0	500	0 (Blank)	0

0.10 M solutions of (9,9-Diphenyl-9H-fluoren-4-yl)boronic acid (BA18), and 2-naphthylboronic acid (BA) were prepared in methanol. To perform 1 mL reactions, seven samples containing 500 µL of 0.10 M BA18 solution and 500 µL of each dilution of the mycolactone A/B (4 to 32 µg/mL) standard solution in **Table 3.1** were introduced into 1.5 mL microtubes and thoroughly mixed. After 10 minutes, the fluorescence spectra were recorded (λ_{ex} 365 nm and λ_{em} from 380 to 700 nm).

3.2.5 Preparation of cyclic boronates from mycolactone

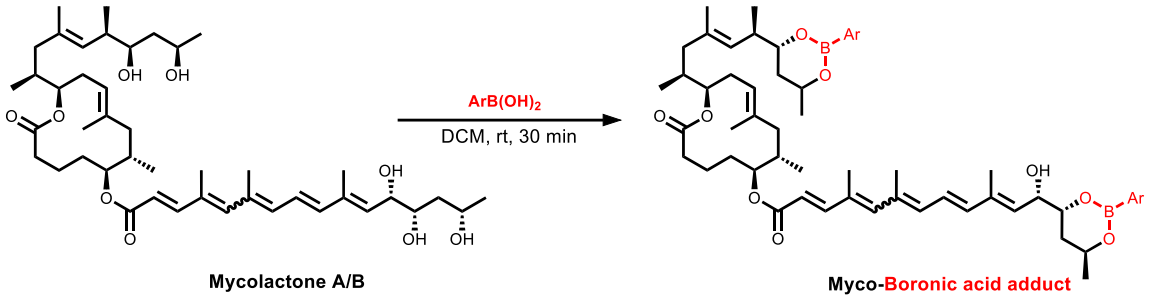

Figure 3.3. General reaction of arylboronic acids and 1,3-diols of mycolactone.

A solution of mycolactone (1 equivalent) was mixed with boronic acid (1 equiv.) in dichloromethane (DCM) (5 mL) and the resulting mixture was stirred for 30 minutes (**Figure 3.3**). The solvent was removed *in vacuo* under a high vacuum (0.1 mm Hg) and the residue was left to dry completely for an hour and submitted for LC-MS analysis (**Figure 3.9**).

3.2.6 Evaluation of patient samples by the f-TLC method

BU and non-BU patient samples confirmed by PCR following the method described by Stinear et. al. [281] were evaluated by the f-TLC method using BA and BA18. The evaluated samples included both fine-needle aspirates (FNA) and swabs. The extraction and detection of mycolactone were done according to a previously reported method [76]. A solution of the sample in ethanol was filtered through a cotton plug into a glass vial. The container from which the sample was filtered was further rinsed with 1 mL ethyl acetate and added to the glass vial through the cotton plug used for the initial filtration. The combined solvents were evaporated to dryness under reduced pressure. Then, 100 µL hexane/ether (1:1) solution was added to the glass vial, rinsed, and transferred by micro syringe into another clean glass vial to separate any contaminating solid from the liquid after which it was air-dried. 50 µL hexane/ether (1:1) was then added to the dried sample and 10 µL of the resuspended sample was spotted onto a 3.3×6.6 cm fluorescent-dye free TLC plate (TLC Silica gel 60, EMD Millipore, Darmstadt, Germany;

Gibbstown, NJ, USA) alongside 50 ng synthetic mycolactone A/B standard in ethyl acetate and a co-spot of 10 µL sample + 50 ng synthetic mycolactone A/B. The plate was developed in chloroform/hexane/methanol (5:4:1; v/v/v) air-dried and dipped in 0.1 M acetone solutions of both BA and (9,9-Diphenyl-9H-fluoren-4-yl)boronic acid (BA18), then heated for 60 seconds at 100 °C on a hot plate. The glass side of the plate was wiped with acetone on a paper towel. 365 nm UV lamp was used to view the plates. The fluorescent band at a retention factor of 0.23 from the synthetic mycolactone used as the control was compared to that of the patient sample. The results after the plates were developed were verified by another person in the laboratory before they were reported. The analysts who performed the PCR were blinded to certain relevant patient information (except for age, and gender) to ensure that there was no diagnosis bias [76].

3.3 Results

3.3.1 Fluorescent thin-layer chromatography (f-TLC) analysis

The TLC profiles of twenty-six commercially available arylboronic acids including 2-naphthylboronic acid (BA) are represented in (**Appendix 7**). Based on a visual comparison of fluorescent band intensities across all the TLC profiles, three of the boronic acids (BA15, BA18, and BA21) were shown to be visually superior to BA (**Figure 3.2**). That is, they produced excellent and highly intense yellow fluorescence bands on a blue background of the glass-backed TLC plate under 365 nm UV light than BA (**Table 3.2**). Following these promising results, the three were selected for further quantitation and spectroscopic investigations.

Table 3.2. Comparison of TLC profiles of BA, BA15, BA18 and BA21.

Entry	Boronic acid	Structure	TLC
BA	2-naphthylboronic acid	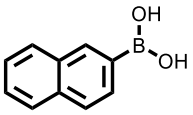	
BA15	[1,1':4',1"-terphenyl]-2-ylboronic acid	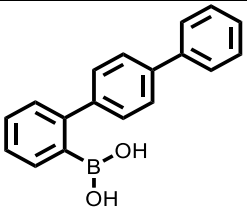	
BA18	(9,9-Diphenyl-9H-fluoren-4-yl)boronic acid	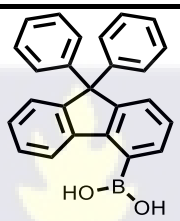	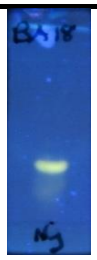
BA21	(3-(Naphthalen-1-yl)phenyl)boronic acid	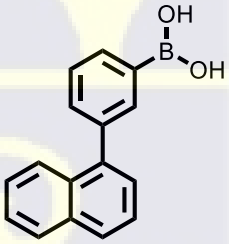	

Using 1–5 µL calibrated micropipettes, various volumes of working concentration of synthetic mycolactone (10 ng/µL) ranging from 1 µL – 9 µL, (equivalent to 10 ng – 90 ng) were spotted on the TLC plate, developed as indicated, and dipped in the 0.1 M concentrations of BA, BA15, BA18, and BA21. Like the previous finding, the three boronic acids gave more intense fluorescent bands compared with BA for all the concentrations. BA18 produced the most visibly intense fluorescence bands out of the three chosen boronic acids **(Figure 3.4)**.

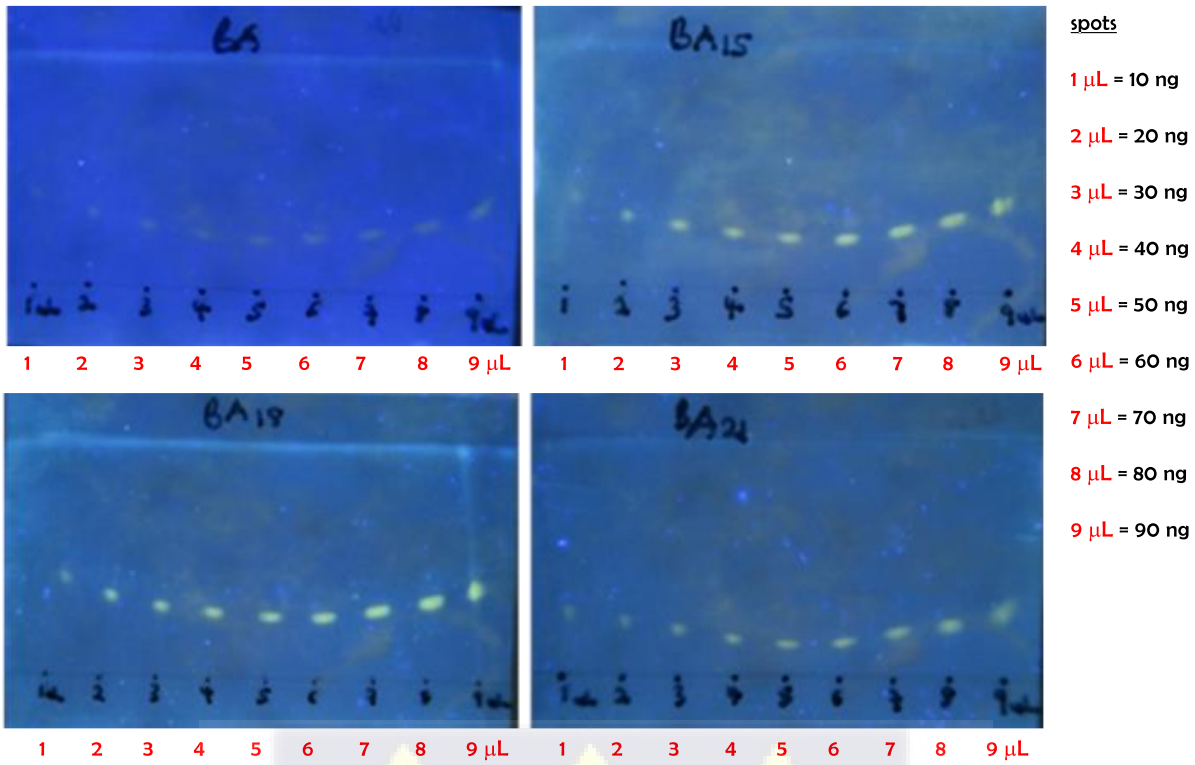

Figure 3.4. Comparative TLCs of BA, BA15, BA18, and BA21 for detecting various concentrations of synthetic mycolactone A/B.

3.3.2 UV–vis spectra

Next, I performed UV-vis measurements to determine the absorption maximum spectra of mycolactone A/B and myco-boronic acid adducts. The UV–vis spectra of the free mycolactone A/B and its boronic acids adducts are shown in **Figure 3.5**. The absorption maxima (λ_{max}) of the free mycolactone A/B was 362 nm while values of 272 nm, 270 nm, and 286 nm respectively were obtained for BA15, BA18, and BA21.

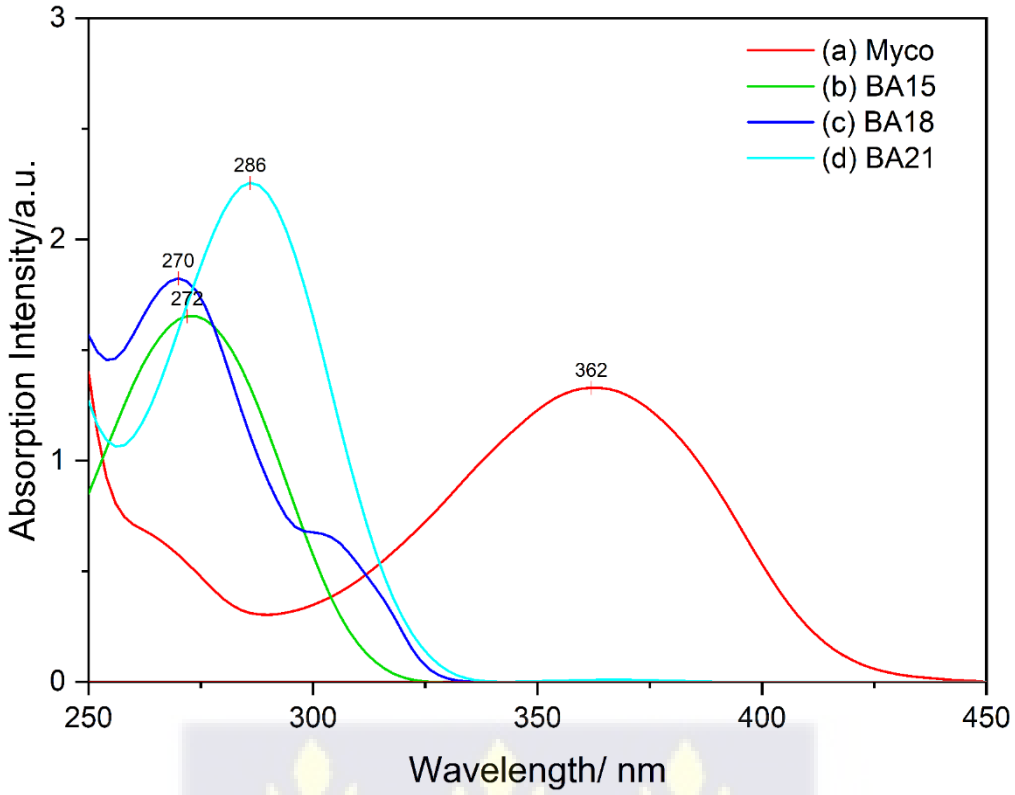

Figure 3.5. Absorption spectra of (a) mycolactone A/B; (b) BA15; (c) BA18; (d) BA21

3.3.3 Fluorescence spectra of complexes

In another experiment, I assessed the fluorescence-enhancing ability of the boronate ester formation between mycolactone A/B and our three most promising boronic acids (BA15, BA18, and BA21) (**Figure 3.6A**). When mycolactone A/B was excited at 365 nm in cyclohexane, the pentaenoate gave fluorescence emission at 537 nm. After coupling BA18 to the 1,3-diol, the fluorescence intensity was remarkably enhanced at the same wavelength (**Figure 3.6B**). Additionally, it was noted that as mycolactone concentration increased (0 – 20 µg/mL), the intensity of the fluorescence increased (**Figure 3.6C)**. Therefore, a plot of the fluorescence intensity at 537 nm versus the concentration of mycolactone produced a linear fit with a regression coefficient of 0.93 (**Figure 3.6D)**.

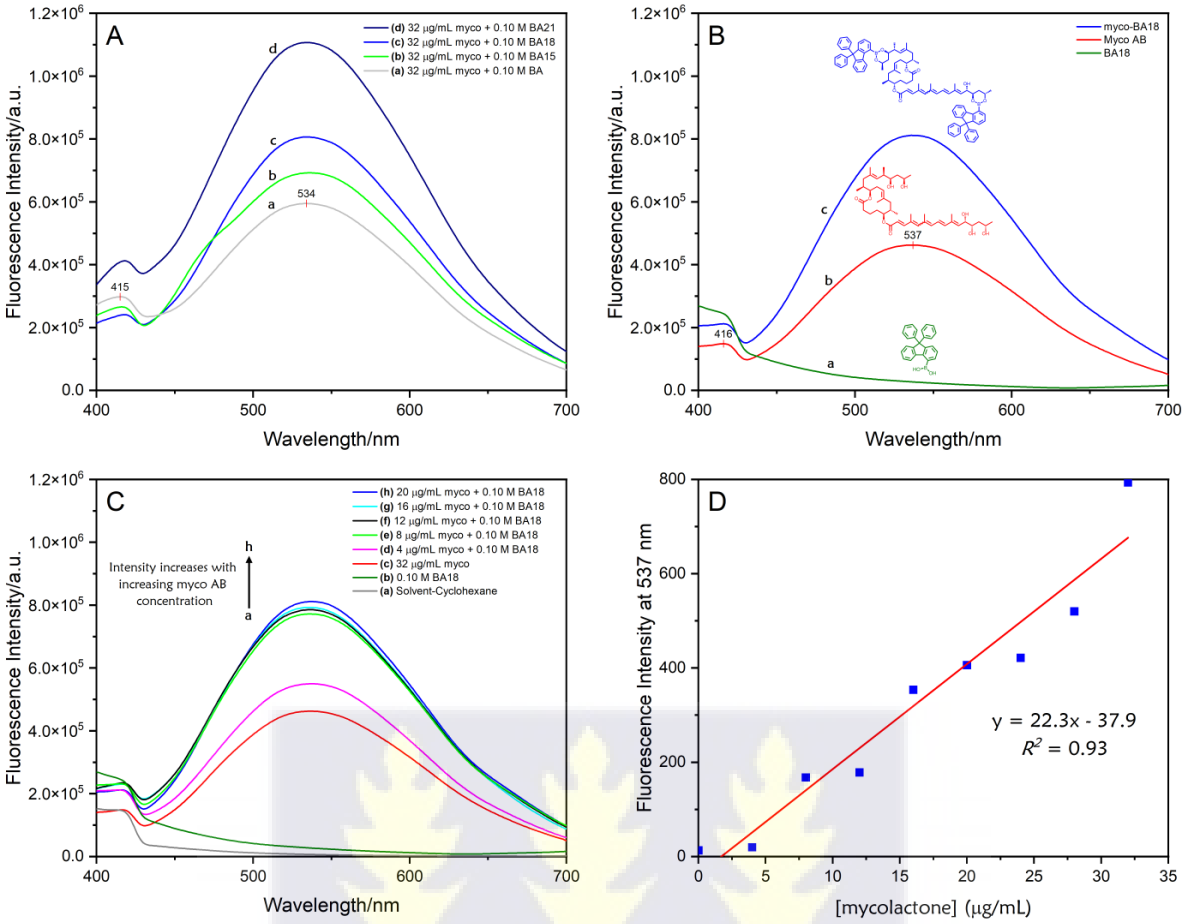

Figure 3.6. Fluorescence emission spectra and linearity plot of fluorescence intensity verse varying concentrations of mycolactone A/B.

To examine the correlation between excitation and emission spectral shifts, I plotted the excitation peak versus the corresponding emission peak for myco-BA18 boronate complex in cyclohexane and methanol respectively (**Figure 3.7A**). From the plot, I observed an emission peak maximum at a higher wavelength (λex_{max} 537 nm) as compared to the excitation peak maximum (λem_{max} 362 nm). Then I determined the Stokes' shift for the myco-BA18 boronate complex from the excitation and emission spectral peak maxima to be 175 nm. A significant fluorescence enhancement was visually observed on the TLC at 537 nm with (blue) the boronic

acid compared to that without (red) using a 365 nm UV lamp (**Figure 3.7B)**.

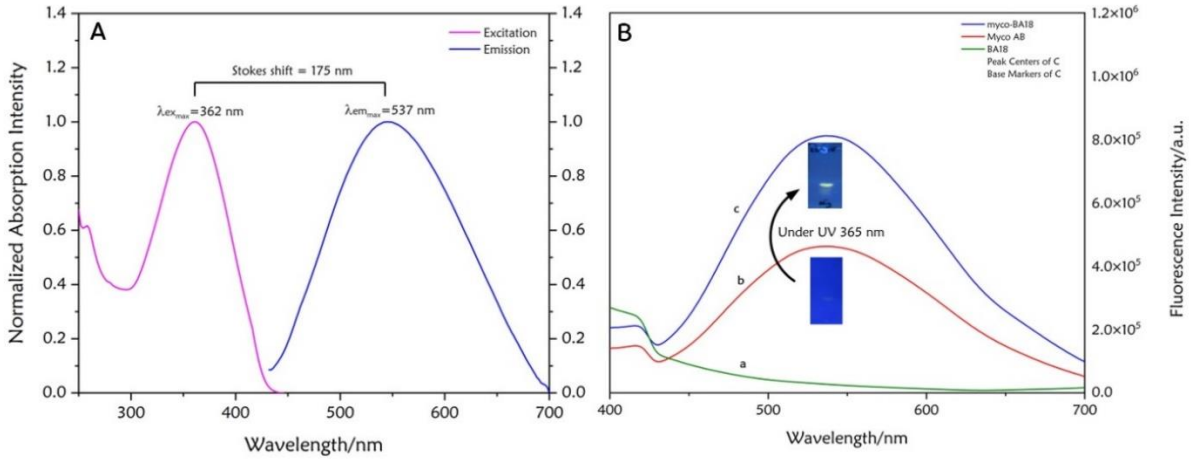

Figure 3.7. (A) Excitation and emission maxima plots and the calculated Stokes shift of myco-BA18 complex; (B) TLC plate of myco-BA18 adduct viewed under 365 nm UV.

3.3.4 High-resolution mass spectrometry (HRMS) analysis of mycolactone–boronic acid adducts.

High-resolution mass spectroscopic (MS) analysis was performed to confirm the formation of the mycolactone–BA15 adduct. First, MS analysis of mycolactone A/B was performed, and the chromatogram obtained is shown in (**Appendix 2**). The sodium adduct of mycolactone A/B, represented by the formula $C_{44}H_{70}O_9Na$ is the source of the intense molecular ion peak observed at m/z 765.4760. This matches with the mass of previously published literature on the toxin [11]. Mycolactone A/B was then reaction with B15 as shown in **Figure 3.8** and the reaction mixture was again analysed using LC-MS.

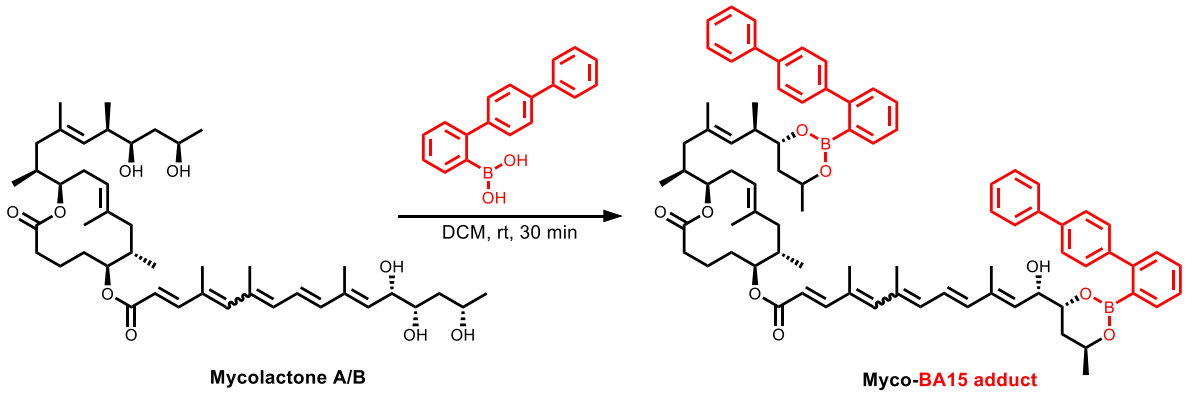

Figure 3.8. Reaction scheme of mycolactone A/B and BA15.

Analysis using the HR-MS confirmed that the reaction proceeded successfully. The LC-MS data revealed that the myco-BA15 boronate ester adduct was produced as shown in **Figure 3.9** and **Appendix 2.** It is determined that the myco-BA15 sodium adduct, with elemental formula $C_{80}H_{92}B_2O_9Na$, corresponding to sodium adduct $[M+Na]^+$ is responsible for a novel signal seen at *m/z* 1241.6823. This observation validates the synthesis of the adduct. The MS data also supports fluorescence intensity data observed on TLC.

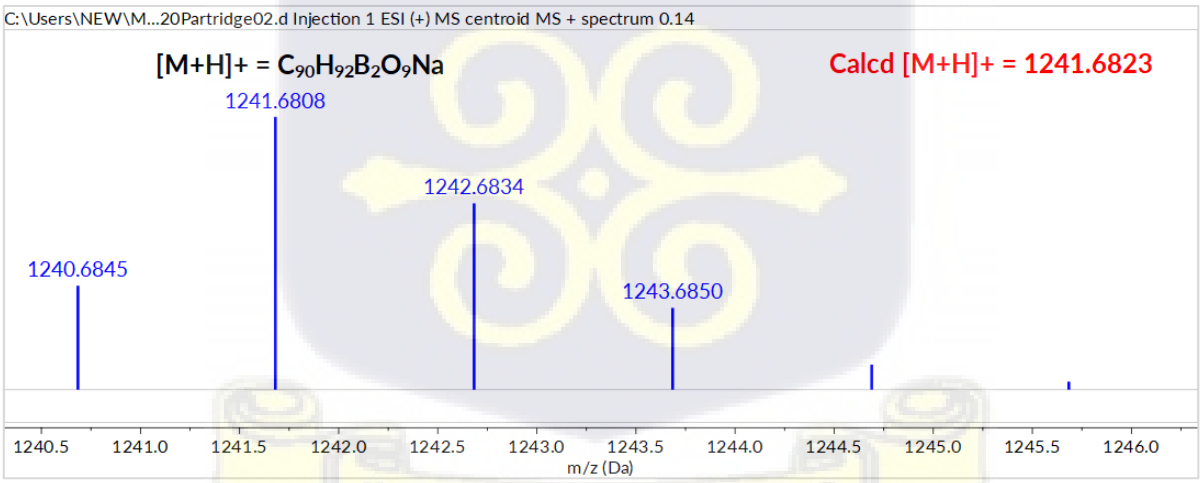

Figure 3.9. ESI-MS spectrum of myco A/B–BA15 complex.

3.3.5 Validation of BA18 in comparison with BA using real samples

TLC profiles of five (5) PCR-positive confirmed BU patient samples that were analysed by the f-TLC method using BA and BA18 as derivatizing agents were compared. Two separate measurements were conducted following experimental protocols described previously [76] (**Figure 3.10)**. In the first measurement (**top panel**), BA was used to form adducts with mycolactone whereas in the second measurement (**bottom panel)**, B18 was employed. As was observed in previous TLC plates where synthetic mycolactone was used, B18 gave profiles of superior fluorescence intensities of the myco-B18 adduct spots with real clinical samples compared to that of BA. The TLC profiles were also easier to read even for samples with background interference, for example, SA and LM respectively. Furthermore, four (4) confirmed PCR-negative samples from non-BU patients were analysed with the f-TLC method using BA18 and the results were compared with the positive cases (**Figure 3.11)**. The results showed that though there were background interferences in some cases, the TLC profiles were clearly seen to be negative which is indicative that they were non-BU samples (**top panel**, **Figure 3.11)**.

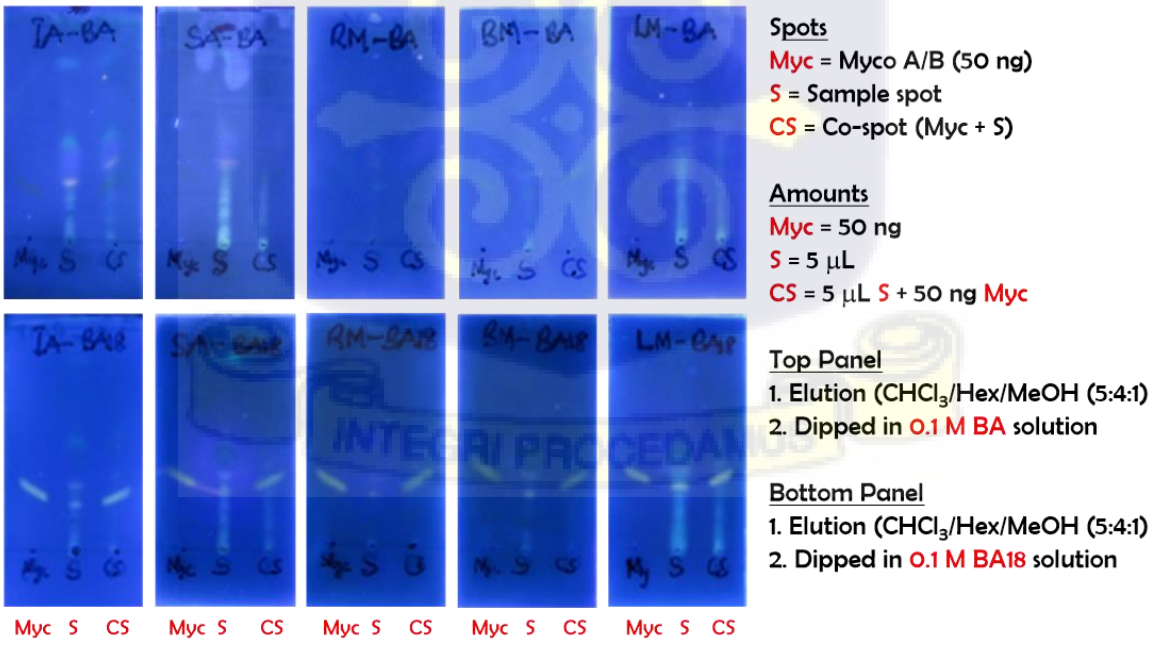

Figure 3.10. TLC profiles of PCR-confirmed positive confirmed BU cases.

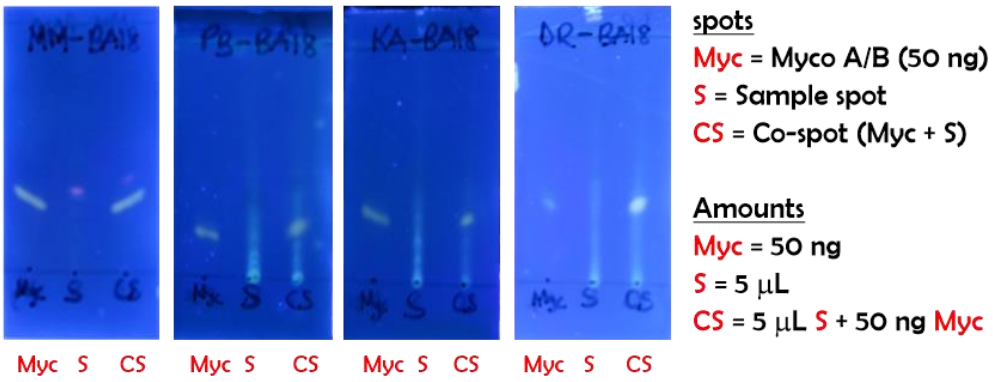

Figure 3.11. TLC profiles of PCR-confirmed negative non-BU cases.

3.4 Discussion

Different arylboronic acids purchased from various vendors were subjected to complexation reactions with the 1,3-diol motifs on the mycolactone A/B structure on TLC plates. The TLC plates were developed according to f-TLC method which uses the boronic acid as the fluorescence enhancer [74]. The developed plates were viewed under a 365 nm UV light. Mycolactone A/B was not very fluorescent on its own, however, its fluorescence intensity when bound to a boronic acid along the 1,3-diols increased under ultraviolet light. The Woodward-Fieser rule has been used to predict the position of the longest wavelength $\pi \rightarrow \pi^*$ UV band of these compounds and to correlate the electronic transitions and structures of α,β-unsaturated ketones [282, 283]. To predict the lowest energy $\pi \rightarrow \pi^*$ electronic transition of mycolactone, I computed the empirical longest UV wavelength using the parent Fieser value for α,β-unsaturated esters of 195 nm [284]. The computation showed that the pentaenoate region contributed a total of 4 extra double bonds (+30 each) and 3 methyl-substituted double bonds contributed +18 each. The total computed absorption maximum was 369 nm while the experimentally measured value on UV was of 362 nm. These findings were corroborated with the UV-vis analysis of the fatty acid side chain of mycolactone A/B [280]. These findings suggest that, though two cyclic boronates were formed, only the boronate of the southern side

chain that contains the pentanoate chromophore was activated when irradiated at 365 nm. Therefore the northern side chain boronate did not add to the increased fluorescence intensity under UV light [285]. Also, the excitation of mycolactone alone at an excitation wavelength of 365 nm presented weak fluorescence at 537 nm. However, a significant turn-on fluorescent enhancement was observed at the same 537 nm with a Stokes shift of 175 nm (**Figure 3.7A**) after the complexation was triggered with the boronic acid. The fluorescence was visible on TLC when viewed under UV lamp (**Figure 3.7B)**. The change in fluorescence intensity could firstly be attributed to the formation of the arylboronate on the southern chain [74, 280]. As a result, there is energy transfer from the excited pentaenoate moiety because it serves as a fluorophore to a fluorogenic acceptor (BA18) leading to the enhanced fluorescence [74].

3.5 Conclusion

Twenty-six arylboronic acids were purchased and evaluated as alternatives for BA using f-TLC. Arylboronic acid complexation of all the evaluated boronic acids with mycolactone A/B was observed and the formation of the adducts was confirmed by HRMS. All the evaluated boronic acids gave fluorescence intensities, albeit, with varying fluorescence band intensities. Three of boronic acids (BA15, BA18, and BA21) particularly returned superior profiles. In a related complexation experiment, BA, BA15, BA18, and BA21 were reacted with serial amounts of mycolactone (10 ng/µL – 90 ng/µL) and similar results were observed where myco-BA18 adduct gave the most intense fluorescence bands. Upon UV-vis measurements of mycolactone A/B and myco-boronic acid adducts, absorption maxima (λ_{max}) of 362 nm was obtained for mycolactone A/B and the rest were 272 nm (BA15), 270 nm (BA18), and 286 nm (BA21). Also, the Woodward-Fieser rule was used to estimate which portion of mycolactone was excited at 365 nm upon complexation with the boronic acid. It was observed that the boronate on the southern side chain containing the pentanoate chromophore was excited

whereas the northern side was not. Finally, improved fluorescent intensities of boronic acid adducts were observed for PCR-confirmed clinical samples when the TLC profiles of BA18 and BA were compared. Samples with background interference gave profiles that were easier to determine if they were positive or negative BU when the BA18 was used.

CHAPTER FOUR

4 Quantitative and Automated High-Performance Thin Layer Chromatography (HPTLC) for mycolactone detection in Buruli ulcer Diagnostics

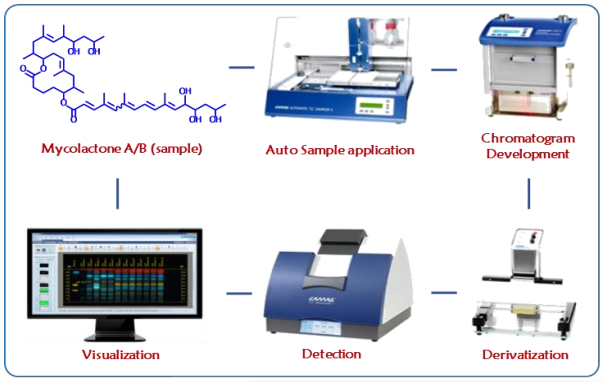

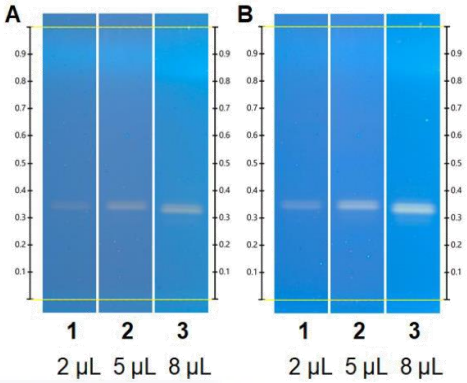

4.1 Background

Buruli ulcer is a skin and subcutaneous tissue disease caused by *Mycobacterium ulcerans*, whose mode of transmission is currently unknown [47, 286]. The disease often manifests clinically in various non-ulcerative forms such as nodules, papules, plaques, and oedema; and later breaks down into ulcerative forms with necrotic tissues and characteristic undermined edges [37, 38]. For a long time, surgical resection was primarily relied upon for the treatment of BU until antibiotic therapy was later introduced by the World Health Organization (WHO) as the first-line treatment [41]. Since the introduction of antibiotic therapy, an all-oral combination dose of rifampicin and clarithromycin for an 8-week duration has been demonstrated to be effective in the treatment of the disease without the need for surgical interventions or with minimum use of surgery. Antibiotics alone are curative in some patients with early lesions (i.e., nodules, papules, plaques, and ulcers of less than 5 cm in diameter)

[287-289]. In many early case instances, antibiotic treatment alone has helped to avert or minimize the serious morbidity and disability challenges that are usually associated with the advanced stages of the disease [48].

As with many other diseases, diagnosis is essential to Buruli ulcer and has thus become the bedrock in the control and management of the disease. It is said that "without diagnostics, medicine is blind" [290]. The need for diagnosis has become even more important because it is only through accurate, specific, sensitive, and rapid diagnosis that the disease can be treated effectively [291]. However, treatment decisions was originally made by differential diagnosis, which relies on clinical judgement by clinicians based on the characteristics of typical BU lesions [48]. Considering the broad resemblance between BU lesions and other skin conditions such as diabetic ulcers, cutaneous leishmaniasis, tropical phagedenic ulcers, or yaws, this approach has proven difficult [292]. As a result of the similarities in manifestations, BU lesions may be mistaken in many instances for the several other skin conditions, which could result in incorrect classification and disease diagnosis. Furthermore, this might result in the misuse of the recommended antibiotics which could potentially lead to resistance to these antibiotics especially in the era of antimicrobial resistance (AMR). Notably, other bacterial diseases such as *M. leprae* and *M. tuberculosis* that use rifampicin as a major component have already shown evidence of antibiotic resistance [293, 294]. Similar resistance patterns are more likely to be observed in *M. ulcerans* if antibiotics are not properly administered based on accurate diagnosis. Therefore, research efforts have been focused on finding specific and sensitive tests for the confirmation of BU to prevent the misuse of these drugs. Currently, clinical laboratories offer tests such as culture to isolate viable organisms, microscopy for the detection of acid-fast bacilli, polymerase chain reaction (PCR) targeting IS*2404* insertion sequence, and histopathological analysis for the detection of *M. ulcerans*. These tests have various limitations, including low sensitivity, high cost, dependence on sophisticated instruments and well-trained

operators, and labour-intensive. Nonetheless, PCR for detecting pathogen-specific DNA, which is usually IS*2404* has proven to be the most sensitive and specific if performed according to established quality assurance protocols [295]. As a result, it is currently regarded as the gold standard for diagnosis of the disease.

M. ulcerans is unique among human mycobacteria because it secretes a toxin called mycolactone (**Figure 4.1**) which is the virulent factor responsible for the pathogenesis of Buruli ulcer [11]. Mycolactone plays a crucial role in suppressing the immune response, promoting tissue damage, and facilitating bacterial spread. Even though the exact mechanism of action of tissue necrosis is not fully understood, it is thought to involve disruption of cell signaling pathways and interference with the host immune response [292]. Mycolactone is believed to be evenly and biosynthetically distributed in tissue samples. This is supported by the detection of intact mycolactone in biological samples taken from all forms and stages of the disease [68]. Additionally, it has been demonstrated through mice and human experiments that mycolactone can be found in peripheral blood [162]. These features coupled with the unique structure of mycolactone make it an attractive and useful biomarker for the development of novel diagnostic tools for Buruli ulcer. Therefore, methods such as thin-layer chromatography (TLC) [11, 70], mass spectrometry [16, 68, 69], or cytotoxicity assays [16] have been developed to detect and quantify mycolactone in tissue samples instead of targeting the *M. ulcerans* bacterium as with other standard tests. More recently, the detection of mycolactone from patient biopsy samples *via* LC–MS [16, 73], loop-mediated isothermal amplification (LAMP) [65, 72], and RNA aptamer binding [71] are being explored.

Kishi and colleagues developed a TLC technique that was sufficiently sensitive, simple-to-use, and less costly called the fluorescent-thin layer chromatography (f-TLC) for the direct detection of mycolactone from the human pathogen *Mycobacterium ulcerans*. The method is

based on the chemical derivatization of mycolactone A/B with 2-naphthylboronic acid (BA) fluorogenic chemosensor (**Figure 4.1**). Two 6-membered cyclic boronates are formed because of the complexation to the 1,3-diol units of mycolactone A/B with BA. Irradiation at 365 nm resulted in fluorescent enhancement around 520 nm which can be observed on thin-layer chromatography plates [74, 77].

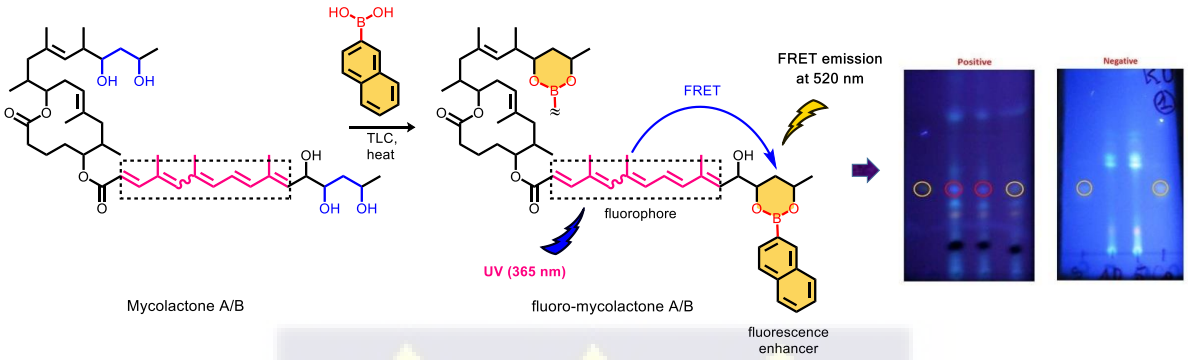

Figure 4.1. Schematic illustration of the working principle of Kishi's improved f-TLC detection of mycolactone exploiting derivatization with 2-naphthylboronic acid as a fluorescence enhancer.

The method has been validated in a mouse footpad model of *M. ulcerans* infection [77] and evaluated for skin tissue samples from Buruli ulcer patients) [75, 76] (**Figure 4.2**).

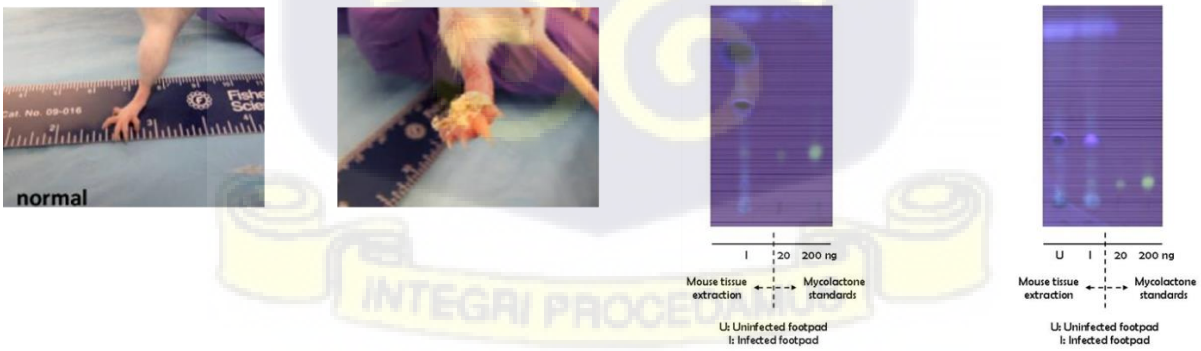

Figure 4.2. Proof of concept of f-TLC method using mouse footpad model (Unpublished Results: K. L. Jackson, P. L. C. Small, P. J. Converse, Y. Kishi).

The use of the f-TLC method for the detection of mycolactone holds great promise. For instance, in the earlier works Amewu et. al.., the method offered a sensitivity of 66.4% which is superior to microscopy (30–60%) or culture (35–60%), but inferior to both histology (82%) and PCR (92–98%) [296, 297]. The f-TLC method also returned 88.5% specificity and a diagnostic accuracy of 82.8% when compared to the gold standard PCR. However, the major drawbacks of the method include background interferences from other co-extracted human tissues which also fluoresces on TLC with similar bands thus hampering the clear identification of mycolactone A/B [76]. In addition, the read-out of the method has not been automated, thus open to a certain degree of subjectivity and human error since reading out the results relies heavily on the experience of the analyzer. To avoid subjectivity and ultimately achieve desirable and improved results with greater reproducibility, there is a need for a method that allows for accurate detection and optimal quantification of mycolactone in clinical samples.

Herein, I evaluated the performance of the high-performance thin layer chromatography (HPTLC) for the quantitative detection of mycolactone. The developed HPTLC method was validated for linearity of calibration, the limit of detection (LOD), the limit of quantification (LOQ), and precision (repeatability). The method may potentially be utilized as an effective tool for quality control purposes in the determination of the levels of mycolactone in clinical samples. The principles could potentially be employed to develop a point-of-care tool for on-field diagnosis of the Buruli ulcer.

4.2 Aims and objectives

4.2.1 Aim

The main aim of the study was to explore the feasibility of using HPTLC for quantitative detection of mycolactone produced by the human pathogen *Mycobacterium ulcerans.*

4.2.2 Objectives

The objectives for this study are as follows:

1. To identify, detect and quantify mycolactone.
2. To determine and visualise the locality of mycolactone by using its R_F value.
3. To validate the HPTLC method for linearity of calibration, the limit of detection (LOD), the limit of quantification (LOQ), and precision (repeatability).

4.3 Materials and Methods

4.3.1 Reagents and Chemicals

Synthetic mycolactone A/B was kindly donated by Professor Yoshito Kishi (Harvard University, Cambridge, MA, USA) through the World Health Organization (WHO), Geneva, Switzerland. Organic solvents were purchased from Roth AG (Karlsruhe, Germany). Diphenylborinic acid aminoethylester (natural products reagent, NP, 96.5–103.5%) and 2-naphthylboronic acid were purchased from Sigma Aldrich (Buchs, Switzerland) and *p*-anisaldehyde from ACROS Organics (New Jersey, USA). All other chemicals and solvents were of analytical reagent grade and used as received without further purification.

4.3.2 HPTLC Method and Chromatographic Conditions

4.3.2.1 Preparation of Standard working Solution of mycolactone.

A 10 ng/µL standard solution of mycolactone A/B was prepared by taking 0.1 mL of the mycolactone stock solution into a glass vial and adding 0.9 mL ethyl acetate to give the required standard for quantification purposes. A calibration curve was plotted between increasing amounts of mycolactone per spot and their peak area response.

4.3.2.2 Preparation of samples clinical samples

Samples for HPTLC were prepared according to the protocol developed and published elsewhere with minor modifications [76, 77, 280]. A solution of the sample in ethanol was filtered through a cotton plug into a glass vial. The container from which the sample was filtered was further rinsed with 1 mL ethyl acetate and added to the glass vial through the cotton plug used for the initial filtration. The combined solvents were evaporated to dryness under reduced pressure. Then, 100 µL hexane/ether (1:1) solution was added to the glass vial, rinsed, and transferred by micro syringe into another clean glass vial to separate any contaminating solid from the liquid after which it was air-dried. PCR confirmed BU and non-BU samples were shipped from Prof Richard Amewu's Lab, Department of Chemistry, University of Ghana to CAMAG (Muttenz, Switzerland). The samples were extracted and were then put in foil-wrapped 4 mL opaque glass vials with 2 mL absolute EtOH and shipped to CAMAG (Muttenz, Switzerland) for analysis.

4.3.2.3 Preparation of derivatization reagents

Natural products reagent (NP): 1 g of diphenylborinic acid aminoethylester is dissolved in 200 mL of ethyl acetate.

Anisaldehyde-sulfuric acid reagent: 10 mL of sulfuric acid is carefully added to an ice-cooled mixture of 170 mL of methanol and 20 mL of acetic acid. To this solution, 1 mL of anisaldehyde is added.

2-naphthylboronic acid (BA) reagent: 1.72 g of the 2-naphthylboronic acid was weighed into a glass jar, dissolved in 100 mL acetone to make up 0.1 M of the 2-naphthylboronic acid solution and stored for use.

4.3.2.4 HPTLC analysis

Table 4.1: Reagents used and their composition.	
Instrumentation	CAMAG HPTLC apparatus consists of an automatic TLC sampler (ATS4), automatic developing chamber (ADC2), documentation device (TLC visualiser 2), automatic derivatiser device and TLC plate heater.
HPTLC plates	Silica gel glass plates 60 F254 (Merck)
Sample application	0.1 mg/mL mycolactone standard: 2, 5, and 5 µL of the standard mycolactone were spotted as 10 mm bands.
Plate development	Plates developed in a 20 × 10 × 4 cm glass twin-trough chamber to a migration distance of 70 mm. Tank saturation: 20 min at 15 °C and a relative humidity of 33% (33% RH), with 25 mL of mobile phase
Mobile phase	Chloroform: hexane : methanol (5:4:1 v/v/v).
Derivatization	• 2-naphthylboronic acid (BA) reagent (1.72 g of the 2-naphthylboronic acid + 100 mL acetone). The plate is sprayed with 3 mL of 2-naphthylboronic acid reagent, followed by heating for 3 min at 100 °C and then visualised. • Anisaldehyde reagent (170 mL methanol + 20 mL acetic acid + 10 mL sulphuric acid + 1 mL anisaldehyde). The plate is sprayed with 3 mL of anisaldehyde reagent, followed by heating for 3 min at 100 °C and then visualised. • Natural product reagent (NP) (1 g 2-aminoethyl diphenylborinate + 100 mL methanol). The plate is heated for 3 min at 100 °C and sprayed with 3 mL of NP.
Visualisation	• The plate is viewed under white reflectance. • The plate is viewed under UV 254 nm radiation. • The plate is viewed under UV 366 nm radiation.
Description of plate	• Track numbers 1, 2, and 3 represent different volumes of mycolactone standard (2, 5 and 8 µL) respectively (R_F = 0.32).

4.3.2.5 Sample Application

The standard solution of mycolactone was spotted on pre-coated TLC plates in the form of narrow bands of lengths 6 mm, with 10 mm from the bottom and left margin and with 8 mm distance between two bands. Samples were applied under a continuous drying stream of nitrogen gas at a constant application rate of 150 nL/s.

4.3.2.6 Mobile Phase and Migration

Plates were developed using the mobile phase consisting of chloroform:hexane:methanol (5:4:1 v/v/v). Linear ascending development was carried out in a 10 cm × 10 cm twin trough glass chamber equilibrated with mobile phase. The optimized chamber saturation time for the mobile phase was 20 min at 25 ± 2 °C. Ten millilitres of the mobile phase (5mL in a trough containing the plate and 5mL in the other trough) was used for each development and allowed to migrate 70 mm, which required 10min. After development, the TLC plates were dried completely.

4.3.2.7 Linearity and Calibration Curve

The linearity of the HPTLC method for the detection of mycolactone was evaluated by generating calibration curves at nine concentration levels. Calibration curves were plotted over a concentration range of 4 – 45 ng/spot. 10 µL of the standard stock solution, mycolactone stock solution was transferred into a glass vial and diluted with 990 µL ethyl acetate to obtain a working solution of 1 ng/µL. Different aliquots of the diluted standard working solution of mycolactone (1 ng/µL) were applied on the HPTLC plate (4, 8, 12, 16, 20, 25, 30, 40, and 45 µL/spot) to obtain a concentration range of 4 – 45 ng/spot and resulting peak areas were evaluated. Afterwards, the plate was developed in chloroform:hexane:methanol (5:4:1 v/v/v) and scanned at the wavelength of maximum absorption of mycolactone (λ_{max} = 364 nm). The calibration curve was then obtained by plotting the peak area (AU) against the various concentrations (n = 9) with the help of the winCATS software.

4.4 Results and Discussion

The specificity of the existing HPTLC method for the detection of mycolactone was first evaluated by performing the analyses on 0.20 mm layers of silica gel 60 F254 HPTLC glass

plates (20 x 10 cm) to determine and visualise the locality of the mycolactone by using the retention factor (R_F) value of 0.32. First, 100 µL of the standard mycolactone A/B (0.1 mg/mL) was transferred into an autosampler vial as a reference solution. Different aliquots (2, 5 and 8 µL) of the reference solutions were applied as three different tracks per plate (tracks 1, 2, and 3, **Figure 4.3**). The aliquots were applied as 10 mm bands (120 nL/s delivery speed, track width 11.4 mm, 8 mm from the lower edge and 20 mm from the left edge). The plates were pre-conditioned to a relative humidity of 33% with saturated $MgCl_2$ solution before development. A mobile phase of chloroform:hexane:methanol (5:4:1 v/v/v) for the f-TLC method for the detection of mycolactone was adopted [75, 76] for elution. The migration distance was 70 mm from the lower edge of the plate. After elution, the HPTLC plates were detected visually under 254 and 366 nm UV lamps prior to derivatization with a good R_F value of 0.32. The digital images of the developed plates were taken under 254 nm and 366 nm to show background colour and spots of mycolactone under both wavelength readings before any derivatization step (**Figure 4.3A** & **4.3B**). Additionally, the *in-situ* UV spectrum of the chromatographic zone of mycolactone was measured with a CAMAG TLC Scanner II (Muttenz, Switzerland) at a wavelength range of 190 – 450 nm. The UV spectrum of mycolactone showed an absorption maximum of 364 nm (λ_{max} = 364 nm) (**Figure 4.3C**). From the images, it was observed that the reference solution applied at 2 µL (track 1) was barely detectable without derivatization under both 254 and 366 nm UV, however, the spots 5 and 8 µL (tracks 2 and 3) were visible even with the derivatization.

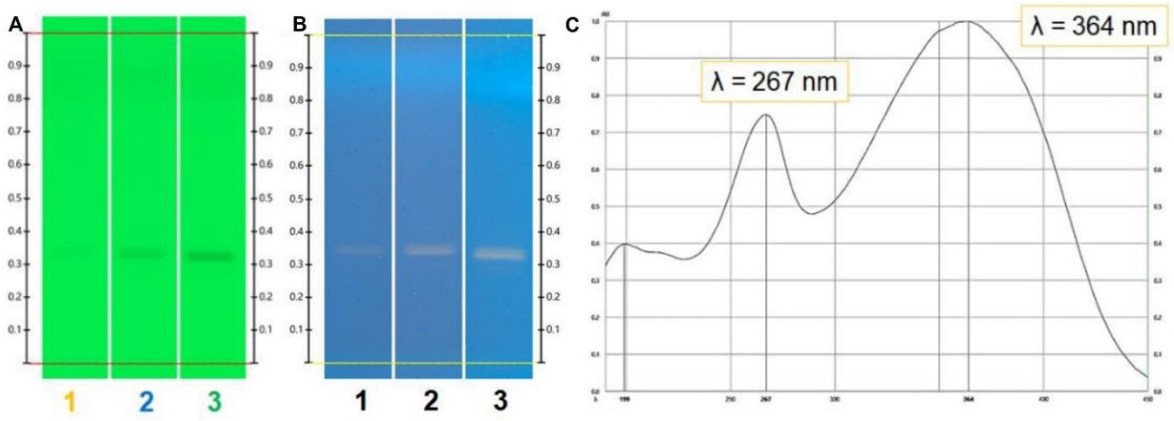

Figure 4.3. HPTLC of mycolactone A/B reference under UV 254 nm prior to derivatization (A), under UV 366 nm prior to derivatization (B), and UV spectrum on HPTLC plate Silica gel 60 F254 (C).

Following the observation above, it was decided to derivatize the mycolactone using various derivatizing agents that are traditionally employed in HPTLC analysis such as anisaldehyde and natural product reagents (NP) reagents because of the advantages they offer including their excellent ability to discriminate all types of samples. Also, anisaldehyde is known to be less toxic and has been used extensively for the detection of catechins [298]. These derivatizing reagents were then compared to 2-naphthylboronic acid which was used in the f-TLC method [75, 76]. For derivatization to occur, the plates were heated on a hotplate at approximately 100 °C for 3 minutes. Digital images of the developed plates observed under UV 366 nm before and after derivatization using 2-naphthylboronic acid are presented in **Figure 4.4.**

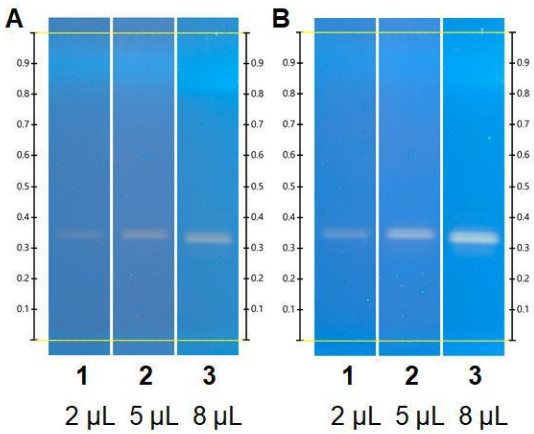

Figure 4.4. HPTLC of mycolactone A/B reference under UV 366 nm (A) prior to derivatization, and under UV 366 nm after derivatization (2-naphtylboronic acid) (B) on HPTLC plate Si gel 60.

Figure 4.5 shows the digital images of HPTLC plates that were spotted with different aliquots of mycolactone standards, treated with different derivatization reagents and viewed under various light sources such as UV 254 nm, 366 nm and under white light. For all plates, the reference standard was visible on all the plates as a band that is characterised by specific colours, before and after derivatization with a consistent R_F value of 0.32 which is an indication of the precision and reproducibility of the HPTLC method in detecting mycolactone. There are visually evident differences in band intensities observed when each HPTLC panel plate was treated differently. For instance, in **Panel A** (under UV 254 nm underivatized), mycolactone appeared as a black spot over a green background (R_F 0.32). For track 1 (2 µL spot), the mycolactone spot was barely visible. For **Panel B,** which was underivatized and viewed under UV 366 nm, there was no improvement in the intensity of the bands for mycolactone over **Panel A**. However, in **Panel C** where the plate was subsequently derivatized with NP and viewed under UV 366 nm, it exhibited improved band intensities over both **Panels A** and **B**. Derivatization with NP/Anisaldehyde was found to be suitable for visualizing the mycolactone both under UV 366 nm (**Panel D**) and the use of white light (**Panel E**) compared to ultraviolet

radiation at 254 and 366 nm before or after derivatization with only NP. Comparatively, the detection of mycolactone A/B reference seems to be better and most favourable after derivatization with 2-naphthylboronic acid and detection under 366 nm wavelength with visibly intense yellow bands over a blue background (**Panel BA**) than with the other derivatizing reagents and detection conditions except perhaps **Panel D** and **E**. For Panels **BA**, **D**, and **E**, even the spot at 2 µL was clearly visible. Despite the different band intensities and colours under different derivatizing and detection conditions as explained, a reasonable hypothesis suggests that any test sample that contains mycolactone should have the characteristics of mycolactone band with an R_F value of 0.32 provided the same elution solvent system is used. Therefore, the reported R_F value can be used for easy identification of mycolactone in clinical samples of BU patients.

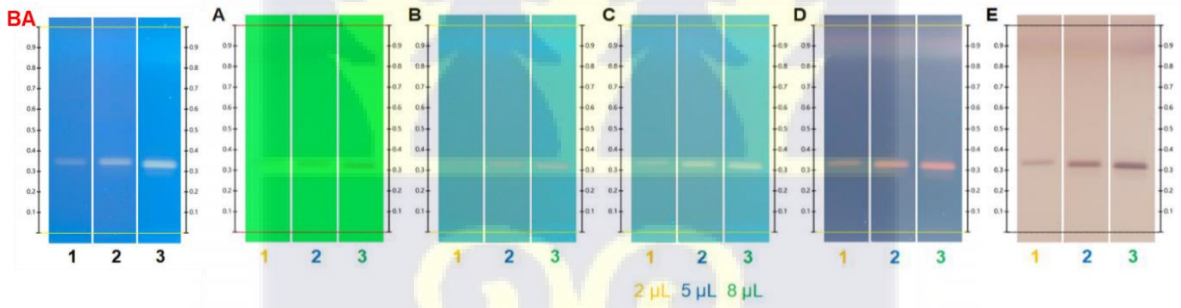

Figure 4.5. HPTLC results of the selected method. BA: derivatized (2-naphthylboronic acid), under UV 366 nm; A: underivatized, under UV 254 nm; B: underivatized, under 366 nm; C: derivatized (NP), under UV 366 nm; D: derivatized (NP/Anisaldehyde), under UV 366 nm; E: derivatized (NP/Anisaldehyde), under white light. Track 1: 2 µL mycolactone standard; Track 2: 5 µL mycolactone standard; Track 3: 8 µL mycolactone standard.

The linearity, limit of detection (LOD), and limit of quantitation (LOQ) of the method to detect mycolactone were determined by densitometry measurements at 364 nm prior to derivatization. Densitometry is best performed at the wavelength of maximum absorption for visible/UV

absorption [299]. The smallest amount of mycolactone that can provide a visual response was considered the limit of detection [300]. At each concentration of the reference solution, the area under the curve of each spectrum was measured and the data was represented in **Table 4.2**

Table 4.2: Validation data of caffeine standards obtained from HPTLC chromatograms.

Vial No.	Mycolactone standard concentration (ng/µL)	Peak Area	R_F value
1	4	0.000258	0.32
2	8	0.000477	0.32
3	12	0.000510	0.32
4	16	0.000828	0.32
5	20	0.000923	0.32
6	25	0.001110	0.32
7	30	0.001332	0.32
8	40	0.001689	0.32
9	45	0.001678	0.32

Quantitative calibration of HPTLC data can usually be fitted appropriately using a polynomial regression, however, there is often a linear range within the working range that can be fitted with a satisfactory linear regression. Thus, a calibration plot of peak area against concentration was then constructed from the data and was observed to be linear in the range of from 4 to 45 ng/spot for mycolactone with intercept and slope values of 1.68×10^{-4} and 3.64×10^{-5} respectively and with a correlation coefficient greater than 0.97 (**Figure 4.6**). The sensitivity of the HPTLC method for the detection of mycolactone was determined by calculating LOD and LOQ. The approach used for the calculation of LOD and LOQ was based on signal-to-noise ratio which is estimated by comparing the measured signals from samples of known low concentrations of analyte with those of blank samples and establishing the minimum concentration at which the analyte can be reliably detected. According to literature, a signal-to-noise ratio of 3 is considered acceptable for estimating the LOD and of 10 for the LOQ [298,

301]. The limit of detection (LOD) and limit of quantification (LOQ) were based on the comparison of standard deviation (SD) of multiple measurements (n = 9) of the band area and the slope of the calibration curve [302, 303]. Thus, from the linear equation generated from the calibration line that was fitted, the LOD and LOQ were calculated using the following equations.

$$\mathrm{LOD} = 3 \times \frac{\mathrm{N}}{\mathrm{B}}$$

$$\mathrm{LOQ} = 10 \times \frac{\mathrm{N}}{\mathrm{B}}$$

where *N* is the standard deviation (SD) of the peak area (n = 9), taken as a measure of the noise, and *B* is the slope of the corresponding calibration curve. The LOD and LOQ for mycolactone were estimated to be 6.6 and 22 ng/spot respectively.

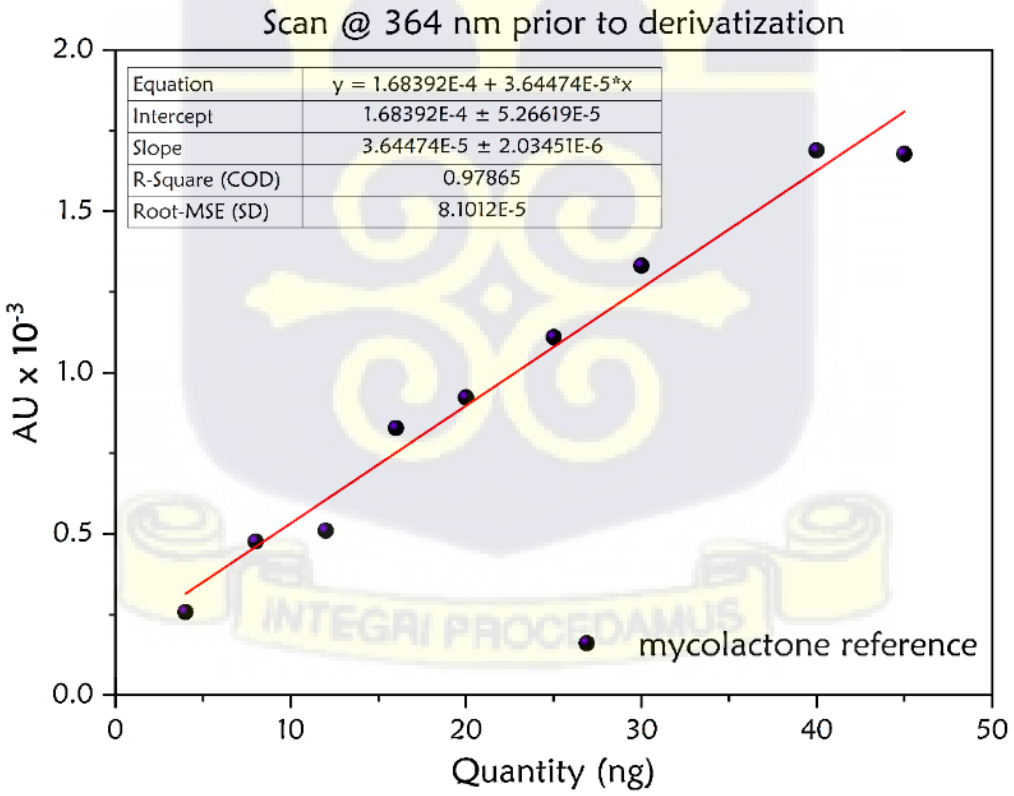

Figure 4.6. LOD, LOQ and linearity range of mycolactone.

Subsequently, preliminary evaluation of the HPTLC was attempted using clinical samples that were confirmed as BU and non-BU by PCR following the method described by Stinear et. al. [281]. For the non-BU sample (Non-BU; S21349) (**Figure 4.7**; tracks 2 – 4), it was found that after derivatization with 2-naphthylboronic acid/anisaldehyde reagent, as expected, none of the zones corresponded to the mycolactone reference solution with an R_F value of 0.32. On the other hand, when a PCR-positive BU sample (BU; S21338) was analyzed (**Figure 4.7**; tracks 5 – 7), although the expectation was to have matching R_F values for both the sample and the mycolactone reference solution, the contrary was observed. After derivatization with NP/Anisaldehyde, many bands with different R_F values were detected on the plates but none of them in both BU and non-BU samples corresponded to the mycolactone reference solution with an R_F value of 0.32. Therefore, I could not confirm the presence of mycolactone in the BU sample (BU; S21338).

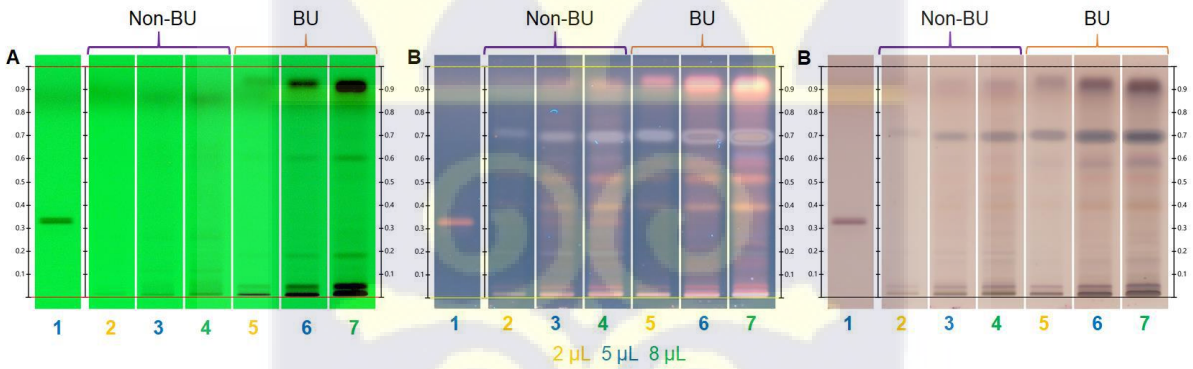

Figure 4.7. HPTLC of negative (non-BU; S21349) and positive (BU; S21338) samples under UV 254 nm prior to derivatization (A), under UV 366 nm (B), and under white light after derivatization NP/Anisaldehyde (subsequent derivatization) (B) on HPTLC plate Silica gel 60 F254.

4.4.1 Densitometric Scanning of BU and Non-Bu Samples

Following failed attempts to detect mycolactone in the BU sample (BU; S21338) on the HPTLC plate under UV 254 nm, UV 366 nm and white light before and after derivatization with NP/Anisaldehyde, I subjected the BU and Non-BU samples prior to derivatization to a densitometric scan at 364 nm and compared to the mycolactone A/B reference solution (**Figure 4.8**). Interestingly, a small absorbance peak was detected at the same R_F value of approximately 0.32 as the mycolactone A/B reference solution for the BU sample where the non-BU sample remains essentially flat. Based on these findings, it could be concluded that indeed, the positive BU sample had mycolactone present in it whereas the negative non-BU sample did not. Therefore, my inability to detect mycolactone using the HPTLC could be attributed to mycolactone levels in the analysed sample falling under detection limit of the HPTLC (6.6 ng) below which mycolactone cannot be detected.

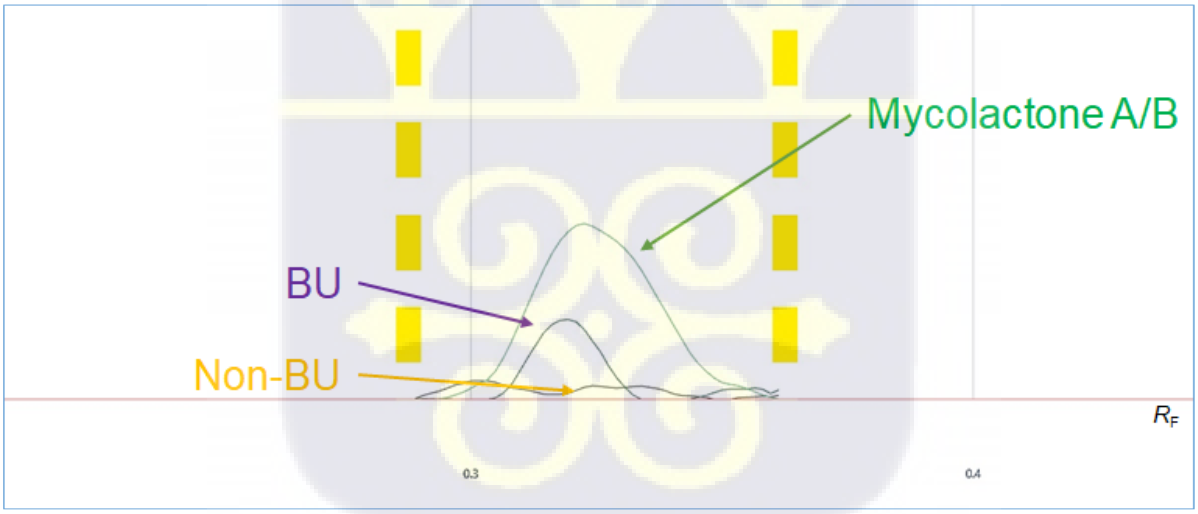

Figure 4.8. Densitometric scans at 364 nm prior to derivatization of a non-BU and a BU sample on HPTLC plate Silica gel 60 F254.

4.5 Conclusion

In place of the f-TLC technique, we have successfully used the HPTLC for the quantitative detection of mycolactone based on the working principles of the f-TLC method developed by Kishi and co-workers. Acceptable performance and semi-automation have been achieved using the HPTLC method. Mycolactone reference solution has been successfully detected on HPTLC Silica gel 60 with an R_F value of 0.32. which is good for the quantification. The quantification has been achieved either by densitometry scanning at the absorption maximum of the mycolactone (λ_{max} = 364 nm) or by an estimation of limits of detection and quantification based on image evaluation at 364 nm. For the validated HPTLC method, the linear range was 4 – 45 ng for mycolactone with an R^2 = 0.98. The LOD value was 6.6 ng while the LOQ value was found to be 22 ng. Preliminary results show that HPTLC offers advantages over conventional f-TLC because different steps are automated allowing for the achievement of increased resolution, and more accurate quantitative measurements. The results also show that the HPTLC technique could become useful in overcoming the uncertainty in droplet size and position as compared to when the sample is applied to the TLC plate by hand.

CHAPTER FIVE

5 Molecular recognition of Mycolactone: Rational design and synthesis of a library of fluorescent arylboronic acid chemosensor dyes for mycolactone detection.

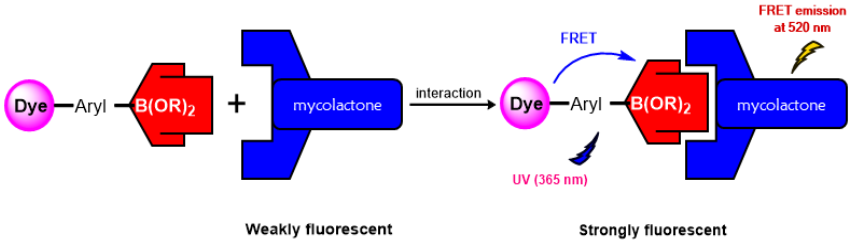

5.1 Background and Rationale

Over the years, researchers, inspired by certain biological processes in nature looked for new concepts, that allow for the selective molecular recognition of target molecules that play important roles in complex chemical processes in various disciplines such as medicine, biology, agriculture, biomedical, environmental, and social sciences [304]. Molecular recognition is achieved by the utility of chemosensors. Chemosensors are molecules of abiotic origin that signal the presence of matter or energy. A fluorescent chemosensor therefore is a compound that interacts with an analyte in such a way as to produce a detectable fluorescent signal [305]. Fluorescent chemosensors are of particular interest in supramolecular chemistry because of their ability to recognise guest species as well as their high selectivity, sensitivity, and simplicity [306, 307].

Generally, a fluorescent chemosensor is composed of a recognition moiety that interacts with an analyte of interest and relays the recognition event through a signalling unit. Thus, the engineering of appropriate fluorescent chemosensors with the right recognition and signalling moieties can result in favourable interactions with specific analytes of interest. However, to

achieve this, a comprehensive understanding of the role and chemistry of the target analyte is required. Mycolactone A/B is the target analyte in this research. It plays a significant role in the virulence, pathogenicity, and cytotoxicity of Buruli ulcer disease – thus, the detection of its presence in biological samples is necessary for the diagnosis of the disease. The chemistry of mycolactone A/B has been extensively studied [83, 184-186]. Structurally, it is a polyketide macrolide toxin composed of a 12-membered macrocyclic lactone core (C1–C11) with two laterally attached side chains; a C-linked northern side chain (C12–C20) with two hydroxyl groups in 1,3-diol positions at C17 and C19; and a C5-O-linked polyunsaturated acyl southern side chain (C1'–C16') possessing a conjugated pentaenoic acid ester chromophore and three hydroxyl groups, two of which are in 1,3-diol positions at C13' and C15' [167, 182] (**Figure 5.1**).

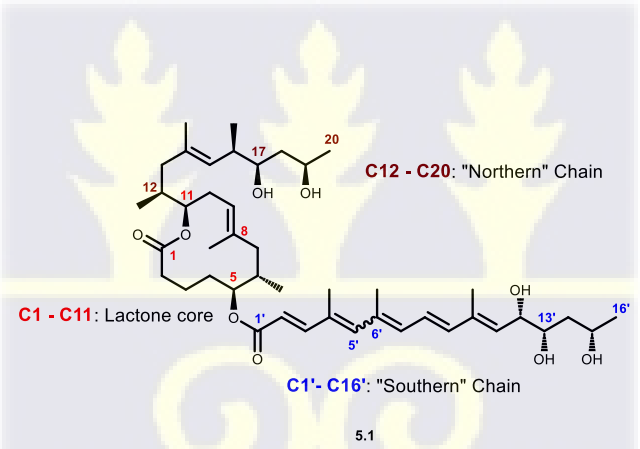

Figure 5.1. Structure of mycolactone A/B.

A boronic acid motif can be explored as a recognition unit in the design of chemosensors to exploit the 1,3-diol moieties on the structure of the analyte. This is because boronic acids and their derivatives have the unique ability to form five- or six-membered boronate ester complexes with 1,2- or 1,3-diols that are present on biologically relevant molecules [253, 308]. The phenomenon of the complexation of boronic acids with polyols to form boronate esters dates to over 70 years but remains an area of research interest. The first reported use of boronic acids as recognition units for cis 1,2- or 1,3-diol-containing compounds was published by

Lorand and Edwards in 1959. They demonstrated the complexation equilibria of aqueous benzeneboronate ion with several polyols and compared the association constants to that of borate [259]. Following the early seminal work of Lorand and Edwards, boronic acids have greatly evolved into an area of research for molecular recognition thus gaining significant interest in the design of many fluorescent chemosensors because of their selective binding behaviour, particularly for diols. The first fluorescent boronic acid-based sensor was developed later in 1992 by Yoon and Czarnik for saccharide sensing [279]. Since then, the boronic acid functionality has increasingly become a very important recognition moiety in the design and synthesis of molecular recognition chemosensors because of their high stability, environmental friendliness, general low toxicity, and relatively inexpensive nature. Moreover, a considerable number of biological molecules possess polyhydroxy motifs. Therefore, the selective binding behaviour of the boronic acid unit has been explored for the detection of diol-containing analytes based on the "lock-and-key" concept of enzyme-substrate recognition [309]. Because of the unique properties of the boronic acid functionality that has positioned it as an invaluable receptor, researchers have made tremendous efforts in the design of several fluorescent boronic acid chemosensors for the specific recognition and detection of various biological polyol molecules including saccharides, catechol, glycoproteins, catecholamines, and dopamine as well as anions such as cyanides and fluoride [253, 257, 310, 311]. However, no chemosensor has been designed and developed for the molecular recognition of mycolactone. Considering the unique structure of mycolactone, I hypothesised that boronate ester formation between the diol moieties of mycolactone and a boronic acid binding site attached to a fluorescent molecule would allow for signal transduction that could be exploited for mycolactone detection. Therefore, I employed various fluorescent dyes (fluorophores) such as 9-aminoacridine, 8-aminoquinoline, azo, BODIPYs, coumarins, fluorescein, and rhodamines dyes, which are all

amenable to boronic acid tethering to design, synthesize and completely characterize various fluorescent arylboronic acid dye chemosensors.

5.2 Design strategy and synthesis of arylboronic acid chemosensors fluorescent dyes for mycolactone detection

Given the abundance of literature precedence on the ability of boronic acid to bind generally to polyols, my interest has been in using arylboronic acid receptors for the detection of mycolactone. In Akolgo et. al., various boronic acids were found to be efficient at selectively detecting mycolactone, the mechanism of which was attributed to the potential formation of boronate complexes between the boronic acid units and the 1,3-diol moieties present in the mycolactone structure [312]. These findings provided me with some guidance to further explore the use of fluorescent arylboronic acid chemosensors to study their possible selectivity for mycolactone. Consequently, a library of arylboronic acid fluorescent chemosensors for mycolactone detection was designed and synthesised. The following requirements of fluorescent chemosensors guided my design; selectivity and affinity for the analyte of interest (mycolactone), easily synthesized from readily available commercial starting materials and reagents, produce a strong signal change that can easily be detected upon mycolactone recognition, and an appropriate fluorophore scaffold with high fluorescence quantum yield, and adequate solubility. The fluorophore scaffold should also have excitation and emission profiles in the visible or near-infrared region, or be suitable for two-photon excitation, to minimize interference from autofluorescence [313]. Other criteria that were considered include efficient signal transduction, emission of detectable intensities of UV or visible radiation, or other quantifiable signal [273]. After the successful design, the synthesis of the library of fluorescent arylboronic acid chemosensors involved the use of synthetic combinatorial approaches to conjugate various classes of fluorescent dyes (chromophore or fluorophore) of

interest with inherent beneficial photophysical characteristics to a recognition moiety (the boronic acid unit) either directly or through a linker. I selected suitable dyes such as 9-aminoacridine, 8-aminoquinoline, azo, BODIPYs, coumarins, fluorescein, and rhodamines dyes because these are already well-known fluorophores with excellent photophysical properties including large excitation and emission maxima, extinction coefficient, high fluorescence quantum yield (Φ), large Stokes shift, high brightness, adequate solubility, good thermal and photostability and sufficient chemical stability [271, 314, 315] (**Figure 5.2**). Secondly, these dyes are commercially available and can be coupled to diverse functional groups.

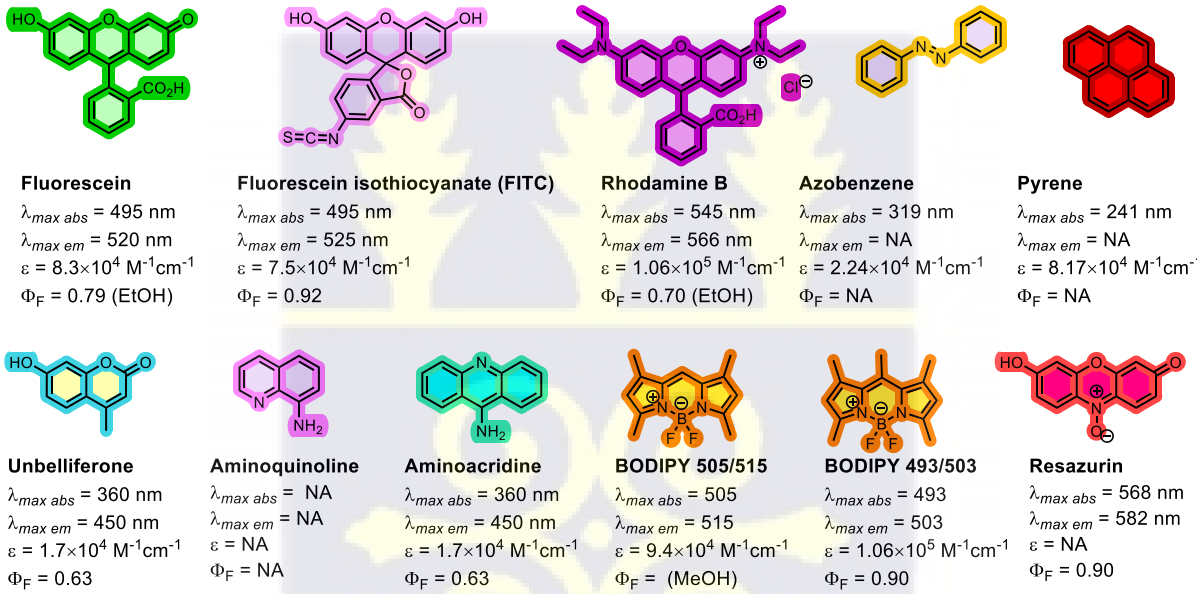

Figure 5.2. Structures of common fluorescent dyes.

5.3 Results and Discussion

5.3.1 Synthesis of various arylboronic acid chemosensors fluorescent dyes

5.3.1.1 Synthesis of the building blocks through Miyaura borylation

The syntheses of the various boronic ester building blocks were accomplished *via* a palladium-catalyzed Miyaura borylation of aryl halides with a diboron reagent such as bis(pinacolato)diboron (B_2pin_2). Potassium acetate (KOAc) was employed as the base, and the reaction was carried out in 1,4-dioxane at 80 °C for 16 h [316-318]. The protected boronate esters were readily purified by silica gel chromatography to obtain analytically pure and white crystalline pinacol boronate ester solids in excellent yields (**Scheme 5.1**). Interestingly, these boronate ester solids are all indefinitely bench-stable under air compared to their corresponding boronic acids.

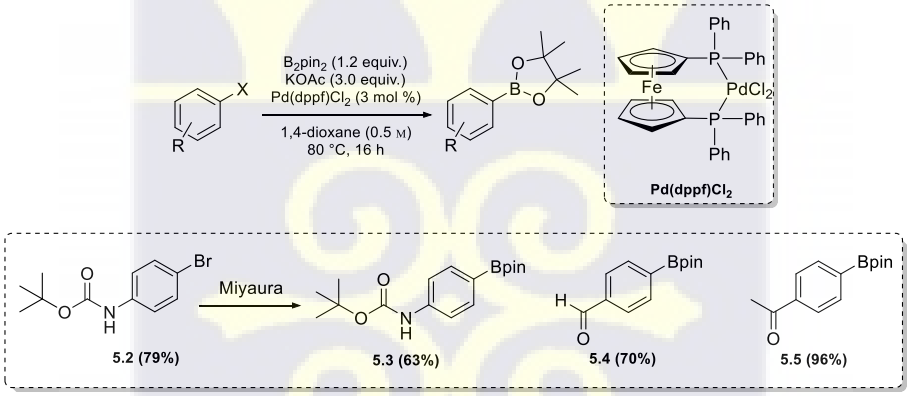

Scheme 5.1. Palladium-catalyzed Miyaura borylation of aryl halides utilizing bis(pinacolato)diboron.

The ^1H NMR and ^{13}C NMR spectra of **5.4** are represented in **Figure 5.3** and **Figure 5.4** respectively. In the ^1H NMR spectrum, a singlet at δ_H = 10.02 ppm attributed to the aldehydic proton, two doublets (δ_H = 7.94 and 7.83 ppm, J = 8.2 Hz) attributed to the methine protons on

the phenyl ring, and another singlet at δ_H = 1.33 ppm attributed to the four tertiary pinacol methyl groups with integrals ratio 1:2:2:12 were found (**Figure 5.3**).

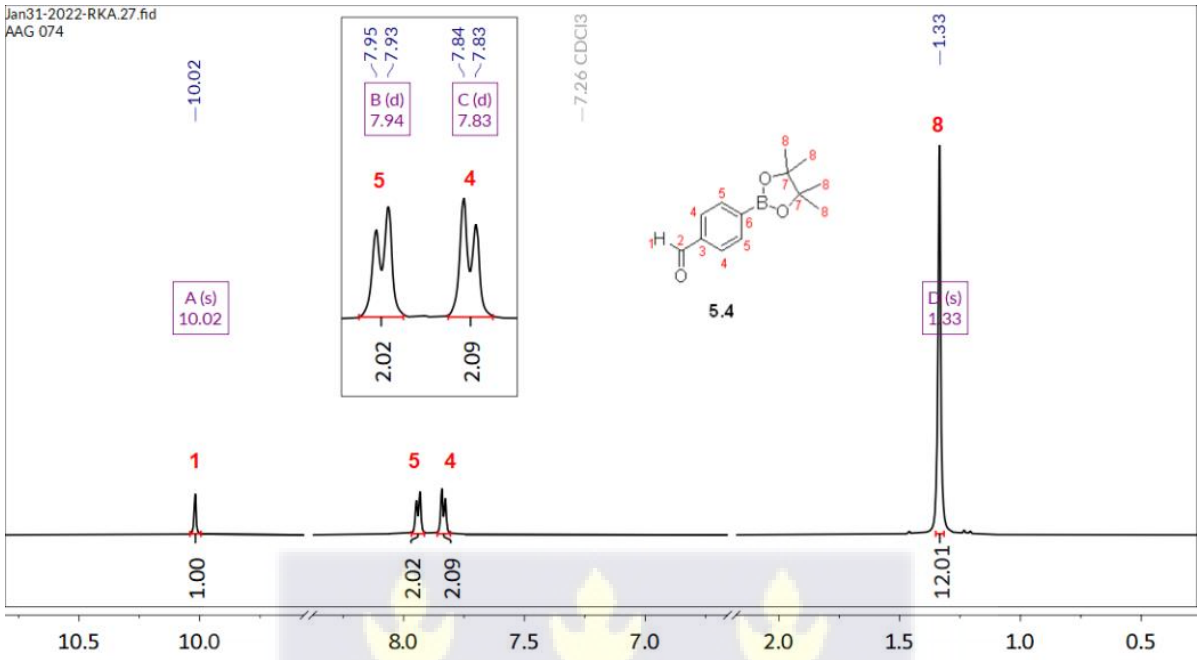

Figure 5.3. ^{1}H NMR spectrum (500 MHz, $CDCl_3$) of 4-(4,4,5,5-tetramethyl-1,3,2-dioxaborolan-2-yl)benzaldehyde **5.4**.

The ^{13}C NMR spectrum of compound **5.4** showed signals from 6 out 7 chemically different carbon environments (**Figure 5.4**). The signal at δ_C = 25.2 ppm is attributed to four pinacol methyl carbons whereas the signal at δ_C = 84.7 ppm corresponds to the two aliphatic quaternary carbons. The signals at δ_C = 129.0 and 135.6 ppm are attributed to methine groups on the phenyl ring. The remaining signal at δ_C = 138.5 ppm is attributed to the quaternary carbon C3. However, the signal originating from the other quaternary carbon C6 which is directly bonded to boron was not observed in ^{13}C NMR spectra due to broadening [319]. The aldehydic carbonyl signal occurred at δ_C = 192.9. The structure of compound **5.4** was confirmed with ESI-QTOF HRMS data with $[M+Na]^+$ $[C_{13}H_{17}BO_3Na]^+$ peak found at *m/z* found: 255.1172 compared to the exact *calcd.* mass of *m/z* = 255.1168.

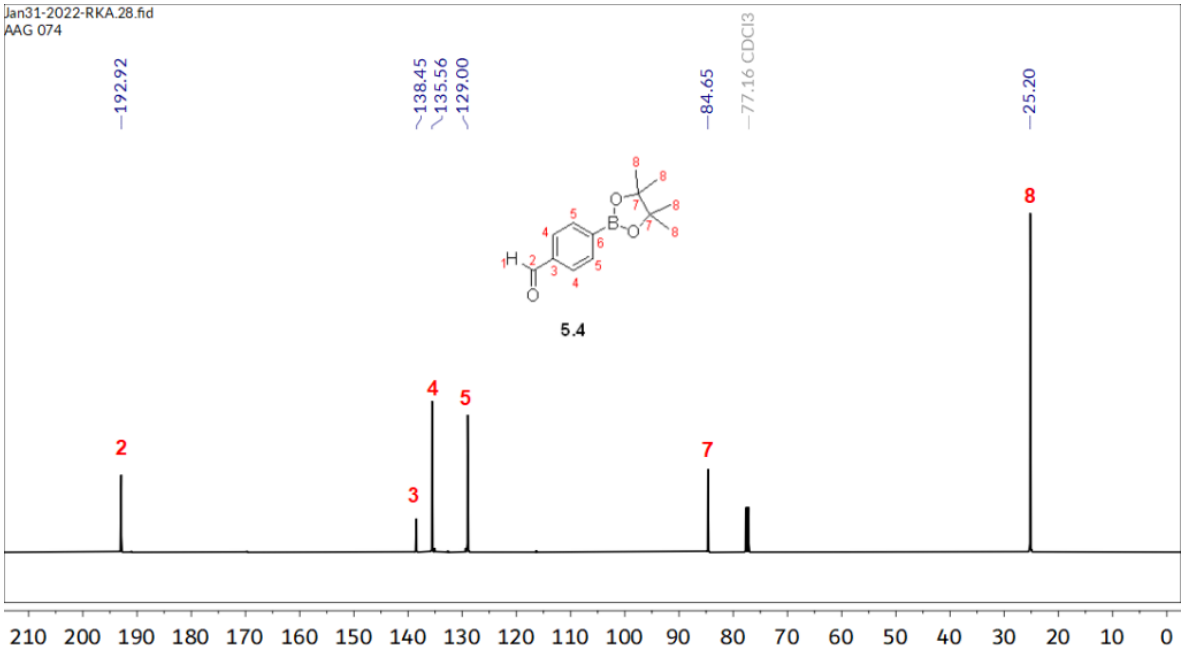

Figure 5.4. ^{13}C NMR spectrum (126 MHz, $CDCl_3$) of 4-(4,4,5,5-tetramethyl-1,3,2-dioxaborolan-2-yl)benzaldehyde **5.4.**

With building blocks suitable for incorporation into other reactions in hand, the synthesis of various arylboronates requiring the use of these building blocks commenced. The Bpin protective groups were found to be completely stable to various reaction conditions.

5.3.1.2 Coumarin-tagged boronic acids.

Coumarin and its derivatives are widely used as fluorescent probes because of their excellent chromogenic and fluorogenic properties such as high fluorescence quantum yields, large Stokes shifts, excellent photostability, and thermal stability [320-326]. Based on this knowledge, two coumarin-tagged boronic acids were designed and synthesized (**Schemes 5.2** and **5.4**). The coumarin moiety serves as the fluorophore core and the boronic acid is the reaction unit. The synthesis of the target probe **AAG113** was achieved in four chemical steps as shown in **Scheme 5.2**.

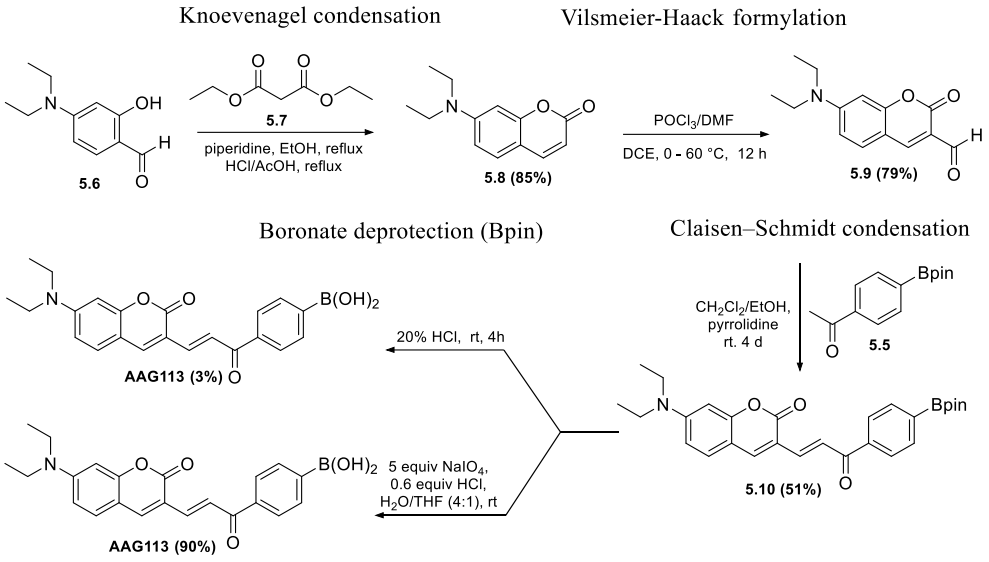

Scheme 5.2. Synthesis routes of coumarin-tagged boronic acid **AAG113**.

The first step of the synthesis is *via* Knoevenagel condensation reaction of 4-(diethylamino)-2-hydroxybenzaldehyde **5.6** with diethyl malonate **5.7** in the presence of piperidine, cyclized and then decarboxylated to afford 7-(diethylamino)-2H-chromen-2-one **5.8** in good yield (85%). In a detailed NMR analysis, the aliphatic region of the ^{1}H NMR spectrum gave a quartet at δ_H = 3.40 ppm (J = 7.2 Hz) and a triplet at δ_H = 1.20 ppm (J = 7.2 Hz) with an integral ratio of 2:3. The aromatic region has four doublets at δ_H 7.53, 7.23, 6.46, and 6.01 ppm and one doublet of doublets at δ_H = 6.56 ppm (J = 8.8, 2.5 Hz) with integral ratio of 1 : 1 : 1 : 1 : 1 (**Figure 5.5**).

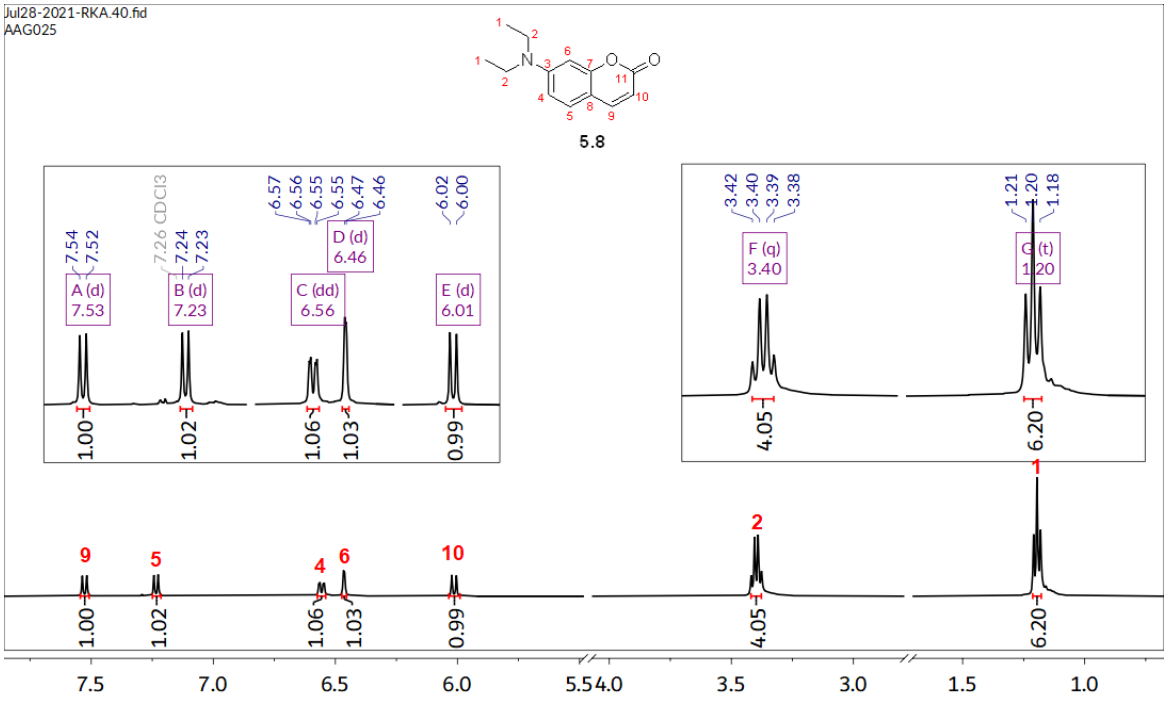

Figure 5.5. ^{1}H NMR spectrum (500 MHz, $CDCl_3$) of 7-(diethylamino)-2H-chromen-2-one **5.8**.

Subsequently, compound **5.8** was subjected to Vilsmeier–Haack formylation in the presence of 1,2-dichloroethane (DCE) to produce 7-(diethylamino)coumarin-3-carbaldehyde **5.9** in 79% [326]. A plausible mechanism for the formylation reaction has been depicted in **Scheme 5.3.** The first step involves the reaction of a substituted amide such as DMF with phosphorus oxychloride ($POCl_3$) which leads to the removal of the amide and substituting it with a chlorine molecule to produce a substituted chloroiminium ion **5.16** called the Vilsmeier reagent (named after Anton Vilsmeier and Albrecht Haack). After the formation of the Vilsmeier reagent, the electron-rich aromatic ring of 7-(diethylamino)-2*H*-chromen-2-one **5.9** then attacks the iminium ion **5.16** that was generated in the first step leading to a loss of aromaticity in **5.18**. A deprotonation step of **5.18** which uses another molecule of DMF restores aromaticity in **5.19**, which is followed by the release of a chloro ion to form another iminium intermediate **5.20**. Aqueous work-up then leads to the aryl aldehyde final product **5.25** [327-329].

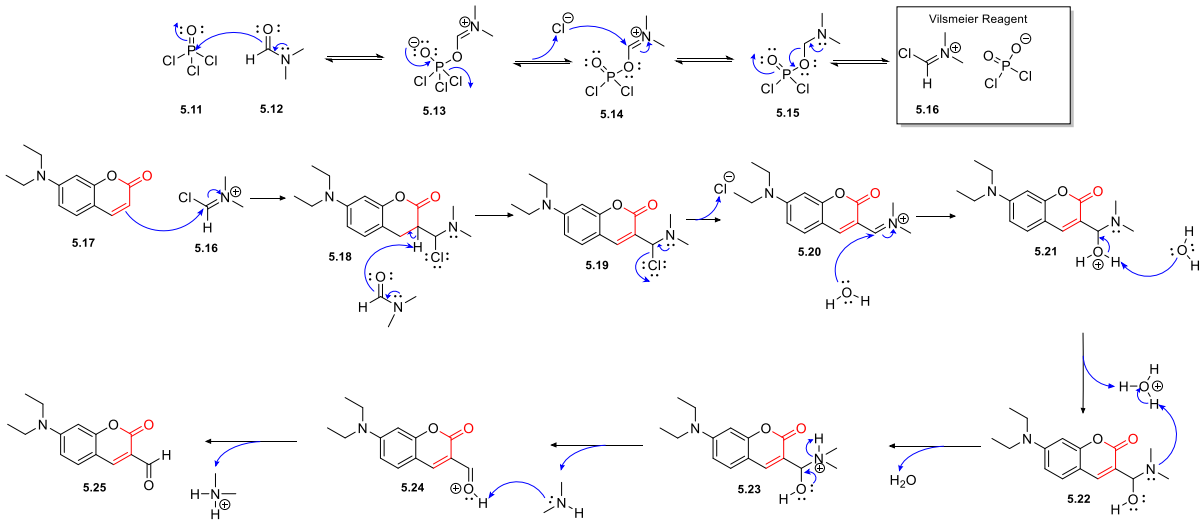

Scheme 5.3. Plausible Mechanism of Vilsmeier–Haack reaction.

The formylation was deemed successful by the confirmation of the distinctive and unmistakable singlet at δ_H = 10.10 ppm observed in the ^{1}H NMR spectrum which integrated for a single proton. This is characteristic of aldehydic protons [330] (**Figure 5.6b**).

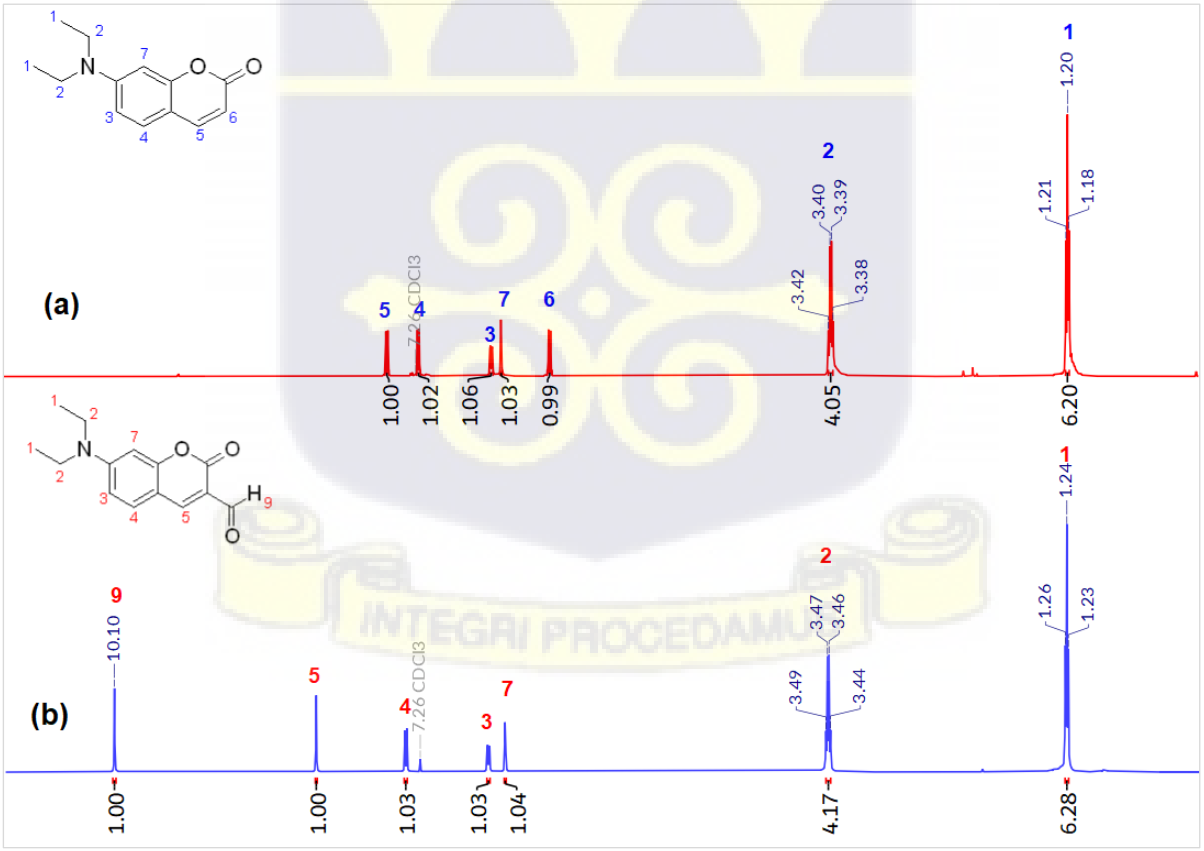

Figure 5.6. ^{1}H NMR spectra (500 MHz, $CDCl_3$) demonstrating the formation of aldehyde. (**a**) 7-(diethylamino)-2H-chromen-2-one **5.8**, (**b**) 7-(diethylamino)coumarin-3-carbaldehyde **5.9**. The singlet signal observed downfield at δ_H = 10.10 ppm indicates the presence of expected aldehyde formed by Vilsmeier–Haack formylation.

The ^{13}C NMR spectrum of **5.9** showed signals from 12 distinct carbons (**Figure 5.7**): the peaks at δ_C =12.6 and 45.4 ppm and were attributed to two methyl and two methylene groups carbons respectively, 4 distinct carbon peaks (δ_C = 162.0, 159.1, 153.6 and 114.5 ppm) were attributed to the four olefinic quaternary carbons, four signals were assigned to the 4 methine groups (δ_C = 145.5, 132.6, 108.4, and 97.3 ppm), and the remaining two signals were attributed carbonyl group carbons (δ_C =188.0 and 162.0 ppm). The observation of carbonyl carbon peak δ_C =188.0 ppm which was not present on the ^{13}C NMR of compound **5.8 (Appendix 1.14)** is assigned to the formaldehyde carbonyl peak which further corroborated the success of the formylation reaction. Moreover, there is also the presence of a carbonyl stretching band at 1709 cm^{-1} on FTIR spectrum (**Appendix 3.4**).

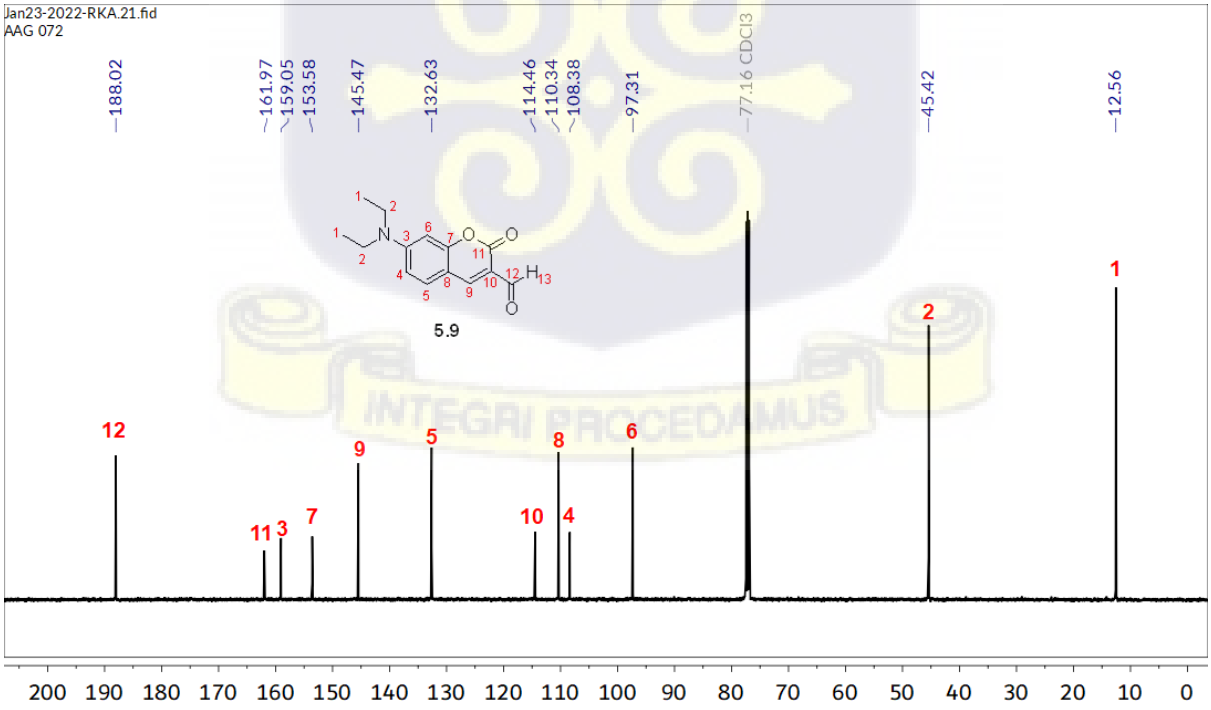

Figure 5.7. ^{13}C NMR spectrum (126 MHz, $CDCl_3$) of 7-(diethylamino)-2-oxo-2H-chromene-3-carbaldehyde **5.9**.

Next, a base-catalyzed Claisen–Schmidt condensation of 7-(diethylamino)coumarin-3-carbaldehyde **5.9** with 1-(4-(4,4,5,5-tetramethyl-1,3,2-dioxaborolan-2-yl)phenyl)ethan-1-one **5.5** building block using a catalytic amount of pyrrolidine in CH_2Cl_2/EtOH afforded the chalcone target molecule **5.10** (yield = 51%) with extended conjugations [331]. The ^1H NMR spectrum had the Bpin singlet peak integrating for 12 protons (4 × CH_3) at δ_H = 1.32 ppm. The triplet at δ_H = 1.15 ppm and the quartet at δ_H = 3.48 ppm with integral ratio of 3:2 represent the methyl and methylene groups respectively (**Figure 5.8)**.

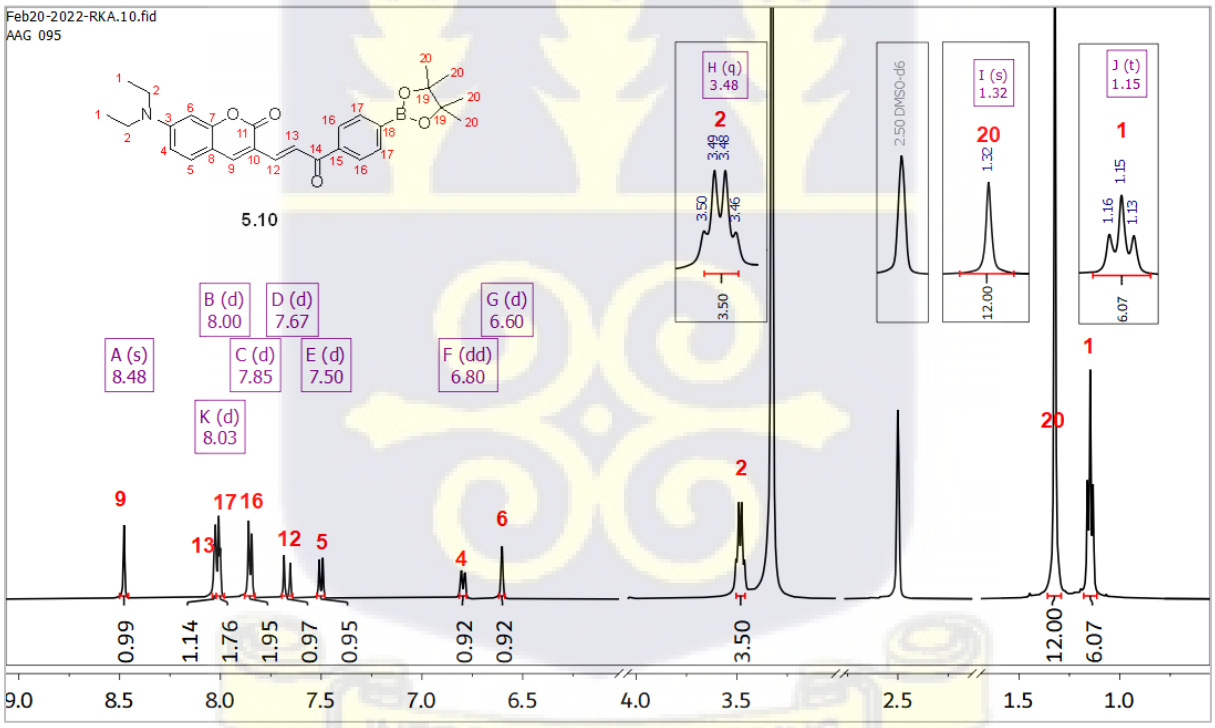

Figure 5.8. ^1H NMR spectrum (500 MHz, DMSO-d_6) of *(E)*-7-(diethylamino)-3-(3-oxo-3-(4-(4,4,5,5-tetramethyl-1,3,2-dioxaborolan-2-yl)phenyl)prop-1-en-1-yl)-*2H*-chromen-2-one **5.10**.

Afterwards, the chalcone **5.10** which had a protected boronate ester was subjected to deprotection protocols to yield the corresponding boronic acid **AAG113**. Two different synthetic approaches were attempted for the deprotection. Firstly, the deprotection was attempted using various concentrations of hydrochloric acid. No deprotection was observed when 5% HCl was used with a reaction time of 2 hours as confirmed by ^{1}H NMR (**Figure 5.9b**). However, when 20% HCl was used with a reaction time of 4 hours, it resulted in the formation of the desired boronic acid albeit in low yield (3%) (**Figure 5.9c**). ^{1}H NMR analysis of the product showed that the desired final compound was prepared following the disappearance of the Bpin peak at δ_H = 1.32 ppm (**Figure 5.9c**)**.** The second deprotection approach that led to the smooth formation of the corresponding boronic acid with an improved yield (up to 90%) involved oxidative hydrolysis of the pinacol-protecting group of the boronic ester **5.10** with aqueous sodium periodate ($NaIO_4$) [82, 332]. The mass of the desired compound was confirmed by electrospray ionization high-resolution mass spectrometry (ESI-HRMS). LC-MS analysis gave the molecular ion $[M+H]^+$ peak at *m/z* 392.1680.

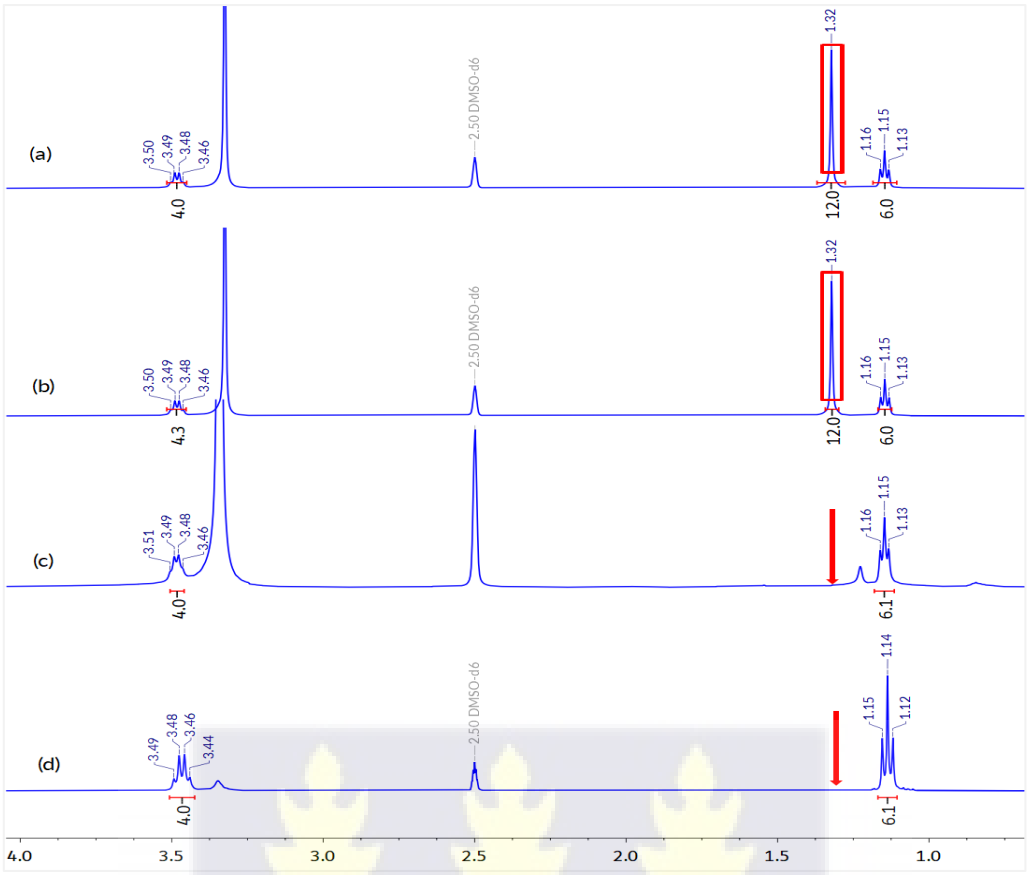

Figure 5.9. ^{1}H NMR spectra (500 MHz, DMSO-d_6) showing comparative deprotection of the Bpin group at different reaction conditions. (**a**) protected boronate (**b**) 5% HCl, 2 h (**c**) 20% HCl, 4 h (**d**) $NaIO_4$. The expected singlet Bpin peak at δ_H = 1.32 ppm in (**a**) and (**b**) disappears completely in (**c**) and (**d**), suggesting a successful deprotection reaction in both 20% HCl and $NaIO_4$ hydrolysis.

In addition, another coumarin fluorescent dye arylboronic acid was synthesised from 7-hydroxycoumarin (umbelliferone) **5.26**. Unbelliferone is a known fluorophore with a high quantum yield [333, 334]. The coumarin-tagged boronic acid derivative in **Scheme 5.4** was synthesised according to the procedure reported by Palanisamy *et al*. *via* a one-step alkylation reaction of 4-methylumbelliferone **5.26** with 4-bromomethylphenylboronic acid **5.27** in the presence of anhydrous potassium carbonate in dry DMF at 70 °C [335] to afford **AAG143** in 76% yield after purification. The product was fully characterised by NMR, LC-MS, and single-

crystal X-ray diffraction data (**Figures 5.10, 5.11** & **5.12)**. The ^{1}H NMR spectrum of AAG143 revealed one tertiary methyl group at δ_H = 2.38 ppm (d, *J* = 1.3 Hz, 3H). Also, the resonance of the aliphatic oxygen-linked methylene moiety was found at δ_H = 5.23 ppm (s, 2H) as a singlet. The two perfect doublets at δ_H = 7.81 and 7.42 ppm (*J* = 7.8 and 8.0 Hz) integrating for two protons each are attributed to the aromatic methine groups on the phenyl ring bearing the boronic acid unit. The peak at δ_H = 8.06 ppm integrating for two protons was assigned to the two OH groups on the boron atom. This was confirmed by the single broad resonance peak at δ_B = 28.9 ppm on the ^{11}B NMR spectrum which is characteristic of a trivalent boron compound (**Appendix 1.27**). The molecular weight of **AAG143** was also confirmed by ESI-QTOF HRMS. The ESI-MS exhibited a strong peak at *m/z* = 311.1096 at a retention time of 7.5 min which was assigned to the $[M+H]^+$ (exact mass *calcd.* for $[C_{17}H_{16}BO_5]^+$: 311.1091) (**Figure 5.12**) Finally, single-crystal X-ray diffraction analysis was performed to confirm the structure of **AAG143**.

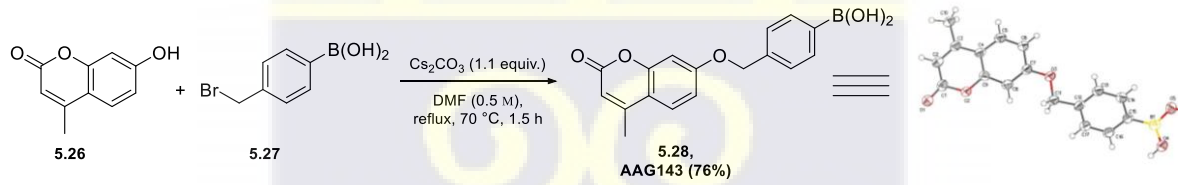

Scheme 5.4. Synthetic route to arylboronic acid dye.

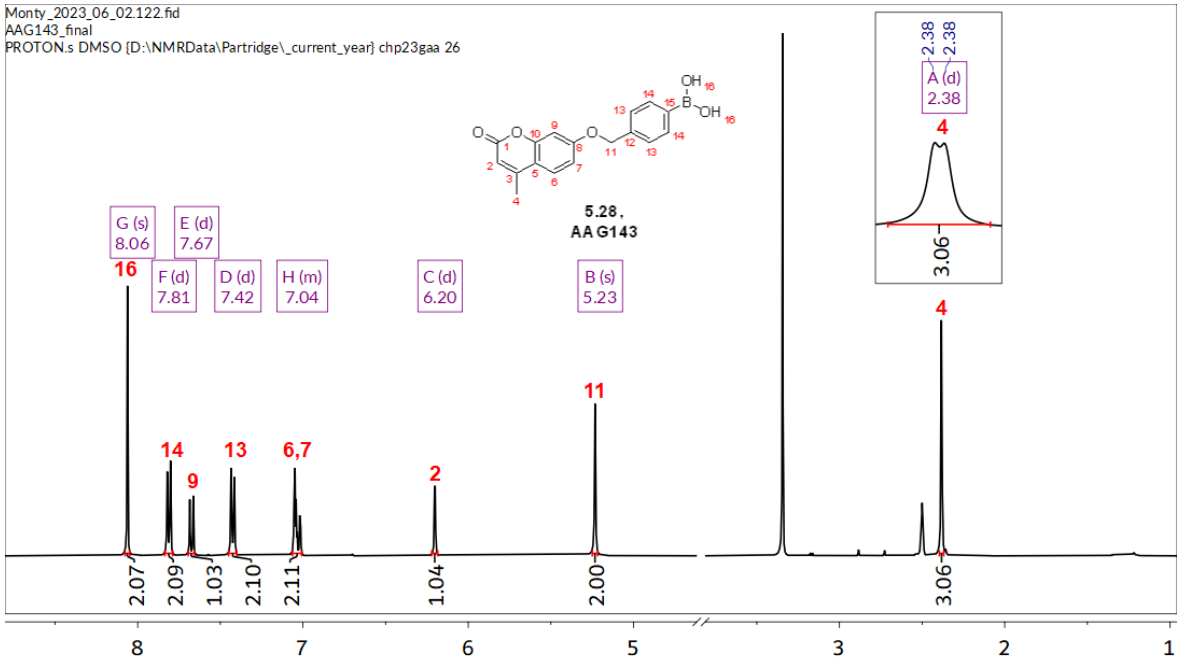

Figure 5.10. ^{1}H NMR spectrum (400 MHz, DMSO-d_6) of (4-(((4-methyl-2-oxo-2H-chromen-7-yl)oxy)methyl)phenyl)boronic acid **AAG143**.

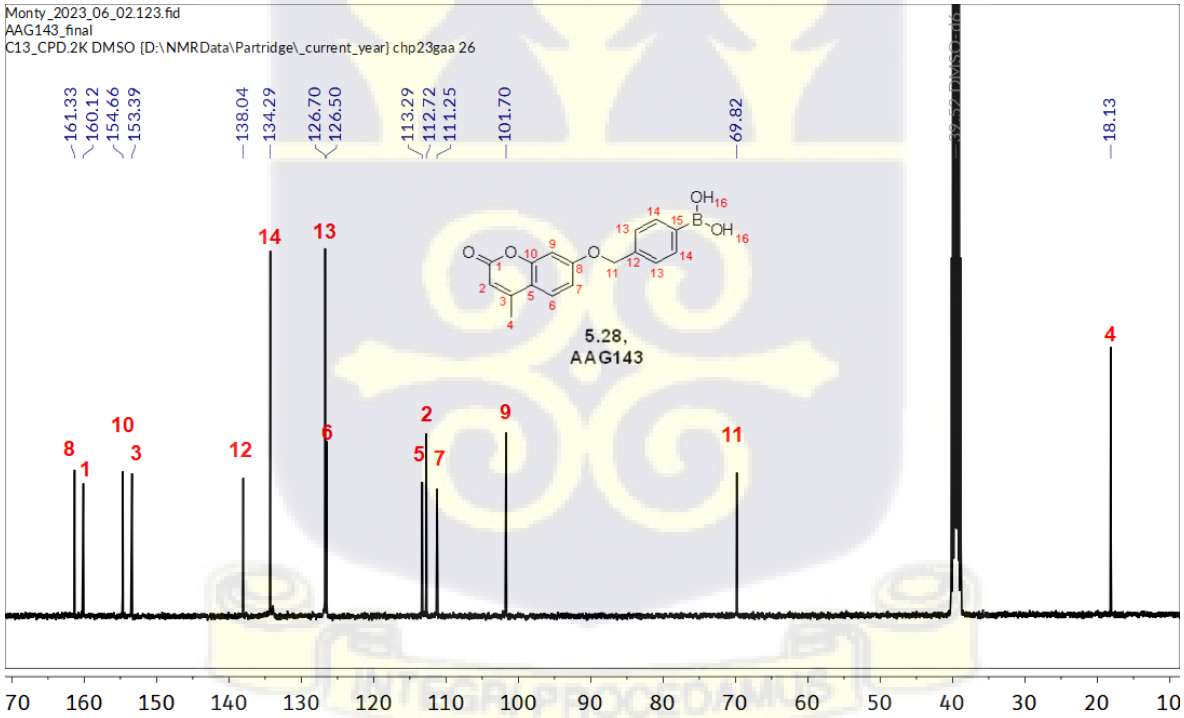

Figure 5.11. ^{13}C NMR spectrum (101 MHz, DMSO-d_6) of (4-(((4-methyl-2-oxo-2H-chromen-7-yl)oxy)methyl)phenyl)boronic acid **AAG143.**

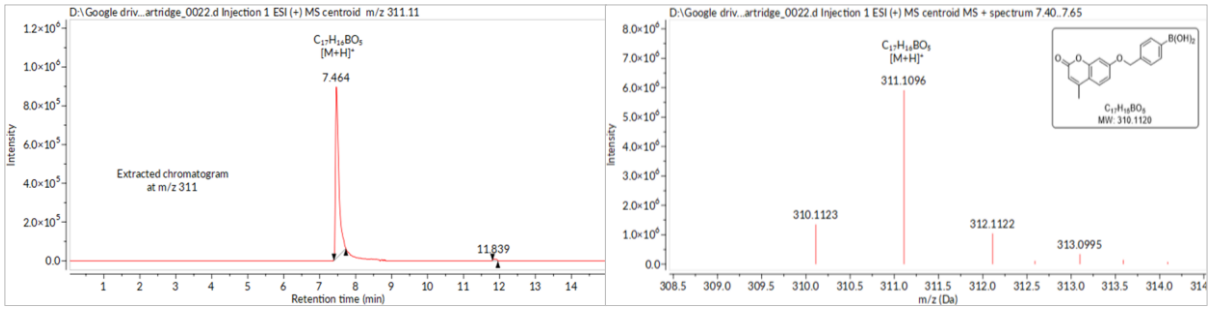

Figure 5.12. ESI-QTOF HRMS spectrum of (4-(((4-methyl-2-oxo-2H-chromen-7-yl)oxy)methyl)phenyl)boronic acid **AAG143.**

5.3.1.3 9-Aminoacridine-tagged boronic acid dyes

In another development, 9-aminoacridine-tagged boronic acid dyes were prepared. 9-aminoacridine is a quinoline derivative that contains a tacrine-like moiety (**Figure 5.13**). Acridine and its derivatives are important quinoline structural derivatives that are generally planar tricyclic aromatic molecules which fluoresce at shorter wavelength regions [336, 337]. Acridine-based fluorescence chemosensors have recently been synthesized and employed by Wang *et al*. for the selective detection of Fe^{3+} and Ni^{2+} ions [338].

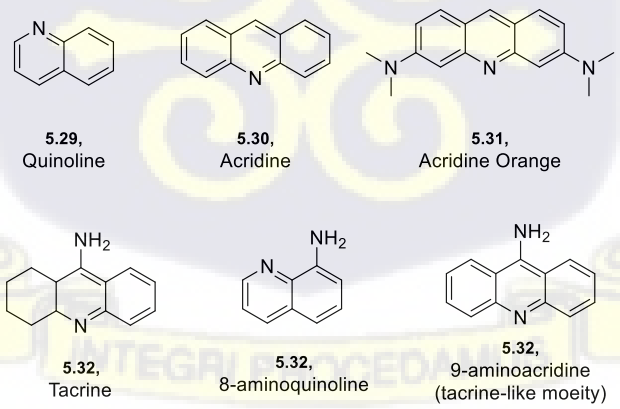

Figure 5.13. Structures of quinoline and quinoline derivatives.

Harnessing the advantages of the acridine moiety, a new arylboronic acid fluorescent chemosensor was prepared by coupling an aminoacridine fluorophore to a (4-(aminomethyl)phenyl)boronic acid *via* a chloroacetyl chloride linker in three steps (**Scheme 5.5).**

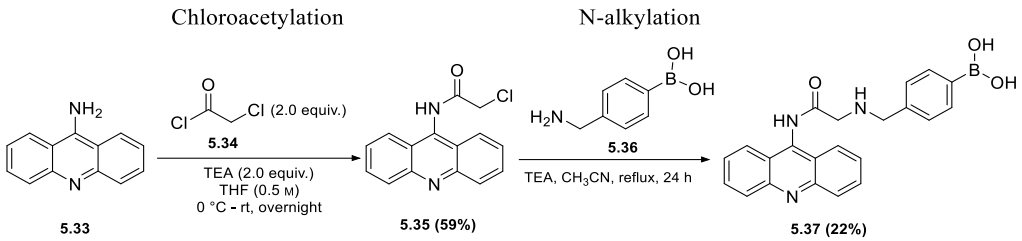

Scheme 5.5. Synthetic route to (4-(((2-(acridin-9-ylamino)-2-oxoethyl)amino)methyl)phenyl)boronic acid **5.37**.

N-(acridin-9-yl)-2-chloroacetamide **5.35** was prepared by reacting a commercially available 9-aminoacridine **5.33** with chloroacetyl chloride **5.34** according to chloroacetylation reaction procedures as described in the literature [339-341]. This step was carried out in the presence of a catalytic amount of triethylamine (TEA). Chloroacetyl chloride plays a key role in synthetic and biological chemistry as a bifunctional linker for alcohols and amines [342] and thus was employed to prepare the *N*-(acridin-9-yl)-2-chloroacetamide **5.35** as a suitable building block for the next steps. The reaction was run overnight under room temperature, and the isolated yield was 59%. The (4-(aminomethyl)phenyl)boronic acid was alkylated with the *N*-(9-acridinyl)-2-chloroacetamide using triethylamine (TEA) as a catalyst under reflux in acetonitrile (CH_3CN) for 24 h to provide the target compound (4-(((2-(acridin-9-ylamino)-2-oxoethyl)amino)methyl)phenyl)boronic acid **5.37 (AAG103)** in 22% yield. The intermediate and target compound were fully characterized by ^{1}H NMR, ^{13}C NMR, high-resolution mass spectrometry (HRMS), and infrared (IR) spectroscopic methods. The spectroscopic

information obtained strongly correlated with their structures. ^{1}H NMR spectrum of **5.37** showed two active hydrogens in the low field (δ_H = 9.56 and 9.24 ppm) which are assigned to the NH group. All the aromatic methine protons occurring between 6.90 and 7.58 ppm integrated for a total of twelve (12) protons while the two aliphatic methylene groups occurred as singlets at δ_H = 3.23 and 2.95 ppm respectively (**Figure 5.14**).

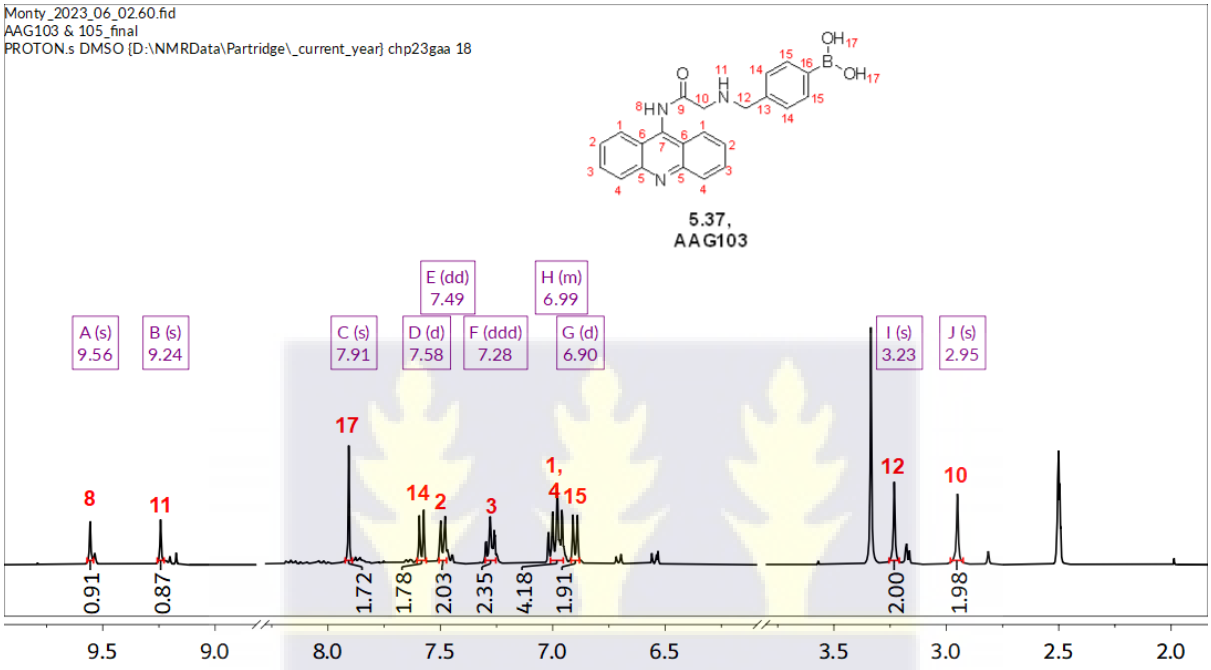

Figure 5.14. ^{1}H NMR spectrum (400 MHz, DMSO-*d*$_6$) of (4-(((2-(acridin-9-ylamino)-2-oxoethyl)amino)methyl)phenyl)boronic acid **5.37** (**AAG103**).

5.3.1.4 8-aminoquinoline-tagged boronic acid dyes

8-aminoquinoline contains a quinoline moiety which is a well-known fluorophore unit. Quinoline is particularly desirable because of their good coordination properties and their ability to form hydrogen bonds as a result of the presence of nitrogen in the ring as well as its small molecular size [343, 344]. Furthermore, quinolines are well known for their good metal affinity hence are becoming a leading candidate in the design of fluorescent probes for metals such as zinc and their applications in more complex biological research [344]. More

importantly, the chemistry of quinoline is also well established and a plethora of synthetic methods are available to functionalize the core moiety [344]. With the advantages that the quinoline moiety offers particularly in the design of fluorescent chemosensors, attempts were made to synthesize an aminoquinoline-tagged boronic acid following the procedure previously employed in **Scheme 5.5** to synthesize aminoacridine boronic acid derivative **5.37** (**Scheme 5.6**). The chloroacetylation of 8-aminoquinoline afforded the 2-chloro-*N*-(quinolin-8-yl)acetamide in 61% yield. However, except for dimethylamine **5.40**, all the reaction with other amines such as **5.3** and **5.41** used failed.

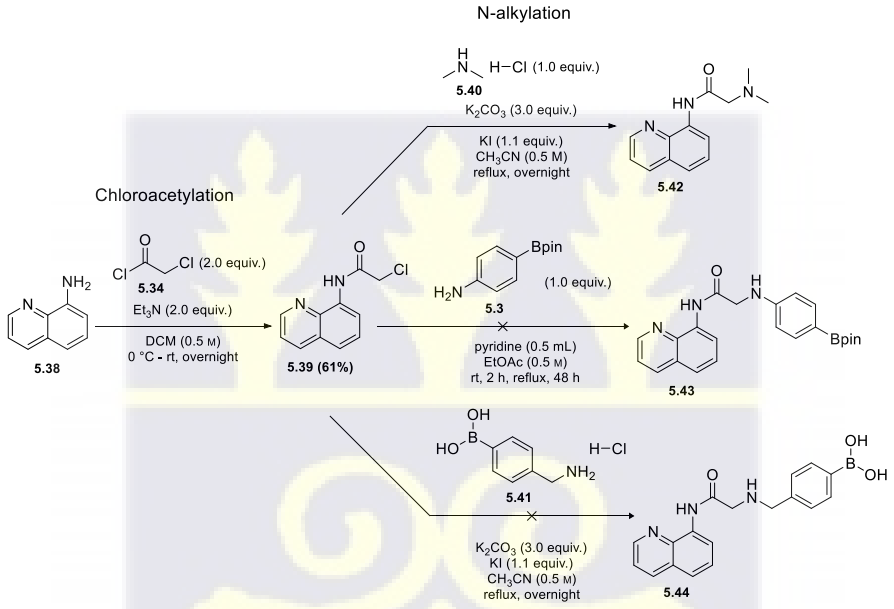

Scheme 5.6. Unsuccessful *N*-alkylation of 4-(3,3,4,4-tetramethylborolan-1-yl)aniline and (4-(aminomethyl)phenyl)boronic acid

Thus, an alternative route to synthesize the aminoquinoline-tagged boronic acid target compound **5.44** (**AAG126**) was employed. The synthesis was achieved in five steps as depicted in **Scheme 5.7**.

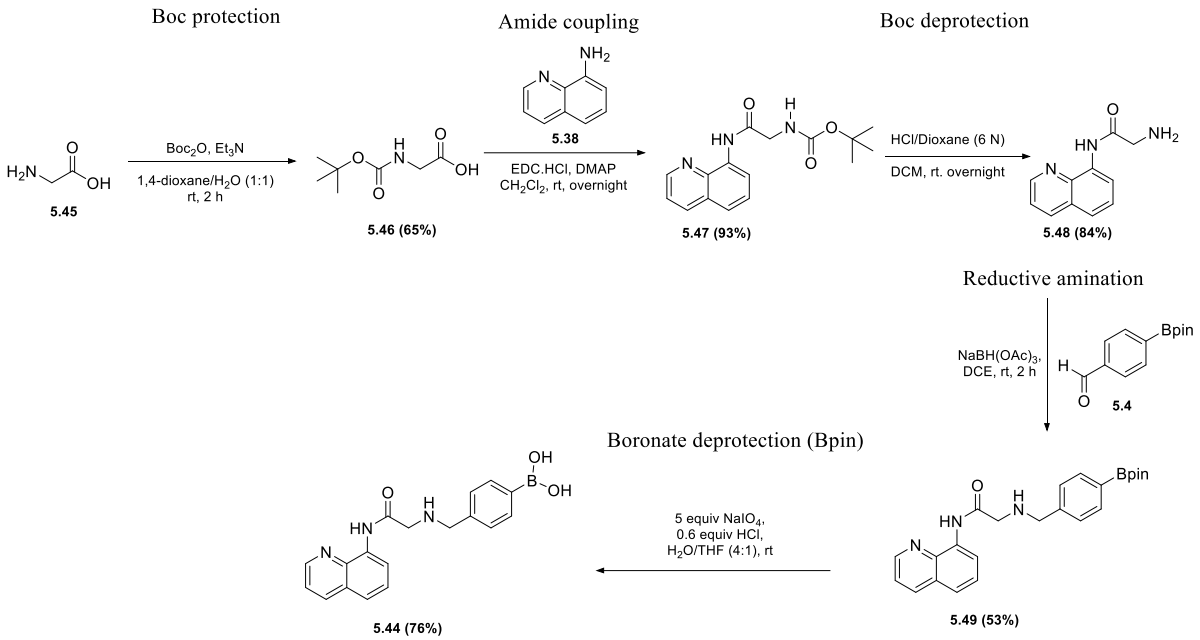

Scheme 5.7. Synthetic route to (4-(((2-oxo-2-(quinolin-8-ylamino)ethyl) amino)methyl)phenyl)boronic acid **5.44 (AAG126).**

This route involves *Boc*-protection of the amino group (glycine) by reacting with *di-tert*-butyl dicarbonate (*Boc*$_2$O) under basic conditions in a 1,4-dioxane/H_2O mixture to afford *Boc*-Gly-OH in excellent yield under 2 hours followed by amide coupling between the carboxylic acid functionality of the *N-Boc* protected glycine **5.46** and 8-aminoquinoline **5.38** in CH_2Cl_2 in the presence of EDC.HCl/DMAP as the activation/amide coupling agent. The plausible mechanism of the EDC coupling of the amine to the carboxylic acid is provided in **Scheme 5.8**. Reaction of the carboxylic acid group of the *N-boc*-protected glycine **5.46** with 1-(3-Dimethylaminopropyl)-3-ethylcarbodiimide (EDC) in the presence of hydroxybenzotriazole (HOBt) results in the formation of reactive HOBt ester **5.50**. The role of 4-dimethylaminopyridine (DMAP) is important in this coupling reaction, as it functions as an acyl transfer agent forming the highly reactive acyliminium ion intermediate **5.52** as proposed by Steglich in the esterification reaction [345, 346]. The reaction of HOBt ester with electron-

deficient amines is expected to be slow, however, the reaction of the amines with acyl iminium ion **5.52** should be relatively faster providing the coupling product **5.47** with the regeneration of DMAP [347]. In principle, only a catalytic amount of DMAP is needed, therefore, in this reaction, I used 5 mol% equivalence of DMAP and the resultant yield was excellent (93%).

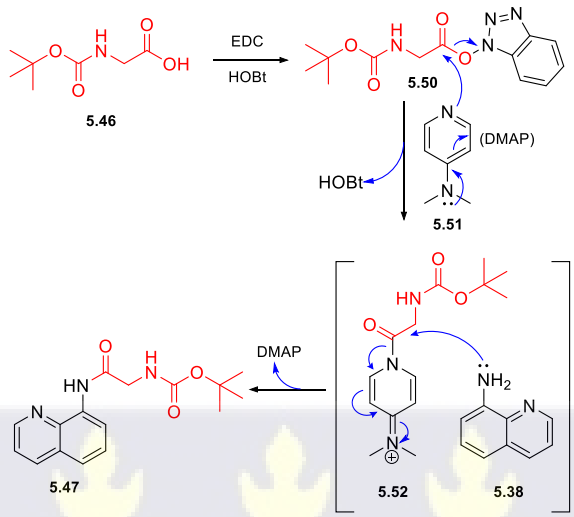

Scheme 5.8. Proposed mechanism of EDC amide coupling of 8-aminoquinoline and *Boc*-Gly-OH.

The next step was to obtain the free amine through deprotection of the *N-Boc* group by using the traditional approach based on TFA-induced cleavage as reported peviously [348] or with HCl (6 M) in dioxane at room temperature [349, 350]. Both methods gave the desired products in excellent yield. The proposed mechanism is shown in **Scheme 5.9**. First, the *tert*-butylcarbamate becomes protonated by hydrogen chloride (HCl) which triggers the production of a *t-butyl* cation **5.54** and carbamic acid **5.55**, which was subsequently decarboxylated to yield the free amine **5.48**. Since *N-Boc* deprotection reactions generate carbon dioxide (CO_2) gas as a by-product, these reactions must not be run in closed systems to allow for the escape of the excess build-up of CO_2 gas.

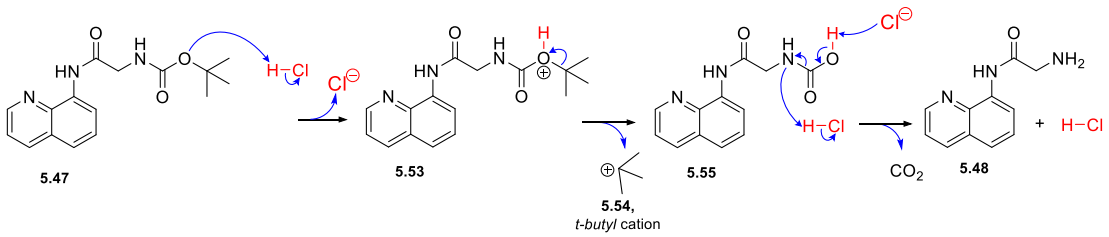

Scheme 5.9. Proposed mechanism of HCl/dioxane (6 N) deprotection of *N-Boc* group.

The resultant free base was characterised by NMR (**Figure 5.15**) and used in the next step without further purification.

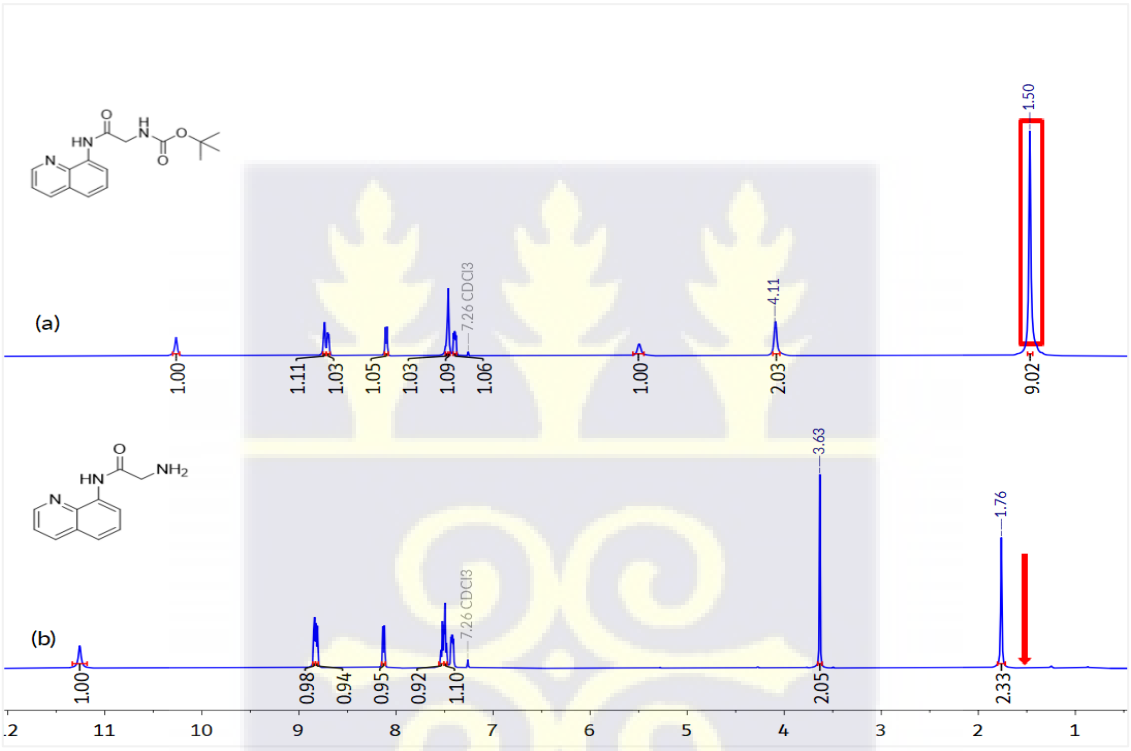

Figure 5.15. ^{1}H NMR spectra (500 MHz, DMSO-d_6) showing deprotection of *N-Boc* group. (**a**) *N-Boc* protected amine with a signal at δ_H = 1.50 ppm, (**b**) Deprotected amine in which the *N-Boc* peak at δ_H = 1.50 ppm disappears completely.

After the successful deprotection of the *N-Boc* group to obtain the free amine **5.48**, it was then coupled to the aldehyde functionality of the pinacol-protected 4-formylphenylboronic acid **5.4**

building block that was previously synthesized as shown in **Scheme 5.7** under reductive amination conditions to give the aminomethyl derivative **5.49.** Sodium triacetoxyborohydride ($NaBH(OAc)_3$) was chosen as the reducing agent over others such as sodium cyanoborohydride ($NaBH_3CN$) and the less bulky hydride reagents, $NaBH_4$ because of its high efficiency in reductive amination reactions with unreactive amines leading to faster, better yields, and with fewer side products. Secondly, $NaBH(OAc)_3$ has been reported to be more selective for direct reductive aminations of ketones and aldehydes relative to the sodium cyanoborohydride alternative [351]. The other advantage of acetoxyborohydride is the avoidance of the production of toxic by-products such as NaCN and HCN that are usually associated with the use of $NaBH_3CN$ [257]. My preferred reaction solvent was 1,2-dichloroethane (DCE) even though other similar amination reactions have been carried out in other solvents such as tetrahydrofuran (THF) and acetonitrile (CH_3CN). The final step in the synthesis of (4-(((2-oxo-2-(quinolin-8-ylamino)ethyl)amino)methyl)phenyl)boronic acid **5.44** (**AAG126**) was the deprotection of the boronate ester using the optimized procedure of $NaIO_4$.

5.3.1.5 Fluorescein-tagged boronic acid dyes

The synthesis of fluorescein-tagged boronic acid **5.60** was performed following the procedure in **Scheme 5.10**. First, esterification of cyclic fluorescein **5.56** was carried out in the presence of a catalytic amount of concentrated sulfuric acid in methanol to afford fluorescein methyl ester **5.57** in an excellent yield (93%). The fluorescein methyl ester intermediate **5.57** was first characterized by X-ray crystallography. Then the ester was refluxed with an excess amount of hydrazine hydrate in methanol *via* hydrazinolysis to produce the desired fluorescein hydrazide **5.58** with a yield of 96% yield [352].

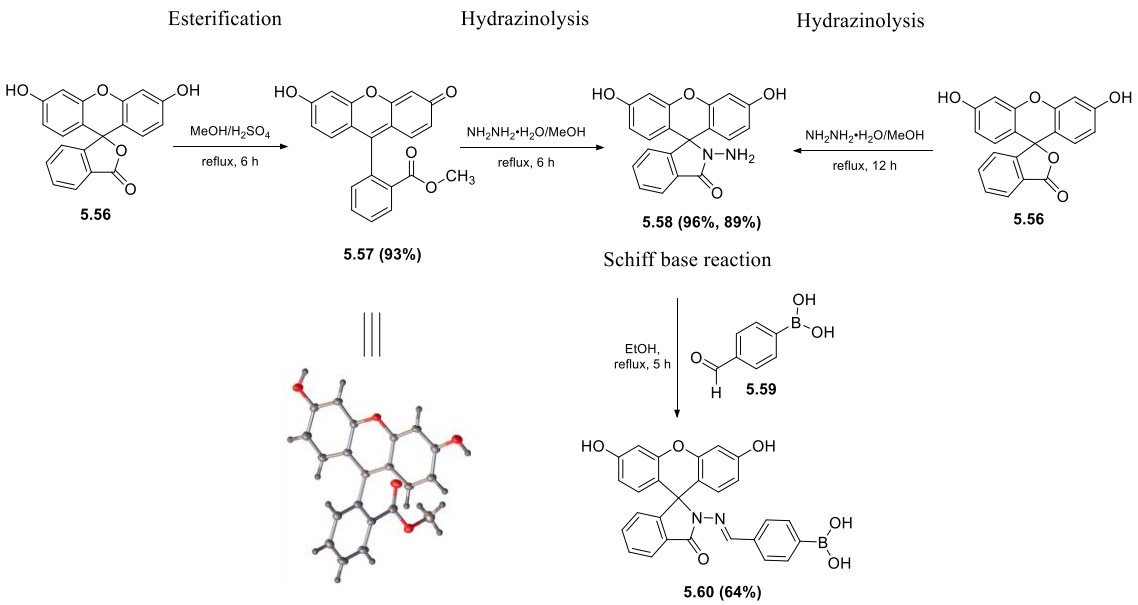

Scheme 5.10. Synthetic route to *(E)*-(4-(((3',6'-dihydroxy-3-oxospiro[isoindoline-1,9'-xanthen]-2-yl)imino)methyl)phenyl)boronic acid.

The plausible mechanism for the hydrazinolysis step is shown in **Scheme 5.11**. It involves the nucleophilic attack by the lone pair of electrons from hydrazine hydrate followed by proton transfer from an amine group onto the oxygen bound to the ring carbon. This was followed by intramolecular nucleophilic attack by -NH at the carbon bearing the carbonyl (C=O) leading to the cyclization of the resulting fluorescein hydrazide **5.58**.

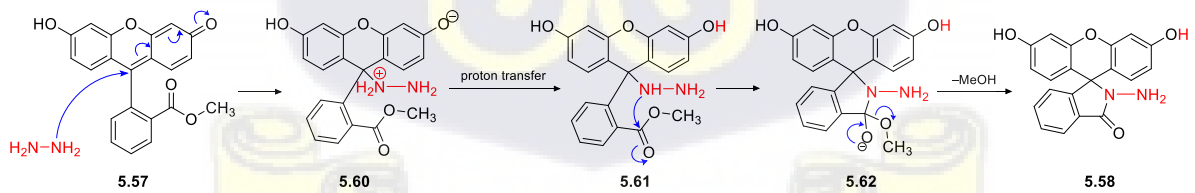

Scheme 5.11. The plausible mechanism for the hydrazinolysis step.

An alternative method for the preparation of fluorescein hydrazide **5.58** (in 89% yield) involved the direct hydrazinolysis of the cyclic fluorescein **5.56** using excess hydrazine hydrate under

reflux in methanol for 12 h. Finally, through Schiff base reaction, the fluorescein hydrazide **5.56** was coupled to 4-formylphenylboronic acid **5.59** to form the fluorescein-tagged arylboronic acid chemosensor **5.60 (AAG138)** in 64% yield. After purification, the structure of the target compound **5.60** was confirmed by ^{1}H NMR, ^{13}C NMR and HR-MS (**Figure 5.16, Appendix 1**).

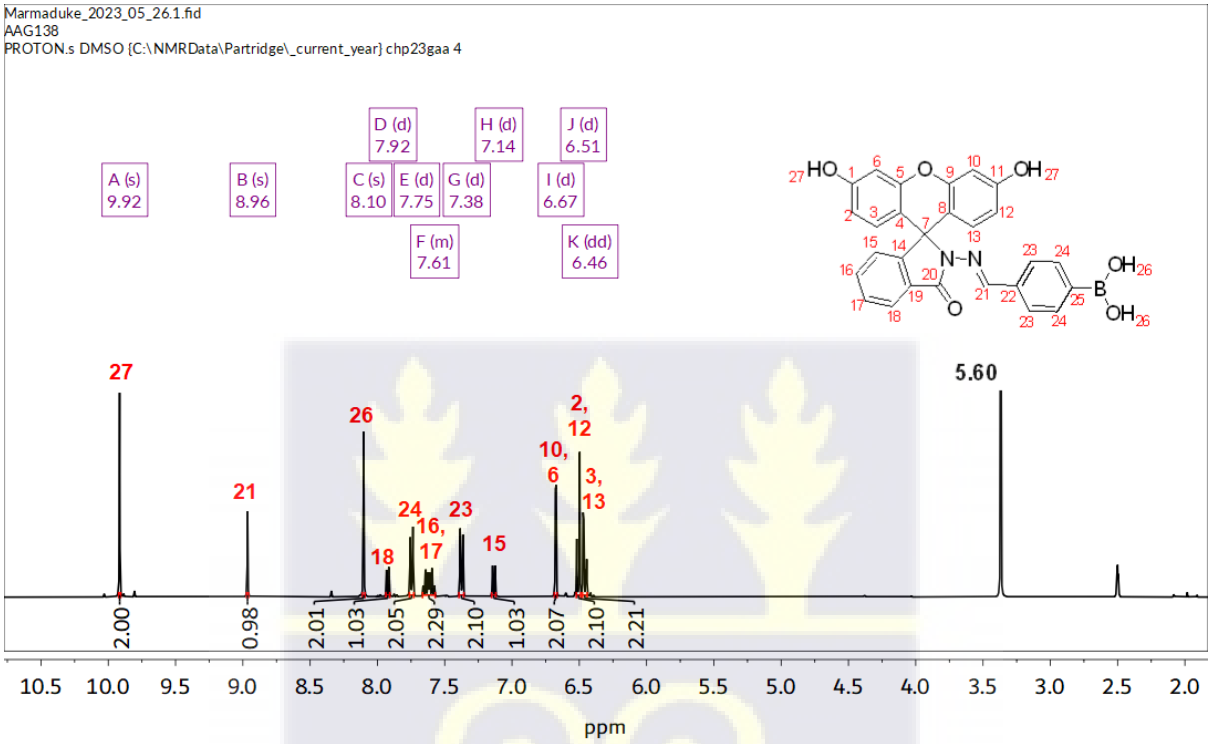

Figure 5.16. ^{1}H NMR spectrum (400 MHz, DMSO-d_6) of fluorescein-tagged arylboronic acid chemosensor **5.60 (AAG138).**

A second fluorescein boronic acid was synthesized *via* a one-step reaction of fluorescein isothiocyanate isomer I and 3-aminobenzeneboronic acid (**Scheme 5.12**). The fluorescein isothiocyanate contains a an electrophilic carbon atom that readily reacted with nucleophile (amine) using dimethylformamide (DMF) as the solvent to form thiourea compound **5.65 (AAG023)** in 68% yield [353, 354].

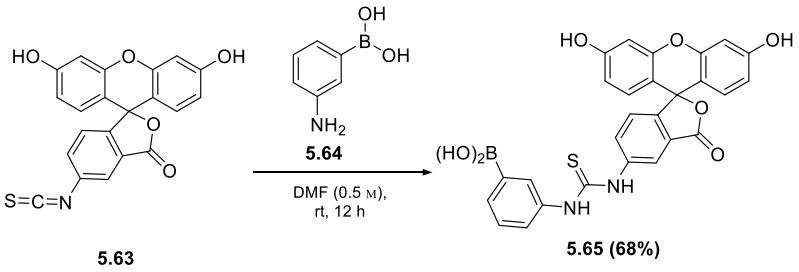

Scheme 5.12. Synthesis of (3-(3-(3',6'-dihydroxy-3-oxo-3H-spiro[isobenzofuran-1,9'-xanthen]-5-yl)thioureido)phenyl)boronic acid.

5.3.1.6 Rhodamine-tagged boronic acid dye

Rhodamine dye fluorophores are part of the family of xanthenes along with fluorescein and eosin dyes [355]. The structures of xanthene chromophore and rhodamine dyes are shown in **Figure 5.17**. The carboxylic acid group of rhodamine dyes undergo intramolecular cyclization and the open form **5.68** is highly fluorescent, whereas the spirocyclic form **5.67** is essentially nonfluorescent [355-357].

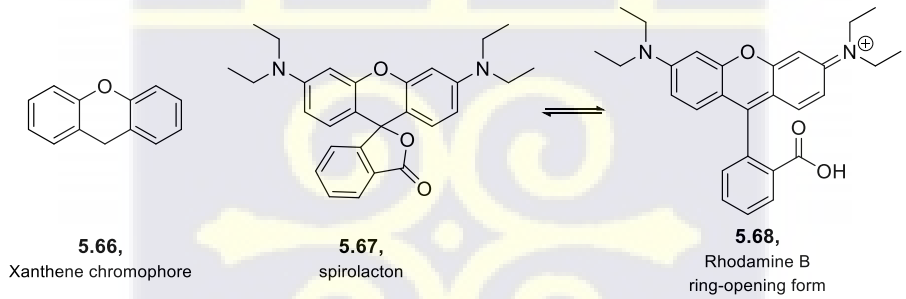

Figure 5.17. Molecular structure of Xanthene and Rhodamine B dye.

Rhodamine dyes and their derivatives have also been used extensively, in particular, as chemosensors either *in vitro* or *in vivo* in the detection of metals including Hg(II) [358-360], peroxynitrite [315], Cu(II) [361], Fe(III) [362], Cr(III) [362], and many more other analytes. Rhodamine derivatives are also employed as molecular switches [363]. Rhodamine B was chosen as the fluorescent dye for use in this study due to the high fluorescence quantum

efficiency, high molar extinction coefficients, and low cost. A rhodamine-tagged boronic acid **5.70** was readily synthesized from rhodamine B by a two-step reaction where rhodamine B was treated with excess hydrazine in methanol to give rhodamine B hydrazide **5.69** in 68% yield (**Scheme 5.13**). The hydrazide was further converted into the designed product **5.70** through a Schiff base reaction with the introduction of 4-formylphenylboronic acid **5.59** (73%). The structures were confirmed by ^{1}H NMR, ^{13}C NMR, and mass spectroscopic and spectrometric analysis (**Appendices 1, 2 & 3**).

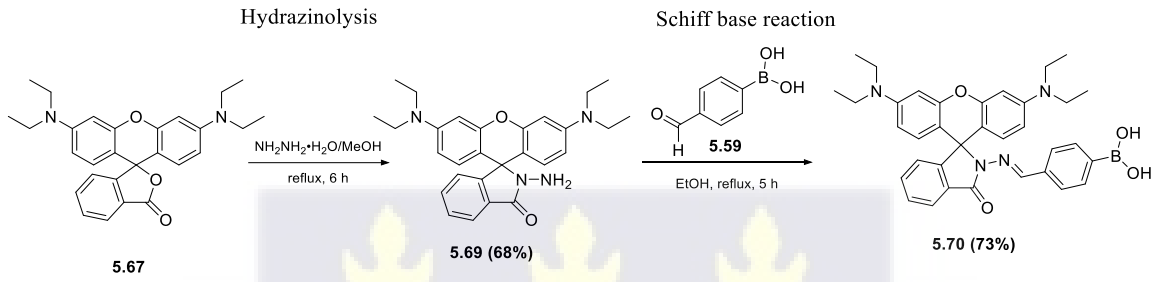

Scheme 5.13. Synthesis of (E)-(4-(((3',6'-bis(diethylamino)-3-oxospiro[isoindoline-1,9'-xanthen]-2-yl)imino)methyl)phenyl)boronic acid.

The proposed mechanism for the preparation of the rhodamine hydrazide route is represented in **Scheme 5.14**.

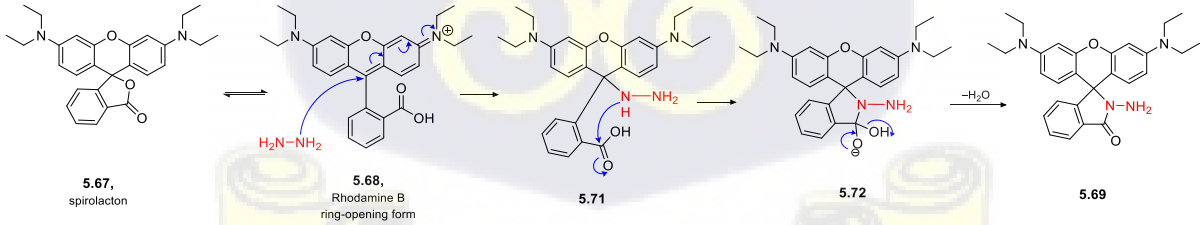

Scheme 5.14. Proposed mechanism for the reaction of hydrazine with rhodamine B (hydrazinolysis).

5.3.1.7 BODIPY-tagged boronic acid dyes

4,4-difluoro-4-bora-3a-4a-diaza-s-indacene (simply known as BODIPY, difluoroboron dipyrromethene) and its derivatives are fluorescent organic dye molecules that were first discovered by Treibs and Kreuzer in 1968 [364] **(Figure 5.18)**. Since then, several BODIPY and their derivatives have become the most popular dye molecules among the multitude of fluorescent dyes available with widespread applications in various areas including tunable laser dyes, biological labelling [365-367], as fluorescent switches, and fluorophores in sensors and labels, and light-harvesting systems in electroluminescent devices [368-370]. The interest in BODIPY chromophores can be attributed to their favourable physicochemical characteristics and desirable photophysical properties [371, 372], such as high fluorescence quantum yields, relatively large molar absorption coefficient, narrow emission bandwidths, and tunable fluorescent properties as well as relatively high thermal and photochemical stabilities [373-376]. These molecules generally have excitation/emission wavelength in visible region with stable excited states. Other advantages include ease of modification of BODIPY chemically for the synthetic accessibility of various derivatives, and good solubility in common solvents [377]. As a result, a significant number of BODIPY derivatives have since been synthesized and characterized [373, 374]. Also, there is an abundance of literature that supports the synthetic versatility of the BODIPY chromophore which allows for far-reaching structural modifications resulting in the alteration of the electronic, optical and chemical properties of the dye [378].

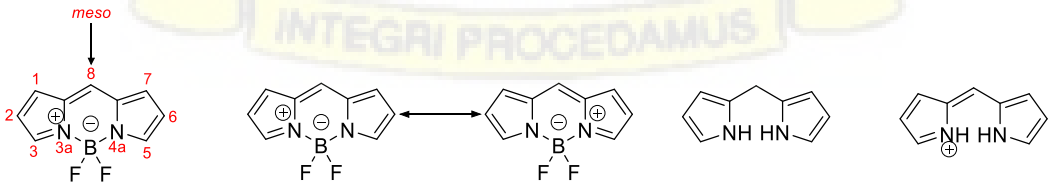

5.73, IUPAC numbering system of BODIPY core

5.74 **5.75** BODIPY core delocalized structures with for charges indicated

5.76, Dipyrromethane core

5.77, Dipyrromethene

Figure 5.18. Representation of the BODIPY framework showing the IUPAC numbering system, delocalized structures, dipyrromethene and dipyrromethene cores.

Thus, a procedure for the introduction of an arylboronic acid unit onto a BODIPY core was developed to take advantage of the desirable photophysical properties outlined above. Two approaches were employed to synthesise the boron dipyrromethene (BODIPY)-tagged boronic acid dye **5.83 (AAG156)** (**Scheme 5.15)**. The first route involved the use of the pinacol-protected 4-formylphenylboronic acid **5.4** building block which had already been prepared whereas in the second route, 4-formylphenylboronic acid **5.59** was attempted directly without protecting it to reduce the number of steps especially in instances where purification and hydrolysis of the boronate proved challenging.

The synthesis began with an acid-catalyzed condensation between two equivalents of 2,4-dimethylpyrrole **5.78** and a suitable electrophile such as pinacol-protected 4-formylphenylboronic acid **5.4** to form a dipyrromethane intermediate **5.79** followed by the addition of a few drops of trifluoroacetic acid (TFA). The complete consumption of the aldehyde was monitored by TLC. The dipyrromethane intermediate **5.79** was unstable and was therefore not isolated but converted directly to a dipyrromethene **5.80** in an oxidation step carried out using either 2,3-dichloro-5,6-dicyano-p-benzoquinone (DDQ) or 2,3,5,6-tetrachloro-p-benzoquinone (*p*-chloranil) as oxidants [379]. The dipyrromethene **5.80** was subsequently subjected to a boron trifluoride etherate ($BF_3 \cdot Et_2O$) complexation reaction catalyzed by triethylamine (Et_3N) to afford the borondifluoride complex **5.81** in 47% yield [380, 381]. The last step involved the deprotection of the boronate ester **5.81,** in the case where the protected boronate aldehyde was used, to obtain the BODIPY dye **5.83 (AAG156)** as a red crystalline solid (89% yield).

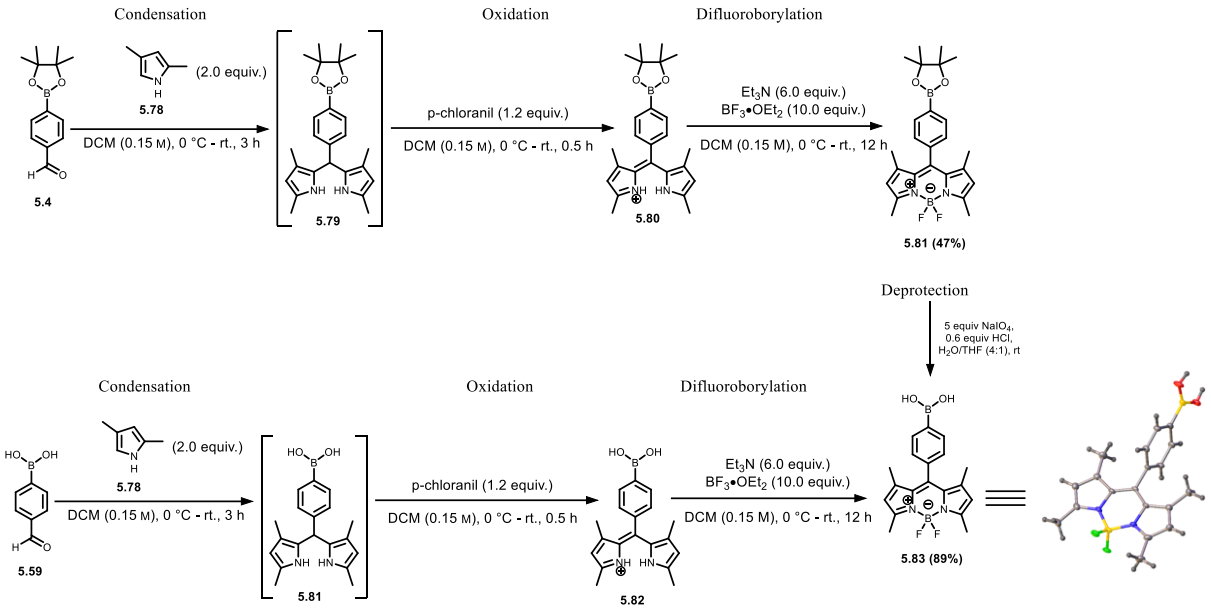

Scheme 5.15. Synthesis of BODIPY-tagged boronic acid **5.83** via two routes.

The structures were all confirmed by ^{1}H NMR, ^{13}C NMR, and X-ray crystallography (**Appendix 4**). The ^{1}H NMR of the final product is represented in **Figure 5.19**. The spectrum has 4 singlets with chemical shifts at δ_H = 1.32, 2.44, 6.17, and 8.25 ppm with integral ratios of 3:3:1:1. The four protons on the phenyl ring integrate for two perfect doublets at δ_H = 7.33 and 7.96 ppm with same coupling constants, J = 7.9 Hz. Next, LC-MS analysis was performed which gave the $[M+H]^+$ $[C_{19}H_{21}B_2F_2N_2O_2]^+$ peak at *m/z* found: 369.1763 compared to the exact *calcd.* mass of *m/z* = 369.1757.

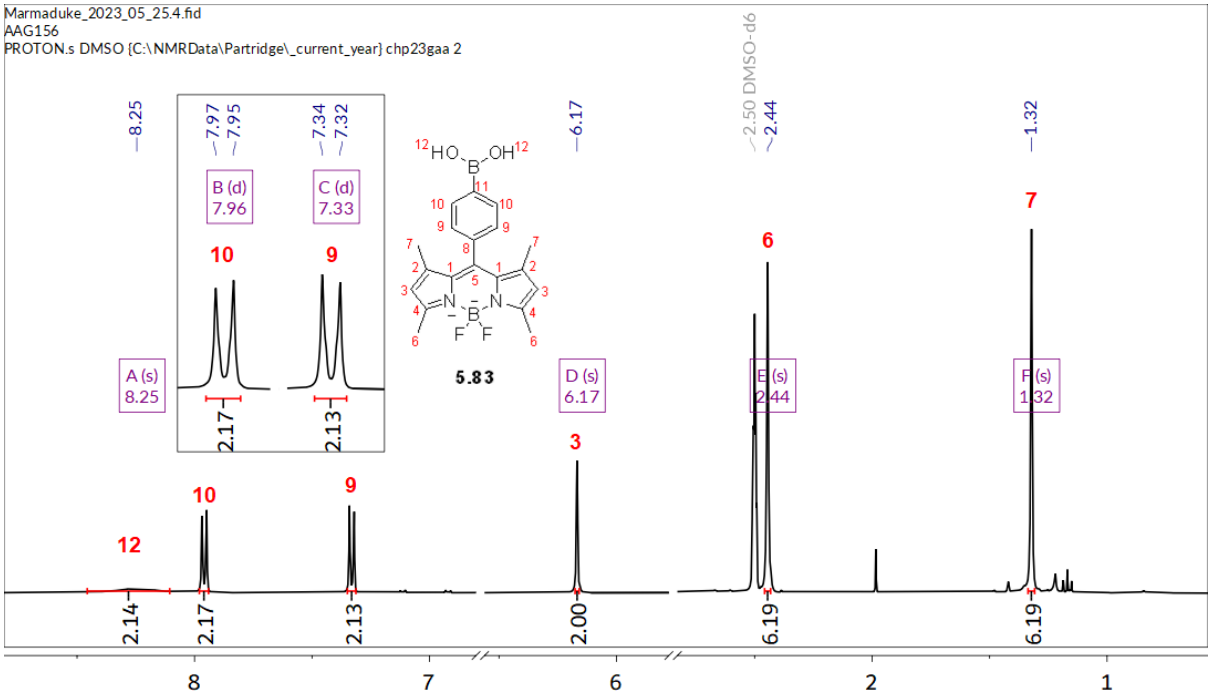

Figure 5.19. ^{1}H NMR spectrum (400 MHz, DMSO-d_6) of BODIPY dye **5.83.**

In a related experiment, a single-crystal diffraction analysis was measured for **AAG156,** and the crystal structure was obtained (**Figure 5.20**). The X-ray crystal structure of BODIPY **5.83** reveals that the molecule is virtually planar. This is corroborated by the following structure refinement data. The boron atom has a slightly distorted tetrahedral coordination with the two fluorine atoms being perpendicularly oriented with respect to the dipyrrin plane. The B1–N1 and B1–N2 bond lengths are 1.536(2) Å and 1.534(2) Å respectively. Likewise, the B1–F1 and B1–F2 bond lengths are 1.412(2) Å and 1.407(2) Å respectively. The bond distances of the two B–N and two B–F are virtually identical which is an indication that **AAG156** possess single B–N and B–F bonds. Also, the average N1–B1–N2 and F1–B1–F2 angles are 107.75(12) ° and 106.82(12)°, respectively. This also presupposes that there is an expected delocalisation of the positive charge. Lastly, the summarised crystal data for **5.83** are as follows; $C_{19}H_{20}B_2F_2N_2O_2$ (M =367.99 g/mol): triclinic, space group P-1 (no. 2), a = 9.0882(7) Å, b = 10.5364(8) Å, c = 10.7238(9) Å, α = 92.199(2)°, β = 97.276(2)°, γ = 107.655(2)°, V =

967.42(13) Å^3, Z = 2, T = 100 K, μ(MoKα) = 0.093 mm^{-1}, $\rho calc$ = 1.263 g/cm^3, 28108 reflections measured (4.07° ≤ 2Θ ≤ 57.462°), 5006 unique (R_{int} = 0.0551, R_{sigma} = 0.0428) which were used in all calculations. The final R_1 was 0.0473 (I > 2σ(I)) and wR_2 was 0.1313 (all data).

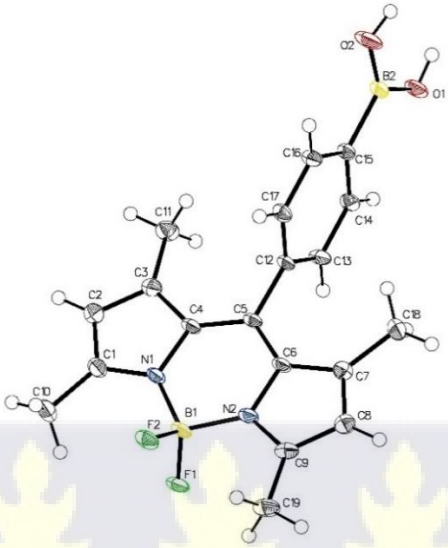

Figure 5.20. ORTEP representation of the compound **AAG156** investigated by X-ray structure analysis; atomic labelling shown with 30% probability displacement ellipsoids.

The proposed mechanism for the synthesis of BODIPY dyes is represented in **Scheme 5.16**. In the proposed mechanism, TFA catalyses the substitution of the aldehyde oxygen because of an attack by dimethylpyrrole **5.78**, followed by proton abstraction from the NH in **5.84** resulting in **5.85** which rearranges to **5.86** which is then attacked by a second dimethylpyrrole followed by rearrangement to form the dipyrromethane intermediate **5.79** which is oxidized to dipyrromethene **5.80**. The dipyrromethene can undergo complexation in a standard fashion to symmetric BODIPY **5.81**.

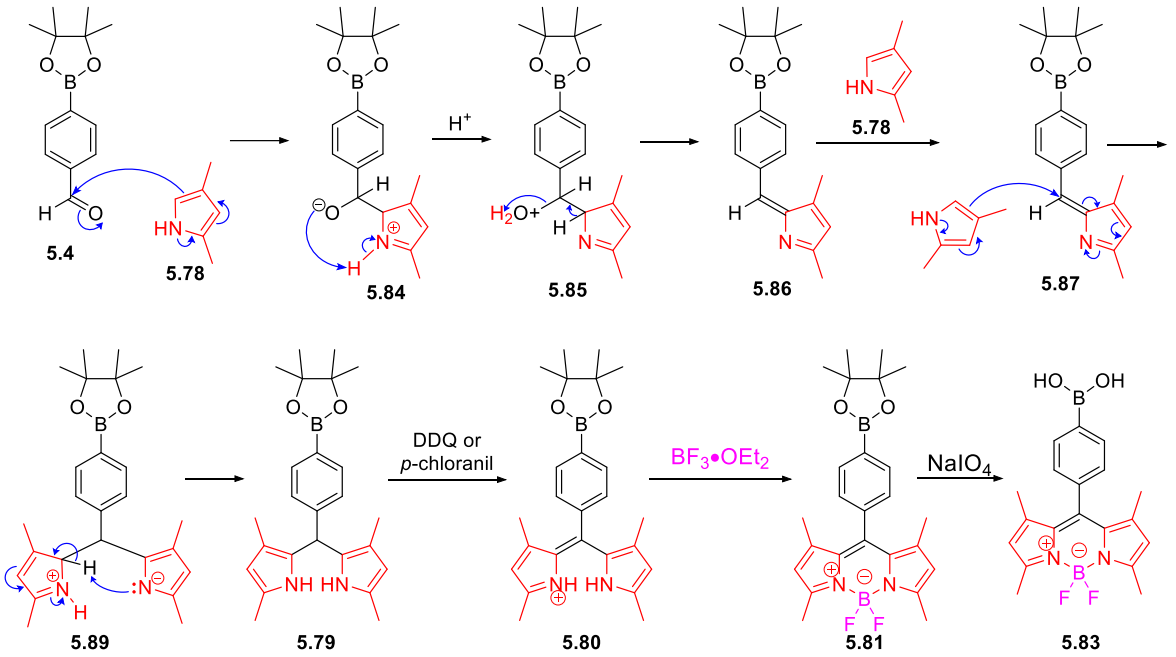

Scheme 5.16. One-pot condensation of 2,4-dimethylpyrrole and pinacol-protected 4-formylphenylboronic acid to yield BODIPY dyes.

5.3.1.8 Azo-tagged boronic acid dyes

Boronic acid azo dyes were used in the 1940s for investigations in the treatment of cancer by boron neutron capture therapy (BNCT) [382]. However, in 1991, a boronic acid azo dye synthesized from 4-aminophenylboronic acid was found to be sensitive to a selection of saccharides [383]. Subsequently, various conjugates of azo dyes have been developed as saccharide and sugar sensors [384-386].

A range of boronic acid appended azo dyes in which subtle modifications are made to the electronic configuration of the azo chromophore by varying the substituent groups on the azo aromatic ring were synthesised. The potential of these dyes as colour sensors for mycolactone detection was then assessed**.** A variety of azo-tagged boronic acid dyes were synthesized as depicted in **Scheme 5.17**. The first step involved the synthesis of (2-((m-tolylamino)methyl)phenyl)boronic acid **5.86** by reductive amination followed by diazotization

of various anilines containing electron-withdrawing groups such as *p*-NO_2, *p*-COOH, *p*-OCH_3, and *m*-COOH in the presence of an aqueous solution of sodium nitrite ($NaNO_2$) in concentrated HCl medium at 0 °C to form the corresponding diazonium salts. The destruction of excess sodium nitrite after the diazotization reaction step was required because nitrites are toxic and can be harmful to the environment. This was achieved by using a common nitrous *acid scavenger* such as sulfamic acid (H_3NSO_3) that reacts with nitrous acid (HNO_2) to form stable and non-toxic compounds [387, 388]. The diazonium salts that were formed in the previous step were not isolated but coupled *in situ* with (2-((*m*-tolylamino)methyl)phenyl)boronic acid **5.86** in a basic medium (NaOH) to give the respective target products which were fully characterized by ^{1}H NMR, ^{13}C NMR and HR-LCMS spectroscopic and spectrometric analysis. It is worth noting that the pH of the reaction mixture plays a significant role in the coupling reaction and therefore a careful balance must be struck between the equilibria governing the coupling component and the diazo component. The coupling reactions of the various aniline diazonium salts with the (2-((m-tolylamino)methyl)phenyl)boronic acid **5.86** occur predominantly para to the electron-donating anilinic nitrogen because of steric effects. This was directed by incorporating a methyl group meta to the anilinic nitrogen in the amine coupling agent, and it resulted in the exclusive para coupling products [389]. This design approach enabled me to make target dyes that avoided potentially difficult separation of isomers.

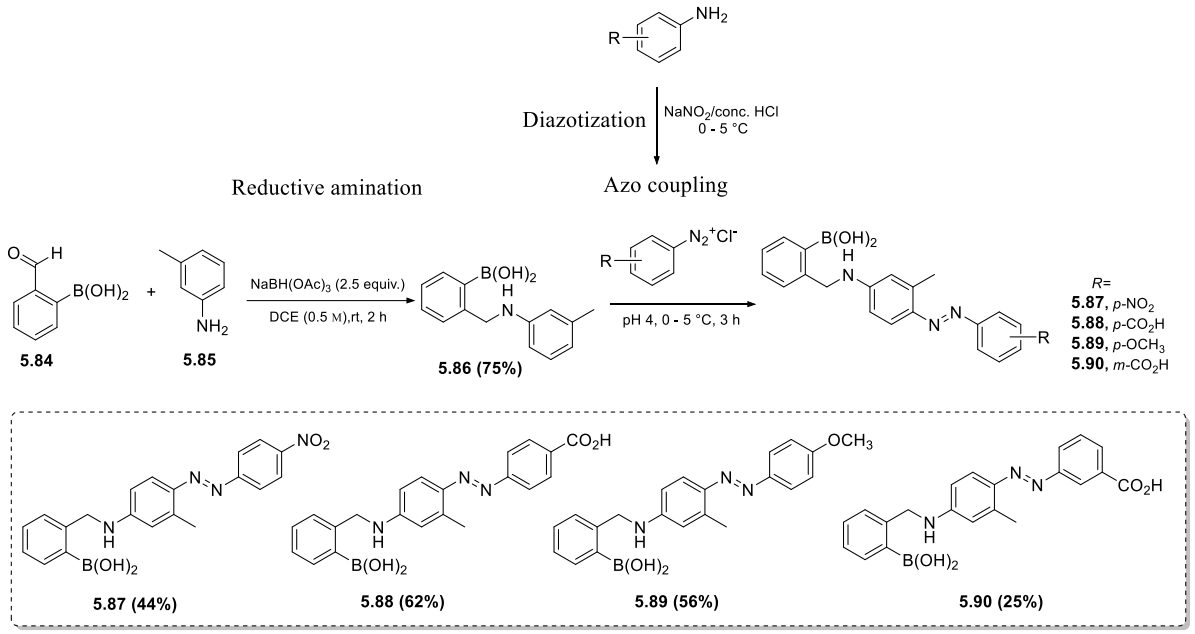

Scheme 5.17. Synthetic route to (E)-(2-(((3-methyl-4-(phenyldiazenyl)phenyl)amino) methyl)phenyl)boronic acid derivatives

5.3.2 Photophysical properties of the different arylboronic acid chemosensor dyes

A total of 14 boronic acids were investigated for their photophysical properties including twelve (12) synthesized fluorescent arylboronic acid chemosensors and two (2) commercially available boronic acids (2-naphthylboronic acid (BA) and 9,9-diphenyl-9H-fluoren-4-ylboronic acid (BA18). **Figure 5.26** summarizes the chemical structures, molecular weight, and category of dyes based on the parent chromophore from which the respective compounds were derived. They include one BODIPY, four azo dyes, two fluoresceins, one rhodamine, two coumarins, one 9-aminoacridine, and one 8-aminoquinoline boronic acid derivatives.

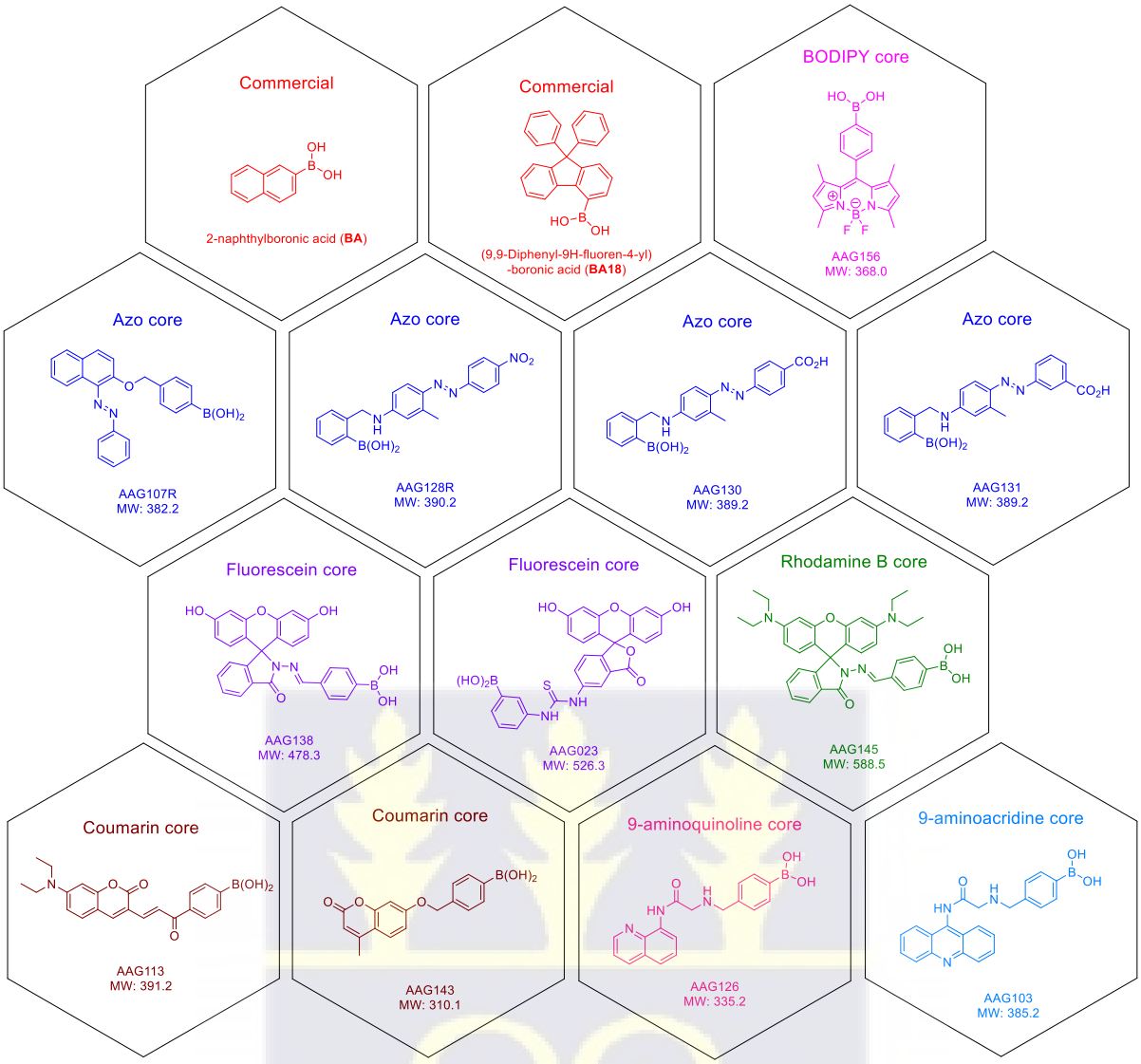

Figure 5.21. Structures of synthesized fluorescent arylboronic acid dyes were included in this study. The characteristic chromophore cores of the structures are highlighted in different colours.

A complete set of basic photophysical quantities such as absorption maxima (λ_{abs}^{max}), emission maxima (λ_{em}^{max}), Stokes shift ($\Delta\lambda$), molar extinction coefficient (ε), fluorescence quantum yield (Φ_F), and brightness were determined in ethanol, dimethyl sulfoxide, and methanol through absorption and emission spectroscopy techniques. The main photophysical data are summarized in **Table 5.1**.

The UV-vis absorption spectra of the different synthesized compounds are depicted in **Figure 5.27** and **Appendix 5**. The absorption maxima wavelengths are recorded in **Table 5.1**. The UV–vis spectroscopy was also used to obtain the experimental extinction coefficient (ε). The ε values were computed using the Beer-Lambert law (A = εcl) with solutions of known concentrations, where A is absorbance; ε the extinction coefficient for the dye; c is the sample concentration; l is the pathlength of the sample cuvette. It was observed that the synthesized compounds were characterized by ε ranging from very low values for AAG143 (ε = 248 ±16 $M^{-1}cm^{-1}$ at 403 nm) to the largest for AAG113 (ε = 52816 ± 1481 $M^{-1}cm^{-1}$ at 456 nm).

Table 5.1. Photophysical properties of synthesized fluorescent arylboronic acid dyes

Dye	MW [gmol^{-1}]	Solvent	λ_{abs}^{max} [nm]	λ_{em}^{max} [nm]	Stokes Shift ($\Delta\lambda$) [nm]	ε [M^{-1}cm^{-1}]	Quantum yield (Φ_F)	Brightness [M^{-1}cm^{-1}]
AAG023	526.3	EtOH	480	525	45	9368.7	0.47	4403.3
AAG113	391.2	EtOH	456	590	134	52816.1	0.78	41196.6
AAG126	335.2	DMSO	318	405	87	6468.8	0.031	200.5
AAG128R	390.2	EtOH	464	-	-	21695.7		ND
AAG130	389.2	EtOH	416	-	-	20550.8		ND
AAG131	389.2	EtOH	398	-	-	27245.4		ND
AAG138	478.3	EtOH	301	347	46	21486.3		ND
AAG143	310.1	DMSO	403	448	45	247.6	0.24	59.4
AAG145	588.5	EtOH	540	569	29	296.5	0.48	142.3
AAG156	368.0	EtOH	496	508	12	29259.1	0.70	20481.4
AAG103	385.2	MeOH	248.5	429	180.5	ND		ND
AAG107R	382.2	MeOH	335	384	49	ND		ND
BA	172.0	MeOH	275	328	53	ND		ND
BA18	362.2	MeOH	270	333	63	ND		ND

Maximum absorption wavelength (λ_{abs}^{max}), maximum emission wavelength (λ_{em}^{max}), Stokes shift ($\Delta\lambda$): calculated as the difference between λ_{abs}^{max} and λ_{em}^{max}, molar extinction coefficient (ε), fluorescence quantum yield (Φ_F): calculated by comparing to fluorescence reference standards with known quantum yield values such as Rhodamine B (Φ_F = 0.70 in EtOH), Quinine sulfate (Φ_F = 0.51 in 0.1 M H_2SO_4), and Brightness: this parameter was calculated using the formula: Brightness = Extinction Coefficient (ε) × Fluorescence Quantum Yield (Φ_F), ND = not determined.

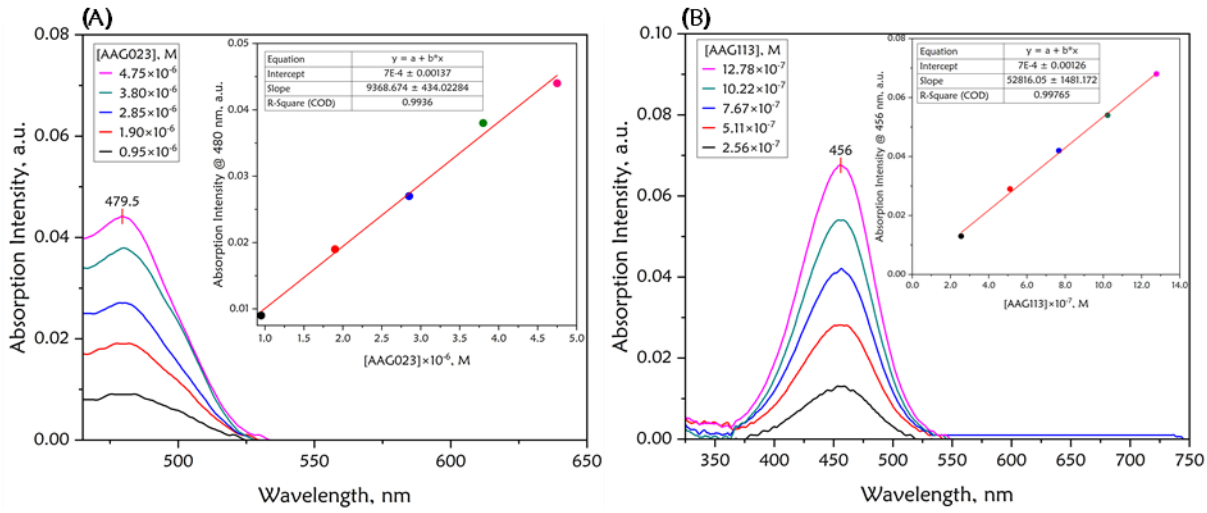

Figure 5.22. Absorbance spectra of various dyes in different organic solvents; **Insets:** respective linearity plots for the evaluation of molar extinction coefficients (ε) for the dyes at the absorption maxima.

Additionally, the fluorescence emission curves were obtained by exciting the compounds at the absorption maxima (**Table 5.2**). The normalized fluorescence emission spectra of the synthesized compounds are shown in **Figure 5.28**. The maximum emission bands are as follows; AAG023 (λ_{em} = 525 nm at λ_{ex} = 480 nm), AAG113 (λ_{em} = 590 nm at λ_{ex} = 456 nm), AAG126 (λ_{em} = 405 nm at λ_{ex} = 318 nm), AAG138 (λ_{em} = 347 nm at λ_{ex} = 301 nm), AAG143 (λ_{em} = 448 nm at λ_{ex} = 403 nm), AAG145 (λ_{em} = 569 nm at λ_{ex} = 540 nm), and AAG156 (λ_{em} = 508 nm at λ_{ex} = 496 nm). The Stokes shift ($\Delta\lambda$), defined as the difference between absorption maxima (λ_{abs}^{max}) and emission maxima (λ_{em}^{max}) was calculated for the various compounds. The relative fluorescence quantum yield (Φ_F) was determined relative to Rhodamine B in ethanol and Quinine sulfate in 0.1 M H_2SO_4 from fluorescence measurements according to the following relationship:

$$\Phi_{F,S} = \Phi_{F,R}\left(\frac{m_S}{m_R}\right)\left(\frac{\eta_S^2}{\eta_R^2}\right)$$

where: m is the slope of the line obtained from the plot of the integrated fluorescence intensity vs. absorbance, η is the refractive index of solvent and the subscripts R and S refer to the reference and unknown sample respectively; Φ_S and Φ_R are the fluorescence quantum yield of the sample and that of the standard respectively. The quantum yields were corrected for the differing refractive index of the solvent used for the sample and reference. Refractive indices (25 °C) were taken to be 1.3326, 1.3593, and 1.4793 for water, ethanol, and DMSO respectively [390]. In instances where the same solvent was used for both reference and unknown sample as a solvent, $\left(\eta_S^2 / \eta_R^2\right)$ will be 1, so the fluorescence quantum yield of the unknown (Φ_S) was obtained directly from the quotient of the two slopes. The reference standard should match the absorption and the emission wavelength region of the sample. For this reason, Rhodamine B and Quinine sulfate were chosen as reference standards for the various dyes. Fluorescence spectra of the varying concentrations of unknown samples and references are shown in **Figure 5.28** and **Appendix 6.1** with the absorbance values and integrated intensities (area under curve) of both samples and corresponding reference shown in **Table 5.2.**

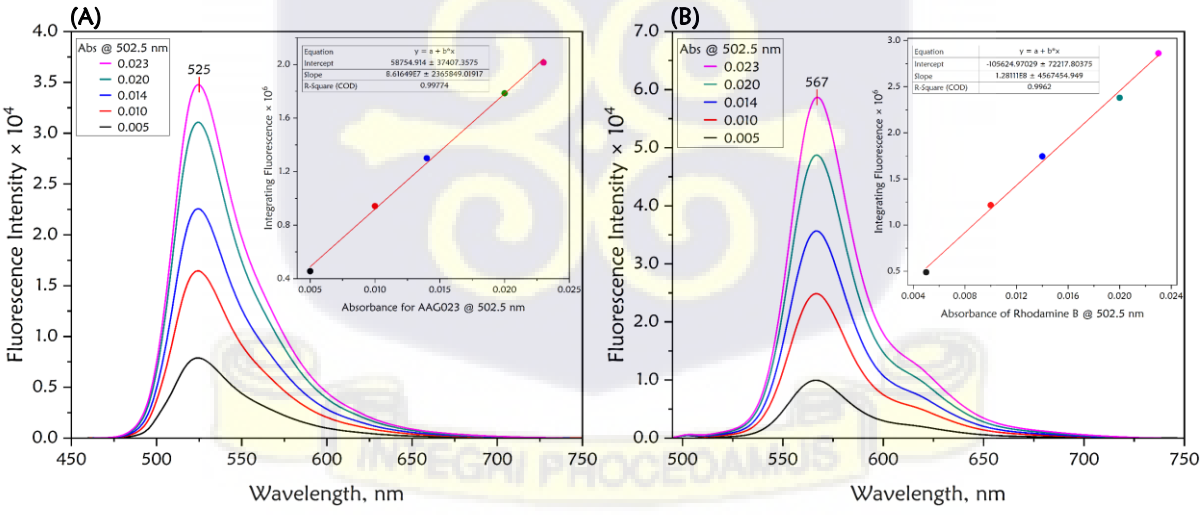

Figure 5.23. Fluorescence emission spectra of sample AAG023 (left) and reference Rhodamine B (right) with varying absorbance. **Inset:** Calibration curves of integrated fluorescence intensity (area under curve) against absorbance for sample respectively.

Table 5.2. Absorbance, and Integrated fluorescence intensities (Areas) for various samples and References

Absorbance @ 502.5 nm	**Integrated Fluorescence Intensity**	
	AAG023	**Rhodamine B**
0.023	2014294.3	2863728.4
0.020	1785124.7	2380927.6
0.014	1300128.5	1745938.7
0.010	942578.1	1216051.1
0.005	455519.6	489246.6
Slope	**861649000.0**	**128111000.0**
Absorbance @ 499 nm	**AAG113**	**Rhodamine B**
0.020	2619195.0	2549829.2
0.016	2158588.5	2121340.3
0.012	1682211.2	1495319.2
0.009	1204913.3	1066673.4
0.004	591676.7	415287.3
Slope	**128197000.0**	**115445000.0**
Absorbance @ 332 nm	**AAG126**	**Quinine sulfate**
0.080	406256.1	10254500.0
0.066	331390.9	8717544.0
0.053	269142.8	7633669.7
0.040	195980.9	5868201.1
0.030	134100.4	4435606.5
Slope	**5383876.6**	**114494000.0**
Absorbance @ 358 nm	**AAG143**	**Quinine sulfate**
0.072	2384944.0	9169983.2
0.058	2080661.1	7757302.9
0.051	1560798.8	6858240.1
0.038	1032764.1	5131493.2
0.028	510273.4	3945263.9
Slope	**43905200.0**	**120830000.0**
Absorbance @ 544.5 nm	**AAG145**	**Rhodamine B**
0.078	6696547.2	8871962.3
0.064	6251111.1	7476185.8
0.048	4931408.8	5593976.4
0.032	3405442.5	3872951.0
0.017	1858555.0	1555633.8
Slope	**81524200.0**	**118451000.0**

Absorbance @ 502.5 nm	**AAG156**	**Rhodamine B**
0.023	3049627.7	2863728.4
0.019	2613267.2	2380927.6
0.014	1973366.8	1745938.7
0.010	1360672.8	1216051.1
0.005	731821.0	489246.6
Slope	**127606000.0**	**128111000.0**

Finally, the brightness of each of the synthesized dyes was calculated from the molar absorption coefficient at the excitation wavelength and the fluorescence quantum yield values. Brightness is defined as the product of ε and Φ_F ($B = \Phi_F \times \varepsilon$). The brightness values allow for more practically meaningful comparisons between different dyes and as a result, can be used to determine the analytical sensitivity from the fluorophore side [271, 391, 392].

From the data obtained, the fluorescence emissions of most of the compounds occurred at longer wavelengths in the visible region of the electromagnetic spectrum as compared to the absorption spectra. This can be explained by the general principle that there are usually energy losses associated with absorption and emission spectra, thus, shifting the fluorescence spectra to longer wavelengths [270]. The fluorescence observed can be attributed to $n \rightarrow \pi^*$ or $\pi \rightarrow \pi^*$ transition states [269]. The $\Delta\lambda$ values ranged from the least for AAG156 ($\Delta\lambda$ = 12 nm) to sufficiently large Stokes shift values ($\Delta\lambda > 80$ nm) for AAG126, AAG113, and AAG103, with $\Delta\lambda$ values of 87, 134, and 180.5 nm respectively. AAG156, a BODIPY analogue, showed an intense absorption band with a maximum at 496 nm assigned at spin-allowed π-π^* transitions, high molar extinction coefficient ($\varepsilon = 29259 \pm 450$ $M^{-1}cm^{-1}$ at 496 nm), emission maximum at 508 nm with the lowest calculated $\Delta\lambda$ value of 12 nm. These properties are characteristic of BODIPY chromophore subunits and consistent with reported data [373, 393]. On the other hand, AAG113 with a high $\Delta\lambda$ value of 134 nm has the coumarin core moiety.

Some of the synthesized compounds such as AAG128R, AAG130, and AAG131 did not show fluorescence. Incidentally, all three compounds are azo dyes and this was not surprising because as a general rule, these categories of dyes do not fluoresce [394]. Here, the absorbed energy is dissipated by the medium or emitted as phosphorescence, which has a longer lifetime for the excited state [269]. However, all three synthesized azo dyes are characterized by high molar extinction coefficient values for example AAG128R ($\varepsilon = 21696 \pm 1997$ $M^{-1}cm^{-1}$ at 464 nm), AAG130 ($\varepsilon = 20551 \pm 360$ $M^{-1}cm^{-1}$ at 416 nm), and AAG131 ($\varepsilon = 27245 \pm 467$ $M^{-1}cm^{-1}$ at 398 nm). The quantum yields for these dyes were not determined due to a lack of significant fluorescence emissions at their respective absorption maxima values and also because very small quantum yield values have been acquired for other azo dyes [395, 396]. Unlike the azo dyes AAG128R, AAG130 and AAG131, this was not the case for AAG107R, a Sudan I derivative which is also an azo dye. Fluorescence was observed with AAG107R giving an emission maximum at 384 nm and a $\Delta\lambda$ value of 49 nm. As a general principle, small-molecule fluorophores require a high degree of aromaticity to have absorptions in the visible region of the spectrum [270, 307]. Therefore, it can be inferred that the extension of the π-conjugation system that emanates from the aromaticity within the naphthalene fragment present in Sudan I dyes may be responsible for the fluorescence observed in AAG107R. This could elicit a shift in the absorption and emission spectra [392].

The compound with the largest molar extinction coefficient ($\varepsilon = 52816 \pm 1481$ $M^{-1}cm^{-1}$ at 456 nm), $\Delta\lambda$ value of 134 nm, $\Phi_F = 0.78$ and brightness value (41196.6 $M^{-1}cm^{-1}$) was AAG113, a coumarin derivative. This is typical of coumarin derivatives which are usually characterized by high molar extinction coefficients in the near-UV and visible range, high fluorescence emission and as a result, have found many uses as fluorescent chromophores for several applications [397, 398].

Based on the excellent photophysical properties of AAG113, the fluorescent properties of AAG113 toward mycolactone were investigated. Sensitive detection of mycolactone was achieved through fluorescence spectroscopy as shown in **Figure 5.29.** For instance, free AAG113 (2.5×10^{-3} mg/mL) exhibited weaker fluorescence intensity at the emission maximum of 581 nm. However, the fluorescence intensity gradually increased as the concentration of mycolactone increased from 0 to 8.0×10^{-3} mg/mL (0–1.6 equiv.). The enhanced fluorescence of AAG113 was also visually observed on f-TLC plates when coupled with mycolactone and under a 365 nm UV lamp, as shown in **Figure 5.30**.

This can be explained by the coupling of the boronic acid moiety in the structure of AAG113 with the 1,3-diol moieties of mycolactone to form 6-membered cyclic boronate esters as has been established in the previous section on the proof-of-concept studies. The formation of the boronate coupled with the chromophore of the mycolactone resulted in the enhanced fluorescence. A calibration curve was obtained between the concentration of mycolactone and fluorescence intensity at 581 nm with good linearity (R^2 = 0.9886) (**Inset, Figure 5.29**). The limit of detection (LOD) and limit of quantification (LOQ) were estimated to be 0.85 ng/µL (signal-to-noise ratio (S/N) × 3) and 2.84 ng/µL (signal-to-noise ratio (S/N) × 10) respectively; where *N* is the standard deviation (SD) of the peak area (n = 8), taken as a measure of the noise, and *B* is the slope of the corresponding calibration curve. This reveals that the AAG113 could detect a nanomolar-level concentration of mycolactone.

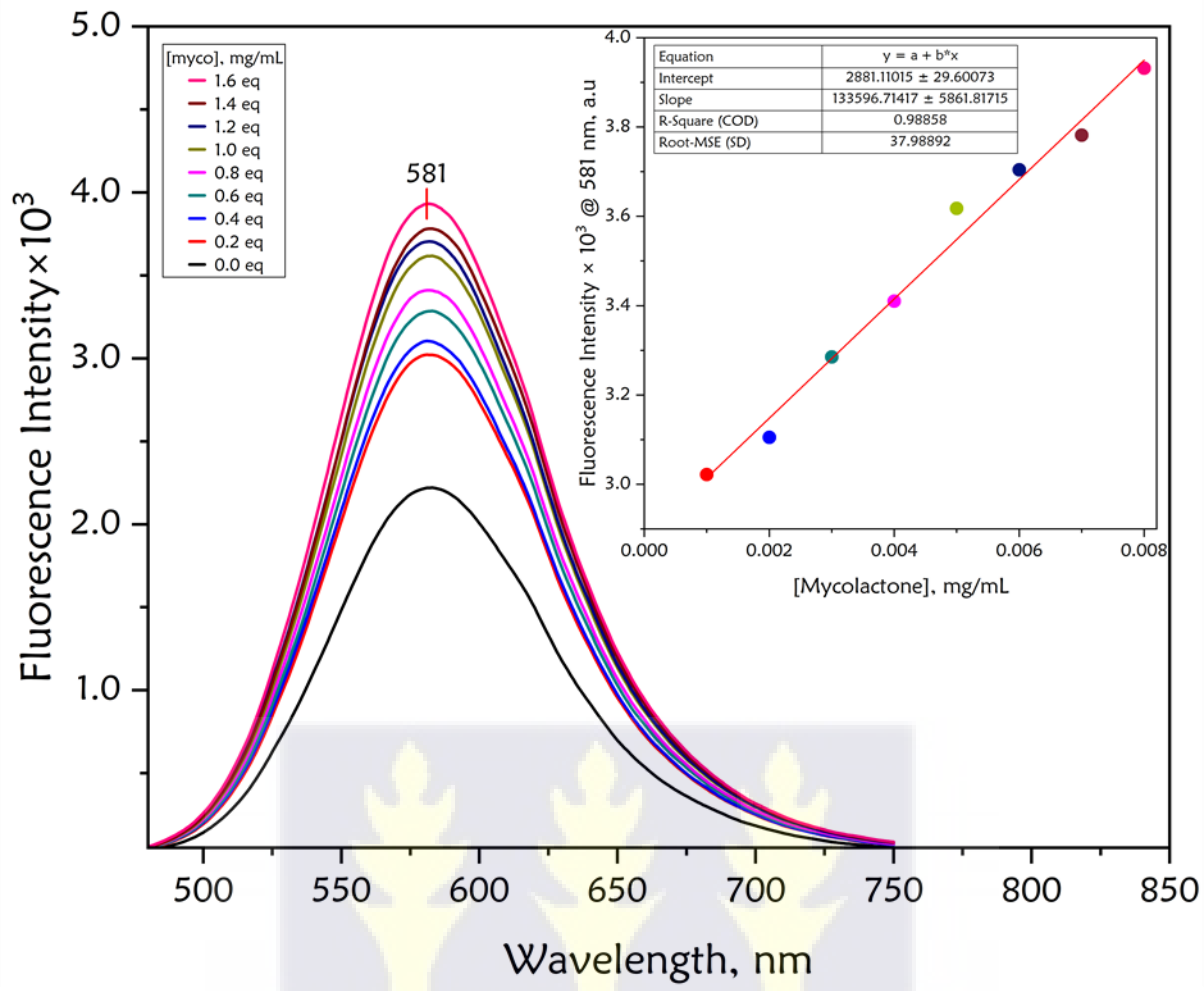

Figure 5.24. Fluorescence spectra of coumarin dye AAG113 (0.0025 mg/mL) upon gradual addition of serial concentrations of mycolactone (from bottom to top, 0 – 0.008 mg/mL) in ethanol. **Inset:** Plot of the linear relationship between the fluorescence intensity and varying concentrations of mycolactone.

5.3.3 Detection of mycolactone by the f-TLC method using the synthesized dyes

Boronic acids form reversible cyclic boronate complexes with 1,2- or 1,3-diols and this property has been demonstrated earlier using various diols and a 4-tolylboronic acid. This unique property makes boronic acids useful selective and sensitive detection reagents for diols in TLC. For instance, boronic acids have been employed in the detection of mycolactone on thin-layer chromatography (TLC) [74, 312]. Here, the synthesized aryl boronic acids coupled

to mycolactone and the resulting fluorescent boronate complexes were visualized under a benchtop UV lamp (365 nm). The detection of mycolactone spots on TLC plates was optimized by using different concentrations of the synthesized boronic acids. **Figure 5.30** shows the images of the fluorescence response of 5 µL/spot of synthetic mycolactone after dipping in 0.1 mM and 0.01 mM acetone concentrations of various synthesized fluorescent aryl boronic acid chemosensors together with the two boronic acids previously reported for use in the f-TLC method which were obtained commercially (BA and BA18).

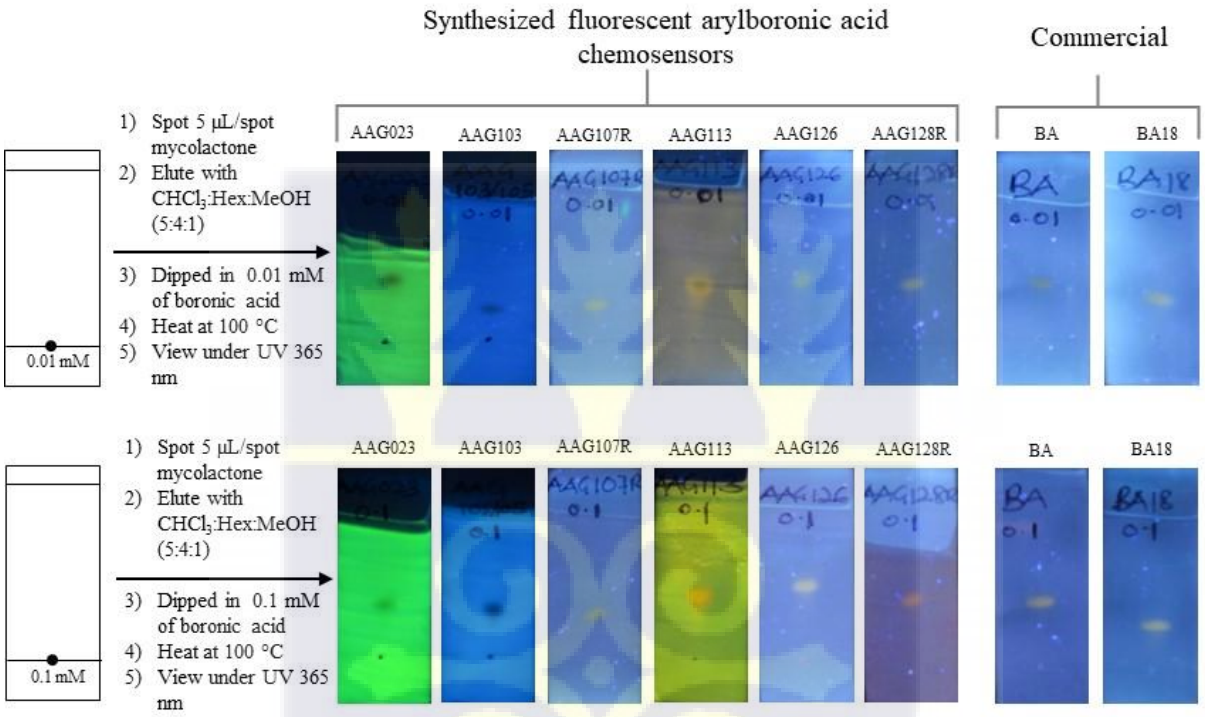

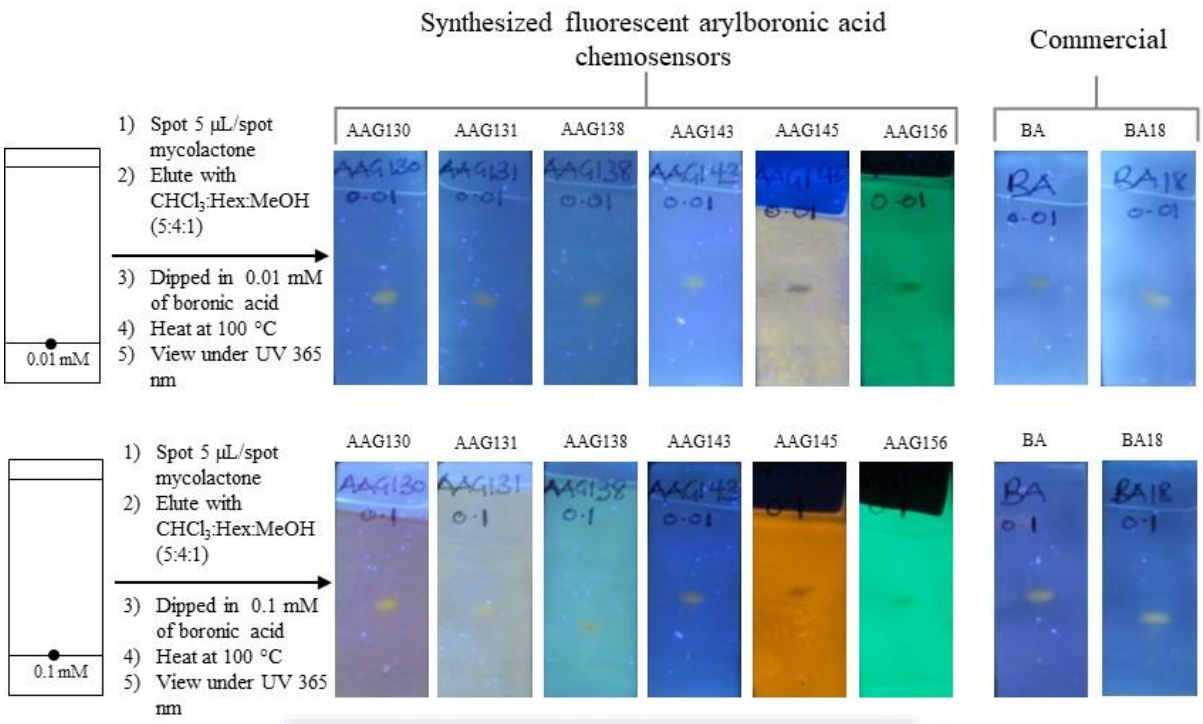

Figure 5.25. Images of the fluorescence response of 5 µL/spot of synthetic mycolactone after dipping in 0.1and 0.01 mM acetone concentrations of various synthesized fluorescent aryl boronic acid chemosensors compared to two commercial boronic acids under 365 nm UV light.

First, a remarkable enhancement of fluorescence intensity of mycolactone was generally observed after dipping in either 0.01 mM or 0.1 mM solutions of the various boronic acids, particularly after heating to approximately 100 °C. In this study, glass-backed TLC plates are used for the purpose of heating. The esterification reactions in the proof-of-concept studies occurred under room temperature conditions in *n*-pentane under 30 minutes whereas the reaction on the solid TLC support proceeded rapidly at elevated temperatures. Dipping the TLC plate into the boronic acid solutions and heating it to 100 °C for just 60 seconds was sufficient to ensure the complete formation of the cyclic boronate esters of the various boronic acid sensors with the 1,3-diols motifs of the mycolactone.

Generally, it was observed that the fluorescence band intensities of mycolactone adducts on TLC plates dipped in 0.1 mM acetone solutions of the synthesized chemosensors appeared more intense than those dipped in the same concentration of the commercially available BA and BA18 solutions except for AAG023, AAG107R, AAG131, AAG145, and AAG156. This observation was similar when 0.01 mM solutions of the boronic acids was used. Unlike other spots, it was observed that the mycolactone adduct spots appeared black on different backgrounds in solutions of AAG023, AAG103, AAG145 and AAG156. AAG023 produced the most intense black spot in the 0.01 mM solution while the AAG103 plate had the most intense black spot in the 0.1 mM solution.

Compounds AAG113, AAG126, AAG128R and AAG130 had outstanding fluorescent bands on TLC, especially in 0.1 mM solutions. In the case of AAG023, AAG131, AAG138, AAG145, and AAG156, the mycolactone adduct of TLC plates dipped in 0.1 mM solutions showed weak fluorescent band intensities in comparison to the band intensities of plates that were dipped in the 10-fold lower concentrations of the same boronic acids. This could partly be as a result of fluorescence quenching leading to the reduced fluorescence bands on TLC [269]. Should this be the case, then, this concentration range might be unsuitable for evaluating these boronic acids because of the dramatic concentration quenching of the fluorescence.

5.4 Experimental

5.4.1 General information

All reactions were performed using standard laboratory equipment and glassware. All reagents and solvents used were supplied by commercial sources without further purification unless specified. All air-sensitive reactions were carried out under a nitrogen atmosphere using an oven-dried apparatus.

5.4.2 Thin Layer Chromatography (TLC)

Thin layer chromatography (TLC) was performed on Merck silica gel 60 F254 aluminium-backed plates pre-coated with silica with a thickness of 0.20 mm. Plates were visualized using either ultraviolet light of 254 nm or 365 nm or by dipping the plates into solutions of vanillin, ninhydrin, or potassium permanganate followed by heating. All column chromatography was performed under 'flash' conditions using silica gel mesh 40-63.

5.4.3 Fourier-transform infrared (FT-IR) Spectroscopy

Infrared (IR) spectra were recorded on a Perkin Elmer 100 FT-IR instrument on the neat compounds. Products were placed directly onto the spectrometer diamond plate and compressed. The spectrum was processed in the software and displayed. The relevant and characteristic absorptions were reported in wavenumbers (cm^{-1}) with the intensities of the bands recorded as; broad (b), strong (s), medium (m), and weak (w).

5.4.4 Nuclear Magnetic Resonance (NMR) Spectra

Nuclear magnetic resonance (NMR) spectroscopy was performed on Brüker Avance III 400 and 500 MHz spectrometers, where proton NMR (^{1}H NMR) spectra and carbon NMR (^{13}C NMR) spectra and ^{11}B NMR were acquired at the indicated 101, 126, 128, 377 and 400 MHz as dilute solutions in the indicated deuterated solvent at ambient temperature. All spectra were recorded in deuterated dimethyl sulfoxide (DMSO-d_6), deuterated acetone (acetone-d_6) or deuterated chloroform ($CDCl_3$) obtained from Sigma Aldrich. All chemical shifts (δ) are reported in parts per million (ppm) relative to residual protonated solvent peak (δ_H: $CHCl_3$ = 7.26 ppm, DMSO-d_6 = 2.50 ppm) or the solvent itself (δ_C: $CDCl_3$ = 77.0 ppm, DMSO-d_6 = 39.52 ppm). Chemical shifts (δ) were measured in parts per million (ppm) and referenced against the internal reference peaks. Coupling constants (*J*) were measured in hertz (Hz). NMR assignments were determined through the interpretation of one- and two-dimensional spectra.

All multiplicities are designated by the following abbreviations: s = singlet, br s = broad singlet, d = doublet, dt = doublet triplet, td = triplet doublet, ddd = doublet doublet of doublets of doublets, q = quartet, br q = broad quartet, m = multiplet. All coupling constants (*J*) are reported in Hertz (Hz). Peaks are listed in decreasing chemical shift in the following format: chemical shift (integration (^{1}H), multiplicity (^{1}H), coupling constant (^{1}H).

5.4.5 Mass Spectra (MS)

High-resolution mass spectra were recorded at the Mass Spectrometry Service at the Department of Chemistry, University of Sheffield using a 1260 Infinity LC (Agilent Technologies), coupled to a Quadrupole-Time of Flight tandem mass spectrometer 6530 Infinity Q-ToF detector (Agilent Technologies) by a Jet Stream ESI interface (Agilent Technologies). The LC conditions were: Zorbax Extend-C18 column (2.1 mm × 50 mm, 1.8 µm particle size); 0.4 mL/min flow rate; 1 µL injection volume for MS experiments. and 10 µL for MSMS experiments; 40 °C column temperature. Separation was achieved using a gradient of water with 0.1% formic acid (eluent A) and acetonitrile with 0.1% formic acid (eluent B). The elution gradient was programmed as follows: initial conditions 5% B, followed by a linear gradient to 95% B in 15 min. The ESI operating conditions were drying gas (N_2, purity > 98%): 350 °C and 11 L/min; capillary voltage 4.0 kV; nebulizer gas 40 psig; sheath gas (N2, purity > 98%): 375 °C and 11 L/min. High-resolution MS spectra were acquired in the positive mode in the 100–2400 m/z range.

5.4.6 Single-Crystal X-Ray Diffraction (SCXRD)

Single crystal X-ray data were collected on a Bruker D8 VENTURE diffractometer (Bruker, Karlsruhe, Germany) (Bruker AXS, Karlsruhe, Germany), equipped with a PHOTON 100 CMOS detector with graphite monochromatized Cu-Kα radiation (λ = 1.54178 Å) or a Bruker X8 Apex-II diffractometer, equipped with an Apex-II CCD area detector diffractometer

(Bruker, Karlsruhe, Germany) with graphite monochromatized Mo-Kα radiation (λ = 0.71073 Å). The two devices are in the Department of Chemistry of the University of Sheffield. A suitable crystal was mounted in Fomblin oil on a MiTeGen MicroLoop and cooled in a stream of cold N_2 to 100 K. Data were corrected for absorption using empirical methods (SADABS) [399-401] based upon symmetry equivalent reflections combined with measurements at different azimuthal angles. All crystal structures were solved and refined against F^2 values using ShelXT [402] for the solution and ShelXL [403] for refinement accessed via the Olex2 program [404]. All non-hydrogen atoms were refined with anisotropic displacement parameters. All hydrogen atoms were added at calculated positions and refined with a riding model and isotropic displacement parameters fixed in magnitude relative to the attached carbon atoms. Details regarding the structures and a summary table of crystallographic and data collection parameters are provided in **Appendix 4**.

5.4.7 Synthesis and characterization

5.4.7.1 General Procedures

5.4.7.1.1 General Procedure 1: *Boc* protection of Aryl amines

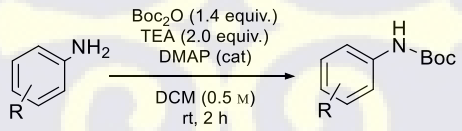

To a mixture of halo aniline (1.0 equiv.), triethylamine (TEA, 2.0 equiv.), *N, N*-dimethylaminopyridine (DMAP, cat. amount, 5 mol%) dissolved in anhydrous CH_2Cl_2 (20 mL) was added to di-*tert*-butyl dicarbonate (*Boc*$_2$O, 1.4 equiv.) at 0 °C. The reaction mixture was allowed to warm to room temperature and stirred for 2 hr. After the reaction was quenched with 5% $NaHCO_3$, the mixture was extracted with DCM (3 x 20 mL), followed by brine. The organic layer was combined and dried over anhydrous $MgSO_4$, followed by drying under a

high vacuum. The crude product was purified by flash column chromatography to obtain the product.

***Tert*-butyl (4-bromophenyl)carbamate 5.2.**

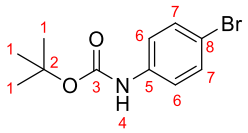

5.2

The title compound was prepared according to **General Procedure 1** using 4-bromoaniline (4.00 g, 24 mmol), TEA, (4.86 g, 6.6 mL, 29 mmol), Boc_2O (7.33 g, 33.6 mmol) and DMAP (147 mg, 1.2 mmol) in anhydrous CH_2Cl_2 (20 mL). The crude product was purified by flash column chromatography using hexane/ethyl acetate (9:1) to afford *tert*-butyl 4-bromophenylcarbamate **5.2** (5.13 g, 79% yield). **^{1}H NMR** (500 MHz, $CDCl_3$) δ 7.49 (d, *J* = 8.5 Hz, 2H, **H6**), 7.16 (d, *J* = 8.7 Hz, 2H, **H7**), 1.43 (s, 9H, **H1**). **^{13}C NMR** (126 MHz, $CDCl_3$) δ 152.0 (**C3**), 138.2 (**C5**), 132.4 (**C7**), 130.1 (**C6**), 122.1 (**C8**), 84.2 (**C2**), 28.3 (**C1**).

5.4.7.1.2 General Procedure 2: Pd-catalyzed Miyaura borylation of aryl halides utilizing Bis(pinacolato)diboron

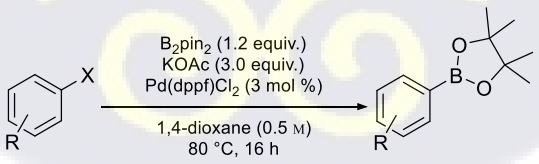

Using a variation of the procedure of Miyaura et al.[405], a mixture of aryl halide (1.0 equiv.), bis(pinacolato)diboron or (1.2 equiv.), KOAc (3.0 equiv.), and $Pd(dppf)Cl_2$ (3% mol) in dry 1,4-dioxane in an oven-dried two-necked round-bottom flask was degassed for 5-10 minutes using N_2 gas and stirred at 80 °C for 16 hours (overnight). Upon completion (as monitored by TLC), the reaction mixture was allowed to cool, filtered through a plug of celite, washed with

EtOAc (200 mL), extracted twice with water (2 x 50 mL), and then with brine. The organic layer was dried with anhydrous $MgSO_4$, filtered, and concentrated *in vacuo*. The crude material was purified by flash chromatography to give the corresponding boronic ester.

***Tert*-butyl (4-(4,4,5,5-tetramethyl-1,3,2-dioxaborolan-2-yl)phenyl)carbamate 5.3.**

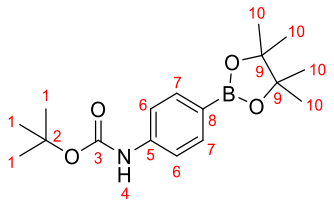

5.3

The title compound was prepared according to **General Procedure 2** using the *Boc*-protected compound, *tert*-butyl (4-bromophenyl)carbamate **5.2** (7.47 g, 27.4 mmol), B_2pin_2 (8.36 g, 32.9 mmol), KOAc (8.01 g, 82.3 mmol), $PdCl_2$(dppf) (60 mg) in 1,4-dioxane (30 mL). The crude product was purified on silica gel using hexane/ethyl acetate = 50:1 (*V*:*V*) to obtain product **5.3** as a white solid (5.51 g, 63% yield). **^{1}H NMR** (500 MHz, $CDCl_3$) δ 7.77 (d, *J* = 7.9 Hz, 2H, **H7**), 7.22 (d, *J* = 7.8 Hz, 2H, **H6**), 1.43 (s, 9H, **H1**), 1.34 (s, 12H, **H10**). **^{13}C NMR** (126 MHz, $CDCl_3$) δ 152.0 (**C3**), 141.5 (**C5**), 135.4 (**C7**), 127.1 (**C6**), 84.0 (**C9**), 83.5 (**C2**), 28.1 (**C1**), 25.0 (**C10**), (**C8** bonded to B not observed due to broadening).

Synthesis of 4-(4,4,5,5-tetramethyl-1,3,2-dioxaborolan-2-yl)benzaldehyde, 5.4.

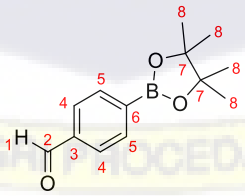

5.4

The title compound was prepared according to **General Procedure 2** using 4-bromobenzaldehyde (1.0 g, 5.4 mmol), B_2pin_2 (1.65 g, 6.5 mmol), KOAc (1.59 g, 16.2 mmol),

$PdCl_2$(dppf) (119 mg, 0.162 mmol) in 1,4-dioxane (20 mL). The crude product was purified on silica gel using DCM (100%) to obtain product **5.4** as a white solid (872 mg, 70% yield). **^{1}H NMR** (400 MHz, $CDCl_3$) δ_H 10.02 (s, 1H, **H1**), 7.94 (d, *J* = 8.2 Hz, 2H, **H5**), 7.83 (d, *J* = 8.2 Hz, 2H, **H4**), 1.33 (s, 12H, **H8**). **^{13}C NMR** (101 MHz, $CDCl_3$) δ_C 192.9 (**C2**), 138.4 (**C3**), 135.6 (**C4**), 129.0 (**C5**), 84.7 (**C7**), 25.2 (**C8**), (**C6** bonded to B not observed due to broadening). **LC-MS**: retention time: 9.4 min; **ESI-QTOF HRMS** (m/z): for $[C_{13}H_{18}BO_3]^+$ $[M+H]^+$: exact mass *calcd.*: 233.1349; found: 233.1358; for $[C_{13}H_{17}BO_3Na]^+$ $[M+Na]^+$: exact mass *calcd.*: 255.1168; found: 255.1172.

1-(4-(4,4,5,5-tetramethyl-1,3,2-dioxaborolan-2-yl)phenyl)ethan-1-one, 5.5.

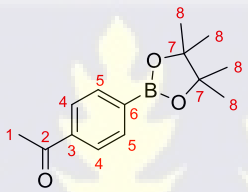

5.5

The title compound was prepared according to **General Procedure 2** using 4-bromoacetophenone (5.0 g, 25.1 mmol), and B_2pin_2 (7.65 g, 30.1 mmol), KOAc (7.39 g, 75.3 mmol), $PdCl_2$(dppf) (551 mg, 0.75 mmol) in 1,4-dioxane (20 mL). The crude product was purified on silica gel using hexane/ethyl acetate＝50∶1 (*V*∶*V*) to obtain the product **5.5** as a white solid (6.15 g, 96% yield). **^{1}H NMR** (500 MHz, $CDCl_3$) δ_H 7.90 (d, *J* = 6.3 Hz, 2H, **H4**), 7.87 (d, *J* = 6.3 Hz, 2H, **H5**), 2.58 (s, 3H, **H1**), 1.33 (s, 12H, **H8**). **^{13}C NMR** (126 MHz, $CDCl_3$) δ_C 198.7 (**C2**), 139.3 (**C3**), 135.2 (**C5**), 127.6 (**C4**), 84.5 (**C7**), 27.0 (**C1**), 25.2 (**C8**), (**C6** bonded to B not observed due to broadening).

General Procedure 3: *Boc* protection of Glycine

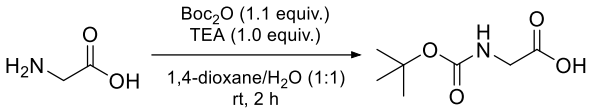

Glycine (1.0 equiv.) was dissolved in a dioxane-water (1:1) mixture. Triethylamine (1.0 equiv.) and di-*tert*-butyl decarbonate (*Boc*$_2$O) (1.1 equiv.) were added and the mixture was stirred for 2 h at room temperature. After evaporation of the volatiles, redissolving in water/diethyl ether for extraction. The aqueous phase was recovered, and the pH was adjusted to 2 with a 2 N solution of HCl. The mixture was extracted with ethyl acetate, dried over $MgSO_4$, and concentrated *in vacuo* to yield a white crystalline product.

Synthesis of 2-(*tert*-butoxycarbonylamino)acetic acid 5.45.

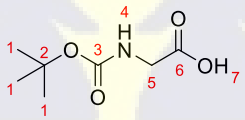

5.45

Based on the **General Procedure 3** adopted from Ear *et al[406]*, Glycine (10.0 g, 133.2 mmol, 1.0 equiv.) was dissolved in a dioxane-water (1:1) (200 mL) mixture. Triethylamine (18.5 mL, 133.2 mmol, 1.0 equiv.) and di-*tert*-butyl dicarbonate (31.98 g, 146.5 mmol, 1.1 equiv.) were added and the mixture was stirred for 2 h at room temperature. After evaporation of the volatiles, redissolving in water/diethyl ether (150 mL/250 mL) for extraction. The aqueous phase was recovered, and the pH was adjusted to 2 with a 2 M solution of HCl. The mixture was extracted with ethyl acetate (2 x 150 mL), dried over $MgSO_4$, and concentrated *in vacuo*, to yield white crystalline product **5.45**, yield (15.08 g, 65% yield). The data were consistent with the literature [406].

^{1}H NMR (400 MHz, DMSO-d_6) δ_H 7.05 (t, *J* = 6.2 Hz, 1H, **H4**), 3.57 (d, *J* = 6.2 Hz, 2H, **H5**), 1.38 (s, 9H, **H1**). **^{13}C NMR** (101 MHz, DMSO-d_6) δ_C 171.8 (**C6**), 155.9 (**C3**), 78.1 (**C2**), 41.8 (**C5**), 28.2 (**C1**). **LC-MS**: retention time: 4.7 min; **ESI-QTOF HRMS** (m/z): for $[C_{14}H_{17}BNO_2]^+$ $[M+H]^+$: exact mass *calcd.*: 198.0742; found: 198.0756.

5.4.7.1.3 General Procedure 4: *Boc* deprotection of amine

To a solution of the *Boc*-protected compound (1.0 equiv.) in anhydrous CH_2Cl_2 (0.5 M), trifluoroacetic acid (3.5 mL) was added and stirred for 1 h at room temperature. The excess reagent and solvent were evaporated under reduced pressure. The resulting sticky viscous mass was neutralized by saturated $NaHCO_3$ solution and extracted with CH_2Cl_2 (3 × 25 mL), dried over anhydrous $MgSO_4$, and evaporated under reduced pressure. The product was collected and used for the next steps without further purification.

4-(4,4,5,5-tetramethyl-1,3,2-dioxaborolan-2-yl)aniline 5.3b.

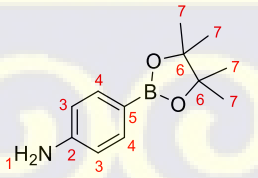

5.3b

The title compound was prepared according to **General Procedure 4** using tert-butyl (4-(4,4,5,5-tetramethyl-1,3,2-dioxaborolan-2-yl)phenyl)carbamate **5.3** (5.51 g) in anhydrous CH_2Cl_2 (0.5 M), trifluoroacetic acid (3.5 mL). The product **5.3b** was collected and used for the next steps without further purification (2.7 g, 73% yield). **^{1}H NMR** (500 MHz, $CDCl_3$) δ 7.47 (d, *J* = 7.9 Hz, 2H, **H4**), 7.02 (d, *J* = 8.0 Hz, 2H, **H3**), 1.10 (s, 12H, **H1**). **^{13}C NMR** (126 MHz, $CDCl_3$) δ 141.2 (**C2**), 136.4 (**C4**), 119.8 (**C3**), 84.1 (**C6**), 25.3 (**C7**), (**C5** bonded to B not observed due to broadening).

5.4.7.1.4 General Procedure 5: Reductive amination

Amine (1.2 equiv.) and aldehyde (1.0 equiv.) were dissolved in 1, 2-dichloroethane. The reaction mixture was then charged with sodium triacetoxyborohydride (1.5 equiv.) and stirred under nitrogen for 1 h. After an hour, additional sodium triacetoxyborohydride (1.0 equiv.) was added to the reaction mixture, and it was stirred for a further 1 h. The reaction mixture was then quenched with a saturated $NaHCO_3$ solution. The aqueous phase was extracted with CH_2Cl_2, and the combined organics dried over anhydrous $MgSO_4$ and concentrated to dryness *in vacuo* to afford the product.

5.4.7.1.5 General Procedure 6: Synthesis of 2-chloroacetamides (Method 1)

Chloroacetyl chloride was dissolved in dry CH_2Cl_2 at 0 °C and was added slowly to a stirred mixture of the amine and triethylamine in CH_2Cl_2 under N_2, the reaction mixture was stirred overnight at room temperature. The reaction mixture was quenched with distilled water and was then extracted with CH_2Cl_2. The combined organic layer was washed with 10% aqueous HCl solution and dried over anhydrous Na_2SO_4, evaporated and recrystallized from ethanol to afford solid products.

5.4.7.1.6 General Procedure 7: Synthesis of 2-chloroacetamides (Method 2)

Chloroacetyl chloride (1.0 equiv.) in THF was added dropwise while stirring to a mixture of amine (1.0 equiv.) and TEA (2.0 equiv.) in THF at 0 – 5 °C and stirred for 4 h. The solvent was evaporated under reduced pressure. The residue was washed with water to remove TEA.HCl before being dried and recrystallized from ethanol.

5.4.7.1.7 General Procedure 8: Amidation

A mixture of amine (1.0 equiv.), DMAP (5 mol%) and *Boc*-Gly-OH (2.0 equiv.) in dichloromethane were stirred in an ice bath (~0 °C) for 30 minutes, followed by an addition of EDC·HCl (2.0 equiv.). The reaction mixture was stirred at 0 °C for 2 hours and stirred overnight at room temperature. The crude was extracted with NH_4Cl (aq). The organic layer was dried over $MgSO_4$, filtered, and concentrated under a vacuum. The crude product was purified through silica-gel column chromatography to afford the product.

5.4.7.1.8 General Procedure 9: Amination

Chloroacetamide (1.0 equiv.), amine (1.2 equiv.), and triethylamine (TEA, 2.0 equiv.) were dissolved in acetonitrile (MeCN), stirred, and refluxed for 1 d. The residue was dissolved in methylene chloride and washed five times with 10 mL of water. The organic layer was dried over anhydrous Na_2SO_4. The solvent was removed under reduced pressure to obtain the crude product, which was purified by silica gel column chromatography.

5.4.7.1.9 General Procedure 10: Deprotection of pinacol boronate esters

Deprotection of pinacol boronate esters was performed according to the procedure by Akgun [407]. Pinacol boronate ester (1.0 equiv.) was dissolved in THF: water (4:1 ml) (4:1 v/v). Then, sodium periodate (3.0 equiv.) was added to the solution and stirred at room temperature for 30 min under an ambient atmosphere. Lastly, HCl (0.2 mL, 1 N) was added to the reaction mixture, which was stirred for 24 h at room temperature. The reaction mixture was concentrated *in vacuo*. Then it was dissolved in EtOAc (30 mL) and washed with water (1 × 8 mL), and brine (1 × 8 mL). The organic fraction was dried ($MgSO_4$), filtered and concentrated *in vacuo* to obtain the corresponding boronic acid.

5.4.7.1.10 General Procedure 11: Imine formation

Aldehyde (1.1 equiv.) was dissolved in 20 mL of a mixture of ethanol/toluene (90:10) and then amine (1.0 equiv.) was added. A Dean-Stark trap was fixed to the reaction vessel and filled with 10 mL of the same solvent mixture for the azeotropic removal of water. The reaction was then allowed to stir for 16 h at 100 °C at which time TLC showed that the amine starting material had fully reacted. The solvent was removed under vacuum, and the product was recrystallized to obtain the product.

5.4.7.2 Categories of fluorescent arylboronic acid chemosensor dyes

5.4.7.2.1 Coumarin dyes

Synthesis of 7-(diethylamino)-*2H*-chromen-2-one 5.8.

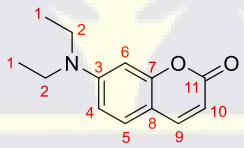

5.8

A mixture of 4-(diethylamino) salicylaldehyde (6.0 g, 28.69 mmol) and diethyl malonate (10.84 g, 67.75 mmol) in 90 mL anhydrous ethanol was treated with 3 mL of piperidine and then refluxed for 13 h. After removing the solvent, 120 mL of mixed solution (concentrated HCl:glacial acetic acid＝1:1 (*V*:*V*)) was added to the crude product and refluxed for another 7 h. The reaction solution was poured into 300 mL of water after cooling to room temperature. The solution's pH was adjusted to 5 with NaOH. The solid was filtered and purified over silica gel (hexane: ethyl acetate＝9:1 (*v*/*v*)) to give a beige solid **5.8** (yield: 85%). **^{1}H NMR** (500 MHz, $CDCl_3$) δ_H 7.53 (d, *J* = 9.3 Hz, 1H, **H9**), 7.23 (d, *J* = 8.7 Hz, 1H, **H5**), 6.56 (dd, *J* = 8.8, 2.5 Hz, 1H, **H4**), 6.46 (d, *J* = 2.5 Hz, 1H, **H6**), 6.01 (d, *J* = 9.3 Hz, 1H, **H10**), 3.40 (q, *J* = 7.2

Hz, 4H, **H2**), 1.20 (t, *J* = 7.2 Hz, 6H, **H1**). **^{13}C NMR** (126 MHz, $CDCl_3$) δ_C 162.4 (**C11**), 156.7 (**C3**), 150.7 (**C7**), 143.8 (**C9**), 128.8 (**C5**), 109.0 (**C10**), 108.7 (**C8**), 108.3 (**C4**), 97.4 (**C6**), 44.8 (**C2**), 12.4 (**C1**).

Synthesis of 7-(diethylamino)-2-oxo-*2H*-chromene-3-carbaldehyde 5.9.

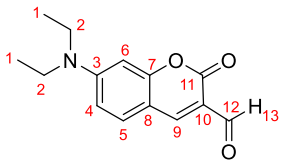

5.9

Under N_2, anhydrous DMF (4.20 g, 57.5 mmol, 4.4 mL, 12.5 equiv.) was dropped into phosphoryl chloride ($POCl_3$) (1.76 g, 11.5 mmol, 1.1 mL, 2.5 equiv.) with stirring for 6 h in an ice bath. The solution of 7-(diethylamino)-*2H*-chromen-2-one **5.8** (1.00 g, 4.6 mmol, 1.0 equiv.) in anhydrous 1,2-dichloroethane (50 mL) was added to the above solution, and the mixture was stirred at 60 ℃ for 12 h. After completing, the mixture was poured into ice water and neutralized with NaOH solution (20%) to pH 7. The formed precipitate was filtered off and washed three times with water. The residue was chromatographed on silica, eluting with ethyl acetate/hexane (1:1, v/v) to form **5.9** as an orange-red solid product (yield: 79%). **^{1}H NMR** (500 MHz, $CDCl_3$) δ_H 10.10 (s, 1H, **H13**), 8.23 (s, 1H, **H9**), 7.39 (d, *J* = 9.0 Hz, 1H, **H5**), 6.63 (dd, *J* = 9.0, 2.5 Hz, 1H, **H4**), 6.47 (d, *J* = 2.5 Hz, 1H, **H6**), 3.46 (q, *J* = 7.2 Hz, 4H, **H2**), 1.24 (t, *J* = 7.1 Hz, 6H, **H1**). **^{13}C NMR** (126 MHz, $CDCl_3$) δ_C 188.0 (**C12**), 162.0 (**C11**), 159.0 (**C3**), 153.6 (**C7**), 145.5 (**C9**), 132.6 (**C5**), 114.5 (**C10**), 110.3 (**C8**), 108.4 (**C4**), 97.3 (**C6**), 45.4 (**C2**), 12.6 (**C1**). **FTIR** (cm^{-1}): υ (C–H st) 2879, υ(C=O st, carboxyl) 1709, υ(C=C st) 1609.

Synthesis of (*E*)-7-(diethylamino)-3-(3-oxo-3-(4-(4,4,5,5-tetramethyl-1,3,2-dioxaborolan-2-yl)phenyl)prop-1-en-1-yl)-*2H*-chromen-2-one 5.10.

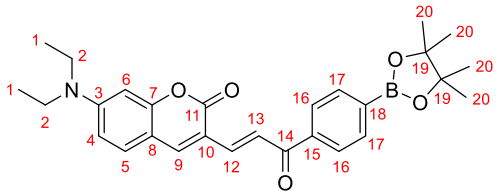

5.10

Compound **5.9** (0.50 g, 2.0 mmol, 1.0 equiv.) and 1-(4-(4,4,5,5-tetramethyl-1,3,2-dioxaborolan-2-yl)phenyl)ethan-1-one (**5.5**, 0.98 g, 4.0 mmol, 2.0 equiv.) were added to 20 mL of the mixed solvent (CH_2Cl_2/anhydrous CH_3CH_2OH=1∶1 (*v*/*v*)), then 10 drops of pyrrolidine were dropped into the above solution. The mixture was stirred at room temperature for 4 d, and the solvent was removed under reduced pressure. The residue was added to 40 mL of hexane/ethyl acetate (*v*/*v*=1∶1) to yield red precipitations. The precipitates were collected on a filter funnel to give compound **5.10** as a bright red solid (yield: 51%). **^{1}H NMR** (500 MHz, DMSO-d_6) δ_H 8.48 (s, 1H, **H9**), 8.03 (d, *J* = 3.2 Hz, 1H, **H18**), 8.00 (d, *J* = 4.4 Hz, 2H, **H17**), 7.85 (d, *J* = 7.7 Hz, 2H, **H16**), 7.67 (d, *J* = 15.4 Hz, 1H, **H12**), 7.50 (d, *J* = 8.9 Hz, 1H, **H5**), 6.80 (dd, *J* = 9.0, 2.4 Hz, 1H, **H4**), 6.60 (d, *J* = 2.3 Hz, 1H, **H6**), 3.48 (q, *J* = 7.1 Hz, 4H, **H2**), 1.32 (s, 12H, **H20**), 1.15 (t, *J* = 7.0 Hz, 6H, **H1**). **^{13}C NMR** (126 MHz, DMSO-d_6) δ_C 189.1 (**C14**), 160.0 (**C11**), 156.5 (**C3**), 152.0 (**C7**), 146.0 (**C12**), 140.0 (**C9**), 139.9 (**C15**), 134.8 (**C17**), 130.7 (**C5**), 127.4 (**C16**), 120.7 (**C10**), 113.1 (**C13**), 110.0 (**C8**), 108.4 (**C4**), 96.3 (**C6**), 84.1 (**C19**), 44.3 (**C2**), 24.7 (**C20**), 12.4 (**C1**), (**C18** bonded to B not observed due to broadening).

(*E*)-(4-(3-(7-(diethylamino)-2-oxo-*2H*-chromen-3-yl)acryloyl)phenyl)boronic acid (AAG113).

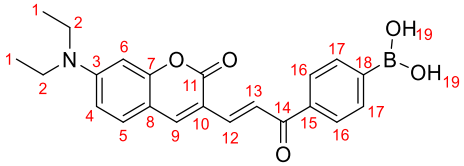

AAG113

The title compound was prepared according to **General Procedure 10**. **(***E***)**-7-(diethylamino)-3-(3-oxo-3-(4-(4,4,5,5-tetramethyl-1,3,2-dioxaborolan-2-yl)phenyl)prop-1-en-1-yl)-*2H*-chromen-2-one **5.10** (150 mg, 0.36 mmol, 1.0 equiv.) was dissolved in THF: water (4:1 mL) (4:1 v/v). Then sodium periodate (231 mg, 1.08 mmol, 3.0 equiv.) was added to the solution and stirred at room temperature for 30 min under an ambient atmosphere. Lastly, HCl (0.2 mL, 1 N) was added to the reaction mixture, which was stirred for 24 h at room temperature. The reaction mixture was concentrated *in vacuo*. Then it was dissolved in EtOAc (30 mL) and washed with water (1 × 8 mL), and brine (1 × 8 mL). The organic fraction was dried ($MgSO_4$), filtered and concentrated *in vacuo* to obtain pure **(***E***)**-(4-(3-(7-(diethylamino)-2-oxo-*2H*-chromen-3-yl)acryloyl)phenyl)boronic acid **AAG113** (yield: 90%). **^{1}H NMR** (400 MHz, DMSO-d_6) δ_H 8.47 (s, 1H, **H9**), 8.29 (s, 2H, **H19**), 8.06 (d, *J* = 19.8 Hz, 1H, **H5**), 8.00 – 7.95 (m, 4H, **H16, H17**), 7.66 (d, *J* = 15.4 Hz, 1H, **H12**), 7.48 (d, *J* = 9.0 Hz, 1H, **H13**), 6.78 (dd, *J* = 9.0, 2.4 Hz, 1H, **H4**), 6.59 (d, *J* = 2.4 Hz, 1H, **H6**), 3.47 (q, *J* = 7.0 Hz, 4H, **H2**), 1.14 (t, *J* = 7.0 Hz, 6H, **H1**). **^{13}C NMR** (101 MHz, DMSO-d_6) δ_C 189.2 (**C14**), 160.0 (**C11**), 156.5 (**C3**, 151.9 (**C7**), 145.5 (**C12**), 139.4 (**C9**), 139.0 (**C15**), 134.4 (**C17**), 130.7 (**C5**), 127.0 (**C16**), 120.9 (**C10**), 113.2 (**C13**), 109.9 (**C8**), 108.4 (**C4**), 96.3 (**C6**), 44.3 (**C2**), 12.4 (**C1**), (**C18** bonded to B not observed due to broadening). **^{11}B NMR** (128 MHz, DMSO-d_6) δ_B 28.4. **LC-MS**: retention time: 8.8 min; **ESI-QTOF HRMS** (m/z): for $[C_{22}H_{23}BNO_5]^+$ $[M+H]^+$: exact mass

calcd.: 392.1669; found: 392.1680. **FTIR** (cm^{-1}): υ(O–H st) 3378, υ(C–H st) 2974, υ(C=O st, carboxyl) 1719, υ(C=C st) 1560.

(4-(((4-methyl-2-oxo-*2H*-chromen-7-yl)oxy)methyl)phenyl)boronic acid AAG143 (5.28).

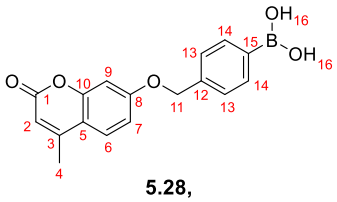

5.28, AAG143

4-Bromomethylphenylboronic acid (297 mg, 1.0 mmol) and 4-methylumbelliferone (4-MU) (194 mg, 1.1 mmol) were dissolved in 5 mL dry dimethylformamide (DMF). Cesium chloride (360 mg, 1.1 mmol) was then added and stirred at 70 °C for 1.5 h. The solution was extracted using CH_2Cl_2 and deionized water after the mixture was cooled to room temperature. The organic layer was collected, dried over anhydrous magnesium sulfate, and concentrated. The crude material was purified using a silica column (hexane: ethyl acetate =5:3) to afford **AAG143** as a white solid (298 mg, 76%). **^{1}H NMR** (400 MHz, DMSO-d_6) δ_H 8.06 (s, 2H, **H16**), 7.81 (d, *J* = 7.8 Hz, 2H, **H14**), 7.67 (d, *J* = 8.6 Hz, 1H, **H9**), 7.42 (d, *J* = 8.0 Hz, 2H, **H13**), 7.06 – 7.01 (m, 2H, **H6, H7**), 6.20 (d, *J* = 1.4 Hz, 1H, **H2**), 5.23 (s, 2H, **H11**), 2.38 (d, *J* = 1.3 Hz, 3H, **H4**). **^{13}C NMR** (101 MHz, DMSO-d_6) δ_C 161.3 (**C8**), 160.1 (**C1**), 154.7 (**C10**), 153.4 (**C3**), 138.0 (**C12**), 134.3 (**C14**), 126.7 (**C13**), 126.5 (**C6**), 113.3 (**C5**), 112.7 (**C2**), 111.2 (**C7**), 101.7 (**C9**), 69.8 (**C11**), 18.1 (**C4**), (**C15** bonded to B not observed due to broadening). **^{11}B NMR** (128 MHz, DMSO-d_6) δ_B 28.9. **LC-MS**: retention time: 7.5 min; **ESI-QTOF HRMS** (m/z): for $[C_{17}H_{16}BO_5]^+$ $[M+H]^+$: exact mass *calcd.*: 311.1091; found: 311.1096. **FTIR** (cm^{-1}): υ(N–H st) 3328, υ(O–H st) 3224, υ(C–H st) 2938, υ(C=O st, carboxyl) 1691, υ(C=C st) 1604.

5.4.7.2.2 9-aminoacridine dyes

Synthesis of *N*-(acridin-9-yl)-2-chloroacetamide 5.35.

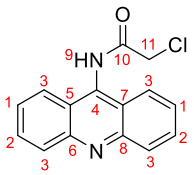

5.35

The title compound was prepared according to **General Procedure 7**. Chloroacetyl chloride (1.15 g, 10.2 mmol, 0.8 mL, 2.0 equiv.) in THF (20 mL) was added dropwise while stirring to a mixture of 9-aminoacridine (1.00 g, 4.0 mmol, 1.0 equiv.) and TEA (1.03 g, 10.2 mmol, 1.4 mL, 2.0 equiv.) in THF at 0 – 5 °C. The reaction mixture was then stirred for 4 h. The solvent was evaporated under reduced pressure. The residue was washed with water to remove TEA.HCl before being dried and recrystallized from ethanol (yield: 59%). **^{1}H NMR** (400 MHz, DMSO-d_6) δ_H 12.19 (s, 1H, **H9**), 8.48 (d, 4H, **H3**), 8.23 (dd, J = 9.0, 6.5 Hz, 2H, **H1**), 7.87 (dd, 2H, **H2**), 4.84 (s, 2H, **H11**). **^{13}C NMR** (101 MHz, DMSO-d_6) δ_C 166.6 (**C10**), 141.5 (**C6, C8**), 135.8 (**C5, C7**), 126.9 (**C3**), 125.9 (**C1**), 121.4 (**C2**), 43.2 (**C11**). **LC-MS**: retention time: 4.7 min; **ESI-QTOF HRMS** (m/z): for $[C_{15}H_{12}ClN_2O]^+$ $[M+H]^+$: exact mass *calcd.*: 271.0638; found: 271.0750.

(4-(((2-(acridin-9-ylamino)-2-oxoethyl)amino)methyl)phenyl)boronic acid 5.37 (AAG103).

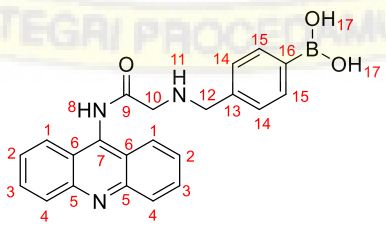

5.37, AAG103

The title compound was prepared according to **General Procedure 9**. *N*-(acridin-9-yl)-2-chloroacetamide **5.35** (536 mg, 1.98 mmol, 1.1 equiv.), (4-(aminomethyl)phenyl)boronic acid (270 mg, 1.80 mmol, 1.0 equiv.), and triethylamine (TEA, 0.5 mL, 3.60 mmol, 2.0 equiv.) were dissolved in acetonitrile (MeCN, 30 mL), stirred, and refluxed for 1 d. The oily residue was dissolved in methylene chloride and washed five times with 10 mL of water. The organic layer was dried over anhydrous Na_2SO_4. The solvent was removed under reduced pressure to obtain the crude product, which was purified by silica gel column chromatography (Hexanes: EtOAc - 9:1) (yield: 22%). **^{1}H NMR** (400 MHz, DMSO-d_6) δ_H 9.56 (s, 1H, **H8**), 9.24 (s, 1H, **H11**), 7.91 (s, 2H, **H17**), 7.58 (d, J = 7.9 Hz, 2H, **H14**), 7.49 (dd, J = 7.9, 1.5 Hz, 2H, **H2**), 7.28 (ddd, J = 8.3, 5.8, 1.5 Hz, 2H, **H3**), 7.02 – 6.95 (m, 4H, **H1, H4**), 6.90 (d, J = 7.7 Hz, 2H, **H15**), 3.23 (s, 2H, **H12**), 2.95 (s, 2H, **H10**). **^{13}C NMR** (101 MHz, DMSO-d_6) δ_C 171.4 (**C9**), 140.3 (**C5**), 138.6 (**C7**), 134.0 (**C13**), 128.7 (**C15**), 128.0 (**C3**), 126.6 (**C14**), 119.5 (**C1**), 119.1 (**C2**), 114.9 (**C6**), 114.1 (**C4**), 53.3 (**C12**), 52.1 (**C10**), (**C16** bonded to B not observed due to broadening). **^{11}B NMR** (128 MHz, DMSO-d_6) δ_B 29.18. **LC-MS**: retention time: 0.5 min; **ESI-QTOF HRMS** (m/z): for $[C_{22}H_{21}BN_3O_3]^+$ $[M+H]^+$: exact mass *calcd.*: 386.1676; found: 386.1683. **FTIR** (cm^{-1}): υ(N–H st) 3328, υ(C-H st, carboxyl) 2976, υ(C=O st, amide) 1673, υ(C=C st and C=N st) 1613–1477.

5.4.7.2.3 8-aminoquinoline dyes

Synthesis of *tert*-butyl (2-oxo-2-(quinolin-8-ylamino)ethyl)carbamate 5.47.

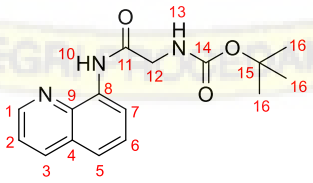

5.47

The title compound was prepared according to **General Procedure 8**. A mixture of 8-aminoquinoline (2.56 g, 17.7 mmol, 1.0 equiv.), DMAP (108 mg, 5 mol%) and *Boc*-Gly-OH, **5.47** (1.22 g, 6.94 mmol, 2.0 equiv.) in dichloromethane (100 mL) were stirred in an ice bath (~0 °C) for 30 minutes, followed by an addition of EDC·HCl (1.33 g, 6.94 mmol, 2.0 equiv.). The reaction mixture was stirred at 0 °C for 2 hours and stirred overnight at room temperature. The crude was extracted with NH_4Cl (aq.) (100 mL). The organic layer was dried over $MgSO_4$, filtered, and concentrated under a vacuum. The crude product was purified through silica-gel column chromatography using hexane/ethyl acetate (3:2) as an eluent to afford tert-butyl (2-oxo-2-(quinolin-8-ylamino)ethyl)carbamate **5.47** as a white solid (4.95 g, 93% yield). The data were consistent with the literature [408]. **^{1}H NMR** (500 MHz, $CDCl_3$) δ_H 10.26 (s, 1H, **H10**), 8.74 (d, *J* = 4.2 Hz, 1H, **H1**), 8.70 (dd, *J* = 6.3, 2.7 Hz, 1H, **H3**), 8.10 (d, *J* = 8.3 Hz, 1H, **H7**), 7.48 (d, *J* = 8.4 Hz, 1H, **H5**), 7.46 (s, 1H, **H2**), 7.40 (dd, *J* = 8.3, 4.2 Hz, 1H, **H6**), 5.51 (s, 1H, **H13**), 4.11 (d, *J* = 5.9 Hz, 2H, **H12**), 1.50 (s, 9H, **H16**). **^{13}C NMR** (126 MHz, $CDCl_3$) δ_C 168.1 (**C11**), 156.1 (**C14**), 148.3 (**C1**), 138.4 (**C9**), 136.4 (**C8**), 133.9 (**C3**), 128.0 (**C4**), 127.3 (**C6**), 122.0 (**C2**), 121.7 (**C5**), 116.8 (**C7**), 80.3 (**C15**), 45.4 (**C12**), 28.4 (**C16**). **LC-MS**: retention time: 8.0 min; **ESI-QTOF HRMS** (m/z): for $[C_{16}H_{20}N_3O_3]^+$ $[M+H]^+$: exact mass *calcd.*: 302.1505; found: 302.1523.

***Boc* deprotection of *tert*-butyl (2-oxo-2-(quinolin-8-ylamino)ethyl)carbamate 5.48**

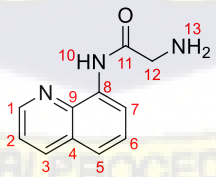

5.48

Based on the procedure by Ear *et al*, *tert*-butyl (2-oxo-2-(quinolin-8-ylamino)ethyl)carbamate **5.47** (3.00 g, 9.96 mmol, 1.0 equiv.) was dissolved in CH_2CI_2 (150 mL) and HCI-dioxane (4

M solution, 20 mL) was added and the mixture was stirred at rt overnight. The reaction was monitored by TLC. After completion of the reaction, the solvents were removed *in vacuo* to obtain the hydrochloride salt of the amine. The residue was dissolved in diethyl ether and extracted with NaOH (2 M) and Et_2O. the organic layer was dried over $MgSO_4$ and the solvent was evaporated under reduced pressure to obtain the product 2-amino-*N*-(quinolin-8-yl)acetamide **5.48** (1.68 g, 84% yield). **^{1}H NMR** (500 MHz, $CDCl_3$) δ_H 11.25 (s, 1H, **H10**), 8.85 (d, 1H, **H1**), 8.82 (dd, 1H, **H3**), 8.14 (d, 1H, **H7**), 7.56 – 7.47 (m, 2H, **H2, H5**), 7.43 (dd, *J* = 8.3, 4.2 Hz, 1H, **H6**), 3.64 (s, 2H, **H13**), 1.81 (s, 2H, **H12**). **^{13}C NMR** (126 MHz, $CDCl_3$) δ_C 171.9 (**C11**), 148.9 (**C1**), 139.3 (**C9**), 136.6 (**C8**), 134.6 (**C3**), 128.4 (**C4**), 127.7 (**C6**), 122.1 (**C2**), 121.9 (**C5**), 116.9 (**C7**), 46.5 (**C12**). **LC-MS**: retention time: 1.1 min; **ESI-QTOF HRMS** (m/z): for $[C_{11}H_{12}N_3O]^+$ $[M+H]^+$: exact mass *calcd.*: 202.0980; found: 202.0997; for $[C_{11}H_{11}N_3ONa]^+$ $[M+Na]^+$: exact mass *calcd.*: 224.0800; found: 224.0804.

Synthesis of *N*-(quinolin-8-yl)-2-((4-(4,4,5,5-tetramethyl-1,3,2-dioxaborolan-2-yl)benzyl)amino)acetamide 5.49.

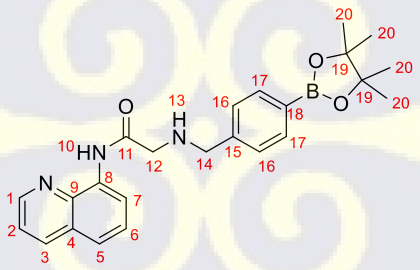

5.49

The title compound was prepared according to **General Procedure 5**. 2-amino-N-(quinolin-8-yl)acetamide **5.48** (0.82 g, 4.07 mmol, 1.2 equiv.) and 4-(4,4,5,5-tetramethyl-1,3,2-dioxaborolan-2-yl)benzaldehyde **5.4** (0.79 g, 3.39 mmol, 1.0 equiv.) were dissolved in 1, 2-dichloroethane (50 mL). The reaction mixture was then charged with sodium triacetoxyborohydride (1.08 g, 1.5 equiv.). The reaction was then stirred under nitrogen for 1

h. After an hour, additional sodium triacetoxyborohydride (0.75 g, 1.0 equiv.) was added to the reaction and the mixture was stirred for a further 1 h. The reaction mixture was then quenched with saturated $NaHCO_3$ solution (100 mL). The aqueous phase was extracted with CH_2Cl_2 (2 x 100 mL), and the combined organics dried over anhydrous $MgSO_4$ and concentrated to dryness *in vacuo* to afford *N*-(quinolin-8-yl)-2-((4-(4,4,5,5-tetramethyl-1,3,2-dioxaborolan-2-yl)benzyl)amino)acetamide **5.49** as a white solid (0.75 g, 53% yield). **^{1}H NMR** (400 MHz, $CDCl_3$) δ_H 11.61 (s, 1H, **H10**), 8.92 (dd, *J* = 4.2, 1.7 Hz, 1H, **H1**), 8.82 (dd, *J* = 7.0, 2.0 Hz, 1H, **H3**), 8.17 (d, *J* = 8.2 Hz, 1H, **H7**), 7.83 (d, *J* = 7.4 Hz, 2H, **H17**), 7.62 (d, *J* = 7.8 Hz, 2H, **H16**), 7.59 – 7.49 (m, 2H, **H2, H5**), 7.48 (dd, *J* = 8.3, 4.3 Hz, 1H, **H6**), 3.94 (s, 2H, **H14**), 3.61 (s, 2H, **H12**), 1.36 (s, 12H, **H20**). **^{13}C NMR** (101 MHz, $CDCl_3$) δ_C 170.4 (**C11**), 148.6 (**C1**), 142.8 (**C9**), 139.1 (**C15**), 136.3 (**C8**), 135.2 (**C17**), 134.5 (**C3**), 128.2 (**C4**), 128.0 (**C16**), 127.5 (**C6**), 121.8 (**C2**), 121.7 (**C5**), 116.6 (**C7**), 83.9 (**C19**), 54.4 (**C14**), 53.4 (**C12**), 25.0 (**C20**), (**C18** bonded to B not observed due to broadening). **^{11}B NMR** (128 MHz, $CDCl_3$) δ_B 31.6. **LC-MS**: retention time: 6.9 min; **ESI-QTOF HRMS** (m/z): for $[C_{24}H_{29}BN_3O_3]^+$ $[M+H]^+$: exact mass *calcd.*: 418.2302; found: 418.2320; for $[C_{24}H_{28}BN_3O_3Na]^+$ $[M+Na]^+$: exact mass *calcd.*: 440.2121; found: 440.2123.

(4-(((2-oxo-2-(quinolin-8-ylamino)ethyl)amino)methyl)phenyl)boronic acid 5.44 (AAG126).

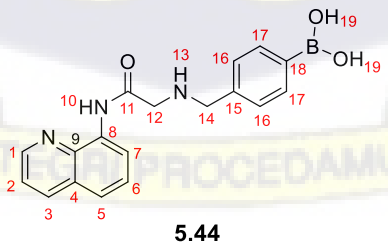

5.44

The title compound was prepared according to **General Procedure 10**. *N*-(quinolin-8-yl)-2-((4-(4,4,5,5-tetramethyl-1,3,2-dioxaborolan-2-yl)benzyl)amino)acetamide **5.49** (150 mg, 0.36

mmol, 1.0 equiv.) was dissolved in THF: water (4:1 mL) (4:1 v/v). Then, sodium periodate (231 mg, 1.08 mmol, 3.0 equiv.) was added to the solution and stirred at room temperature for 30 min under an ambient atmosphere. Lastly, HCl (0.2 mL, 1 N) was added to the reaction mixture, which was stirred for 24 h at room temperature. The reaction mixture was concentrated *in vacuo*. Then it was dissolved in EtOAc (30 mL) and washed with water (1 × 8 mL), and brine (1 × 8 mL). The organic fraction was dried ($MgSO_4$), filtered and concentrated *in vacuo* to obtain pure (4-(((2-oxo-2-(quinolin-8-ylamino)ethyl)amino)methyl)phenyl)boronic acid **5.44 (AAG126)** as a white solid (yield: 76%). **^{1}H NMR** (400 MHz, DMSO-*d*$_6$) δ_H 11.62 (s, 1H, **H10**), 8.98 (dd, *J* = 4.2, 1.7 Hz, 1H, **H1**), 8.71 (dd, *J* = 7.6, 1.4 Hz, 1H, **H3**), 8.43 (dd, *J* = 8.3, 1.7 Hz, 1H, **H7**), 8.00 (s, 2H, **H19**), 7.78 (d, *J* = 8.0 Hz, 2H, **H17**), 7.69 – 7.68 (m, 1H, **H13**), 7.66 (dd, *J* = 2.7, 1.4 Hz, 1H, **H6**), 7.62 – 7.57 (m, 2H, **H2, H6**), 7.53 (d, *J* = 7.9 Hz, 2H, **H16**), 3.82 (s, 2H, **H14**), 3.40 (s, 2H, **H12**). **^{13}C NMR** (101 MHz, DMSO-*d*$_6$) δ_C 170.5 (**C11**), 149.0 (**C1**), 138.1 (**C9**), 136.6 (**C15**), 134.2 (**C8**), 134.1 (**C17**), 133.9 (**C3**), 127.9 (**C4**), 127.4 (**C16**), 127.1 (**C6**), 122.3 (**C2**), 121.7 (**C5**), 115.4 (**C7**), 53.2 (**C14**), 52.6 (**C12**). **^{11}B NMR** (128 MHz, DMSO-*d*$_6$) δ_B 29.09. **LC-MS**: retention time: 5.2 min; **ESI-QTOF HRMS** (m/z): for $[C_{18}H_{19}BN_3O_3]^+$ $[M+H]^+$: exact mass *calcd.*: 336.1519; found: 336.1524. **FTIR** (cm^{-1}): υ (O–H st) 3265, υ(C–H st) 2829, υ(C=O st, amide) 1669, υ(C=C st and C=N st) 1604–1524.

5.4.7.2.4 Fluorescein dyes

3-(3-(3',6'-Dihydroxy-3-oxo-3*H*-spiro[isobenzofuran-1,9'-xanthene]-5-yl)thioureido)phenylboronic acid (40).

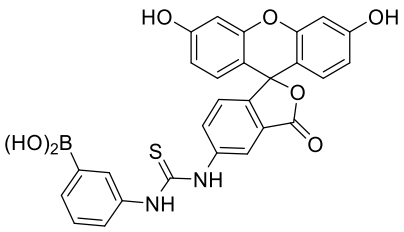

5.65

3-Aminobenzeneboronic acid (0.35 g, 2.57 mmol) was added to a solution of fluorescein isothiocyanate isomer I (1.00 g, 2.57 mmol) in DMF (5 mL). The reaction mixture was stirred at room temperature for 12 h and then poured into methanol (10 mL). The solvents were removed *in vacuo* the residue was then dissolved in the minimum amount of fresh methanol. Chloroform was added and the product was obtained as a bright orange precipitate (920 mg, 68% yield). **LC-MS**: retention time: 7.0 min; **ESI-QTOF HRMS** (m/z): for $[C_{27}H_{20}BN_2O_7S]^+$ $[M+H]^+$: exact mass *calcd.*: 527.1084; found: 527.1123.

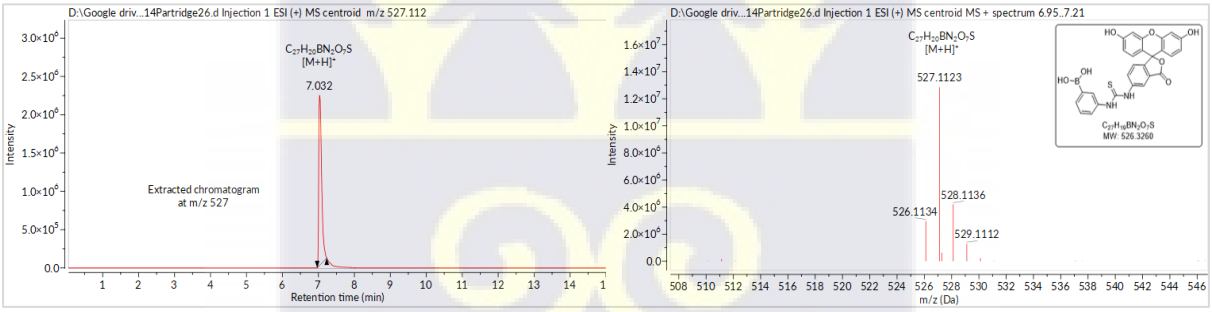

Synthesis of fluorescein methyl ester 5.57

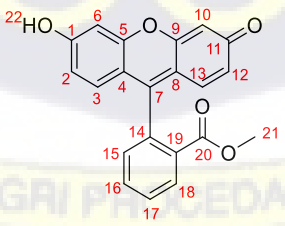

5.57

To fluorescein (1.0 g, 3.1 mmol) methanol solution (10 mL) in a 50 mL round-bottom flask, was added concentrated sulfuric acid (98%) (1 mL). The solution was refluxed and stirred for

4 h. After cooling, excess methanol was removed under reduced pressure and excess water was added to the residue. The red solid formed was washed with water several times and filtered in a vacuum until almost free from fluorescence. After drying in a vacuum, the crude product was redissolved and columned using CH_2Cl_2: methanol (10:1) to obtain red solid fluorescein methyl ester **5.57** (93% yield). **^{1}H NMR** (400 MHz, DMSO-*d*$_6$) δ_H 8.31 (dd, *J* = 7.8, 1.3 Hz, 1H, **H18**), 7.96 (td, *J* = 7.5, 1.4 Hz, 1H, **H16**), 7.88 (td, *J* = 7.7, 1.4 Hz, 1H, **H17**), 7.55 (dd, *J* = 7.5, 1.4 Hz, 1H, **H15**), 7.31 (d, *J* = 9.2 Hz, 2H, **H6, H10**), 7.24 (d, *J* = 2.2 Hz, 2H, **H2, H12**), 7.10 (dd, *J* = 9.2, 2.2 Hz, 2H, **H3, H13**), 3.57 (s, 3H, **H21**). **^{13}C NMR** (101 MHz, DMSO-*d*$_6$) δ_C 171.5, 165.0, 158.1, 133.3, 133.1, 132.3, 130.9, 130.3, 129.1, 120.7, 116.0, 102.5, 52.6. **LC-MS**: retention time: 6.8 min; **ESI-QTOF HRMS** (m/z): for $[C_{21}H_{15}O_5]^+$ $[M+H]^+$: exact mass *calcd.*: 347.0920; found: 347.0934.

Synthesis of fluorescein hydrazide 5.58

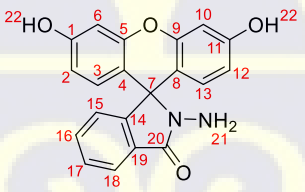

5.58

Fluorescein methyl ester **5.57** (0.40 g) and hydrazine hydrate (0.24 g, 4.8 mmol) were added to methanol (5 mL), refluxed, and stirred for 6 h. After collecting by filtration, the light brown precipitate was washed with a small amount of methanol and water and dried in a vacuum to obtain the crude product. The crude material was pre-adsorbed onto silica and purified by column chromatography using CH_2Cl_2: MeOH (10:1) to obtain pure straw yellow fluorescein hydrazide **5.58** (96% yield). **^{1}H NMR** (400 MHz, DMSO-*d*$_6$) δ_H 9.80 (s, 2H, **H22**), 7.77 (ddd, *J* = 5.2, 2.4, 0.8 Hz, 1H, **H18**), 7.50 – 7.47 (m, 2H, **H16, H17**), 7.00 – 6.98 (m, 1H, **H15**), 6.59 (d, *J* = 2.3 Hz, 2H, **H6, H10**), 6.45 (dd, *J* = 8.6, 2.4 Hz, 2H, **H2, H12**), 6.40 (d, *J* = 8.6 Hz, 2H,

H3, H13), 4.38 (s, 2H, **H21**). **^{13}C NMR** (101 MHz, DMSO-d_6) δ_C 165.5, 158.2, 152.4, 151.5, 132.6, 129.3, 128.4, 128.0, 123.4, 122.4, 112.0, 110.0, 102.4, 64.6. **LC-MS**: retention time: 6.5 min; **ESI-QTOF HRMS** (m/z): for $[C_{20}H_{15}N_2O_4]^+$ $[M+H]^+$: exact mass *calcd.*: 347.1032; found: 347.1028.

(E)-(4-(((3',6'-dihydroxy-3-oxospiro[isoindoline-1,9'-xanthen]-2-yl)imino)methyl)phenyl)boronic acid 5.60 (AAG138).

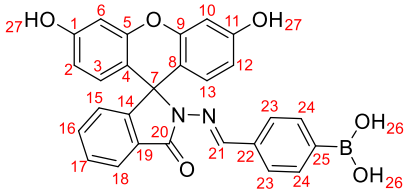

5.60

The title compound was prepared according to the **General procedure 11**. 4-formylphenylboronic acid **5.59** (0.391 mL, 1.77 mmol) was dissolved in 20 mL of a mixture of ethanol/toluene (90:10) and then **5.58** (0.200 g, 0.578 mmol) was added. A Dean-Stark trap was fixed to the reaction vessel and filled with 10 mL of the same solvent mixture for the azeotropic removal of water. The reaction was then allowed to stir for 16 h at 100 °C at which time TLC showed that the starting material had fully reacted. The solvent was removed under vacuum, and the product was recrystallized to obtain the product **5.60** (64% yield). **^{1}H NMR** (400 MHz, DMSO-d_6) δ_H 9.92 (s, 2H, **H27**), 8.96 (s, 1H, **H21**), 8.10 (s, 2H, **H26**), 7.92 (d, J = 7.3 Hz, 1H, **H18**), 7.75 (d, J = 7.9 Hz, 2H, **H24**), 7.68 – 7.55 (m, 2H, **H16, H17**), 7.38 (d, J = 8.0 Hz, 2H, **H23**), 7.14 (d, J = 7.4 Hz, 1H, **H15**), 6.67 (d, J = 2.2 Hz, 2H, **H6, H10**), 6.51 (d, J = 8.6 Hz, 2H, **H2, H12**), 6.46 (dd, J = 8.6, 2.3 Hz, 2H, **H**). **^{13}C NMR** (101 MHz, DMSO-d_6) δ_C 163.7, 158.6, 152.2, 150.5, 148.9, 135.8, 134.5, 134.1, 129.1, 128.9, 128.0, 125.7, 123.8, 123.2, 112.4, 110.1, 102.5, 65.3. **^{11}B NMR** (128 MHz, DMSO-d_6) δ_B 28.1. **LC-MS**: retention time: 7.4 min; **ESI-QTOF HRMS** (m/z): for $[C_{27}H_{20}BN_2O_6]^+$ $[M+H]^+$: exact mass *calcd.*:

479.1414; found: 479.1412. **FTIR** (cm^{-1}): υ (O–H st) 3287, υ(C=O st, amide) 1668, υ(C=C st and C=N st) 1600–1318.

5.4.7.2.5 Rhodamine dyes

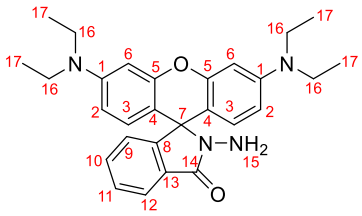

5.69

To a 0.4 g of rhodamine B (I) dissolved in 15 ml of methanol, an excessive hydrazine hydrate (0.5 ml) was added and then the reaction solution was refluxed till the pink colour disappeared. After that, the cooled reaction solution was poured into distilled water and extracted with ethyl acetate (6 × 25 ml). The combined extracts were dried with sodium sulfate anhydrous, filtered, and then evaporated. The solvent yielded 0.27 g (68%) of **5.69**. **^{1}H NMR** (400 MHz, DMSO-*d*$_6$) δ_H 7.79 – 7.73 (m, 1H, **H12**), 7.50 – 7.43 (m, 2H, **H10, H11**), 7.01 – 6.95 (m, 1H, **H9**), 6.37 (t, *J* = 1.4 Hz, 2H, **H2**), 6.33 (d, *J* = 1.4 Hz, 4H, **H3, H6**), 4.26 (s, 2H, **H15**), 3.31 (q, 8H, **H16**), 1.08 (t, *J* = 7.0 Hz, 12H, **H17**). **^{13}C NMR** (101 MHz, DMSO-*d*$_6$) δ_C 165.3 (**C14**), 153.0 (**C5**), 151.9 (**C1**), 148.1 (**C8**), 132.4 (**C10**), 129.6 (**C13**), 128.1 (**C11**), 127.7 (**C3**), 123.5 (**C9**), 122.1 (**C12**), 107.8 (**C4**), 105.5 (**C2**), 97.4 (**C6**), 64.8 (**C7**), 43.7 (**C16**), 12.5 (**C17**). **LC-MS**: retention time: 8.6 min; **ESI-QTOF HRMS** (m/z): for $[C_{28}H_{33}N_4O_2]^+$ $[M+H]^+$: exact mass *calcd.*: 457.2604; found: 457.2596.

(*E*)-(4-(((2-(3',6'-bis(diethylamino)-3-oxospiro[isoindoline-1,9'-xanthen]-2-yl)ethyl)imino)methyl)phenyl)boronic acid 5.70 (AAG145)

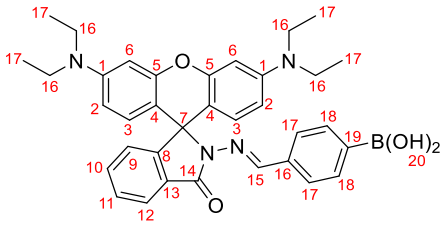

5.70

The title compound was prepared according the **General procedure 11**. 4-formylphenylboronic acid **5.59** (0.391 mL, 1.77 mmol) was dissolved in 20 mL of a mixture of ethanol/toluene (90:10) and then **5.69** (0.200 g, 0.578 mmol) was added. A Dean-Stark trap was fixed to the reaction vessel and filled with 10 mL of the same solvent mixture for the azeotropic removal of water. The reaction was then allowed to stir for 16 h at 100 °C at which time TLC showed that the starting material **5.69** had fully reacted. The solvent was removed under vacuum, and the product was recrystallized to obtain product **5.70** (73% yield). **^{1}H NMR** (400 MHz, $CDCl_3$) δ_H 8.07 (d, *J* = 7.8 Hz, 1H, **H12**), 8.00 (d, *J* = 6.4 Hz, 1H, **H10**), 7.74 (d, *J* = 7.8 Hz, 1H, **H11**), 7.65 – 7.62 (m, 3H, **H9, H20**), 7.56 – 7.53 (d, *J* = 7.1 Hz, 2H, **H18**), 7.47 (d, *J* = 7.1 Hz, 2H, **H17**), 7.14 – 7.09 (m, 1H, **H15**), 6.52 (dd, *J* = 8.9, 6.5 Hz, 2H, **H2**), 6.46 (dd, *J* = 14.9, 2.6 Hz, 2H, **H3**), 6.24 (ddd, *J* = 9.1, 7.2, 2.6 Hz, 2H, **H6**), 3.31 (q, *J* = 9.0, 8.1 Hz, 8H, **H16**), 1.15 (t, *J* = 6.6 Hz, 12H, **H17**). **^{13}C NMR** (101 MHz, $CDCl_3$) δ_C 165.3, 153.4, 153.2, 152.0, 149.1, 149.1, 147.1, 137.5, 135.63, 134.0, 133.6, 133.4, 128.4, 128.1, 127.0, 124.0, 123.6, 108.2, 106.0, 98.0, 58.6, 44.5, 12.7. **^{11}B NMR** (128 MHz, $CDCl_3$) δ_B 29.9. **LC-MS**: retention time: 10.2 min; **ESI-QTOF HRMS** (m/z): for $[C_{35}H_{38}BN_4O_4]^+$ $[M+H]^+$: exact mass *calcd.*: 589.2986; found: 589.2994. **FTIR** (cm^{-1}): υ (O–H st) 3310, υ(C–H st) 2893, υ(C=O st, amide) 1696, υ(C=C st and C=N st) 1614–1306.

5.4.7.2.6 BODIPY dyes

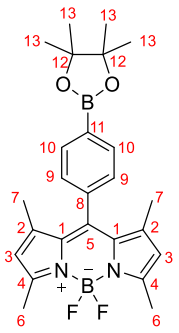

5.81

Synthesis of protected BODIPY dye 5.81.

A mixture of a protected 4-formylphenylboronic acid **5.4** (1.50 g, 6.5 mmol, 1.0 equiv.) and 2,4-dimethyl-*1H*-pyrrole (1.24 g, 13.0 mmol, 2.0 equiv.) was dissolved in anhydrous DCM (40 mL) under nitrogen. TFA (0.4 mL) was added to the mixture and stirred at room temperature for 3 h. The consumption of the aldehyde was monitored by TLC. A solution of *p*-chloranil in DCM (1.92 g, 7.8 mmol, 1.2 equiv.) was added at 0 °C and stirred for 30 min. TEA (3.95 g, 5.4 mL, 39.0 mmol, 6.0 equiv.) was added at 0 °C and stirred for a further 30 min. Thereafter, $BF_3{\cdot}OEt_2$ (9.23 g, 8.0 mL, 65.0 mmol, 10.0 equiv.) was added dropwise, and the reaction was stirred for 12 h at room temperature. The mixture was evaporated under reduced pressure to obtain the crude product. The crude product was purified by silica gel column using hexane/ethyl acetate (1:0→ 9:1) to obtain the desired product in 47% yield. **^{1}H NMR** (500 MHz, $CDCl_3$) δ_H 7.90 (d, *J* = 7.5 Hz, 2H, **H10**), 7.29 (d, *J* = 7.5 Hz, 2H, **H9**), 5.97 (s, 2H, **H3**), 2.55 (s, 6H, **H6**), 1.38 (s, 12H, **H13**), 1.36 (s, 6H, **H7**). **^{13}C NMR** (126 MHz, $CDCl_3$) δ_C 155.6 (**C4**), 143.4 (**C1**), 141.8 (**C2**), 138.0 (**C8**), 135.5 (**C10**), 131.4 (**C5**), 127.5 (**C9**), 121.3 (**C3**), 84.3 (**C12**), 29.8 (**C7**), 25.1 (**C13**), 14.7 (**C6**), (**C11** bonded to B not observed due to broadening). **LC-MS**: retention time: 12.4 min; **ESI-QTOF HRMS** (m/z): for $[C_{25}H_{31}B_2F_2N_2O_2]^+$ $[M+H]^+$: exact mass *calcd.*: 451.2540; found: 451.2555.

Deprotection of protected BODIPY dye 5.81 to obtain 5.83 (AAG156)

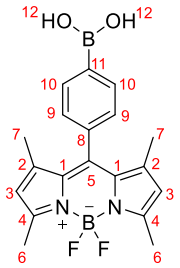

5.83

The title compound was prepared according to **General Procedure 10**. BODIPY dye **5.81** (150 mg, 0.36 mmol, 1.0 equiv.) was dissolved in THF: water (4:1 mL) (4:1 v/v). Then sodium periodate (231 mg, 1.08 mmol, 3.0 equiv.) was added to the solution and stirred at room temperature for 30 min under an ambient atmosphere. Lastly, HCl (0.2 mL, 1 N) was added to the reaction mixture, which was stirred for 24 h at room temperature. The reaction mixture was concentrated *in vacuo*. Then it was dissolved in EtOAc (30 mL) and washed with water (1 × 8 mL), and brine (1 × 8 mL). The organic fraction was dried ($MgSO_4$), and the solids were removed by gravity filtration. The crude product was preabsorbed onto 5 mL of silica and dried under vacuum. Flash chromatography (1:3 hexanes/EtOAc) provided a pure deprotected BODIPY dye **5.83** (89% yield) as a reddish-orange powder as the solvent removal. **^{1}H NMR** (400 MHz, DMSO-d_6) δ_H 8.25 (s, 2H, **H12**), 7.96 (d, J = 7.9 Hz, 2H, **H10**), 7.33 (d, J = 7.9 Hz, 2H, **H9**), 6.17 (s, 2H, **H3**), 2.44 (s, 6H, **H6**), 1.32 (s, 6H, **H7**). **^{13}C NMR** (101 MHz, DMSO-d_6) δ_C 154.8, 150.9, 142.8, 142.2, 135.7, 134.9, 130.6, 129.2, 126.7, 121.4, 113.8, 101.6, 14.3, 14.0. **LC-MS**: retention time: 9.0 min; **ESI-QTOF HRMS** (m/z): for $[C_{19}H_{21}B_2F_2N_2O_2]^+$ $[M+H]^+$: exact mass *calcd.*: 369.1757; found: 369.1763. **FTIR** (cm^{-1}): υ (O–H st) 3201, υ(C–H st) 2916, υ(C=C st and C=N st) 1545–1454.

5.4.7.2.7 Azo dyes

Synthesis of (2-((m-tolylamino)methyl)phenyl)boronic acid 5.86.

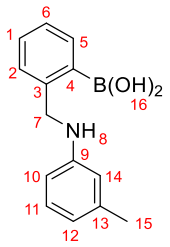

5.86

The title compound was prepared according to **General Procedure 5**. 2-formylbenzeneboronic acid (3.00 g, 20.1 mmol, 1.0 equiv.) and m-toluidine (2.7 mL, 24.1 mmol, 1.1 equiv.) were dissolved in 1, 2-dichloroethane (50 mL). The reaction mixture was then charged with sodium triacetoxyborohydride (6.39 g, 1.5 equiv.). The reaction was then stirred under nitrogen for 1 h. After an hour, additional sodium triacetoxyborohydride (4.26 g, 1.0 equiv.) was added to the reaction and stirred further for another 1 h. The reaction mixture was then quenched with saturated $NaHCO_3$ solution (100 mL). The aqueous phase was extracted with CH_2Cl_2 (2 × 100 mL), and the combined organics dried over anhydrous $MgSO_4$ and concentrated to dryness *in vacuo* to afford (2-((m-tolylamino)methyl)phenyl)boronic acid **5.86** as a cream coloured solid (3.64 g, 75% yield). The material was used without further purification. **^{1}H NMR** (400 MHz, $CDCl_3$) δ_H 7.74 (dd, *J* = 7.6, 1.5 Hz, 1H, **H5**), 7.45 (m, 2H, **H2**, **H12**), 7.38 – 7.32 (m, 3H, **H6, H16**), 7.02 – 6.97 (m, 2H, **H1, H11**), 6.66 (m, 2H, **H10, H14**), 6.52 (s, 1H, **H8**), 4.36 (s, 2H, **H7**), 2.14 (s, 3H, **H15**). **LC-MS**: retention time: 6.4 min; **ESI-QTOF HRMS** (m/z): for $[C_{14}H_{17}BNO_2]^+$ $[M+H]^+$: exact mass *calcd.*: 242.1352; found: 242.1354.

(*E*)-(2-(((3-methyl-4-((4-nitrophenyl)diazenyl)phenyl)amino)methyl)phenyl)boronic acid 5.87.

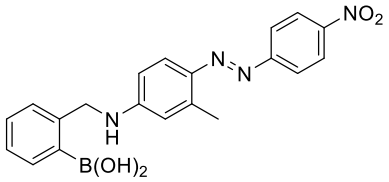

5.87

4-nitroaniline (504 mg, 3.64 mmol, 1.1 equiv.) was mixed in water (2 mL), methanol (2 mL) and hydrochloric acid (2 mL, 5.0 M) and then cooled to 0–5 °C on an ice-bath. A chilled solution of sodium nitrite (186 mg, 2.69 mmol, 1.3 equiv.) was added dropwise. Excess nitrite was destroyed by the addition of sulfamic acid after stirring for 5 minutes. (2-((m-tolylamino)methyl)phenyl)boronic acid (500 mg, 2.07 mmol, 1.0 equiv.) was dissolved in methanol (3 mL) and dilute hydrochloric acid (2 mL, 1 M) then added dropwise to the reaction mixture, which quickly turned red. Sodium acetate was added to raise the pH of the solution to 4 and this was then left to stir at 0–5 °C for 3 hours. Sodium hydroxide (2 M) was slowly added to raise the pH to 7. The resulting precipitate was collected by suction filtration and dried in a desiccator overnight to afford product **5.87** as a dark red solid (44% yield). **^{1}H NMR** (400 MHz, DMSO-*d*$_6$) δ_H 9.86 (s, 1H), 8.39 (d, *J* = 8.9 Hz, 2H), 8.33 (d, *J* = 8.9 Hz, 1H), 8.18 (s, 1H), 8.01 (d, *J* = 8.9 Hz, 2H), 7.92 – 7.85 (m, 2H), 7.75 (d, *J* = 9.1 Hz, 1H), 7.58 – 7.53 (m, 1H), 7.47 (s, 2H, 2H), 7.37 – 7.30 (m, 1H), 4.63 (s, 2H), 2.73 (s, 3H, 3H). **^{13}C NMR** (101 MHz, DMSO-*d*$_6$) δ_C 156.8, 156.1, 153.6, 150.5, 148.3, 147.5, 146.5, 144.1, 142.6, 141.6, 141.5, 133.7, 130.4, 130.3, 129.0, 125.0, 123.0, 122.5, 122.4, 118.7, 116.3, 116.1, 52.7, 17.7. **^{11}B NMR** (128 MHz, DMSO-*d*$_6$) δ_B 32.0. **LC-MS**: retention time: 9.9 min; **ESI-QTOF HRMS** (m/z): for $[C_{20}H_{20}BN_4O_4]^+$ $[M+H]^+$: exact mass *calcd.*: 391.1578; found: 391.1587.

(*E*)-4-((4-((2-boronobenzyl)amino)-2-methylphenyl)diazenyl)benzoic acid 5.88.

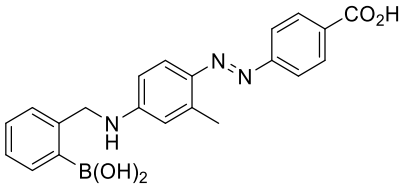

5.88

The above procedure was repeated using 4-aminobenzoic acid (0.11 g, 0.83 mmol) instead of 4-nitroaniline. All other reagents were used in the same mole ratios, to afford **5.88** as an orange–red solid (62% yield). **^{1}H NMR** (400 MHz, DMSO-*d*$_6$) δ_H 13.09 (s, 1H), 9.79 (s, 1H), 8.15 – 8.08 (m, 2H), 8.05 (dd, *J* = 8.6, 1.9 Hz, 1H), 7.90 (dd, *J* = 8.0, 6.3 Hz, 3H), 7.79 (dd, *J* = 8.5, 1.7 Hz, 1H), 7.72 (d, *J* = 9.1 Hz, 1H), 7.68 (dd, *J* = 9.1, 2.3 Hz, 1H), 7.56 (d, *J* = 2.4 Hz, 1H), 7.48 (s, 2H), 7.35 (dd, *J* = 7.8, 4.3 Hz, 1H), 4.64 (s, 2H), 2.73 (s, 3H). **^{13}C NMR** (101 MHz, DMSO-*d*$_6$) δ_C 166.9, 155.1, 149.8, 148.4, 144.0, 140.6, 131.6, 130.6, 130.5, 130.4, 130.2, 122.5, 122.2, 118.8, 116.1, 116.0, 52.7, 48.6, 30.4, 17.7. **^{11}B NMR** (128 MHz, DMSO-*d*$_6$) δ_B 30.4. **LC-MS**: retention time: 8.2 min; **ESI-QTOF HRMS** (m/z): for $[C_{21}H_{21}BN_3O_4]^+$ $[M+H]^+$: exact mass *calcd.*: 390.1625; found: 390.1634. **FTIR** (cm^{-1}): υ(O–H st) 3442, υ(C–H st) 2925, υ(C=O st, carboxyl) 1677, υ(C=C st and C=N st) 1677–1600.

(*E*)-(2-(((4-((4-methoxyphenyl)diazenyl)-3-methylphenyl)amino)methyl)phenyl)boronic acid 5.89.

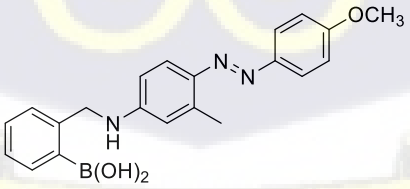

5.89

The previous experiment was repeated using *p*-anisidine (0.61 g, 4.98 mmol, 6 equiv.) instead of 4-aminobenzoic acid. Purification was performed by washing the product (in dichloromethane) with 10% sodium hydrogen carbonate solution (w/w) to remove residual

acetic acid, to yield **5.89** as an orange–brown solid (56% yield). **^{1}H NMR** (400 MHz, DMSO-d_6) δ_H 9.67 (s, 1H), 7.89 (d, J = 7.3 Hz, 1H), 7.84 (d, J = 8.9 Hz, 2H), 7.74 – 7.71 (m, 1H), 7.65 – 7.62 (m, 2H), 7.53 (d, J = 2.0 Hz, 1H), 7.48 – 7.45 (m, 2H), 7.34 (ddt, J = 9.2, 6.6, 3.2 Hz, 1H), 7.10 (d, J = 9.0 Hz, 2H), 7.08 – 7.02 (m, 1H), 4.61 (s, 2H), 3.85 (s, 3H), 2.69 (s, 3H). **^{13}C NMR** (101 MHz, DMSO-d_6) δ_C 161.1, 148.4, 148.3, 146.9, 143.8, 138.9, 130.3, 130.0, 126.6, 126.4, 124.0, 123.4, 123.4, 122.5, 118.8, 115.9, 115.7, 114.5, 114.3, 55.5, 52.7, 17.7. **^{11}B NMR** (128 MHz, DMSO-d_6) δ_B 29.9. **LC-MS**: retention time: 9.8 min; **ESI-QTOF HRMS** (m/z): for $[C_{21}H_{23}BN_3O_3]^+$ $[M+H]^+$: exact mass *calcd.*: 376.1832; found: 376.1836.

(*E*)-3-((4-((2-boronobenzyl)amino)-2-methylphenyl)diazenyl)benzoic acid 5.90.

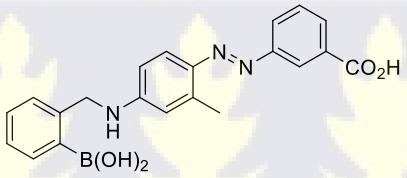

5.90

The previous experiment was repeated using 3-aminobenzoic acid (499 mg, 3.64 mmol) instead of p-anisidine. All other reagents were used in the same mole ratios, to afford **5.90** as a red solid (25% yield). **^{1}H NMR** (400 MHz, DMSO-d_6) δ_H 13.20 (s, 1H), 9.77 (s, 1H), 8.34 (t, J = 1.8 Hz, 1H), 8.25 – 8.16 (m, 1H), 8.10 – 8.03 (m, 3H), 7.89 (d, J = 7.3 Hz, 1H), 7.72 (d, J = 9.1 Hz, 2H), 7.70 – 7.66 (m, 2H), 7.56 (d, J = 2.4 Hz, 1H), 7.48 (s, 2H), 4.64 (s, 2H), 2.73 (s, 3H). **LC-MS**: retention time: 8.5 min; **ESI-QTOF HRMS** (m/z): for $[C_{21}H_{21}BN_3O_4]^+$ $[M+H]^+$: exact mass *calcd.*: 390.1625; found: 390.1630.

5.4.7.2.8 Sudan I dyes boronic acid AAG107R

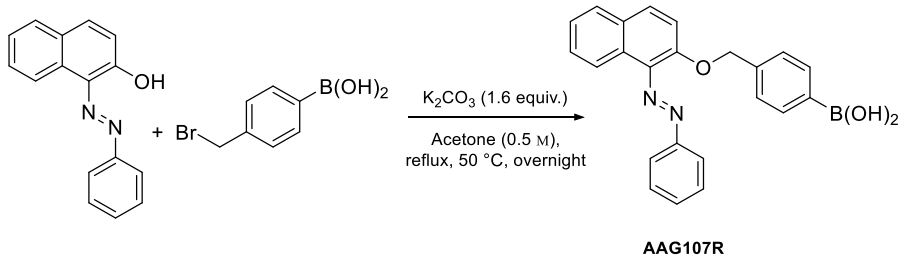

AAG107R

To a heated solution (50 °C) of Sudan I (347 mg, 1.39 mmol, 1.2 equiv.) in acetone (20 mL), potassium carbonate, K_2CO_3 (128 mg, 0.93 mmol, 0.80 equiv.) and 4-(bromomethyl)phenylboronic acid (250 mg, 1.16 mmol, 1.0 equiv.) were added. After 4 h of stirring and heating, additional potassium carbonate, K_2CO_3 (128 mg, 0.93 mmol, 0.80 equiv.) was added, and the suspension was stirred overnight. Finally, the reaction mixture was diluted with EtOAc and the organic layer was washed with 1 M hydrochloric acid (2 × 10 mL) and brine (20 mL), dried over Na_2SO_4, and concentrated *in vacuo*. The resulting solid was further purified using silica gel chromatography affording a pure product.

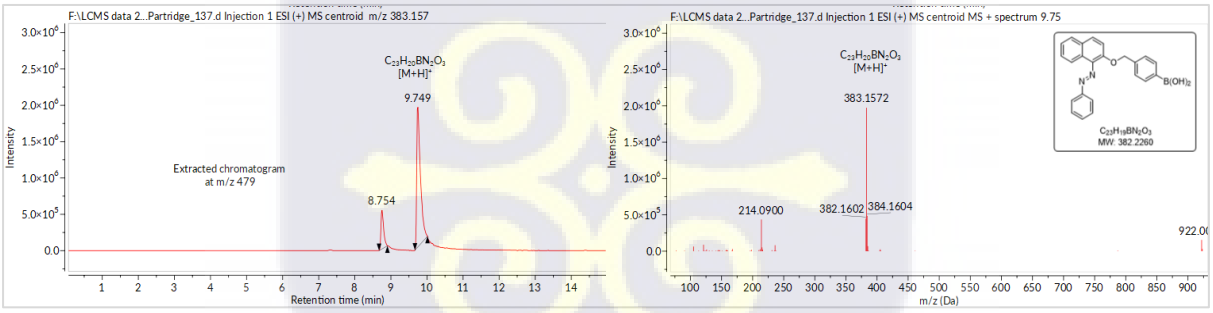

5.4.8 Measurements of photophysical properties of synthesized compounds

Photophysical quantities such as absorption maxima (λ_{abs}^{max}), emission maxima (λ_{em}^{max}), Stokes shift ($\Delta\lambda$), molar extinction coefficient (ε), fluorescence quantum yield (Φ_F), and brightness were determined from absorption and emission data. Photophysical measurements were done at ambient temperature (25 °C). All solvents and reagents were of analytical grade and used as received without further purification. The fluorescent arylboronic acid

chemosensors were synthesized, purified, and fully characterised using various spectroscopic and other techniques as described in previous sections.

5.4.8.1 UV-VIS absorption spectra

Stock solutions of the various synthesized fluorescent arylboronic acid dyes were accurately prepared by weighing masses in known volumes of appropriate organic solvents. Five different concentrations were prepared from the stock solutions by serial dilution for each sample and their respective UV-vis absorption spectra were recorded between 200 and 800 nm by transferring the various solutions into quartz cuvettes of 1-cm optical path length using a Shimadzu UV-1800 spectrophotometer. Using the molar mass of the arylboronic acid dyes, the molar extinction coefficients (ε) were determined at the respective maximum absorption wavelength of the different dyes. ε was computed using the Beer-Lambert law ($A = \varepsilon cl$) with solutions of known concentrations, where: A is absorbance; ε the extinction coefficient for the dye; c is the sample concentration; l is the pathlength of the sample cuvette.

5.4.8.2 Fluorescence emission and excitation spectra

Fluorescence spectra of the synthesized compounds were acquired using a Shimadzu RF-6000 spectrofluorometer (Shimadzu, Kyoto, Japan). Emission spectra were recorded at room temperature with excitation wavelengths set at the λ_{abs}^{max} of the respective dyes and emission range 250–800 nm. The excitation and emission slit widths were set at 5 nm.

5.4.8.3 Fluorescence Quantum Yield Determination

Fluorescence quantum yields of the synthesized fluorescent arylboronic acid chemosensor dyes were determined by the relative comparison procedure [409, 410], using either rhodamine B (Φ_F = 0.70 in ethanol)[411] or quinine sulfate (Φ_F = 0.51 in 0.05 M H_2SO_4) [307, 412]. Quantum yield measurements require low absorbance (optical density), typically below 0.1 at the longest wavelength absorption maxima. Therefore, all solutions of all synthesized

arylboronic dyes were prepared at low concentrations to limit the absorbance values to less than 0.1 in order to avoid any complications with dimer or aggregate formation [413], reduce or minimize possible non-linear effects arising from inner filter (reabsorption effects) [410, 413], eliminate concentration quenching effects, internal filter effects and errors arising from uneven distribution of the excited species in the detected volume [411], which altogether may otherwise skew the resulting quantum yield.

Five different solutions with increasing concentrations of each of the synthesized compounds and the reference standards (rhodamine B and quinine sulfate) were prepared in different solutions and the absorbance of each solution was determined to be between 0.01 – 0.1 in 1 cm optical path length cuvette using a Shimadzu UV-1800 Spectrophotometer. Fluorescence spectra and the integrated fluorescence intensities for varying concentrations of solutions were measured using a Shimadzu RF-6000 spectrofluorometer. For each solution, graphs of the integrated fluorescence intensities as a function of the solution absorption were plotted in each case for both the synthesized dye and the reference standard (either rhodamine B or quinine sulfate). The resulting data points were fitted with linear plots and the slopes were calculated. The quantum yield (Φ_F) is calculated using the slope of the line determined from the plot of the absorbance against the integrated fluorescence intensities. In this case, the quantum yield of the unknown sample can be calculated using the equation:

$$\Phi_{F,S} = \Phi_{F,R}\left(\frac{m_S}{m_R}\right)\left(\frac{\eta_S^2}{\eta_R^2}\right)$$

where: m is the slope of the line obtained from the plot of the integrated fluorescence intensity vs. absorbance, η is the refractive index of solvent and the subscripts $_R$ and $_S$ refer to the reference and unknown sample respectively; Φ_S and Φ_R are the fluorescence quantum yield of the sample and that of the standard respectively. The quantum yields were corrected for the

differing refractive index of the solvent used for the sample and reference. Refractive indices (25 °C) were taken to be 1.3326, 1.3593, and 1.4793 for water, ethanol, and DMSO respectively [390]. In instances where the same solvent was used for both reference and unknown sample as a solvent, $\left(\eta_S^2 / \eta_R^2\right)$ will be 1, so the fluorescence quantum yield of the unknown (Φ_S) was obtained directly from the quotient of the two slopes. The reference standard should match the absorption and the emission wavelength region of the sample. For this reason, Rhodamine B and Quinine sulfate were chosen as reference standards for the various dyes.

5.5 Conclusion

This chapter has demonstrated synthetic approaches for the synthesis of a library of fluorescent arylboronic acid chemosensor dyes by exploiting certain dyes (fluorophores) of interest with beneficial photophysical characteristics. All the synthesized molecules have a boronic acid motif (recognition moiety) that is linked to a fluorescent dye which serves as a signalling moiety for possible selective complexation with the 1,3-diol moieties of mycolactone. All the synthesized dyes have been completely characterized using a set of complementary spectrometric and spectroscopic techniques such as NMR, LC-MS, FT-IR, and X-ray crystallography. The selectivity of boronic acid units for 1,2- and 1,3- diol was established *via* proof-of-concept studies using commonly available diols and boronic acid. Following the successful characterization of the synthesized dyes, their photophysical properties were determined. Likewise, their performance on TLC were also investigated in comparison to BA and BA18. The findings of the study indicated that the synthesized boronic acids were able to detect mycolactone both in solution and on TLC plates selectively and sensitively. From the results, it can be concluded that all the synthesized arylboronic acids are selective for the detection of mycolactone and AAG113 gives the best outcomes in terms of fluorescence on TLC plates.

CHAPTER SIX

6 Conclusion and Future Direction

6.1 Conclusion

The main theme of the thesis focuses on developing fluorescent boronic acid compounds for the molecular recognition of mycolactone, the toxin responsible for causing Buruli ulcer using the f-TLC technique. The underpinning principle relies on the recognition abilities of boronic acid units for 1,3-diols motifs that are characteristic of the mycolactone structure. Therefore, the strategy was to find boronic acid compounds that were either available commercially or *via* synthesis that could effectively detect mycolactone on TLC plates with high sensitivity and specificity.

Chapter One introduces the f-TLC method for the detection of mycolactone and progress made so far in using the method as a rapid diagnostic tool. For instance, an earlier evaluation study of the f-TLC on clinical samples using 2-naphthylboronic acid as a derivatizing agent was conducted by our group. The method is rapid and offers promising sensitivity and specificity values of 66.4% and 88.5% respectively, nevertheless, it suffers background interferences from co-extracted human tissue lipids. In addition, the read-out has not been automated and leads to subjective interpretations of results.

Chapter Two reviews relevant literature on the subject matter including the etymology of the disease, *Mycobacterium ulcerans*, and the biosynthesis and chemical synthesis of mycolactone.

The following chapters discusses attempts made to address the challenges. In Chapter Three of the thesis, a series of 27 commercially available boronic acids were screened as potential alternative fluorogenic reagents to the original 2-naphthylboronic acid (BA). The results were promising with BA18 emerging as the most outstanding candidate. This was confirmed in

clinical samples where myco-BA18 adducts offered superior fluorescence band intensities when coupled to mycolactone on TLC as compared to the original boronic acid.

In Chapter Four, High-Performance Thin layer chromatography (HPTLC) was successfully employed as an automated approach for the quantitative detection of mycolactone based on the working principles of the f-TLC method developed by Kishi and co-workers. Acceptable performance and automation have been achieved using the HPTLC method. A solution of mycolactone was successfully detected on HPTLC Silica gel 60 with an R_F value of 0.32 with a limit of detection (LOD) and limit of quantification (LOQ) for mycolactone estimated to be 6.6 and 22 ng/spot respectively.

In Chapter Five, the selectivity of boronic acid units for 1,2- and 1,3- diol was established *via* a proof-of-concept studies using commonly available diols and 4-tolylboronic acid. Next, design, synthesis, purification, and characterization of a library of fluorescent arylboronic acid was undertaken and the prepared compounds were employed as mycolactone sensors. The synthesized dyes were evaluated for the detection of mycolactone using UV-vis and fluorescence experiments. The synthesized boronic acids were able to detect mycolactone both in solution and on TLC plates selectively and sensitively with AAG113 emerging the best in terms of fluorescence on TLC plates.

6.2 Future Direction

The findings of the research did answer some of the questions but not all. For instance, having identified BA18 and AAG113 as the commercial and synthetic candidates with better performance on TLC that could potentially replace the original BA, there is a need for further investigations of these boronic acids using clinical samples to determine the sensitivity and specificity relative to a gold standard method. Secondly, even though it was demonstrated that mycolactone could be detected and quantified using the HPTLC, the method needs to be

evaluated and validated further using clinical samples together with BA18 and AAG113 as derivatizing reagents. Also, due to matrix interferences from co-extracted human tissues, it was observed that there were significantly more bands with varying R_F in the BU and non-BU clinical samples that were analyzed than anticipated. This shows that the sample preparation process used to get the clinical samples was only, at best, able to concentrate the sample without getting rid of the matrix and so it did not address the problem of background interferences. The clinical performance of the HPTLC method should thus be further assessed using clinical samples by investigating new, affordable sample preparation protocols including pretreatment, extraction, and clean-up procedures such as liquid-liquid extraction (LLE) and solid-phase extraction (SPE) techniques which can decongest mycolactone from clinical samples with the goal of (1) obtaining satisfactory mycolactone recoveries from clinical samples, and (2) eliminating as much matrix interferences from co-extracted human tissues as possible and hence reaching the low detection limits required for this study. Additionally, it is necessary to develop standard operating procedures (SOPs) that provide in-depth explanations of all relevant parameters such as sample preparation, plate setup and handling, sample application, chamber geometry and saturation, humidity control, developing distance, derivatization procedures and observations, documentation (as electronic images) and chromatogram evaluation.

BIBLIOGRAPHY

1. Asiedu K, Raviglione MC, Scherpbier R. Buruli ulcer: Mycobacterium ulcerans infection. World Health Organization; 2000.
2. Bayley AC. Buruli ulcer in Ghana. Br Med J. 1971;2(5758):401-402.
3. Connor DH, Lunn HF. Mycobacterium ulcerans infection (with comments on pathogenesis). Int J Lepr. 1965;33(3):Suppl:698-709.
4. Hayman J. Mycobacterium ulcerans infection. Lancet. 1991;337(8733):124.
5. Demangel C, Stinear TP, Cole ST. Buruli ulcer: reductive evolution enhances pathogenicity of Mycobacterium ulcerans. Nature Reviews Microbiology. 2009;7(1):50-60.
6. Wilson M, Boakye D, Mosi L, Asiedu K. In the case of transmission of Mycobacterium ulcerans in Buruli ulcer disease Acanthamoeba species stand accused. Ghana medical journal. 2011;45(1).
7. Leão SC, Romano MI, Garcia MJ. Tuberculosis, Leprosy, and Other Mycobacterioses. Bioinformatics in Tropical Disease Research: A Practical and Case-Study Approach [Internet]: National Center for Biotechnology Information (US); 2007.
8. MacCallum P, Tolhurst JC, Buckle G. A new mycobacterial infection in man. J Pathol Bacteriol. 1948;60.
9. WHO. Global Buruli ulcer Initiative (GBUI)). 2017.
10. Gunawardana G, Chatterjee D, George KM, Brennan P, Whittern D, Small PLC. Characterization of Novel Macrolide Toxins, Mycolactones A and B, from a Human Pathogen, Mycobacterium ulcerans. Journal of the American Chemical Society. 1999;121(25):6092-6093.
11. George KM, Chatterjee D, Gunawardana G, Welty D, Hayman J, Lee R, et al. Mycolactone: a polyketide toxin from Mycobacterium ulcerans required for virulence. Science. 1999;283(5403):854-857.
12. George KM, Barker LP, Welty DM, Small P. Partial purification and characterization of biological effects of a lipid toxin produced by Mycobacterium ulcerans. Infection and immunity. 1998;66(2):587-593.
13. Adusumilli S, Mve-Obiang A, Sparer T. Mycobacterium ulcerans toxic macrolide, mycolactone, modulates the host immune response and cellular location of M. ulcerans in vitro and in vivo. Cell Microbiol. 2005;7.
14. Read JK, Heggie CM, Meyers WM, Connor DH. Cytotoxic activity of Mycobacterium ulcerans. Infection and Immunity. 1974;9(6):1114-1122.
15. George KM, Pascopella L, Welty DM. A Mycobacterium ulcerans toxin, mycolactone, causes apoptosis in guinea pig ulcers and tissue culture cells. Infect Immunol. 2000;68.
16. Sarfo FS, Phillips RO, Zhang J, Abass MK, Abotsi J, Amoako YA, et al. Kinetics of mycolactone in human subcutaneous tissue during antibiotic therapy for Mycobacterium ulcerans disease. BMC Infect Dis. 2014;14:202.
17. Coutanceau E, Marsollier L, Brosch R, Perret E, Goossens P, Tanguy M, et al. Modulation of the host immune response by a transient intracellular stage of Mycobacterium ulcerans: the contribution of endogenous mycolactone toxin. Cell Microbiol. 2005;7(8):1187-1196.
18. Krieg RE, Hockmeyer WT, Connor DH. Toxin of Mycobacterium ulcerans: production and effects in guinea pig skin. Archives of dermatology. 1974;110(5):783-788.
19. Demangel C, High S. Sec61 blockade by mycolactone: A central mechanism in Buruli ulcer disease. Biol Cell. 2018;110(11):237-248.
20. Silva MT, Portaels F, Pedrosa J. Pathogenetic mechanisms of the intracellular parasite Mycobacterium ulcerans leading to Buruli ulcer. The Lancet infectious diseases. 2009;9(11):699-710.

21. En J, Kitamoto S, Kawashima A, Yonezawa S, Kishi Y, Ishii N, et al. Mycolactone cytotoxicity in Schwann cells could explain nerve damage in Buruli ulcer. PLoS Negl Trop Dis. 2017;11(8):e0005834.
22. Portaels F, Meyers WM, Ablordey A. First cultivation and characterization of Mycobacterium ulcerans from the environment. PLoS Negl Trop Dis. 2008;2.
23. Marion E, Song OR, Christophe T, Babonneau J, Fenistein D, Eyer J, et al. Mycobacterial toxin induces analgesia in buruli ulcer by targeting the angiotensin pathways. Cell. 2014;157(7):1565-1576.
24. En J, Goto M, Nakanaga K, Higashi M, Ishii N, Saito H, et al. Mycolactone is responsible for the painlessness of Mycobacterium ulcerans infection (buruli ulcer) in a murine study. Infection and immunity. 2008;76(5):2002-2007.
25. Yotsu RR, Nakanaga K, Hoshino Y, Suzuki K, Ishii N. Buruli ulcer and current situation in Japan: a new emerging cutaneous Mycobacterium infection. J Dermatol. 2012;39(7):587-593.
26. Debacker M, Portaels F, Aguiar J, Steunou C, Zinsou C, Meyers W, et al. Risk factors for Buruli ulcer, Benin. Emerg Infect Dis. 2006;12(9):1325-1331.
27. Alferink M, de Zeeuw J, Sopoh G, Agossadou C, Abass KM, Phillips RO, et al. Pain Associated with Wound Care Treatment among Buruli Ulcer Patients from Ghana and Benin. PLoS One. 2015;10(6):e0119926.
28. Meka AO, Chukwu JN, Nwafor CC, Oshi DC, Madichie NO, Ekeke N, et al. Diagnosis delay and duration of hospitalisation of patients with Buruli ulcer in Nigeria. Trans R Soc Trop Med Hyg. 2016;110(9):502-509.
29. Ackumey MM, Gyapong M, Pappoe M, Maclean CK, Weiss MG. Socio-cultural determinants of timely and delayed treatment of Buruli ulcer: Implications for disease control. Infect Dis Poverty. 2012;1(1):6.
30. Omansen TF, Almeida D, Converse PJ, Li SY, Lee J, Stienstra Y, et al. High-Dose Rifamycins Enable Shorter Oral Treatment in a Murine Model of Mycobacterium ulcerans Disease. Antimicrob Agents Chemother. 2019;63(2).
31. Barogui Y, Johnson RC, van der Werf TS, Sopoh G, Dossou A, Dijkstra PU, et al. Functional limitations after surgical or antibiotic treatment for Buruli ulcer in Benin. Am J Trop Med Hyg. 2009;81(1):82-87.
32. de Zeeuw J, Omansen TF, Douwstra M, Barogui YT, Agossadou C, Sopoh GE, et al. Persisting social participation restrictions among former Buruli ulcer patients in Ghana and Benin. PLoS Negl Trop Dis. 2014;8(11):e3303.
33. Yotsu RR, Suzuki K, Simmonds RE, Bedimo R, Ablordey A, Yeboah-Manu D, et al. Buruli Ulcer: a Review of the Current Knowledge. Curr Trop Med Rep. 2018;5(4):247-256.
34. Johnson PD, Stinear T, Small PL, Pluschke G, Merritt RW, Portaels F, et al. Buruli ulcer (M. ulcerans infection): new insights, new hope for disease control. PLoS Med. 2005;2(4):e108.
35. Mulder AA, Boerma RP, Barogui Y, Zinsou C, Johnson RC, Gbovi J, et al. Healthcare seeking behaviour for Buruli ulcer in Benin: a model to capture therapy choice of patients and healthy community members. Trans R Soc Trop Med Hyg. 2008;102(9):912-920.
36. Yotsu RR, Murase C, Sugawara M, Suzuki K, Nakanaga K, Ishii N, et al. Revisiting Buruli ulcer. J Dermatol. 2015;42(11):1033-1041.
37. Portaels F, Johnson P, Meyers WM, Organization WH, Initiative GBU. Buruli ulcer: diagnosis of Mycobacterium ulcerans disease: a manual for health care providers. World Health Organization; 2001.
38. Junghanss T, Johnson RC, Pluschke G. Mycobacterium ulcerans disease. 2014.

39. WHO. Buruli ulcer: progress report, 2004-2008. Weekly Epidemiological Record. 2008;83(17):145-154.
40. Portaels F. Laboratory diagnosis of buruli ulcer: a manual for health care providers. World Health Organization; 2014. Report No.: 9241505702.
41. WHO. Treatment of Mycobacterium ulcerans disease (Buruli ulcer). Geneva: World Health Organization; 2012 4 April 2012. 1-76 p.
42. WHO. WHO | Buruli ulcer. WHO. 2019.
43. WHO. The NTD road map: together towards 2030: WHO; 2023 [Available from: https://www.who.int/teams/control-of-neglected-tropical-diseases.
44. WHO. Global Buruli ulcer Initiative (GBUI): WHO; 2023 [cited 2023 25 May 2023]. Available from: https://www.who.int/initiatives/global-buruli-ulcer-initiative-(gbui).
45. WHO. Distribution of Buruli ulcer, worldwide, 2015. 2015.
46. WHO. Buruli ulcer: World Health Organization; 2024 [Available from: https://www.who.int/data/gho/data/themes/topics/buruli-ulcer.
47. Dassi C, Mosi L, Narh CA, Quaye C, Konan DO, Djaman JA, et al. Distribution and Risk of Mycolactone-Producing Mycobacteria Transmission within Buruli Ulcer Endemic Communities in Cote d'Ivoire. Trop Med Infect Dis. 2017;2(1).
48. Röltgen K, Cruz I, Ndung'U JM, Pluschke G. Laboratory Diagnosis of Buruli Ulcer: Challenges and Future Perspectives. Springer International Publishing; 2019. p. 183-202.
49. Nienhuis WA, Stienstra Y, Thompson WA, Awuah PC, Abass KM, Tuah W, et al. Antimicrobial treatment for early, limited Mycobacterium ulcerans infection: a randomised controlled trial. Lancet. 2010;375(9715):664-672.
50. Iddrisah FN, Yeboah-Manu D, Nortey PA, Nyarko KM, Anim J, Antara SN, et al. Outcome of Streptomycin-Rifampicin treatment of Buruli Ulcer in two Ghanaian districts. Pan Afr Med J. 2016;25(Suppl 1):13.
51. Phillips RO, Sarfo FS, Abass MK, Abotsi J, Wilson T, Forson M, et al. Clinical and bacteriological efficacy of rifampin-streptomycin combination for two weeks followed by rifampin and clarithromycin for six weeks for treatment of Mycobacterium ulcerans disease. Antimicrob Agents Chemother. 2014;58(2):1161-1166.
52. Yeboah-Manu D, Bodmer T, Mensah-Quainoo E, Owusu S, Ofori-Adjei D, Pluschke G. Evaluation of decontamination methods and growth media for primary isolation of Mycobacterium ulcerans from surgical specimens. J Clin Microbiol. 2004;42(12):5875-5876.
53. Portaels F, Agular J, Fissette K, Fonteyne P, De Beenhouwer H, De Rijk P, et al. Direct detection and identification of Mycobacterium ulcerans in clinical specimens by PCR and oligonucleotide-specific capture plate hybridization. Journal of clinical microbiology. 1997;35(5):1097-1100.
54. Ablordey A, Swings J, Hubans C, Chemlal K, Locht C, Portaels F, et al. Multilocus variable-number tandem repeat typing of Mycobacterium ulcerans. J Clin Microbiol. 2005;43(4):1546-1551.
55. Tabah EN, Johnson CR, Degnonvi H, Pluschke G, Röltgen K. Buruli Ulcer in Africa. In: Pluschke G, Röltgen K, editors. Buruli Ulcer: Mycobacterium Ulcerans Disease. Cham: Springer International Publishing; 2019. p. 43-60.
56. Etuaful S, Carbonnelle B, Grosset J, Lucas S, Horsfield C, Phillips R, et al. Efficacy of the Combination Rifampin-Streptomycin in Preventing Growth of Mycobacterium ulcerans in Early Lesions of Buruli Ulcer in Humans. Antimicrobial Agents and Chemotherapy. 2005;49(8):3182-3186.
57. Friedman ND, McDonald AH, Robson ME, O'Brien DP. Corticosteroid use for paradoxical reactions during antibiotic treatment for Mycobacterium ulcerans. 2012.

58. O'Brien DP, Robson M, Friedman ND, Walton A, McDonald A, Callan P, et al. Incidence, clinical spectrum, diagnostic features, treatment and predictors of paradoxical reactions during antibiotic treatment of Mycobacterium ulceransinfections. BMC infectious diseases. 2013;13(1):1-10.
59. Doig KD, Holt KE, Fyfe JA. On the origin of Mycobacterium ulcerans, the causative agent of Buruli ulcer. BMC Genomics. 2012;13.
60. Röltgen K, Qi W, Ruf M-T, Mensah-Quainoo E, Pidot SJ, Seemann T, et al. Single nucleotide polymorphism typing of Mycobacterium ulcerans reveals focal transmission of buruli ulcer in a highly endemic region of Ghana. PLoS neglected tropical diseases. 2010;4(7):e751.
61. Vandelannoote K, Meehan CJ, Eddyani M, Affolabi D, Phanzu DM, Eyangoh S, et al. Multiple introductions and recent spread of the emerging human pathogen Mycobacterium ulcerans across Africa. Genome biology and evolution. 2017;9(3):414-426.
62. Babonneau J, Bernard C, Marion E, Chauty A, Kempf M, Robert R, et al. Development of a dry-reagent-based qPCR to facilitate the diagnosis of Mycobacterium ulcerans infection in endemic countries. PLoS neglected tropical diseases. 2015;9(4):e0003606.
63. Grietens KP, Boock AU, Peeters H, Hausmann-Muela S, Toomer E, Ribera JM. "It is me who endures but my family that suffers": social isolation as a consequence of the household cost burden of Buruli ulcer free of charge hospital treatment. PLoS Negl Trop Dis. 2008;2(10):e321.
64. WHO. Ending the neglect to attain the sustainable development goals: a road map for neglected tropical diseases 2021–2030. World Health Organization; 2020.
65. Beissner M, Phillips RO, Battke F, Bauer M, Badziklou K, Sarfo FS, et al. Loop-Mediated Isothermal Amplification for Laboratory Confirmation of Buruli Ulcer Disease-Towards a Point-of-Care Test. PLoS Negl Trop Dis. 2015;9(11):e0004219.
66. Hong H, Demangel C, Pidot SJ, Leadlay PF, Stinear T. Mycolactones: immunosuppressive and cytotoxic polyketides produced by aquatic mycobacteria. Nat Prod Rep. 2008;25(3):447-454.
67. Wansbrough-Jones M, Phillips R. Buruli ulcer: emerging from obscurity. Lancet. 2006;367(9525):1849-1858.
68. Sarfo FS, Phillips RO, Rangers B, Mahrous EA, Lee RE, Tarelli E, et al. Detection of Mycolactone A/B in Mycobacterium ulcerans-Infected Human Tissue. PLoS Negl Trop Dis. 2010;4(1):e577.
69. Sarfo FS, Converse PJ, Almeida DV, Zhang J, Robinson C, Wansbrough-Jones M, et al. Microbiological, histological, immunological, and toxin response to antibiotic treatment in the mouse model of Mycobacterium ulcerans disease. PLoS Negl Trop Dis. 2013;7(3):e2101.
70. George KM, Pascopella L, Welty DM, Small PL. A Mycobacterium ulcerans toxin, mycolactone, causes apoptosis in guinea pig ulcers and tissue culture cells. Infect Immun. 2000;68(2):877-883.
71. Sakyi SA, Aboagye SY, Otchere ID, Liao AM, Caltagirone TG, Yeboah-Manu D. RNA Aptamer That Specifically Binds to Mycolactone and Serves as a Diagnostic Tool for Diagnosis of Buruli Ulcer. PLoS Negl Trop Dis. 2016;10(10):e0004950.
72. Ablordey A, Amissah DA, Aboagye IF, Hatano B, Yamazaki T, Sata T, et al. Detection of Mycobacterium ulcerans by the loop mediated isothermal amplification method. PLoS Negl Trop Dis. 2012;6(4):e1590.
73. Hong H, Gates PJ, Staunton J, Stinear T, Cole ST, Leadlay PF, et al. Identification using LC-MSn of co-metabolites in the biosynthesis of the polyketide toxin mycolactone by

a clinical isolate of Mycobacterium ulcerans. Chem Commun (Camb). 2003(22):2822-2823.
74. Spangenberg T, Kishi Y. Highly sensitive, operationally simple, cost/time effective detection of the mycolactones from the human pathogen Mycobacterium ulcerans. Chemical communications. 2010;46(9):1410-1412.
75. Wadagni A, Frimpong M, Phanzu DM. Simple, rapid Mycobacterium ulcerans disease diagnosis from clinical samples by fluorescence of mycolactone on thin layer chromatography. PLoS Negl Trop Dis. 2015;9.
76. Amewu RK, Akolgo GA, Asare ME, Abdulai Z, Ablordey AS, Asiedu K. Evaluation of the fluorescent-thin layer chromatography (f-TLC) for the diagnosis of Buruli ulcer disease in Ghana. PLOS ONE. 2022;17(8):e0270235.
77. Converse PJ, Xing Y, Kim KH, Tyagi S, Li SY, Almeida DV, et al. Accelerated detection of mycolactone production and response to antibiotic treatment in a mouse model of Mycobacterium ulcerans disease. PLoS Negl Trop Dis. 2014;8(1):e2618.
78. Land KJ, Boeras DI, Chen X-S, Ramsay AR, Peeling RW. REASSURED diagnostics to inform disease control strategies, strengthen health systems and improve patient outcomes. Nature microbiology. 2019;4(1):46-54.
79. Tharmaraj V, Pitchumani K. d-Glucose sensing by (E)-(4-((pyren-1-ylmethylene)amino)phenyl) boronic acid via a photoinduced electron transfer (PET) mechanism. RSC Advances. 2013;3(29):11566-11570.
80. Curtius H, Kaiser G, Müller E, Bosbach D. Radionuclide release from research reactor spent fuel. Journal of Nuclear Materials. 2011;416(1):211-215.
81. Wu X, Chen X-X, Jiang Y-B. Recent advances in boronic acid-based optical chemosensors. Analyst. 2017;142(9):1403-1414.
82. Hall DG. Boronic Acids. 2011.
83. Kishi Y. Chemistry of mycolactones, the causative toxins of Buruli ulcer. Proc Natl Acad Sci U S A. 2011;108(17):6703-6708.
84. Guo Z, Shin I, Yoon J. Recognition and sensing of various species using boronic acid derivatives. Chemical Communications. 2012;48(48):5956-5967.
85. Lacina K, Skládal P, James TD. Boronic acids for sensing and other applications - a mini-review of papers published in 2013. Chemistry Central Journal. 2014;8(1):60.
86. Kaur G, Fang H, Gao X, Li H, Wang B. Substituent effect on anthracene-based bisboronic acid glucose sensors. Tetrahedron. 2006;62(11):2583-2589.
87. Wu W, Mitra N, Yan EC, Zhou S. Multifunctional hybrid nanogel for integration of optical glucose sensing and self-regulated insulin release at physiological pH. Acs Nano. 2010;4(8):4831-4839.
88. Wu W, Zhou T, Berliner A, Banerjee P, Zhou S. Glucose-Mediated Assembly of Phenylboronic Acid Modified CdTe/ZnTe/ZnS Quantum Dots for Intracellular Glucose Probing. Angewandte Chemie International Edition. 2010;49(37):6554-6558.
89. Huang Y-J, Ouyang W-J, Wu X, Li Z, Fossey JS, James TD, et al. Glucose sensing via aggregation and the use of "knock-out" binding to improve selectivity. Journal of the American Chemical Society. 2013;135(5):1700-1703.
90. Zhai W, Male L, Fossey JS. Glucose selective bis-boronic acid click-fluor. Chemical Communications. 2017;53(14):2218-2221.
91. Whyte GF, Vilar R, Woscholski R. Molecular recognition with boronic acids-applications in chemical biology. J Chem Biol. 2013;6(4):161-174.
92. Pohanka M. Glycated Hemoglobin and Methods for Its Point of Care Testing. Biosensors. 2021;11(3):70.

93. Zhu X, Zhou X, Xing D. Ultrasensitive and selective detection of mercury (II) in aqueous solution by polymerase assisted fluorescence amplification. Biosensors and Bioelectronics. 2011;26(5):2666-2669.
94. Guan R, Chen H, Cao F, Cao D, Deng Y. Two fluorescence turn-on chemosensors for cyanide anions based on pyridine cation and the boronic acid moiety. Inorganic Chemistry Communications. 2013;38:112-114.
95. Lee SA, You GR, Choi YW, Jo HY, Kim AR, Noh I, et al. A new multifunctional Schiff base as a fluorescence sensor for Al 3+ and a colorimetric sensor for CN− in aqueous media: an application to bioimaging. Dalton Transactions. 2014;43(18):6650-6659.
96. Ooyama Y, Furue K, Uenaka K, Ohshita J. Development of highly-sensitive fluorescence PET (photo-induced electron transfer) sensor for water: Anthracene–boronic acid ester. RSC Advances. 2014;4(48):25330-25333.
97. Ooyama Y, Matsugasako A, Oka K, Nagano T, Sumomogi M, Komaguchi K, et al. Fluorescence PET (photo-induced electron transfer) sensors for water based on anthracene–boronic acid ester. Chemical Communications. 2011;47(15):4448-4450.
98. Chung C, Srikun D, Lim CS, Chang CJ, Cho BR. A two-photon fluorescent probe for ratiometric imaging of hydrogen peroxide in live tissue. Chemical Communications. 2011;47(34):9618-9620.
99. Nonaka H, An Q, Sugihara F, Doura T, Tsuchiya A, Yoshioka Y, et al. Phenylboronic Acid-based 19F MRI Probe for the Detection and Imaging of Hydrogen Peroxide Utilizing Its Large Chemical-Shift Change. analytical sciences. 2015;31(4):331-335.
100. Chaicham A, Sahasithiwat S, Tuntulani T, Tomapatanaget B. Highly effective discrimination of catecholamine derivatives via FRET-on/off processes induced by the intermolecular assembly with two fluorescence sensors. Chemical Communications. 2013;49(81):9287-9289.
101. Fu H, Fang H, Sun J, Wang H, Liu A, Sun J, et al. Boronic acid-based enzyme inhibitors: a review of recent progress. Current Medicinal Chemistry. 2014;21(28):3271-3280.
102. Cai B, Luo Y, Guo Q, Zhang X, Wu Z. A glucose-sensitive block glycopolymer hydrogel based on dynamic boronic ester bonds for insulin delivery. Carbohydrate research. 2017;445:32-39.
103. Fang H, Kaur G, Wang B. Progress in boronic acid-based fluorescent glucose sensors. Journal of Fluorescence. 2004;14:481-489.
104. Chang M-H, Chang C-N. Synthesis of three fluorescent boronic acid sensors for tumor marker Sialyl Lewis X in cancer diagnosis. Tetrahedron Letters. 2014;55(32):4437-4441.
105. Chu Y, Wang D, Wang K, Liu ZL, Weston B, Wang B. Fluorescent conjugate of sLex-selective bisboronic acid for imaging application. Bioorganic & medicinal chemistry letters. 2013;23(23):6307-6309.
106. Marco-Dufort B, Iten R, Tibbitt MW. Linking molecular behavior to macroscopic properties in ideal dynamic covalent networks. Journal of the American Chemical Society. 2020;142(36):15371-15385.
107. Yan J, Fang H, Wang B. Boronolectins and fluorescent boronolectins: An examination of the detailed chemistry issues important for the design. Medicinal research reviews. 2005;25(5):490-520.
108. WHO. The Global Health Observatory: Number of new reported cases of Buruli ulcer: WHO; 2023 [cited 2023 28 May 2023]. Available from: https://www.who.int/data/gho/data/indicators/indicator-details/GHO/number-of-new-reported-cases-of-buruli-ulcer.

109. Guarner J. Buruli Ulcer: Review of a Neglected Skin Mycobacterial Disease. J Clin Microbiol. 2018;56(4).
110. WHO. Buruli ulcer (Mycobacterium ulcerans infection) 2019 [updated 21 May 2019. Available from: https://www.who.int/news-room/fact-sheets/detail/buruli-ulcer-(mycobacterium-ulcerans-infection).
111. Sizaire V, Nackers F, Comte E. Mycobacterium ulcerans infection: control, diagnosis, and treatment. Lancet Infect Dis. 2006;6.
112. Murchison RI. Address to the Royal Geographical Society. Journal of the Royal Geographical Society of London. 1863:cxiii-cxcii.
113. Grant JA. A walk across Africa; or, Domestic scenes from my Nile journal: Edinburgh: W. Blackwood; 1864.
114. Henry R. Etymologia: Buruli Ulcer. Emerging Infectious Diseases. 2020;26(3):504.
115. Phanzu D, Ablordey A, Imposo D, Lefevre L, Mahema R, Suykerbuyk P, et al. Edematous Mycobacterium ulcerans Infection (Buruli Ulcer) on the Face: A Case Report. The American journal of tropical medicine and hygiene. 2008;77:1099-1102.
116. Nakanaga K, Yotsu RR, Hoshino Y, Suzuki K, Makino M, Ishii N. Buruli ulcer and mycolactone-producing mycobacteria. Jpn J Infect Dis. 2013;66(2):83-88.
117. Cook A. Mengo Hospital Notes. Br Med J. 1970;2:378-379.
118. Chany A-C, Tresse C, Casarotto V, Blanchard N. History, biology and chemistry of Mycobacterium ulcerans infections (Buruli ulcer disease). Natural Product Reports. 2013;30(12):1527-1567.
119. Pradinaud R, Couppié P, Versapuech J. Mycobactérioses cutanées environmentales dont l'infection à Mycobacterium ulcerans ("ulcère de Buruli"). Encycl Méd Chir (Editions Scientifiques et Médicales Elsevier SAS, Paris), Maladies Infectieuses. Paris, Elsevier SAS, Maladies Infectieuses; 2003.
120. Korman TM, Johnson PD, Hayman J. Etymologia: Buruli Ulcer. Emerging Infectious Diseases. 2020;26(12):3104-3104.
121. Bonamonte D, Filoni A, Angelini G. Mycobacterium ulcerans Infection. In: Bonamonte D, Angelini G, editors. Mycobacterial Skin Infections. Cham: Springer International Publishing; 2017. p. 359-387.
122. Buckle G, Tolhurst JC. A new mycobacterial infection in man; cultivation of the new mycobacterial infection in man; cultivation of the new mycobacterium. J Pathol Bacteriol. 1948;60.
123. Fenner F. The significance of the incubation period in infectious diseases. Medical Journal of Australia. 1950;2(23):813-818.
124. Palomino J, Obiang A, Realini L, Meyers W, Portaels F. Effect of oxygen on growth of Mycobacterium ulcerans in the BACTEC system. Journal of clinical microbiology. 1998;36(11):3420-3422.
125. Clancey JK, Dodge OG, Lunn HF. Mycobacterial skin ulcers in Uganda. Lancet. 1961;2.
126. Connor DH, Washington CM, Fletcher LH. Buruli ulceration. A clinicopathologic study of 38 Ugandans with Mycobacterium ulcerans ulceration. Arch Pathol. 1966;81.
127. Lunn H, Connor D, Wilks N, Barnley G, Kamunvi F, Clancey J, et al. Buruli (Mycobacterial) Ulceration in Uganda.(A New Focus of Buruli Ulcer in Madi District, Uganda.). East African Medical Journal. 1965;42(6):275-288.
128. Janssens P, Quertinmont M, Sieniawski Jt, Gatti F. Necrotic tropical ulcers and mycobacterial causative agents. Tropical and geographical medicine. 1959;11(4):293-312.
129. Clancey J, Dodge R, Lunn H. Study of a mycobacterium causing skin ulceration in Uganda. Ann Soc Belg Med Trop. 1962;42:585-590.

130. Dodge O, Lunn H. Buruli ulcer: a mycobacterial skin ulcer in a Uganda child. Journal of Tropical Medicine and Hygiene. 1962;65(6):139-142.
131. Gehringer M, Altmann KH. The chemistry and biology of mycolactones. Beilstein J Org Chem. 2017;13:1596-1660.
132. de Bär M. Mycobacterium ulcerans infection in a child from Angola: diagnosis by direct detection and culture. Tropical Medicine & International Health. 1998;3(3).
133. Brou T, Broutin H, Elguero E, Asse H, Guegan J-F. Landscape diversity related to Buruli ulcer disease in Cote d'Ivoire. PLoS neglected tropical diseases. 2008;2(7):e271.
134. Stinear TP, Seemann T, Pidot S. Reductive evolution and niche adaptation inferred from the genome of Mycobacterium ulcerans, the causative agent of Buruli ulcer. Genome Res. 2007;17.
135. Sanhueza D, Chevillon C, Bouzinbi N, Godreuil S, Guégan J-F. Chitin increases Mycobacterium ulcerans growth in acidic environments. Microbes and environments. 2018;33(2):234-237.
136. Sanhueza D, Guégan J-F, Jordan H, Chevillon C. Environmental variations in Mycobacterium ulcerans transcriptome: absence of mycolactone expression in suboptimal environments. Toxins. 2019;11(3):146.
137. Deshayes C, Angala SK, Marion E, Brandli I, Babonneau J, Preisser L, et al. Regulation of mycolactone, the Mycobacterium ulcerans toxin, depends on nutrient source. PLoS Neglected Tropical Diseases. 2013;7(11):e2502.
138. Marsollier L, Robert R, Aubry J. Aquatic insects as a vector for Mycobacterium ulcerans. Appl Environ Microbiol. 2002;68.
139. Johnson PD, Azuolas J, Lavender CJ, Wishart E, Stinear TP, Hayman JA, et al. Mycobacterium ulcerans in mosquitoes captured during outbreak of Buruli ulcer, southeastern Australia. Emerg Infect Dis. 2007;13(11):1653-1660.
140. Willson SJ, Kaufman MG, Merritt RW, Williamson HR, Malakauskas DM, Benbow ME. Fish and amphibians as potential reservoirs of Mycobacterium ulcerans, the causative agent of Buruli ulcer disease. Infection Ecology & Epidemiology. 2013;3(1):19946.
141. Group TUB. Epidemiology of Mycobacterium ulcerans infection (Buruli ulcer) at Kinyara, Uganda. Transactions of the Royal Society of Tropical Medicine and Hygiene. 1971;65(6):763-775.
142. Dhungel L, Benbow ME, Jordan HR. Linking the Mycobacterium ulcerans environment to Buruli ulcer disease: Progress and challenges. One Health. 2021;13:100311.
143. Röltgen K, Pluschke G. Epidemiology and disease burden of Buruli ulcer: a review. Res Rep Trop Med. 2015;6:59-73.
144. Ayelo GA, Anagonou E, Wadagni AC, Barogui YT, Dossou AD, Houezo JG, et al. Report of a series of 82 cases of Buruli ulcer from Nigeria treated in Benin, from 2006 to 2016. PLoS Negl Trop Dis. 2018;12(3):e0006358.
145. Tobias NJ, Seemann T, Pidot SJ, Porter JL, Marsollier L, Marion E, et al. Mycolactone gene expression is controlled by strong SigA-like promoters with utility in studies of Mycobacterium ulcerans and buruli ulcer. PLoS Negl Trop Dis. 2009;3(11):e553.
146. Krieg RE, Hockmeyer WT, Connor DH. Toxin of Mycobacterium ulcerans. Production and effects in guinea pig skin. Arch Dermatol. 1974;110(5):783-788.
147. Guenin-Macé L, Ruf M-T, Pluschke G, Demangel C. Mycolactone: more than just a cytotoxin. Buruli ulcer: Mycobacterium ulcerans disease. 2019:117-134.
148. Demangel C, Stinear TP, Cole ST. Buruli ulcer: reductive evolution enhances pathogenicity of Mycobacterium ulcerans. Nat Rev Microbiol. 2009;7(1):50-60.

149. Pimsler M, Sponsler TA, Meyers WM. Immunosuppressive properties of the soluble toxin from Mycobacterium ulcerans. The Journal of infectious diseases. 1988;157(3):577-580.
150. En J, Ishii N, Goto M. [Role of mycolactone in the nerve damage of Buruli ulcer (Mycobacterium ulcerans infection)]. Nihon Hansenbyo Gakkai Zasshi. 2011;80(1):5-10.
151. Bozzo C, Tiberio R, Graziola F, Pertusi G, Valente G, Colombo E, et al. A Mycobacterium ulcerans toxin, mycolactone, induces apoptosis in primary human keratinocytes and in HaCaT cells. Microbes Infect. 2010;12(14-15):1258-1263.
152. Walsh DS, Meyers WM, Portaels F, Lane JE, Mongkolsirichaikul D, Hussem K, et al. High rates of apoptosis in human Mycobacterium ulcerans culture-positive buruli ulcer skin lesions. Am J Trop Med Hyg. 2005;73(2):410-415.
153. Adusumilli S, Mve-Obiang A, Sparer T, Meyers W, Hayman J, Small PL. Mycobacterium ulcerans toxic macrolide, mycolactone modulates the host immune response and cellular location of M. ulcerans in vitro and in vivo. Cell Microbiol. 2005;7(9):1295-1304.
154. Snyder DS, Small PL. Uptake and cellular actions of mycolactone, a virulence determinant for Mycobacterium ulcerans. Microb Pathog. 2003;34(2):91-101.
155. Ranger BS, Mahrous EA, Mosi L, Adusumilli S, Lee RE, Colorni A, et al. Globally distributed mycobacterial fish pathogens produce a novel plasmid-encoded toxic macrolide, mycolactone F. Infect Immun. 2006;74(11):6037-6045.
156. Dobos KM, Small PL, Deslauriers M, Quinn FD, King CH. Mycobacterium ulcerans cytotoxicity in an adipose cell model. Infect Immun. 2001;69(11):7182-7186.
157. Houngbedji GM, Bouchard P, Frenette J. Mycobacterium ulcerans infections cause progressive muscle atrophy and dysfunction, and mycolactone impairs satellite cell proliferation. American journal of physiology Regulatory, integrative and comparative physiology. 2011;300(3):R724-732.
158. Houngbedji GM, Cote CH, Small PL, Frenette J. Limited repair and structural damages displayed by skeletal muscles loaded with mycolactone. Microbes Infect. 2009;11(2):238-244.
159. Torrado E, Adusumilli S, Fraga AG, Small PL, Castro AG, Pedrosa J. Mycolactone-mediated inhibition of tumor necrosis factor production by macrophages infected with Mycobacterium ulcerans has implications for the control of infection. Infect Immun. 2007;75(8):3979-3988.
160. Torrado E, Fraga AG, Castro AG, Stragier P, Meyers WM, Portaels F, et al. Evidence for an intramacrophage growth phase of Mycobacterium ulcerans. Infect Immun. 2007;75(2):977-987.
161. Torrado E, Fraga AG, Logarinho E, Martins TG, Carmona JA, Gama JB, et al. IFN-gamma-dependent activation of macrophages during experimental infections by Mycobacterium ulcerans is impaired by the toxin mycolactone. J Immunol. 2010;184(2):947-955.
162. Hong H, Coutanceau E, Leclerc M, Caleechurn L, Leadlay PF, Demangel C. Mycolactone diffuses from Mycobacterium ulcerans-infected tissues and targets mononuclear cells in peripheral blood and lymphoid organs. PLoS Negl Trop Dis. 2008;2(10):e325.
163. Coutanceau E, Decalf J, Martino A, Babon A, Winter N, Cole ST, et al. Selective suppression of dendritic cell functions by Mycobacterium ulcerans toxin mycolactone. J Exp Med. 2007;204(6):1395-1403.

164. Fraga AG, Cruz A, Martins TG, Torrado E, Saraiva M, Pereira DR, et al. Mycobacterium ulcerans triggers T-cell immunity followed by local and regional but not systemic immunosuppression. Infect Immun. 2011;79(1):421-430.
165. Guenin-Mace L, Carrette F, Asperti-Boursin F, Le Bon A, Caleechurn L, Di Bartolo V, et al. Mycolactone impairs T cell homing by suppressing microRNA control of L-selectin expression. Proc Natl Acad Sci U S A. 2011;108(31):12833-12838.
166. Bieri R, Scherr N, Ruf MT, Dangy JP, Gersbach P, Gehringer M, et al. The Macrolide Toxin Mycolactone Promotes Bim-Dependent Apoptosis in Buruli Ulcer through Inhibition of mTOR. ACS Chem Biol. 2017;12(5):1297-1307.
167. Scherr N, Gersbach P, Dangy JP, Bomio C, Li J, Altmann KH, et al. Structure-activity relationship studies on the macrolide exotoxin mycolactone of Mycobacterium ulcerans. PLoS Negl Trop Dis. 2013;7(3):e2143.
168. Ruf MT, Steffen C, Bolz M, Schmid P, Pluschke G. Infiltrating leukocytes surround early Buruli ulcer lesions, but are unable to reach the mycolactone producing mycobacteria. Virulence. 2017;8(8):1918-1926.
169. Kaser M, Hauser J, Small P, Pluschke G. Large sequence polymorphisms unveil the phylogenetic relationship of environmental and pathogenic mycobacteria related to Mycobacterium ulcerans. Appl Environ Microbiol. 2009;75(17):5667-5675.
170. Yip MJ, Porter JL, Fyfe JA, Lavender CJ, Portaels F, Rhodes M, et al. Evolution of Mycobacterium ulcerans and other mycolactone-producing mycobacteria from a common Mycobacterium marinum progenitor. Journal of bacteriology. 2007;189(5):2021-2029.
171. Pidot SJ, Hong H, Seemann T, Porter JL, Yip MJ, Men A, et al. Deciphering the genetic basis for polyketide variation among mycobacteria producing mycolactones. BMC Genomics. 2008;9:462.
172. Mve-Obiang A, Lee RE, Portaels F, Small PL. Heterogeneity of mycolactones produced by clinical isolates of Mycobacterium ulcerans: implications for virulence. Infect Immun. 2003;71(2):774-783.
173. Marsollier L, Robert R, Aubry J, Saint Andre JP, Kouakou H, Legras P, et al. Aquatic insects as a vector for Mycobacterium ulcerans. Appl Environ Microbiol. 2002;68(9):4623-4628.
174. Hong H, Spencer JB, Porter JL, Leadlay PF, Stinear T. A novel mycolactone from a clinical isolate of Mycobacterium ulcerans provides evidence for additional toxin heterogeneity as a result of specific changes in the modular polyketide synthase. Chembiochem. 2005;6(4):643-648.
175. Mve-Obiang A, Lee RE, Umstot ES, Trott KA, Grammer TC, Parker JM, et al. A newly discovered mycobacterial pathogen isolated from laboratory colonies of Xenopus species with lethal infections produces a novel form of mycolactone, the Mycobacterium ulcerans macrolide toxin. Infect Immun. 2005;73(6):3307-3312.
176. Trott KA, Stacy BA, Lifland BD, Diggs HE, Harland RM, Khokha MK, et al. Characterization of a Mycobacterium ulcerans-like infection in a colony of African tropical clawed frogs (Xenopus tropicalis). Comp Med. 2004;54(3):309-317.
177. Stragier P, Hermans K, Stinear T, Portaels F. First report of a mycolactone-producing Mycobacterium infection in fish agriculture in Belgium. FEMS Microbiol Lett. 2008;286(1):93-95.
178. Kim HJ, Jackson KL, Kishi Y, Williamson HR, Mosi L, Small PL. Heterogeneity in the stereochemistry of mycolactones isolated from M. marinum: toxins produced by fresh vs. saltwater fish pathogens. Chem Commun (Camb). 2009(47):7402-7404.
179. Kim HJ, Kishi Y. Total synthesis and stereochemistry of mycolactone F. J Am Chem Soc. 2008;130(6):1842-1844.

180. Hong H, Stinear T, Porter J, Demangel C, Leadlay PF. A novel mycolactone toxin obtained by biosynthetic engineering. Chembiochem : a European journal of chemical biology. 2007;8(17):2043-2047.
181. Nakanaga K, Ogura Y, Toyoda A, Yoshida M, Fukano H, Fujiwara N, et al. Naturally occurring a loss of a giant plasmid from Mycobacterium ulcerans subsp. shinshuense makes it non-pathogenic. Sci Rep. 2018;8(1):8218.
182. Saint-Auret S, Chany AC, Casarotto V, Tresse C, Parmentier L, Abdelkafi H, et al. Total Syntheses of Mycolactone A/B and its Analogues for the Exploration of the Biology of Buruli Ulcer. Chimia (Aarau). 2017;71(12):836-840.
183. Kobayashi Y, Hayashi N, Tan CH, Kishi Y. Toward the creation of NMR databases in chiral solvents for assignments of relative and absolute stereochemistry: proof of concept. Org Lett. 2001;3(14):2245-2248.
184. Fidanze S, Song F, Szlosek-Pinaud M, Small PL, Kishi Y. Complete structure of the mycolactones. J Am Chem Soc. 2001;123(41):10117-10118.
185. Benowitz AB, Fidanze S, Small PL, Kishi Y. Stereochemistry of the core structure of the mycolactones. J Am Chem Soc. 2001;123(21):5128-5129.
186. Song F, Fidanze S, Benowitz AB, Kishi Y. Total Synthesis of Mycolactones A and B. Tetrahedron. 2007;63(26):5739-5753.
187. Song F, Fidanze S, Benowitz AB, Kishi Y. Total synthesis of the mycolactones. Org Lett. 2002;4(4):647-650.
188. van der Werf TS, Stinear T, Stienstra Y, van der Graaf WT, Small PL. Mycolactones and Mycobacterium ulcerans disease. Lancet. 2003;362(9389):1062-1064.
189. Stinear TP, Hong H, Frigui W, Pryor MJ, Brosch R, Garnier T, et al. Common evolutionary origin for the unstable virulence plasmid pMUM found in geographically diverse strains of Mycobacterium ulcerans. Journal of bacteriology. 2005;187(5):1668-1676.
190. Stinear TP, Mve-Obiang A, Small PL, Frigui W, Pryor MJ, Brosch R, et al. Giant plasmid-encoded polyketide synthases produce the macrolide toxin of Mycobacterium ulcerans. Proc Natl Acad Sci U S A. 2004;101(5):1345-1349.
191. Stinear TP, Pryor MJ, Porter JL, Cole ST. Functional analysis and annotation of the virulence plasmid pMUM001 from Mycobacterium ulcerans. Microbiology. 2005;151(Pt 3):683-692.
192. Porter JL, Tobias NJ, Hong H, Tuck KL, Jenkin GA, Stinear TP. Transfer, stable maintenance and expression of the mycolactone polyketide megasynthase mls genes in a recombination-impaired Mycobacterium marinum. Microbiology. 2009;155(Pt 6):1923-1933.
193. Jenkin GA, Stinear TP, Johnson PD, Davies JK. Subtractive hybridization reveals a type I polyketide synthase locus specific to Mycobacterium ulcerans. Journal of bacteriology. 2003;185(23):6870-6882.
194. Townsend CA. Buruli toxin genes decoded. Proc Natl Acad Sci U S A. 2004;101(5):1116-1117.
195. Tafelmeyer P, Laurent C, Lenormand P, Rousselle JC, Marsollier L, Reysset G, et al. Comprehensive proteome analysis of Mycobacterium ulcerans and quantitative comparison of mycolactone biosynthesis. Proteomics. 2008;8(15):3124-3138.
196. Kaser M, Rondini S, Naegeli M, Stinear T, Portaels F, Certa U, et al. Evolution of two distinct phylogenetic lineages of the emerging human pathogen Mycobacterium ulcerans. BMC Evol Biol. 2007;7:177.
197. Porter JL, Tobias NJ, Pidot SJ, Falgner S, Tuck KL, Vettiger A, et al. The cell wall-associated mycolactone polyketide synthases are necessary but not sufficient for mycolactone biosynthesis. PLoS One. 2013;8(7):e70520.

198. Stinear TP, Mve-Obiang A, Small PL, Frigui W, Pryor MJ, Brosch R, et al. Giant plasmid-encoded polyketide synthases produce the macrolide toxin of Mycobacterium ulcerans. Proceedings of the National Academy of Sciences. 2004;101(5):1345-1349.
199. Bali S, Weissman KJ. Ketoreduction in mycolactone biosynthesis: insight into substrate specificity and stereocontrol from studies of discrete ketoreductase domains in vitro. Chembiochem. 2006;7(12):1935-1942.
200. Goto M, Nakanaga K, Aung T, Hamada T, Yamada N, Nomoto M, et al. Nerve damage in Mycobacterium ulcerans-infected mice: probable cause of painlessness in buruli ulcer. Am J Pathol. 2006;168(3):805-811.
201. Marsollier L, Aubry J, Coutanceau E, Andre JP, Small PL, Milon G, et al. Colonization of the salivary glands of Naucoris cimicoides by Mycobacterium ulcerans requires host plasmatocytes and a macrolide toxin, mycolactone. Cell Microbiol. 2005;7(7):935-943.
202. Phillips R, Sarfo FS, Guenin-Mace L, Decalf J, Wansbrough-Jones M, Albert ML, et al. Immunosuppressive signature of cutaneous Mycobacterium ulcerans infection in the peripheral blood of patients with buruli ulcer disease. J Infect Dis. 2009;200(11):1675-1684.
203. Silva MT, Portaels F, Pedrosa J. Pathogenetic mechanisms of the intracellular parasite Mycobacterium ulcerans leading to Buruli ulcer. Lancet Infect Dis. 2009;9(11):699-710.
204. Cadapan LD, Arslanian RL, Carney JR, Zavala SM, Small PL, Licari P. Suspension cultivation of Mycobacterium ulcerans for the production of mycolactones. FEMS Microbiol Lett. 2001;205(2):385-389.
205. van Summeren RP, Feringa BL, Minnaard AJ. New approaches towards the synthesis of the side-chain of mycolactones A and B. Org Biomol Chem. 2005;3(14):2524-2533.
206. Yin N, Wang G, Qian M, Negishi E. Stereoselective synthesis of the side chains of mycolactones A and B featuring stepwise double substitutions of 1,1-dibromo-1-alkenes. Angewandte Chemie (International ed in English). 2006;45(18):2916-2920.
207. Alexander MD, Fontaine SD, La Clair JJ, Dipasquale AG, Rheingold AL, Burkart MD. Synthesis of the mycolactone core by ring-closing metathesis. Chem Commun (Camb). 2006(44):4602-4604.
208. Jackson KL, Li W, Chen CL, Kishi Y. Scalable and efficient synthesis of the mycolactone core. Tetrahedron. 2010;66(13):2263-2272.
209. Judd TC, Bischoff A, Kishi Y, Adusumilli S, Small PL. Structure determination of mycolactone C via total synthesis. Org Lett. 2004;6(26):4901-4904.
210. Aubry S, Lee RE, Mahrous EA, Small PL, Beachboard D, Kishi Y. Synthesis and structure of mycolactone E isolated from frog mycobacterium. Org Lett. 2008;10(23):5385-5388.
211. Wang G, Yin N, Negishi E. Highly stereoselective total synthesis of fully hydroxy-protected mycolactones A and B and their stereoisomerization upon deprotection. Chemistry. 2011;17(15):4118-4130.
212. Gersbach P, Jantsch A, Feyen F, Scherr N, Dangy JP, Pluschke G, et al. A ring-closing metathesis (RCM)-based approach to mycolactones A/B. Chemistry. 2011;17(46):13017-13031.
213. Ko K-S, Alexander MD, Fontaine SD, Biggs-Houck JE, La Clair JJ, Burkart MD. Synthetic studies on the mycolactone core. Organic & Biomolecular Chemistry. 2010;8(22):5159-5165.
214. K. Gurjar M, Cherian J. Studies toward Unique Mycolactone Macrolides from Mycobacterium ulcerans. Heterocycles. 2001;55(6).
215. Blanchard N, Chany A-C, Tresse C, Casarotto V, Bréthous L, Saint-Auret S. Chapter 4 - A Walk Across Africa with Captain Grant: Exploring Mycobacterium ulcerans

Infection with Mycolactone Analogs. In: Harmata M, editor. Strategies and Tactics in Organic Synthesis. 11: Academic Press; 2015. p. 85-117.
216. Wang Y, Dai W-M. Synthesis of the Conjugated Tetraene Acid Side Chain of Mycolactone E by Suzuki–Miyaura Cross-Coupling Reaction of Alkenyl Boronates. European Journal of Organic Chemistry. 2014;2014(2):323-330.
217. Brown CA, Aggarwal VK. Short Convergent Synthesis of the Mycolactone Core Through Lithiation-Borylation Homologations. Chemistry. 2015;21(40):13900-13903.
218. Saint-Auret S, Abdelkafi H, Le Nouen D, Bisseret P, Blanchard N. Synthetic strategies towards mycolactone A/B, an exotoxin secreted by Mycobacterium ulcerans. Organic Chemistry Frontiers. 2017;4(12):2380-2386.
219. Saint-Auret S, Abdelkafi H, Le Nouen D, Guenin-Mace L, Demangel C, Bisseret P, et al. Modular total syntheses of mycolactone A/B and its [(2)H]-isotopologue. Org Biomol Chem. 2017;15(36):7518-7522.
220. Van der Werf TS, Van der Graaf WTA, Tappero JW, Asiedu K. Mycobacterium ulcerans infection. The Lancet. 1999;354(9183):1013-1018.
221. Boulkroun S, Guenin-Macé L, Thoulouze MI. Mycolactone suppresses T cell responsiveness by altering both early signaling and posttranslational events. J Immunol. 2010;184.
222. Hall BS, Hill K, McKenna M, Ogbechi J, High S, Willis AE, et al. The pathogenic mechanism of the Mycobacterium ulcerans virulence factor, mycolactone, depends on blockade of protein translocation into the ER. PLoS pathogens. 2014;10(4):e1004061.
223. Hall B, Simmonds R. Pleiotropic molecular effects of the Mycobacterium ulcerans virulence factor mycolactone underlying the cell death and immunosuppression seen in Buruli ulcer. Biochemical Society Transactions. 2014;42(1):177-183.
224. Anand U, Sinisi M, Fox M, MacQuillan A, Quick T, Korchev Y, et al. Mycolactone-mediated neurite degeneration and functional effects in cultured human and rat DRG neurons: Mechanisms underlying hypoalgesia in Buruli ulcer. Mol Pain. 2016;12.
225. López CA, Unkefer CJ, Swanson BI, Swanson JM, Gnanakaran S. Membrane perturbing properties of toxin mycolactone from Mycobacterium ulcerans. PLoS Computational Biology. 2018;14(2):e1005972.
226. McKenna M, Simmonds RE, High S. Mechanistic insights into the inhibition of Sec61-dependent co-and post-translational translocation by mycolactone. Journal of cell science. 2016;129(7):1404-1415.
227. Guenin-Mace L, Veyron-Churlet R, Thoulouze MI, Romet-Lemonne G, Hong H, Leadlay PF, et al. Mycolactone activation of Wiskott-Aldrich syndrome proteins underpins Buruli ulcer formation. J Clin Invest. 2013;123(4):1501-1512.
228. Guenin-Mace L, Baron L, Chany A-C, Tresse C, Saint-Auret S, Jönsson F, et al. Shaping mycolactone for therapeutic use against inflammatory disorders. Science translational medicine. 2015;7(289):289ra285-289ra285.
229. Bieri R, Scherr N, Ruf M-T, Dangy J-P, Gersbach P, Gehringer M, et al. The Macrolide Toxin Mycolactone Promotes Bim-Dependent Apoptosis in Buruli Ulcer through Inhibition of mTOR. ACS Chemical Biology. 2017;12(5):1297-1307.
230. Claessen JHL, Kundrat L, Ploegh HL. Protein quality control in the ER: balancing the ubiquitin checkbook. Trends in Cell Biology. 2012;22(1):22-32.
231. Baron L, Paatero AO, Morel J-D, Impens F, Guenin-Macé L, Saint-Auret S, et al. Mycolactone subverts immunity by selectively blocking the Sec61 translocon. Journal of Experimental Medicine. 2016;213(13):2885-2896.
232. Isaac C, Mauborgne A, Grimaldi A, Ade K, Pohl M, Limatola C, et al. Mycolactone displays anti-inflammatory effects on the nervous system. PLoS Neglected Tropical Diseases. 2017;11(11):e0006058.

233. Itskanov S, Wang L, Junne T, Sherriff R, Xiao L, Blanchard N, et al. A common mechanism of Sec61 translocon inhibition by small molecules. Nat Chem Biol. 2023;19(9):1063-1071.
234. Ricci D, Demangel C. From Bacterial Toxin to Therapeutic Agent: The Unexpected Fate of Mycolactone. Toxins. 2023;15(6):369.
235. Kawashima A, Kiriya M, En J, Tanigawa K, Nakamura Y, Fujiwara Y, et al. Genome-wide screening identified SEC61A1 as an essential factor for mycolactone-dependent apoptosis in human premonocytic THP-1 cells. PLOS Neglected Tropical Diseases. 2022;16(8):e0010672.
236. Gérard SF, Hall BS, Zaki AM, Corfield KA, Mayerhofer PU, Costa C, et al. Structure of the Inhibited State of the Sec Translocon. Molecular Cell. 2020;79(3):406-415.e407.
237. da Hora GCA, Nguyen JDM, Swanson JMJ. Can membrane composition traffic toxins? Mycolactone and preferential membrane interactions. Biophys J. 2022;121(22):4260-4270.
238. Nguyen JDM, da Hora GCA, Swanson JMJ. Mycolactone A vs. B: Multiscale Simulations Reveal the Roles of Localization and Association in Isomer-Specific Toxicity. Toxins. 2023;15(8):486.
239. Noël J, Sandoz G, Lesage F. Molecular regulations governing TREK and TRAAK channel functions. Channels. 2011;5(5):402-409.
240. Ocaña M, Cendán CM, Cobos EJ, Entrena JM, Baeyens JM. Potassium channels and pain: present realities and future opportunities. European journal of pharmacology. 2004;500(1-3):203-219.
241. Hargreaves K, Dubner R, Brown F, Flores C, Joris J. A new and sensitive method for measuring thermal nociception in cutaneous hyperalgesia. Pain. 1988;32(1):77-88.
242. Babonneau J, Bréard D, Reynaert M-L, Marion E, Guilet D, Saint André J-P, et al. Mycolactone as analgesic: subcutaneous bioavailability parameters. Frontiers in pharmacology. 2019;10:378.
243. En J, Ishii N, Goto M. Role of mycolactone in the nerve damage of Buruli ulcer (Mycobacterium ulcerans infection). Nihon Hansenbyo Gakkai Zasshi= Japanese Journal of Leprosy: Official Organ of the Japanese Leprosy Association. 2011;80(1):5-10.
244. Song O-R, Kim H-B, Jouny S, Ricard I, Vandeputte A, Deboosere N, et al. A bacterial toxin with analgesic properties: hyperpolarization of DRG neurons by mycolactone. Toxins. 2017;9(7):227.
245. Anand U, Facer P, Yiangou Y, Sinisi M, Fox M, McCarthy T, et al. Angiotensin II type 2 receptor (AT2R) localization and antagonist-mediated inhibition of capsaicin responses and neurite outgrowth in human and rat sensory neurons. European journal of pain. 2013;17(7):1012-1026.
246. Zou Z, Tao T, Li H, Zhu X. mTOR signaling pathway and mTOR inhibitors in cancer: progress and challenges. Cell & Bioscience. 2020;10(1):31.
247. Fevereiro J, Fraga AG, Capela C, Sopoh GE, Dossou A, Ayelo GA, et al. Genetic variants in human BCL2L11 (BIM) are associated with ulcerative forms of Buruli ulcer. Emerging Microbes & Infections. 2021;10(1):223-225.
248. Gay-Lussac JL, Thénard LJ. Sur la décomposition et la recomposition de l'acide boracique. Ann Chim Phys. 1808;68:169-174.
249. Davy H. XXIII. Electro-chemical researches, on the decomposition of the earths; with observations on the metals obtained from the alkaline earths, and on the amalgam procured from ammonia. Philosophical Transactions of the Royal Society of London. 1808(98):333-370.

250. Garrett DE. Borates: handbook of deposits, processing, properties, and use: Elsevier; 1998.
251. Yang W, Gao X, Wang B. Boronic acid compounds as potential pharmaceutical agents. Medicinal research reviews. 2003;23(3):346-368.
252. Bapat AP, Sumerlin BS, Sutti A. Bulk network polymers with dynamic B–O bonds: healable and reprocessable materials. Materials Horizons. 2020;7(3):694-714.
253. Springsteen G, Wang B. A detailed examination of boronic acid–diol complexation. Tetrahedron. 2002;58(26):5291-5300.
254. Yan J, Springsteen G, Deeter S, Wang B. The relationship among pKa, pH, and binding constants in the interactions between boronic acids and diols—it is not as simple as it appears. Tetrahedron. 2004;60(49):11205-11209.
255. Silva MP, Saraiva L, Pinto M, Sousa ME. Boronic Acids and Their Derivatives in Medicinal Chemistry: Synthesis and Biological Applications. Molecules. 2020;25(18).
256. Antonio J, Russo R, Carvalho C, Cal P, Gois P. Boronic acids as building blocks for the construction of therapeutically useful bioconjugates. Chemical Society Reviews. 2019;48.
257. DeFrancesco H, Dudley J, Coca A. Boron chemistry: an overview. Boron reagents in synthesis. 2016:1-25.
258. Cho S, Hwang SY, Oh DX, Park J. Recent progress in self-healing polymers and hydrogels based on reversible dynamic B–O bonds: boronic/boronate esters, borax, and benzoxaborole. Journal of Materials Chemistry A. 2021;9(26):14630-14655.
259. Lorand JP, EDWARDS JO. Polyol complexes and structure of the benzeneboronate ion. The Journal of Organic Chemistry. 1959;24(6):769-774.
260. Nishiyabu R, Kubo Y, James T, Fossey J. ChemInform Abstract: Boronic Acid Building Blocks: Tools for Sensing and Separation. Chemical communications (Cambridge, England). 2011;47:1106-1123.
261. Penner MH. Ultraviolet, Visible, and Fluorescence Spectroscopy. In: Nielsen SS, editor. Food Analysis. Cham: Springer International Publishing; 2017. p. 89-106.
262. Al-Rawashdeh NA. Current achievement and future potential of fluorescence spectroscopy. Macro To Nano Spectroscopy InTech. 2012:209-250.
263. Etminan A, Uzunović A, Topčagić A, Žero S, Dizdar M, Klepo L, et al., editors. Quantification of Active Substances in Some Drugs Using by Derivative UV/Vis spectroscopy. CMBEBIH 2019: Proceedings of the International Conference on Medical and Biological Engineering, 16–18 May 2019, Banja Luka, Bosnia and Herzegovina; 2020: Springer.
264. Jomova K, Hudecova L, Lauro P, Simunková M, Barbierikova Z, Malcek M, et al. The effect of Luteolin on DNA damage mediated by a copper catalyzed Fenton reaction. Journal of Inorganic Biochemistry. 2022;226:111635.
265. El Shoubaky GA, Abdel-Daim MM, Mansour MH, Salem EA. Isolation and Identification of a Flavone Apigenin from Marine Red Alga Acanthophora spicifera with Antinociceptive and Anti-Inflammatory Activities. J Exp Neurosci. 2016;10:21-29.
266. Stokes GG, editor On the change of refrangibility of light. Abstracts of the Papers Communicated to the Royal Society of London; 1852: The Royal Society London.
267. Rendell D, Mowthorpe DJ. Fluorescence and phosphorescence spectroscopy: Published on behalf of ACOL, London by Wiley; 1987.
268. Chinen AB, Guan CM, Ferrer JR, Barnaby SN, Merkel TJ, Mirkin CA. Nanoparticle probes for the detection of cancer biomarkers, cells, and tissues by fluorescence. Chemical reviews. 2015;115(19):10530-10574.

269. Spangenberg B, Poole CF, Weins C. Quantitative thin-layer chromatography: a practical survey: Springer Science & Business Media; 2011.
270. Lakowicz JR. Principles of fluorescence spectroscopy: Springer; 2006.
271. Lavis LD, Raines RT. Bright building blocks for chemical biology. ACS chemical biology. 2014;9(4):855-866.
272. Förster T. Zwischenmolekulare energiewanderung und fluoreszenz. Annalen der physik. 1948;437(1-2):55-75.
273. Atwood JL, Steed JW. Supramolecular chemistry: John Wiley & Sons; 2009.
274. Yuan L, Lin W, Zheng K, Zhu S. FRET-based small-molecule fluorescent probes: rational design and bioimaging applications. Accounts of chemical research. 2013;46(7):1462-1473.
275. Clegg RM. Fluorescence resonance energy transfer. Current opinion in biotechnology. 1995;6(1):103-110.
276. Tian X, Murfin L, Wu L, Lewis S, James T. Fluorescent Small Organic Probes for Biosensing. Chemical Science. 2021.
277. Wu L, Huang C, Emery BP, Sedgwick AC, Bull SD, He X-P, et al. Förster resonance energy transfer (FRET)-based small-molecule sensors and imaging agents. Chemical Society Reviews. 2020;49(15):5110-5139.
278. Read JK, Heggie CM, Meyers WM, Connor DH. Cytotoxic activity of Mycobacterium ulcerans. Infect Immun. 1974;9(6):1114-1122.
279. Yoon J, Czarnik AW. Fluorescent chemosensors of carbohydrates. A means of chemically communicating the binding of polyols in water based on chelation-enhanced quenching. Journal of the American Chemical Society. 1992;114(14):5874-5875.
280. Amewu RK, Spangenberg T. Detection of Mycolactone by Thin Layer Chromatography. In: Pluschke G, Röltgen K, editors. Mycobacterium ulcerans: Methods and Protocols. New York, NY: Springer US; 2022. p. 131-149.
281. Stinear T, Ross BC, Davies JK, Marino L, Robins-Browne RM, Oppedisano F, et al. Identification and characterization of IS 2404 and IS 2606: two distinct repeated sequences for detection of Mycobacterium ulcerans by PCR. Journal of clinical microbiology. 1999;37(4):1018-1023.
282. Liljefors T, Allinger NL. The Woodward-Fieser rules and α,β-Unsaturated ketones. Journal of the American Chemical Society. 1978;100(4):1068-1073.
283. Tan B, Soderstrom DN. Qualitative aspects of UV-vis spectrophotometry of beta-carotene and lycopene. Journal of chemical education. 1989;66(3):258.
284. Jag M. Organic spectroscopy: principles and applications. 2000.
285. Yable DK, Canale L, Dupuis P, Haba TC, Zoueu JT, Zissis G, editors. Characterization and Optical Early Diagnosis by Diffuse Reflectance Spectroscopy. 2020 IEEE International Conference on Environment and Electrical Engineering and 2020 IEEE Industrial and Commercial Power Systems Europe (EEEIC / I&CPS Europe); 2020 9-12 June 2020.
286. World Health Organization (2004) Buruli ulcer disease. Mycobacterium ulcerans infection. Corrigendum to No 15, 2004, Weekly Epidem Record, No 20, p 194.
287. Johnson PD. Buruli ulcer: cured by 8 weeks of oral antibiotics? The Lancet. 2020;395(10232):1231-1232.
288. Phillips RO, Robert J, Abass KM, Thompson W, Sarfo FS, Wilson T, et al. Rifampicin and clarithromycin (extended release) versus rifampicin and streptomycin for limited Buruli ulcer lesions: a randomised, open-label, non-inferiority phase 3 trial. The Lancet. 2020;395(10232):1259-1267.
289. Chauty A, Ardant M-F, Adeye A, Euverte H, Guédénon A, Johnson C, et al. Promising clinical efficacy of streptomycin-rifampin combination for treatment of buruli ulcer

(Mycobacterium ulcerans disease). Antimicrobial agents and chemotherapy. 2007;51(11):4029-4035.
290. Schroeder L, Amukele T, M P. Why The World Needs An Essential Diagnostics List. Forbes. 2016 4 August 2016.
291. García-Basteiro AL, DiNardo A, Saavedra B, Silva DR, Palmero D, Gegia M, et al. Point of care diagnostics for tuberculosis. Pulmonology. 2018;24(2):73-85.
292. Demangel C. Immunity against Mycobacterium ulcerans: The subversive role of mycolactone. Immunological Reviews. 2021;301(1):209-221.
293. Li X, Li G, Yang J, Jin G, Shao Y, Li Y, et al. Drug Resistance (Dapsone, Rifampicin, Ofloxacin) and Resistance-Related Gene Mutation Features in Leprosy Patients: A Systematic Review and Meta-Analysis. Int J Mol Sci. 2022;23(20).
294. Borrell S, Gagneux S. Strain diversity, epistasis and the evolution of drug resistance in Mycobacterium tuberculosis. Clinical microbiology and infection. 2011;17(6):815-820.
295. Eddyani M, Lavender C, de Rijk WB, Bomans P, Fyfe J, de Jong B, et al. Multicenter external quality assessment program for PCR detection of Mycobacterium ulcerans in clinical and environmental specimens. PloS one. 2014;9(2):e89407.
296. Siegmund V, Adjei O, Nitschke J, Thompson W, Klutse E, Herbinger KH, et al. Dry reagent-based polymerase chain reaction compared with other laboratory methods available for the diagnosis of Buruli ulcer disease. Clin Infect Dis. 2007;45(1):68-75.
297. Phillips R, Horsfield C, Kuijper S, Lartey A, Tetteh I, Etuaful S, et al. Sensitivity of PCR targeting the IS2404 insertion sequence of Mycobacterium ulcerans in an Assay using punch biopsy specimens for diagnosis of Buruli ulcer. J Clin Microbiol. 2005;43(8):3650-3656.
298. Do T, Santi I, Reich E. A harmonized HPTLC method for identification of various caffeine containing herbal drugs, extracts, and products, and quantitative estimation of their caffeine content. Journal of Liquid Chromatography & Related Technologies. 2019;42(9-10):274-281.
299. Sherma J. Thin-layer chromatography in food and agricultural analysis. Journal of Chromatography A. 2000;880(1):129-147.
300. Vermaak I, Hamman JH, Viljoen AM. High performance thin layer chromatography as a method to authenticate Hoodia gordonii raw material and products. South African Journal of Botany. 2010;76(1):119-124.
301. Meyyanathan SN, Suresh B. HPTLC Method for the Simultaneous Determination of Amlodipine and Benazepril in Their Formulations. Journal of Chromatographic Science. 2005;43(2):73-75.
302. Rubinson KA. Chemical analysis. digital Encyclopedia of Applied Physics. 2003:527-580.
303. Agatonovic-Kustrin S, Babazadeh Ortakand D, Morton DW, Yusof AP. Rapid evaluation and comparison of natural products and antioxidant activity in calendula, feverfew, and German chamomile extracts. Journal of Chromatography A. 2015;1385:103-110.
304. Axthelm Jr, Askes SH, Elstner M, Görls H, Bellstedt P, Schiller A. Fluorinated boronic acid-appended pyridinium salts and 19f nmr spectroscopy for diol sensing. Journal of the American Chemical Society. 2017;139(33):11413-11420.
305. Czarnik AW. Chemosensors of ion and molecule recognition: Springer Science & Business Media; 2012.
306. Wu J-S, Liu W-M, Zhuang X-Q, Wang F, Wang P-F, Tao S-L, et al. Fluorescence Turn On of Coumarin Derivatives by Metal Cations: A New Signaling Mechanism Based on C=N Isomerization. Organic Letters. 2007;9(1):33-36.

307. Valeur B, Berberan-Santos MN. Molecular fluorescence: principles and applications: John Wiley & Sons; 2012.
308. Springsteen G, Wang B. Alizarin Red S. as a general optical reporter for studying the binding of boronic acids with carbohydrates. Chemical Communications. 2001(17):1608-1609.
309. Whyte GF, Vilar R, Woscholski R. Molecular recognition with boronic acids—applications in chemical biology. Journal of Chemical Biology. 2013;6(4):161-174.
310. Pizer R, Tihal C. Equilibria and reaction mechanism of the complexation of methylboronic acid with polyols. Inorganic chemistry. 1992;31(15):3243-3247.
311. Pizer RD, Tihal CA. Mechanism of boron acid/polyol complex formation. comments on the trigonal/tetrahedral interconversion on boron. Polyhedron. 1996;15(19):3411-3416.
312. Akolgo GA, Partridge BM, D. Craggs T, Amewu RK. Alternative boronic acids in the detection of Mycolactone A/B using the thin layer chromatography (f-TLC) method for diagnosis of Buruli ulcer. BMC Infectious Diseases. 2023;23(1):495.
313. Han H-H, Tian H, Zang Y, Sedgwick AC, Li J, Sessler JL, et al. Small-molecule fluorescence-based probes for interrogating major organ diseases. Chemical Society Reviews. 2021.
314. Yuan L, Lin W, Yang Y, Chen H. A unique class of near-infrared functional fluorescent dyes with carboxylic-acid-modulated fluorescence ON/OFF switching: rational design, synthesis, optical properties, theoretical calculations, and applications for fluorescence imaging in living animals. Journal of the American Chemical Society. 2012;134(2):1200-1211.
315. Yang X-F, Guo X-Q, Zhao Y-B. Development of a novel rhodamine-type fluorescent probe to determine peroxynitrite. Talanta. 2002;57(5):883-890.
316. Ishiyama T, Murata M, Miyaura N. Palladium (0)-catalyzed cross-coupling reaction of alkoxydiboron with haloarenes: a direct procedure for arylboronic esters. The Journal of Organic Chemistry. 1995;60(23):7508-7510.
317. Ishiyama T, Itoh Y, Kitano T, Miyaura N. Synthesis of arylboronates via the palladium (0)-catalyzed cross-coupling reaction of tetra (alkoxo) diborons with aryl triflates. Tetrahedron letters. 1997;38(19):3447-3450.
318. Ishiyama T, Ishida K, Miyaura N. Synthesis of pinacol arylboronates via cross-coupling reaction of bis (pinacolato) diboron with chloroarenes catalyzed by palladium (0)–tricyclohexylphosphine complexes. Tetrahedron. 2001;57(49):9813-9816.
319. Draffin SP, Duggan PJ, Duggan SA. Highly fructose selective transport promoted by boronic acids based on a pentaerythritol core. Organic Letters. 2001;3(6):917-920.
320. Wu C, Wang J, Shen J, Bi C, Zhou H. Coumarin-based Hg2+ fluorescent probe: Synthesis and turn-on fluorescence detection in neat aqueous solution. Sensors and Actuators B: Chemical. 2017;243:678-683.
321. Pang B-j, Li Q, Li C-r, Yang Z-y. A highly selective and sensitive coumarin derived fluorescent probe for detecting Hg2+ in 100% aqueous solutions. Journal of Luminescence. 2019;205:446-450.
322. Ma S, Wang K-N, Xing M, Feng F, Pan Q, Cao D. A coumarin-boronic ester derivative as fluorescent chemosensor for detecting H2O2 in living cells. Inorganic Chemistry Communications. 2021;124:108414.
323. Lin C, Zhang M, Yan X, Zhang R, He X, Yuan Y. A Coumarin-boronic Based Fluorescent “ON-OFF” Probe for Hg2+ in Aqueous Solution. Zeitschrift für anorganische und allgemeine Chemie. 2020;646(23-24):1892-1899.

324. Li Q, Hu Y, Hou H-N, Yang W-N, Hu S-L. A new coumarin-carbonothioate-based turn-on fluorescent chemodosimeter for selective detection of Hg2+. Inorganica Chimica Acta. 2018;471:705-708.
325. Abdallah M, Hijazi A, Graff B, Fouassier J-P, Rodeghiero G, Gualandi A, et al. Coumarin derivatives as versatile photoinitiators for 3D printing, polymerization in water and photocomposite synthesis. Polymer Chemistry. 2019;10(7):872-884.
326. Wang Y, Li Y, Yu T, Su W, Ma H, Zhao Y, et al. Functionalized coumarin derivatives containing aromatic-imidazole unit as organic luminescent materials. Dyes and Pigments. 2020;173:107958.
327. Jones G, Stanforth SP. The Vilsmeier Reaction of Fully Conjugated Carbocycles and Heterocycles. Organic Reactions1996. p. 1-330.
328. Vilsmeier A, Haack A. Über die Einwirkung von Halogenphosphor auf Alkyl-formanilide. Eine neue Methode zur Darstellung sekundärer und tertiärer p-Alkylamino-benzaldehyde. Berichte der deutschen chemischen Gesellschaft (A and B Series). 1927;60(1):119-122.
329. Jones G, Stanforth SP. The Vilsmeier Reaction of Non-Aromatic Compounds. Organic Reactions2000. p. 355-686.
330. Klinck R, Stothers J. Nuclear Magnetic Resonance Studies: Part I. The Chemical Shift of the Formyl Proton in Aromatic Aldehydes. Canadian Journal of Chemistry. 1962;40(6):1071-1081.
331. Bai H, Sun Q, Tian H, Qian J, Zhang L, Zhang W. A Long-Wavelength Fluorescent Probe for Saccharides Based on Boronic-Acid Receptor. Chinese Journal of Chemistry. 2013;31(8):1095-1101.
332. Akgun B, Hall DG. Fast and Tight Boronate Formation for Click Bioorthogonal Conjugation. Angewandte Chemie. 2016;128(12):3977-3981.
333. Moriya T. Excited-state reactions of coumarins. VII. The solvent-dependent fluorescence of 7-hydroxycoumarins. Bulletin of the Chemical Society of Japan. 1988;61(6):1873-1886.
334. Aaron J-J, Buna M, Parkanyi C, Antonious MS, Tine A, Cisse L. Quantitative treatment of the effect of solvent on the electronic absorption and fluorescence spectra of substituted coumarins: Evaluation of the first excited singlet-state dipole moments. Journal of fluorescence. 1995;5:337-347.
335. Palanisamy S, Wu P-Y, Wu S-C, Chen Y-J, Tzou S-C, Wang C-H, et al. In vitro and in vivo imaging of peroxynitrite by a ratiometric boronate-based fluorescent probe. Biosensors and Bioelectronics. 2017;91:849-856.
336. Wang C, Wang P, Liu X, Fu J, Xue K, Xu K. Novel enantioselective fluorescent sensors for tartrate anion based on acridinezswsxa. Luminescence. 2017;32(7):1313-1318.
337. Dai Y, Xu K, Li Q, Wang C, Liu X, Wang P. Acridine-based complex as amino acid anion fluorescent sensor in aqueous solution. Spectrochimica Acta Part A: Molecular and Biomolecular Spectroscopy. 2016;157:1-5.
338. Wang C, Fu J, Yao K, Xue K, Xu K, Pang X. Acridine-based fluorescence chemosensors for selective sensing of Fe3+ and Ni2+ ions. Spectrochimica Acta Part A: Molecular and Biomolecular Spectroscopy. 2018;199:403-411.
339. Turan-Zitouni G, Kaplancikli Z, Uçucu Ü, Özdemir A, Chevallet P, Tunali Y. Synthesis of some 2-[(benzazole-2-yl) thio]-diphenylmethylacetamide derivatives and their antimicrobial activity. Phosphorus, Sulfur, and Silicon. 2004;179(11):2183-2188.
340. Kaplancikli ZA, Turan-Zitouni G, Revial G, Guven K. Synthesis and study of antibacterial and antifungal activities of novel 2-[[(benzoxazole/benzimidazole-2-yl) sulfanyl] acetylamino] thiazoles. Archives of pharmacal research. 2004;27(11):1081-1085.

341. Demir Özkay Ü, Özkay Y, Can ÖD. Synthesis and analgesic effects of 2-(2-carboxyphenylsulfanyl)-N-(4-substitutedphenyl) acetamide derivatives. Medicinal Chemistry Research. 2011;20(2):152-157.
342. Olszewska A, Pohl R, Brázdová M, Fojta M, Hocek M. Chloroacetamide-Linked Nucleotides and DNA for Cross-Linking with Peptides and Proteins. Bioconjugate Chemistry. 2016;27(9):2089-2094.
343. Sousa KAP, Lima FMR, Monteiro TO, Silva SM, Goulart MOF, Damos FS, et al. Amperometric Photosensor Based on Acridine Orange/TiO 2 for Chlorogenic Acid Determination in Food Samples. Food Analytical Methods. 2018;11:2731-2741.
344. Czaplinska B, Spaczynska E, Musiol R. Quinoline fluorescent probes for zinc–from diagnostic to therapeutic molecules in treating neurodegenerative diseases. Medicinal Chemistry. 2018;14(1):19-33.
345. Neises B, Steglich W. Simple method for the esterification of carboxylic acids. Angewandte Chemie International Edition in English. 1978;17(7):522-524.
346. Höfle G, Steglich W, Vorbrüggen H. 4-Dialkylaminopyridines as highly active acylation catalysts.[New synthetic method (25)]. Angewandte Chemie International Edition in English. 1978;17(8):569-583.
347. Ghosh AK, Shahabi D. Synthesis of amide derivatives for electron deficient amines and functionalized carboxylic acids using EDC and DMAP and a catalytic amount of HOBt as the coupling reagents. Tetrahedron letters. 2021;63:152719.
348. López-Soria JM, Pérez SJ, Hernández JN, Ramírez MA, Martín VS, Padrón JI. A practical, catalytic and selective deprotection of a Boc group in N,N′-diprotected amines using iron(iii)-catalysis. RSC Advances. 2015;5(9):6647-6651.
349. Han G, Tamaki M, Hruby V. Fast, efficient and selective deprotection of the tert-butoxycarbonyl (Boc) group using HCl/dioxane (4 m). The Journal of Peptide Research. 2001;58(4):338-341.
350. Han G, Tamaki M, Hruby V. Fast, efficient and selective deprotection of the tert-butoxycarbonyl (Boc) group using HCL/dioxane (4 M). The journal of peptide research : official journal of the American Peptide Society. 2001;58:338-341.
351. Abdel-Magid AF, Carson KG, Harris BD, Maryanoff CA, Shah RD. Reductive amination of aldehydes and ketones with sodium triacetoxyborohydride. studies on direct and indirect reductive amination procedures1. The Journal of organic chemistry. 1996;61(11):3849-3862.
352. Rahman AFMM, Park S-E, Kadi AA, Kwon Y. Fluorescein Hydrazones as Novel Nonintercalative Topoisomerase Catalytic Inhibitors with Low DNA Toxicity. Journal of Medicinal Chemistry. 2014;57(21):9139-9151.
353. Kaschula CH, Hunter R. Synthesis and structure–activity relations in allylsulfide and isothiocyanate compounds from garlic and broccoli against in vitro cancer cell growth. Studies in Natural Products Chemistry. 2016;50:1-43.
354. Podhradský D, Drobnica Ľ, Kristian P. Reactions of cysteine, its derivatives, glutathione, coenzyme A, and dihydrolipoic acid with isothiocyanates. Experientia. 1979;35(2):154-155.
355. Beija M, Afonso CA, Martinho JM. Synthesis and applications of Rhodamine derivatives as fluorescent probes. Chemical Society Reviews. 2009;38(8):2410-2433.
356. Kim HN, Lee MH, Kim HJ, Kim JS, Yoon J. A new trend in rhodamine-based chemosensors: application of spirolactam ring-opening to sensing ions. Chemical Society Reviews. 2008;37(8):1465-1472.
357. Lee VY, Sekiguchi A, Kim JS, Yoon J. Biology terface. Chem Soc Rev. 2008;37:1465-1472.

358. Wu D, Huang W, Duan C, Lin Z, Meng Q. Highly sensitive fluorescent probe for selective detection of Hg2+ in DMF aqueous media. Inorganic Chemistry. 2007;46(5):1538-1540.
359. Yang Y-K, Yook K-J, Tae J. A Rhodamine-Based Fluorescent and Colorimetric Chemodosimeter for the Rapid Detection of Hg2+ Ions in Aqueous Media. Journal of the American Chemical Society. 2005;127(48):16760-16761.
360. Kim SK, Swamy K, Chung S-Y, Kim HN, Kim MJ, Jeong Y, et al. New fluorescent and colorimetric chemosensors based on the rhodamine and boronic acid groups for the detection of Hg2+. Tetrahedron Letters. 2010;51(25):3286-3289.
361. Xiang Y, Tong A, Jin P, Ju Y. New Fluorescent Rhodamine Hydrazone Chemosensor for Cu(II) with High Selectivity and Sensitivity. Organic Letters. 2006;8(13):2863-2866.
362. Mao J, Wang L, Dou W, Tang X, Yan Y, Liu W. Tuning the selectivity of two chemosensors to Fe (III) and Cr (III). Organic letters. 2007;9(22):4567-4570.
363. Bossi M, Belov V, Polyakova S, Hell SW. Reversible red fluorescent molecular switches. Angewandte Chemie International Edition. 2006;45(44):7462-7465.
364. Treibs A, Kreuzer FH. Difluorboryl-komplexe von di-und tripyrrylmethenen. Justus Liebigs Annalen der Chemie. 1968;718(1):208-223.
365. Ojida A, Sakamoto T, Inoue M-a, Fujishima S-h, Lippens G, Hamachi I. Fluorescent BODIPY-based Zn (II) complex as a molecular probe for selective detection of neurofibrillary tangles in the brains of Alzheimer's disease patients. Journal of the American Chemical Society. 2009;131(18):6543-6548.
366. Smith NW, Alonso A, Brown CM, Dzyuba SV. Triazole-containing BODIPY dyes as novel fluorescent probes for soluble oligomers of amyloid Aβ1–42 peptide. Biochemical and biophysical research communications. 2010;391(3):1455-1458.
367. Beatty KE, Szychowski J, Fisk JD, Tirrell DA. A BODIPY-cyclooctyne for protein imaging in live cells. ChemBioChem. 2011;12(14):2137-2139.
368. Lin H-Y, Huang W-C, Chen Y-C, Chou H-H, Hsu C-Y, Lin JT, et al. BODIPY dyes with β-conjugation and their applications for high-efficiency inverted small molecule solar cells. Chemical Communications. 2012;48(71):8913-8915.
369. Altan Bozdemir O, Erbas-Cakmak S, Ekiz OO, Dana A, Akkaya EU. Towards unimolecular luminescent solar concentrators: BODIPY-based dendritic energy-transfer cascade with panchromatic absorption and monochromatized emission. Angewandte Chemie. 2011;123(46):11099-11104.
370. Rousseau T, Cravino A, Ripaud E, Leriche P, Rihn S, De Nicola A, et al. A tailored hybrid BODIPY–oligothiophene donor for molecular bulk heterojunction solar cells with improved performances. Chemical communications. 2010;46(28):5082-5084.
371. Karolin J, Johansson LB-A, Strandberg L, Ny T. Fluorescence and absorption spectroscopic properties of dipyrrometheneboron difluoride (BODIPY) derivatives in liquids, lipid membranes, and proteins. Journal of the American Chemical Society. 1994;116(17):7801-7806.
372. Kollmannsberger M, Gareis T, Heinl S, Daub J, Breu J. Electrogenerated Chemiluminescence and Proton-Dependent Switching of Fluorescence: Functionalized Difluoroboradiaza-s-indacenes. Angewandte Chemie International Edition in English. 1997;36(12):1333-1335.
373. Loudet A, Burgess K. BODIPY dyes and their derivatives: syntheses and spectroscopic properties. Chemical reviews. 2007;107(11):4891-4932.
374. Ulrich G, Ziessel R, Harriman A. The chemistry of fluorescent bodipy dyes: versatility unsurpassed. Angewandte Chemie International Edition. 2008;47(7):1184-1201.

375. Boens N, Leen V, Dehaen W. Fluorescent indicators based on BODIPY. Chemical Society Reviews. 2012;41(3):1130-1172.
376. Biagiotti G, Purić E, Urbančič I, Krišelj A, Weiss M, Mravljak J, et al. Combining cross-coupling reaction and Knoevenagel condensation in the synthesis of glyco-BODIPY probes for DC-SIGN super-resolution bioimaging. Bioorganic Chemistry. 2021;109:104730.
377. Mahato P, Saha S, Das P, Agarwalla H, Das A. An overview of the recent developments on Hg 2+ recognition. RSC Advances. 2014;4:36140-36174.
378. Bartelmess J, De Luca E, Signorelli A, Baldrighi M, Becce M, Brescia R, et al. Boron dipyrromethene (BODIPY) functionalized carbon nano-onions for high resolution cellular imaging. Nanoscale. 2014;6(22):13761-13769.
379. Brückner C, Karunaratne V, Rettig SJ, Dolphin D. Synthesis of meso-phenyl-4, 6-dipyrrins, preparation of their Cu (II), Ni (II), and Zn (II) chelates, and structural characterization of bis [meso-phenyl-4, 6-dipyrrinato] Ni (II). Canadian journal of chemistry. 1996;74(11):2182-2193.
380. Shah M, Thangaraj K, Soong ML, Wolford LT, Boyer JH, Politzer IR, et al. Pyrromethene–BF2 complexes as laser dyes: 1. Heteroatom Chemistry. 1990;1(5):389-399.
381. Jameson LP, Dzyuba SV. Expeditious, mechanochemical synthesis of BODIPY dyes. Beilstein Journal of Organic Chemistry. 2013;9:786-790.
382. Snyder H, Weaver C. The preparation of some azo boronic acids. Journal of the American Chemical Society. 1948;70(1):232-234.
383. Smoum R, Srebnik M. Boronated saccharides: potential applications. Studies in Inorganic Chemistry. 2005;22:391.
384. Egawa Y, Miki R, Seki T. Colorimetric sugar sensing using boronic acid-substituted azobenzenes. Materials. 2014;7(2):1201-1220.
385. Hansen JS, Christensen JB, Petersen JF, Hoeg-Jensen T, Norrild JC. Arylboronic acids: A diabetic eye on glucose sensing. Sensors and Actuators B: Chemical. 2012;161(1):45-79.
386. DiCesare N, Lakowicz JR. Spectral Properties of Fluorophores Combining the Boronic Acid Group with Electron Donor or Withdrawing Groups. Implication in the Development of Fluorescence Probes for Saccharides. J Phys Chem A. 2001;105(28):6834-6840.
387. Beda N, Nedospasov A. A spectrophotometric assay for nitrate in an excess of nitrite. Nitric Oxide. 2005;13(2):93-97.
388. Sinan R, Al-Uzri WA. Spectrophotometric Method for Determination of Sulfamethoxazole in Pharmaceutical Preparations by Diazotization-Coupling Reaction. Al-Nahrain Journal of Science. 2011;14(3):9-16.
389. Gordon PF, Gregory P. Organic chemistry in colour: Springer Science & Business Media; 2012.
390. Herráez JV, Belda R. Refractive Indices, Densities and Excess Molar Volumes of Monoalcohols + Water. Journal of Solution Chemistry. 2006;35(9):1315-1328.
391. Resch-Genger U, Grabolle M, Cavaliere-Jaricot S, Nitschke R, Nann T. Quantum dots versus organic dyes as fluorescent labels. Nature Methods. 2008;5(9):763-775.
392. Cavazos-Elizondo D, Aguirre-Soto A. Photophysical Properties of Fluorescent Labels: A Meta-Analysis to Guide Probe Selection Amidst Challenges with Available Data. Analysis & Sensing. 2022;2(5):e202200004.
393. Giacomazzo GE, Palladino P, Gellini C, Salerno G, Baldoneschi V, Feis A, et al. A straightforward synthesis of phenyl boronic acid (PBA) containing BODIPY dyes: new

functional and modular fluorescent tools for the tethering of the glycan domain of antibodies. RSC advances. 2019;9(53):30773-30777.
394. Isak SJ, Eyring EM, Spikes JD, Meekins PA. Direct blue dye solutions: photo properties. Journal of Photochemistry and Photobiology A: Chemistry. 2000;134(1-2):77-85.
395. Dinçalp H, Toker F, Durucasu İ, Avcıbaşı N, Icli S. New thiophene-based azo ligands containing azo methine group in the main chain for the determination of copper(II) ions. Dyes and Pigments. 2007;75(1):11-24.
396. Joshi H, Kamounah FS, Gooijer C, van der Zwan G, Antonov L. Excited state intramolecular proton transfer in some tautomeric azo dyes and schiff bases containing an intramolecular hydrogen bond. Journal of Photochemistry and Photobiology A: Chemistry. 2002;152(1-3):183-191.
397. Rahal M, Mokbel H, Graff B, Toufaily J, Hamieh T, Dumur F, et al. Mono vs. difunctional coumarin as photoinitiators in photocomposite synthesis and 3D printing. Catalysts. 2020;10(10):1202.
398. Rahal M, Graff B, Toufaily J, Hamieh T, Noirbent G, Gigmes D, et al. 3-Carboxylic Acid and Formyl-Derived Coumarins as Photoinitiators in Photo-Oxidation or Photo-Reduction Processes for Photopolymerization upon Visible Light: Photocomposite Synthesis and 3D Printing Applications. Molecules. 2021;26(6):1753.
399. Sheldrick GM. Program for empirical absorption correction of area detector data. SADABS. 1996.
400. Krause L, Herbst-Irmer R, Sheldrick GM, Stalke D. Comparison of silver and molybdenum microfocus X-ray sources for single-crystal structure determination. Journal of applied crystallography. 2015;48(1):3-10.
401. Blessing RH. An empirical correction for absorption anisotropy. Acta Crystallographica Section A: Foundations of Crystallography. 1995;51(1):33-38.
402. Sheldrick G. SHELXT - Integrated space-group and crystal-structure determination. Acta Crystallographica Section A. 2015;71(1):3-8.
403. Sheldrick G. Crystal structure refinement with SHELXL. Acta Crystallographica Section C. 2015;71(1):3-8.
404. Dolomanov O, Bourhis L, Gildea R, Howard J, Puschmann H. _journal_name_full'American Mineralogist'_journal_year 2021 _journal_volume 106 _journal_page_first 1844 _journal_paper_doi 10.2138/am-2021-7785. J Appl Cryst. 2009;42:339-341.
405. Ishiyama T, Murata M, Miyaura N. Palladium(0)-Catalyzed Cross-Coupling Reaction of Alkoxydiboron with Haloarenes: A Direct Procedure for Arylboronic Esters. The Journal of Organic Chemistry. 1995;60(23):7508-7510.
406. Ear A, Amand S, Blanchard F, Blond A, Dubost L, Buisson D, et al. Direct biosynthetic cyclization of a distorted paracyclophane highlighted by double isotopic labelling of l-tyrosine. Organic & Biomolecular Chemistry. 2015;13(12):3662-3666.
407. Akgun B. Boronic Esters as Bioorthogonal Probes in Site-Selective Labeling of Proteins. 2018.
408. Promchat A, Wongravee K, Sukwattanasinitt M, Praneenararat T. Rapid Discovery and Structure-Property Relationships of Metal-Ion Fluorescent Sensors via Macroarray Synthesis. Scientific Reports. 2019;9(1):10390.
409. Lawson-Wood K, Upstone S, Evans K. Determination of Relative Fluorescence Quantum Yields using the FL6500 Fluorescence Spectrometer. Fluoresc Spectrosc. 2018;4:1-5.

410. Würth C, Grabolle M, Pauli J, Spieles M, Resch-Genger U. Relative and absolute determination of fluorescence quantum yields of transparent samples. Nature protocols. 2013;8(8):1535-1550.
411. Brouwer AM. Standards for photoluminescence quantum yield measurements in solution (IUPAC Technical Report). Pure and Applied Chemistry. 2011;83(12):2213-2228.
412. Velapoldi RA, Mielenz K. A Fluorescence Standard Reference Material, Quinine Sulfate Dihydrate: US Department of Commerce, National Bureau of Standards; 1980.
413. Dhami S, Mello Ad, Rumbles G, Bishop S, Phillips D, Beeby A. Phthalocyanine fluorescence at high concentration: dimers or reabsorption effect? Photochemistry and Photobiology. 1995;61(4):341-346.

APPENDICES

Appendix 1: ^{1}H, ^{13}C, and ^{11}B NMR spectra Data

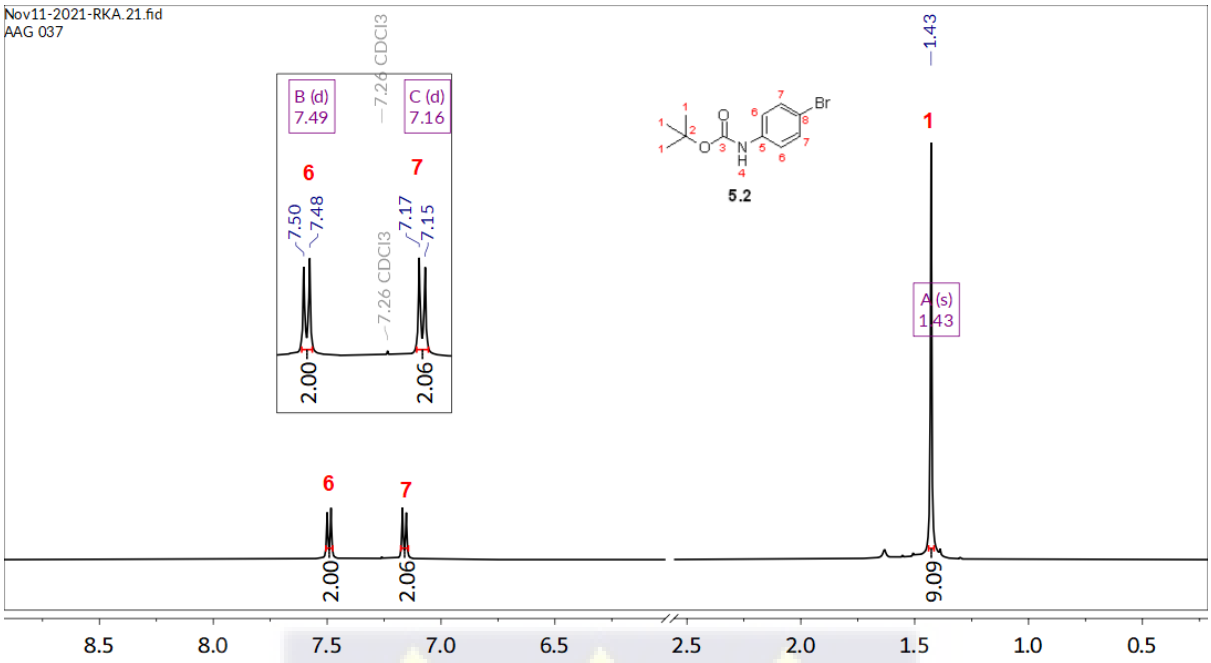

Appendix 1. 1: ^{1}H NMR spectrum (500 MHz, $CDCl_3$) of *tert*-butyl (4-bromophenyl)carbamate **5.2.**

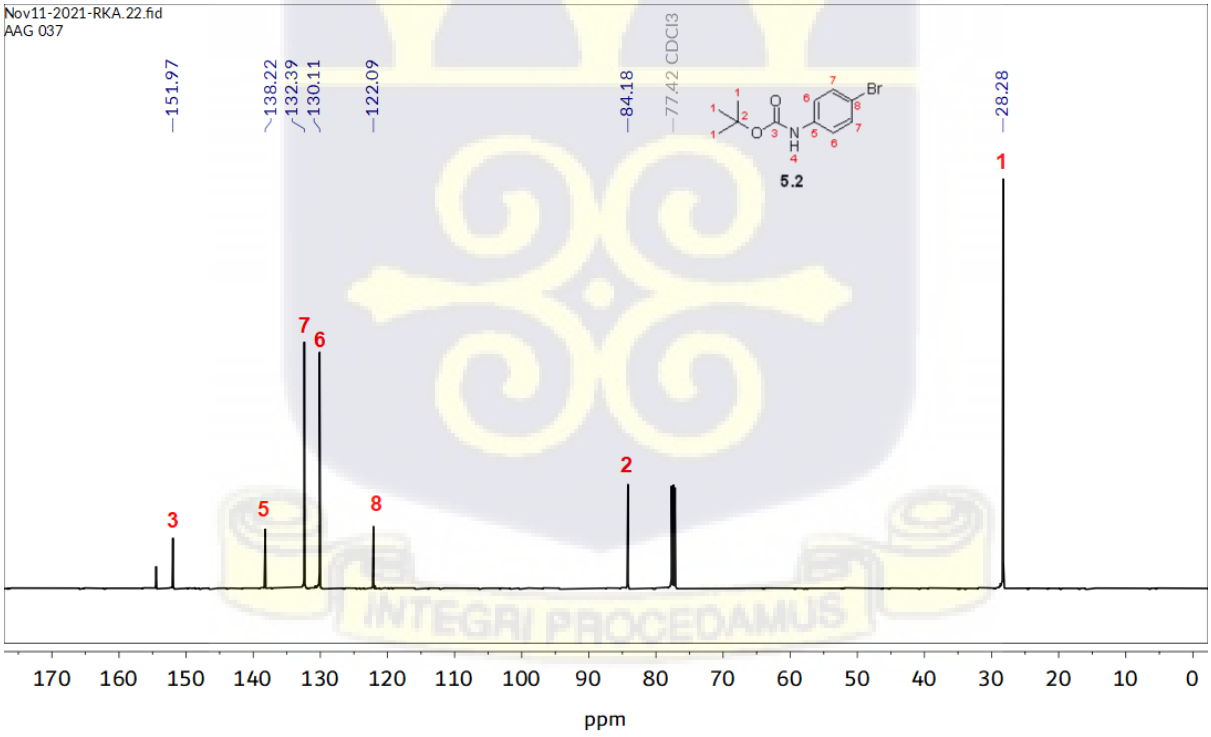

Appendix 1. 2: ^{13}C NMR spectrum (126 MHz, $CDCl_3$) of *tert*-butyl (4-bromophenyl)carbamate **5.2.**

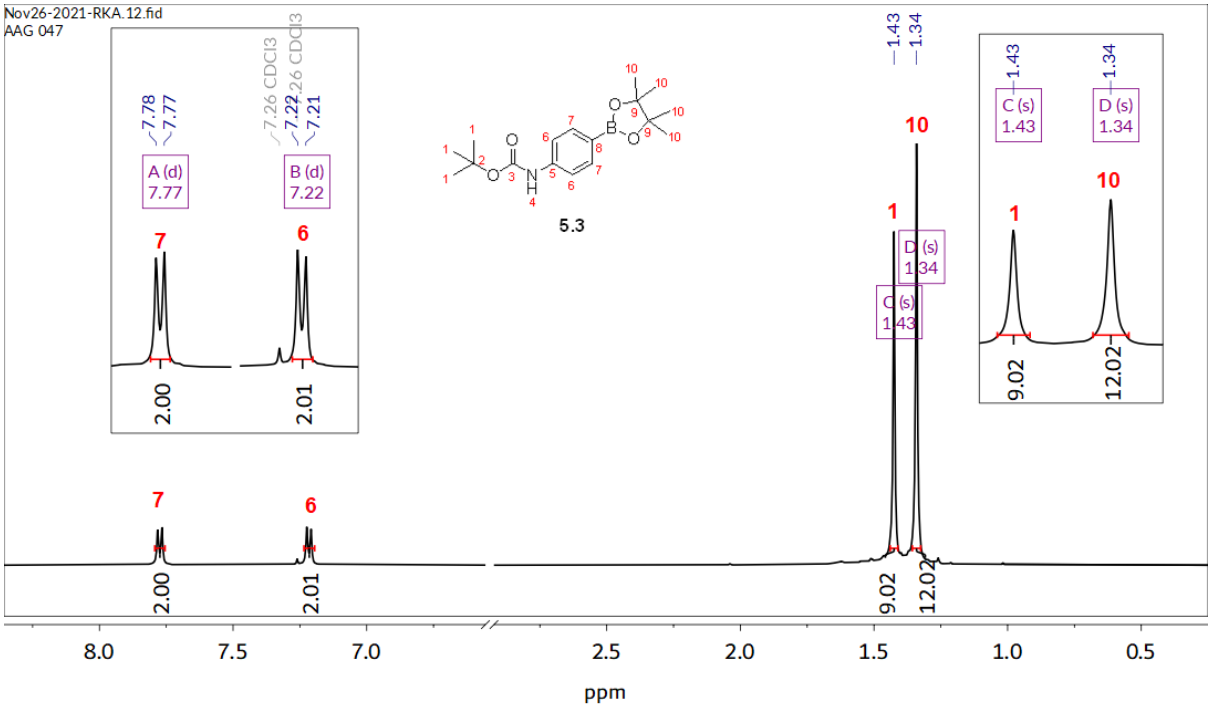

Appendix 1. 3: ^{1}H NMR spectrum (500 MHz, $CDCl_3$) of *tert*-butyl (4-(4,4,5,5-tetramethyl-1,3,2-dioxaborolan-2-yl)phenyl)carbamate **5.3.**

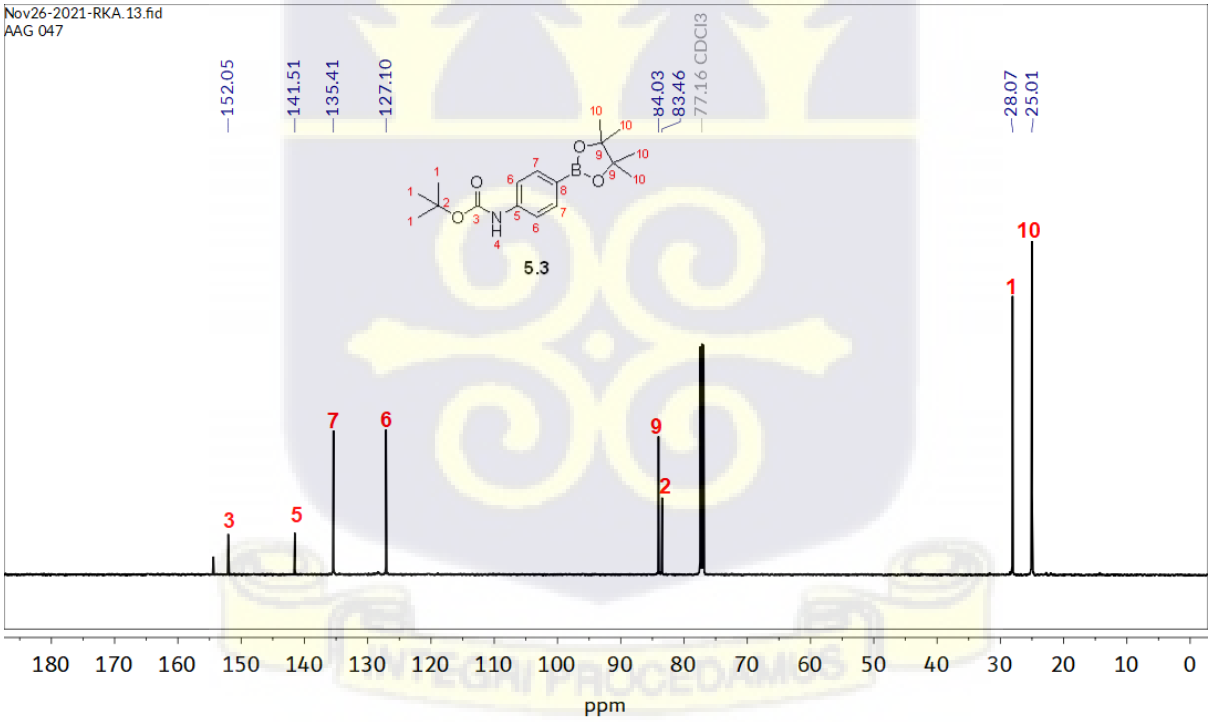

Appendix 1. 4: ^{13}C NMR spectrum (126 MHz, $CDCl_3$) of *tert*-butyl (4-(4,4,5,5-tetramethyl-1,3,2-dioxaborolan-2-yl)phenyl)carbamate **5.3.**

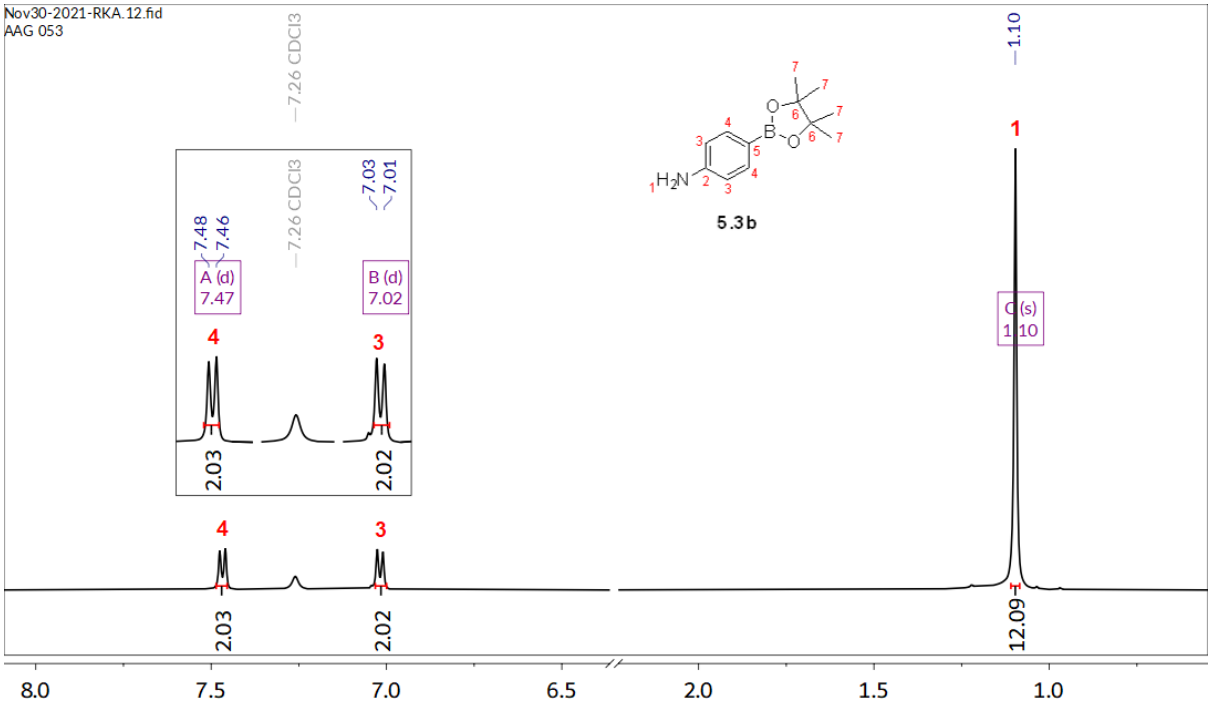

Appendix 1. 5: ^{1}H NMR spectrum (500 MHz, $CDCl_3$) of 4-(4,4,5,5-tetramethyl-1,3,2-dioxaborolan-2-yl)aniline **5.3b.**

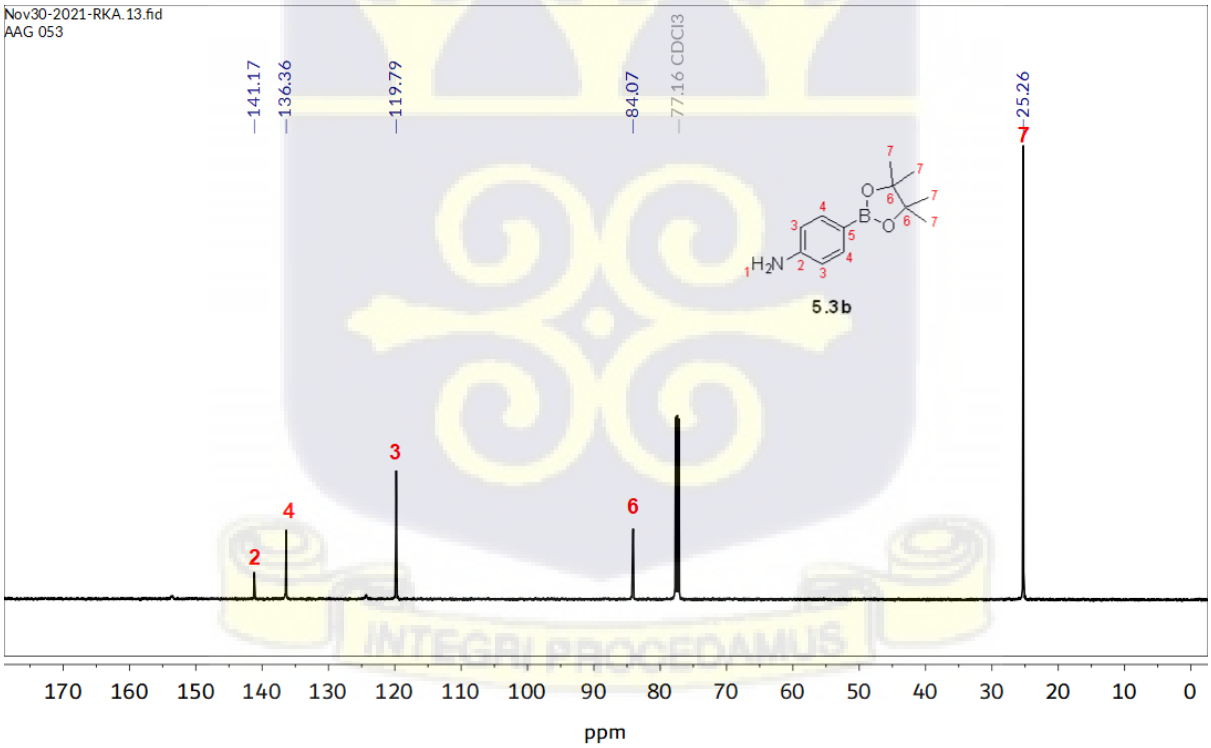

Appendix 1. 6: ^{13}C NMR spectrum (126 MHz, $CDCl_3$) of 4-(4,4,5,5-tetramethyl-1,3,2-dioxaborolan-2-yl)aniline **5.3b.**

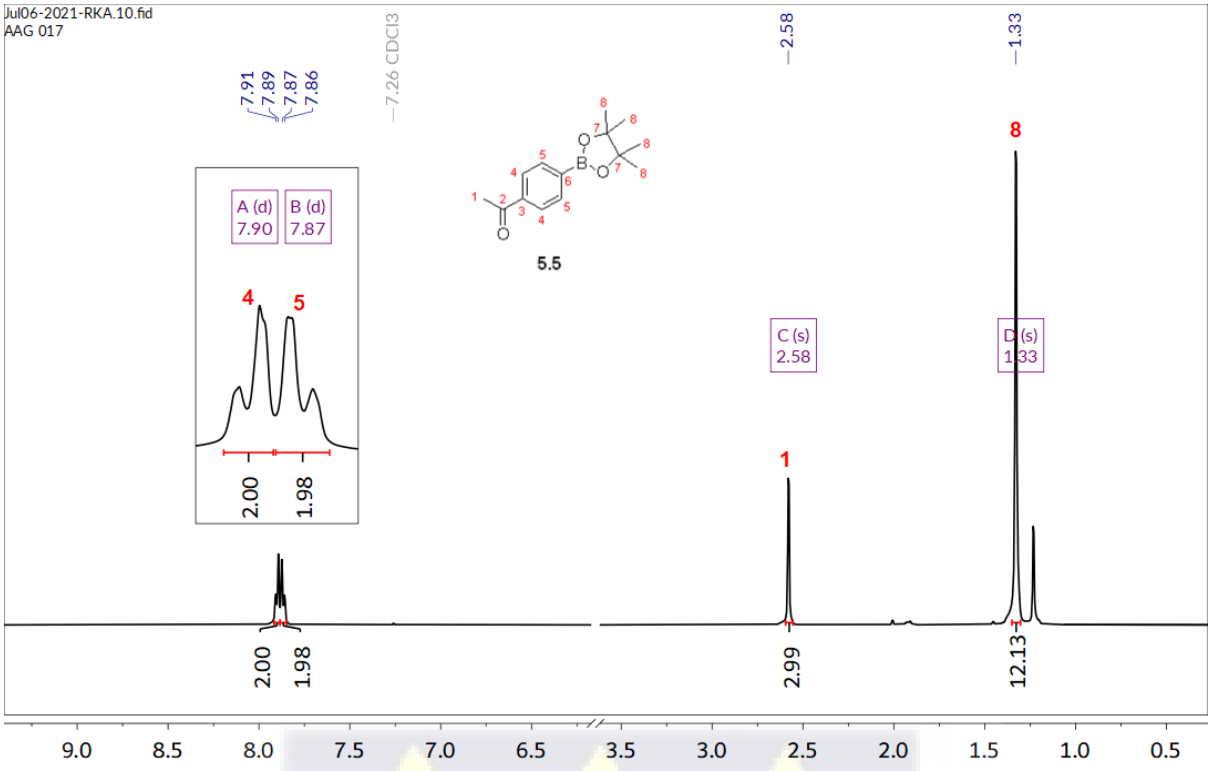

Appendix 1. 7: ^{1}H NMR spectrum (500 MHz, $CDCl_3$) of 1-(4-(4,4,5,5-tetramethyl-1,3,2-dioxaborolan-2-yl)phenyl)ethan-1-one **5.5**.

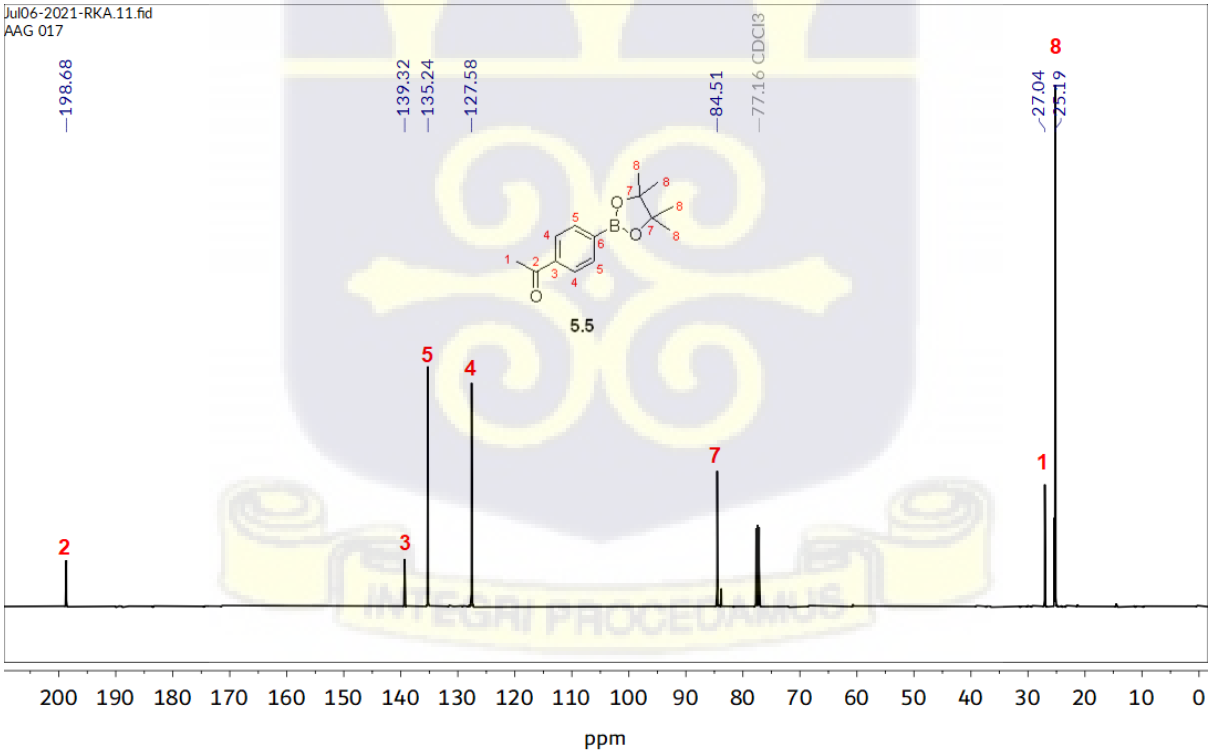

Appendix 1. 8: ^{13}C NMR spectrum (126 MHz, $CDCl_3$) of 1-(4-(4,4,5,5-tetramethyl-1,3,2-dioxaborolan-2-yl)phenyl)ethan-1-one **5.5.**

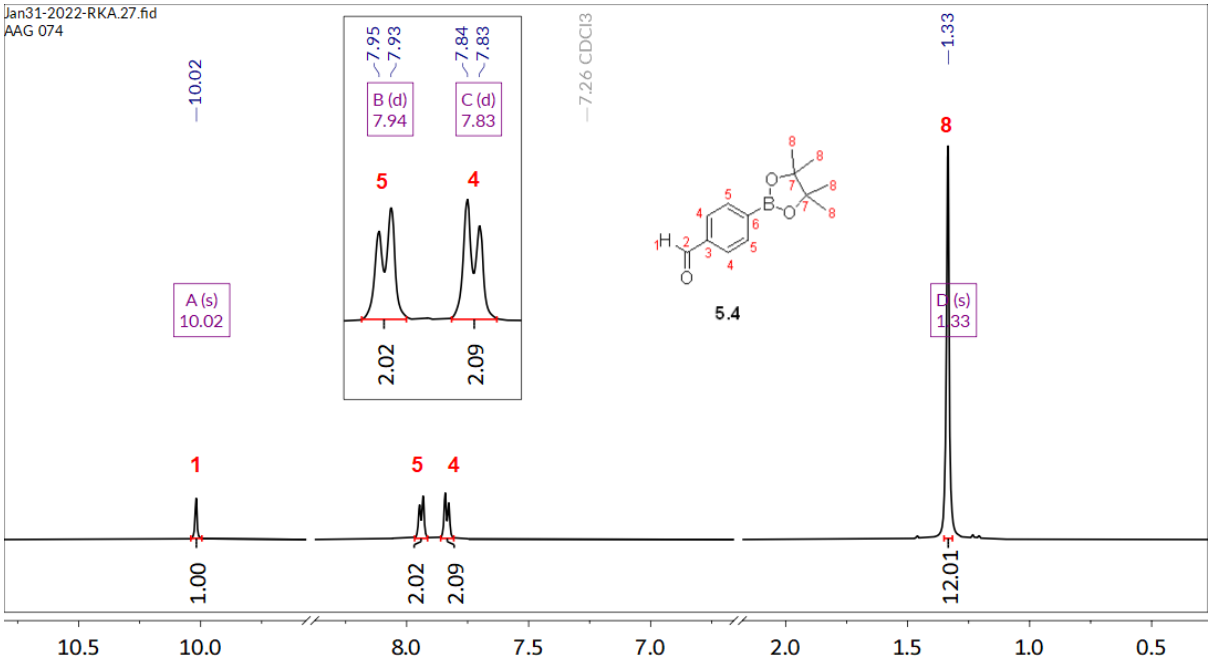

Appendix 1. 9: ^{1}H NMR spectrum (400 MHz, $CDCl_3$) of 4-(4,4,5,5-tetramethyl-1,3,2-dioxaborolan-2-yl)benzaldehyde **5.4.**

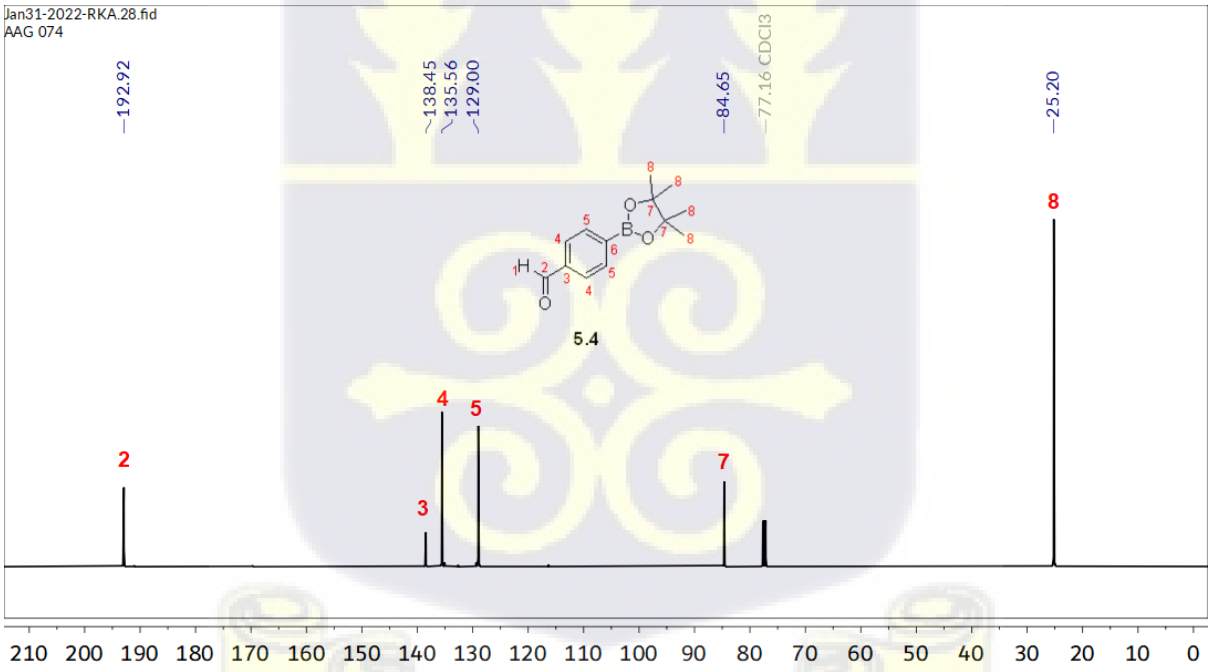

Appendix 1. 10: ^{13}C NMR spectrum (101 MHz, $CDCl_3$) of 4-(4,4,5,5-tetramethyl-1,3,2-dioxaborolan-2-yl)benzaldehyde **5.4.**

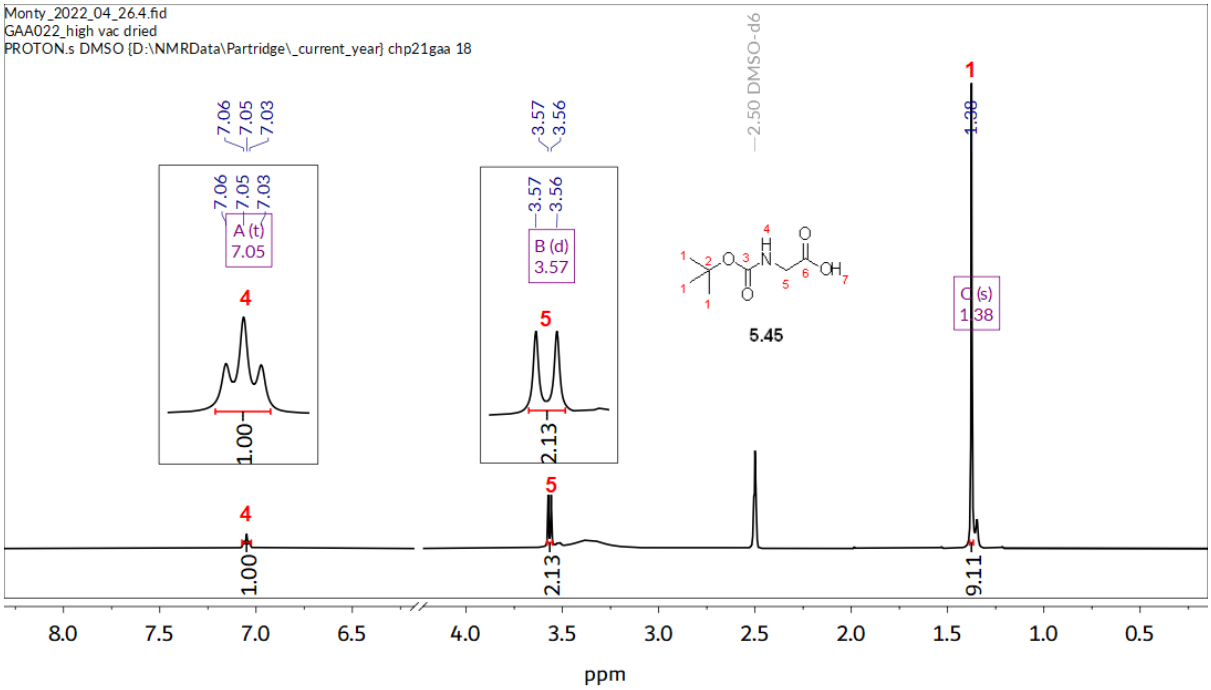

Appendix 1. 11: ^{1}H NMR spectrum (400 MHz, DMSO-d_6) of 2-(tert-butoxycarbonylamino)acetic acid **5.45.**

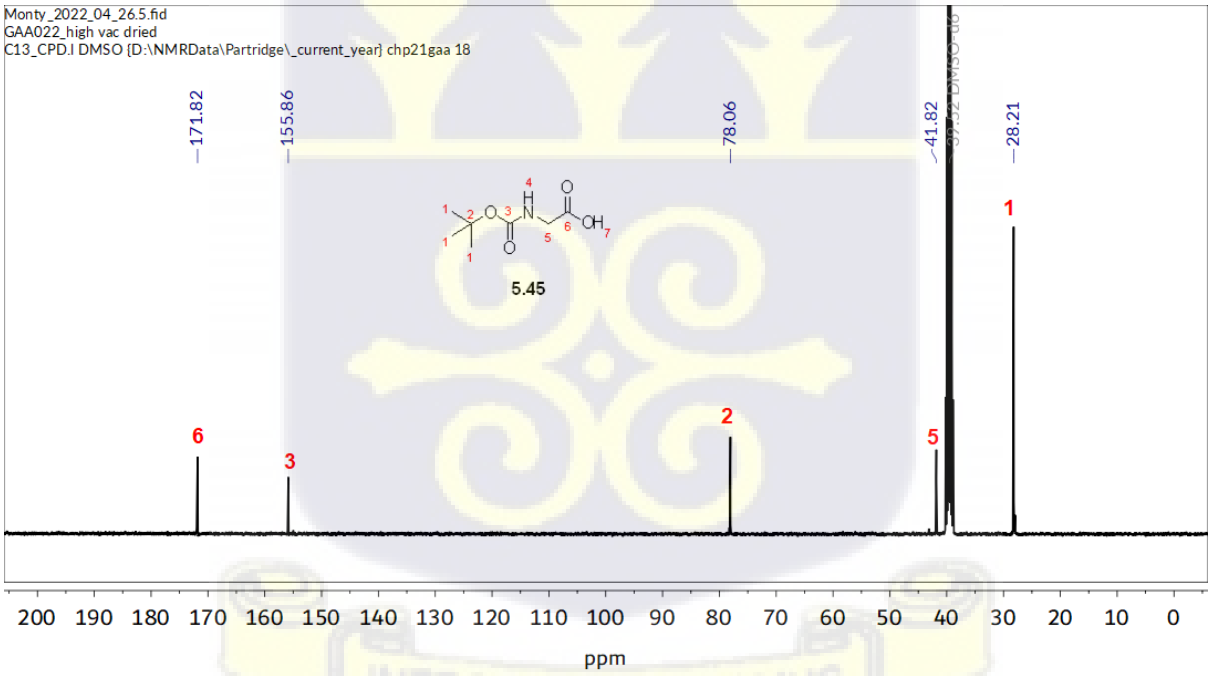

Appendix 1. 12: ^{13}C NMR spectrum (101 MHz, DMSO-d_6) of 2-(tert-butoxycarbonylamino)acetic acid **5.45**.

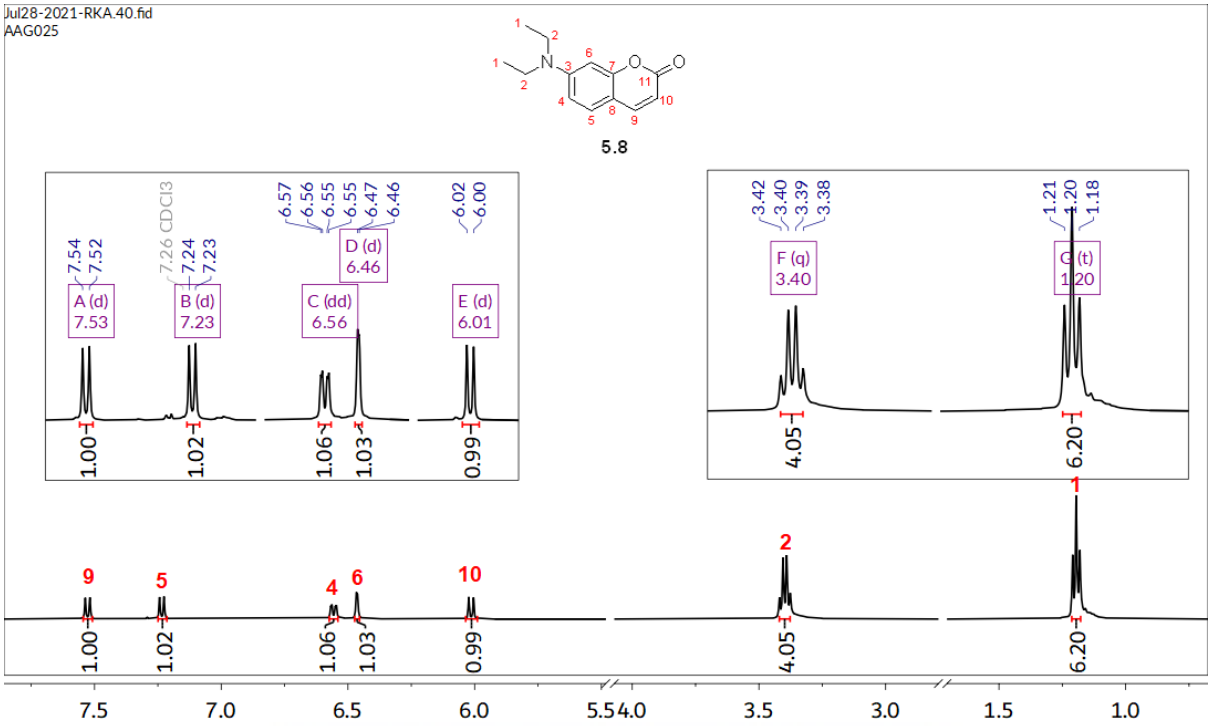

Appendix 1. 13: ^{1}H NMR spectrum (500 MHz, $CDCl_3$) of 7-(diethylamino)-2H-chromen-2-one **5.8.**

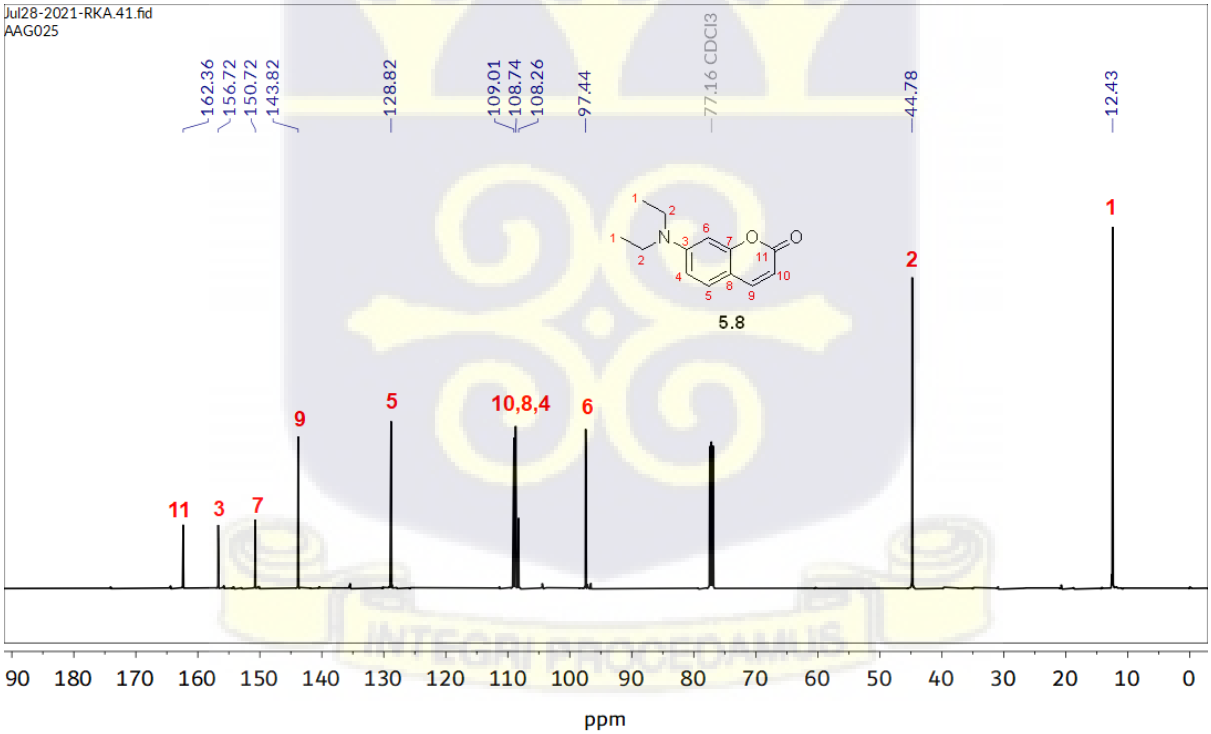

Appendix 1. 14: ^{13}C NMR spectrum (126 MHz, $CDCl_3$) of 7-(diethylamino)-2H-chromen-2-one **5.8.**

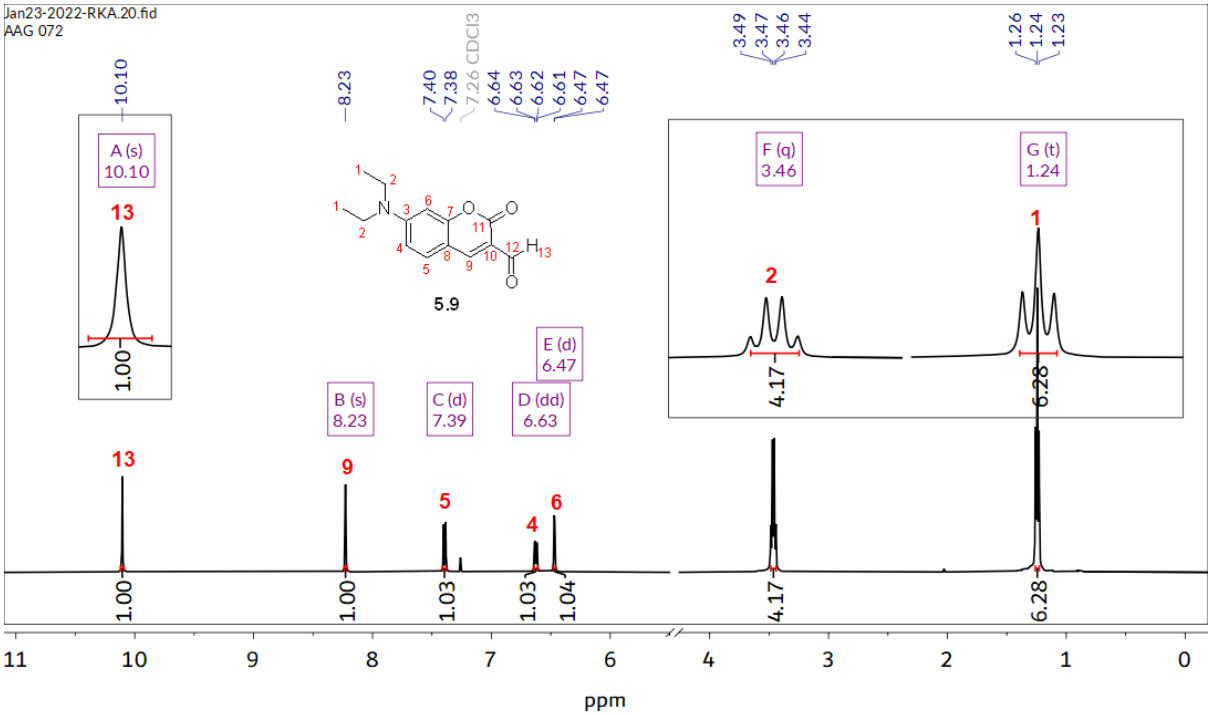

Appendix 1. 15: ^{1}H NMR spectrum (500 MHz, $CDCl_3$) of 7-(diethylamino)-2-oxo-2H-chromene-3-carbaldehyde **5.9.**

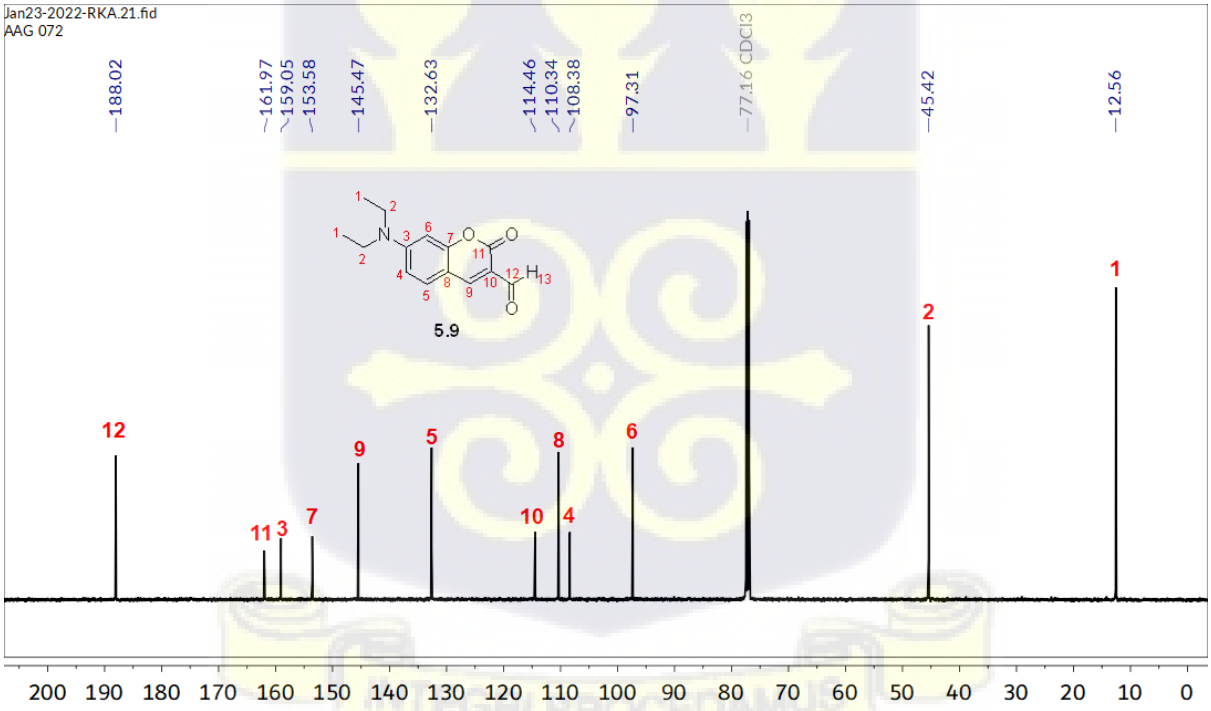

Appendix 1. 16: ^{13}C NMR spectrum (126 MHz, $CDCl_3$) of 7-(diethylamino)-2-oxo-2H-chromene-3-carbaldehyde **5.9.**

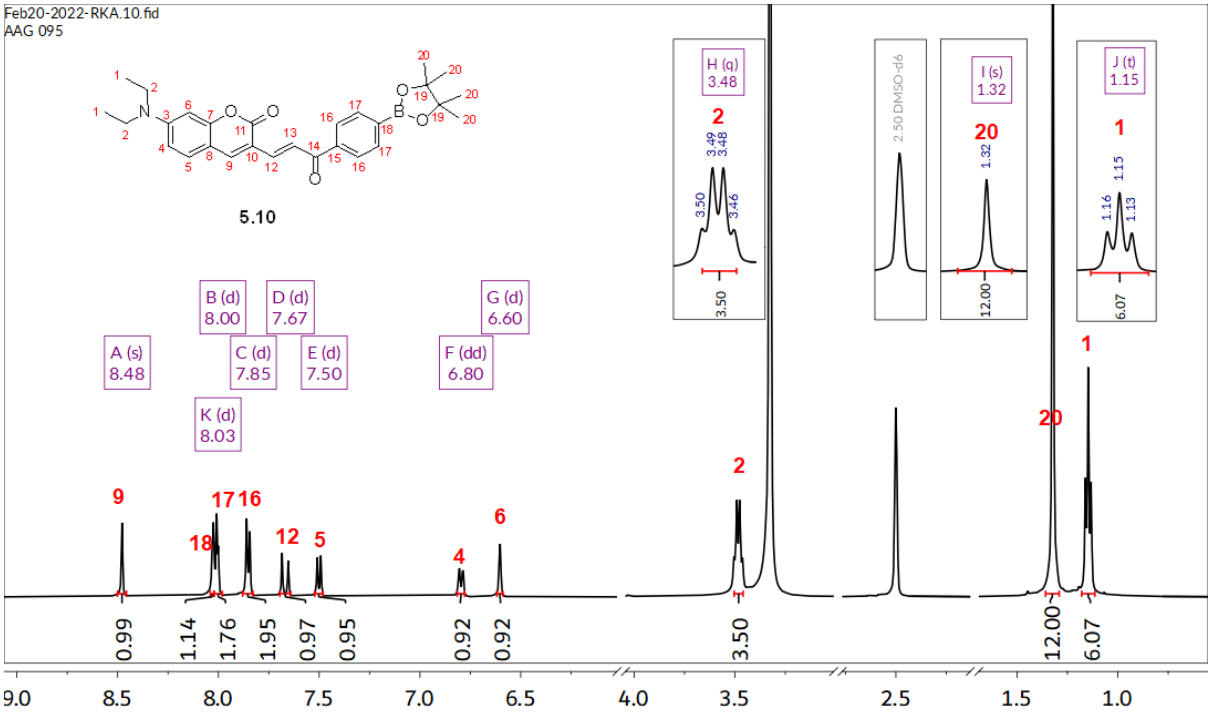

Appendix 1. 17: ^{1}H NMR spectrum (500 MHz, DMSO-*d*$_6$) of (E)-7-(diethylamino)-3-(3-oxo-3-(4-(4,4,5,5-tetramethyl-1,3,2-dioxaborolan-2-yl)phenyl)prop-1-en-1-yl)-2H-chromen-2-one **5.10.**

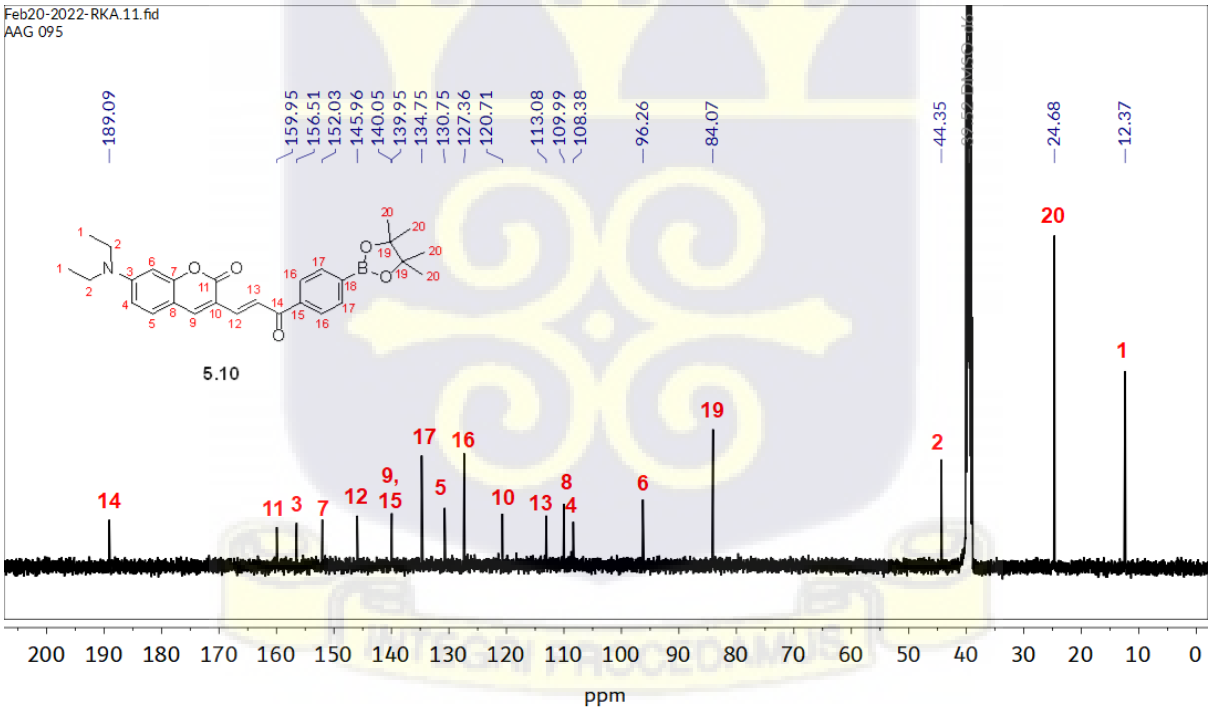

Appendix 1. 18: ^{13}C NMR spectrum (126 MHz, DMSO-*d*$_6$) of (E)-7-(diethylamino)-3-(3-oxo-3-(4-(4,4,5,5-tetramethyl-1,3,2-dioxaborolan-2-yl)phenyl)prop-1-en-1-yl)-2H-chromen-2-one **5.10.**

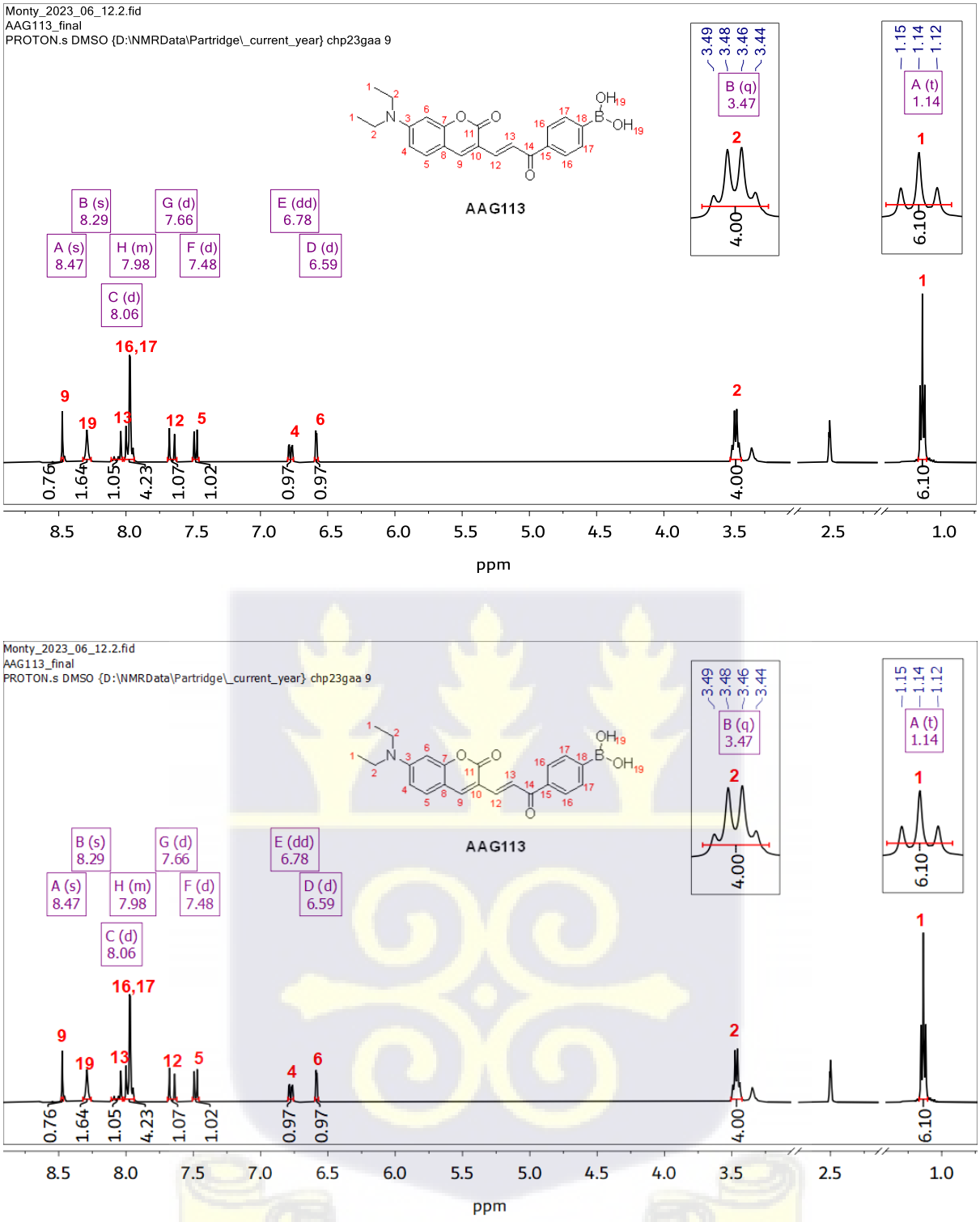

Appendix 1. 19: ^{1}H NMR spectrum (400 MHz, DMSO-d_6) of (E)-(4-(3-(7-(diethylamino)-2-oxo-2H-chromen-3-yl)acryloyl)phenyl)boronic acid **AAG113.**

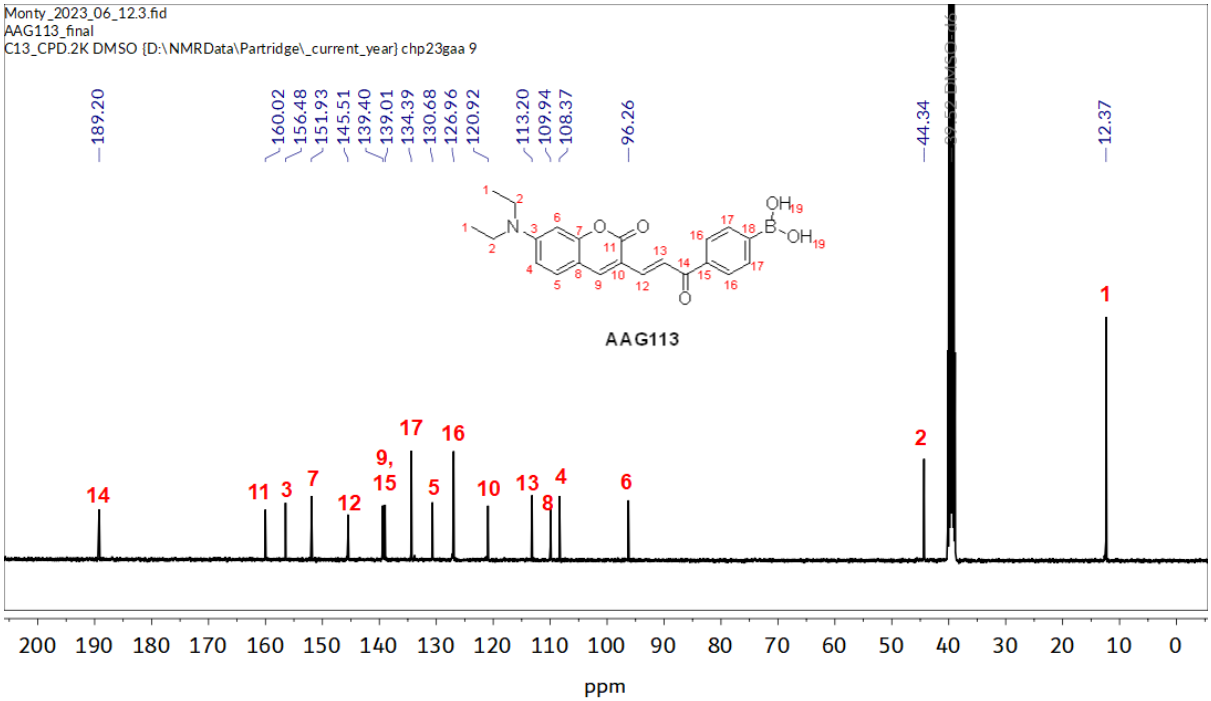

Appendix 1. 20: ^{13}C NMR spectrum (101 MHz, DMSO-d_6) of (E)-(4-(3-(7-(diethylamino)-2-oxo-2H-chromen-3-yl)acryloyl)phenyl)boronic acid **AAG113.**

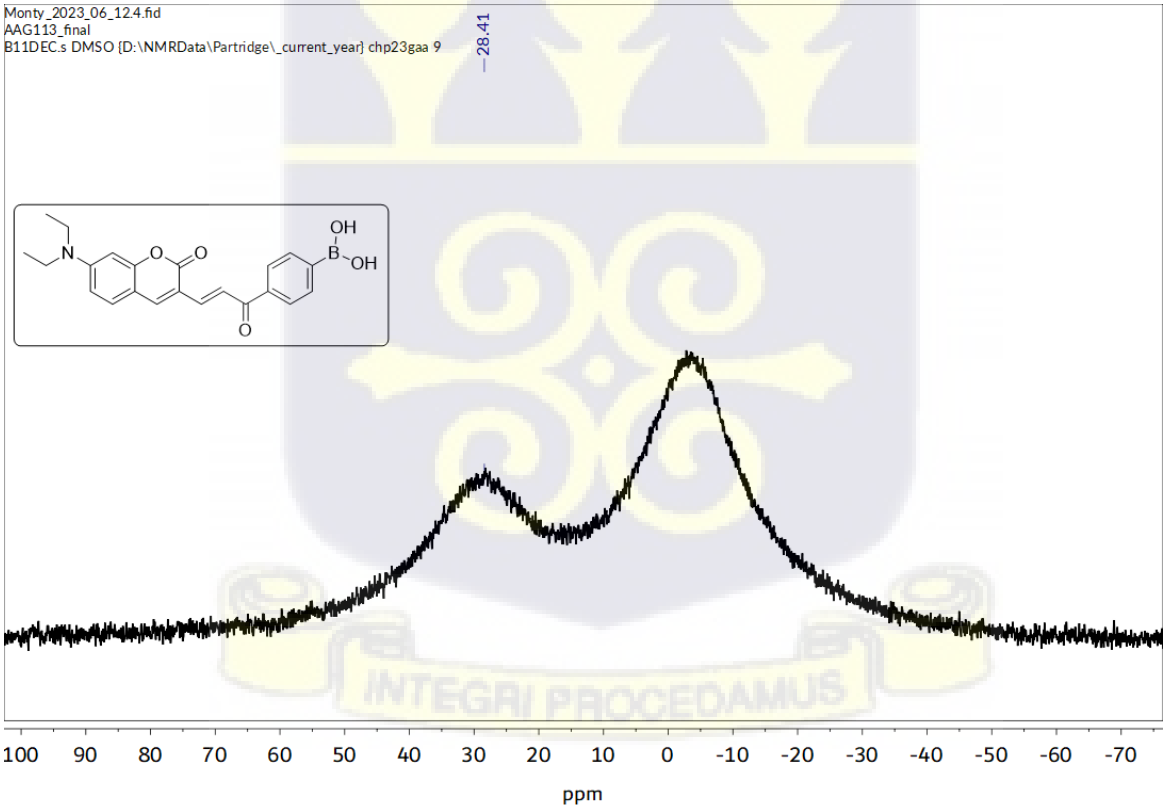

Appendix 1. 21: ^{11}B NMR (128 MHz, DMSO-d_6) of (E)-(4-(3-(7-(diethylamino)-2-oxo-2H-chromen-3-yl)acryloyl)phenyl)boronic acid **AAG113.**

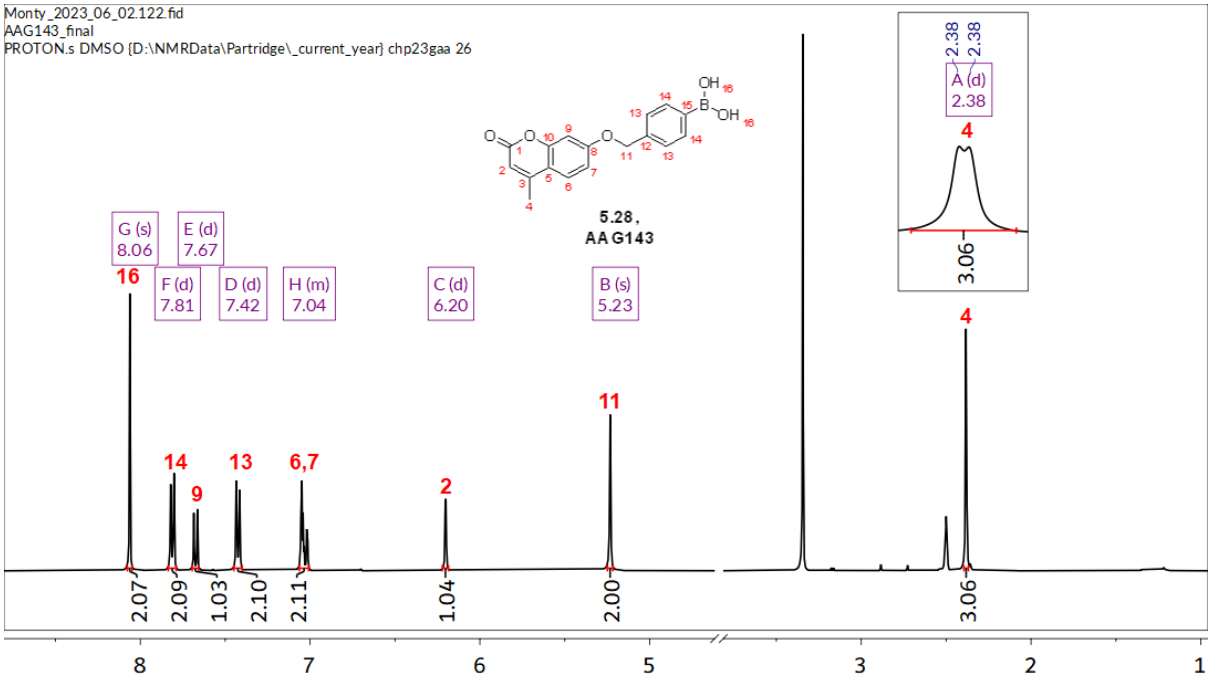

Appendix 1. 22: ^{1}H NMR spectrum (400 MHz, DMSO-d_6) of (4-(((4-methyl-2-oxo-2H-chromen-7-yl)oxy)methyl)phenyl)boronic acid **5.28 (AAG143).**

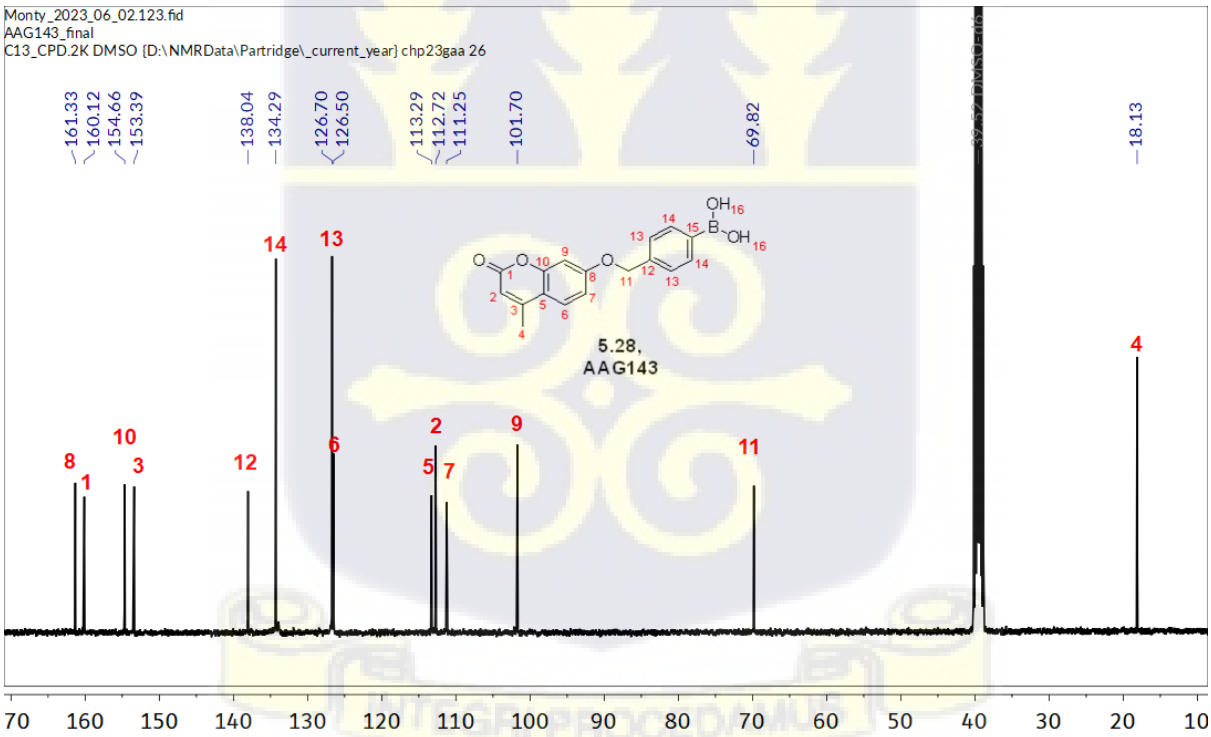

Appendix 1. 23: ^{13}C NMR spectrum (101 MHz, DMSO-d_6) of (4-(((4-methyl-2-oxo-2H-chromen-7-yl)oxy)methyl)phenyl)boronic acid **5.28 (AAG143).**

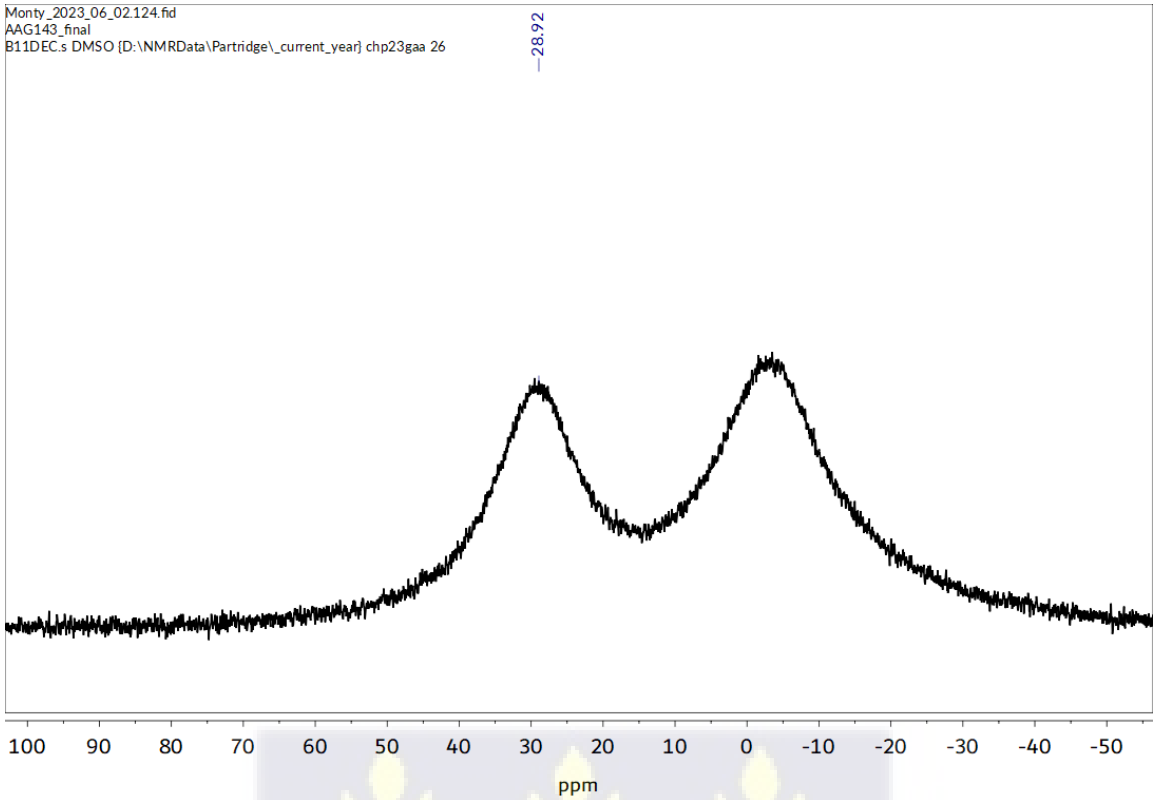

Appendix 1. 24: ^{11}B NMR (128 MHz, DMSO-d_6) of (4-(((4-methyl-2-oxo-2H-chromen-7-yl)oxy)methyl)phenyl)boronic acid **5.28 (AAG143).**

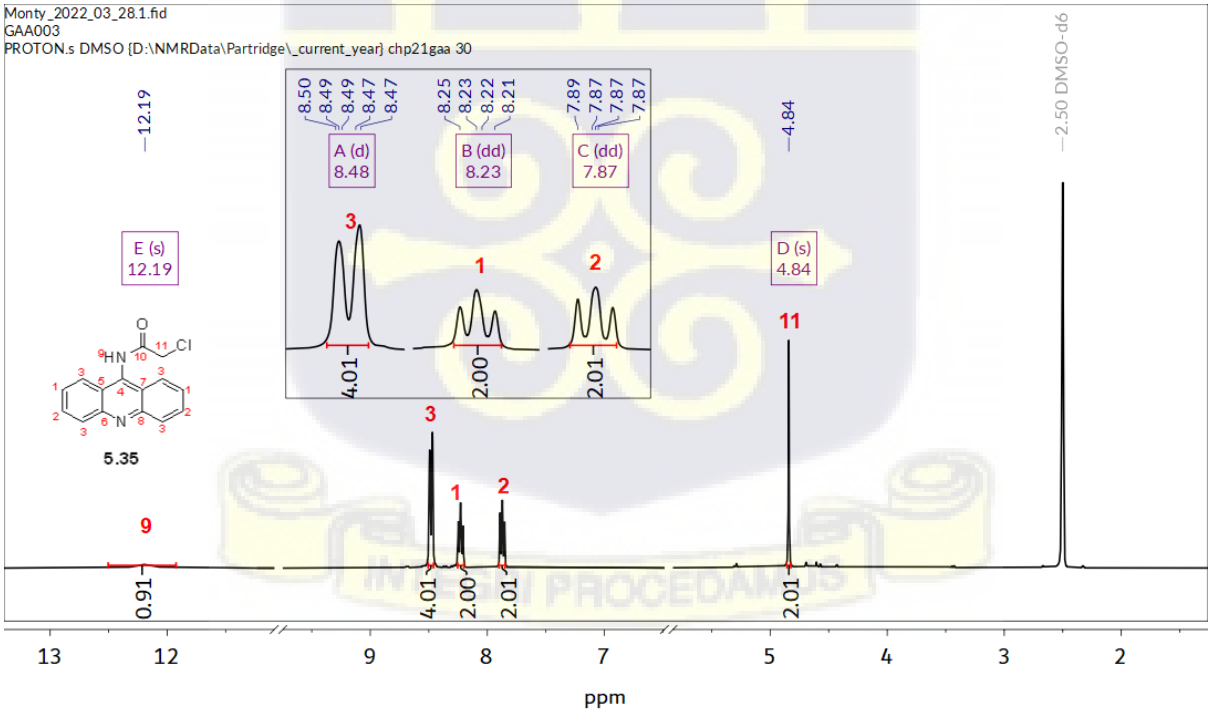

Appendix 1. 25: ^{1}H NMR spectrum (400 MHz, DMSO-d_6) of N-(acridin-9-yl)-2-chloroacetamide **5.35.**

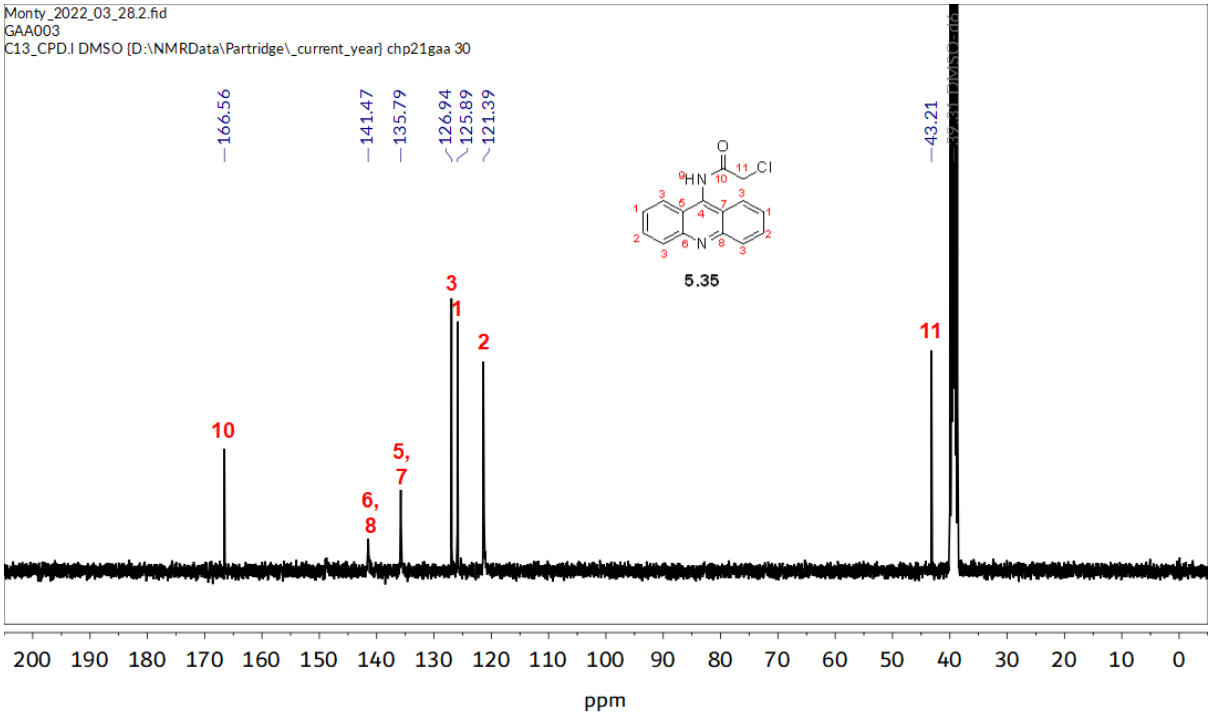

Appendix 1. 26: ^{13}C NMR spectrum (101 MHz, DMSO-d_6) of N-(acridin-9-yl)-2-chloroacetamide **5.35.**

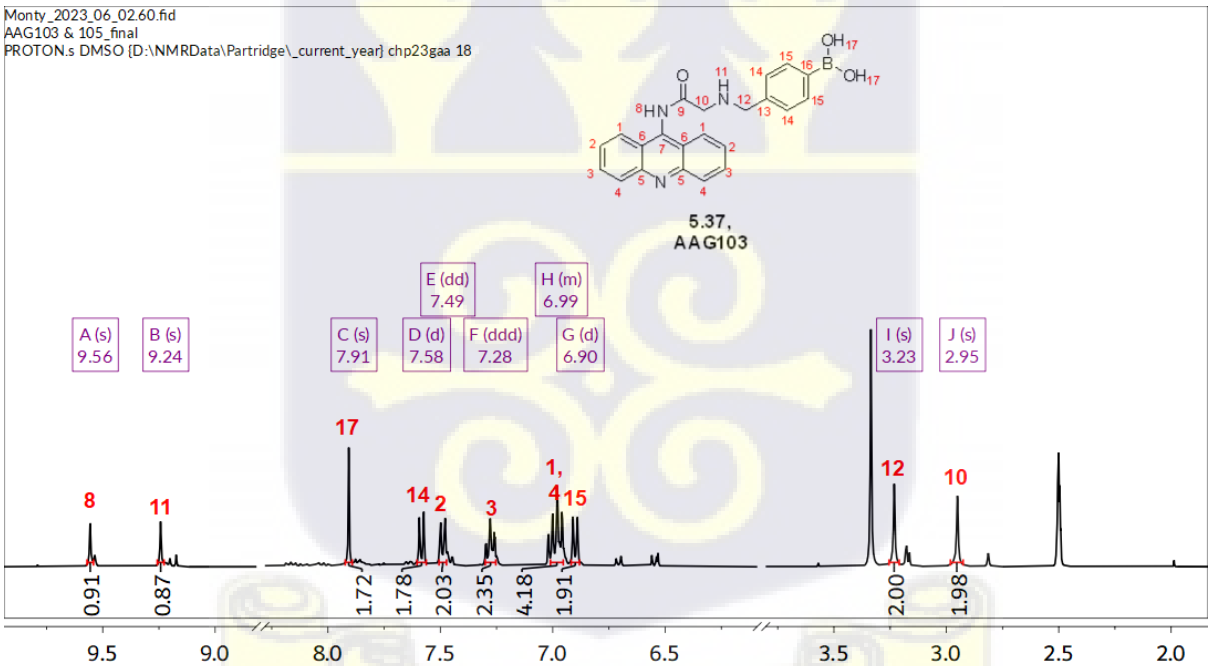

Appendix 1. 27: ^{1}H NMR spectrum (400 MHz, DMSO-d_6) of (4-(((2-(acridin-9-ylamino)-2-oxoethyl)amino)methyl)phenyl)boronic acid **5.37 (AAG103).**

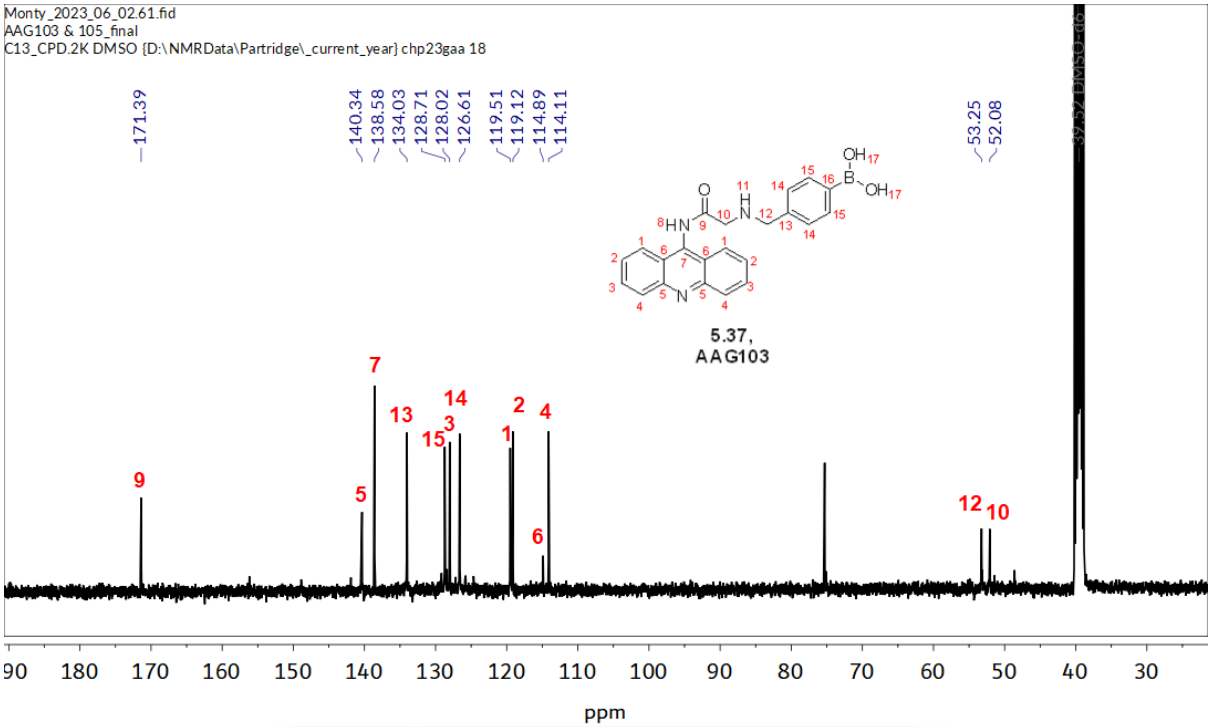

Appendix 1. 28: ^{13}C NMR spectrum (101 MHz, DMSO-d_6) of (4-(((2-(acridin-9-ylamino)-2-oxoethyl)amino)methyl)phenyl)boronic acid **5.37 (AAG103).**

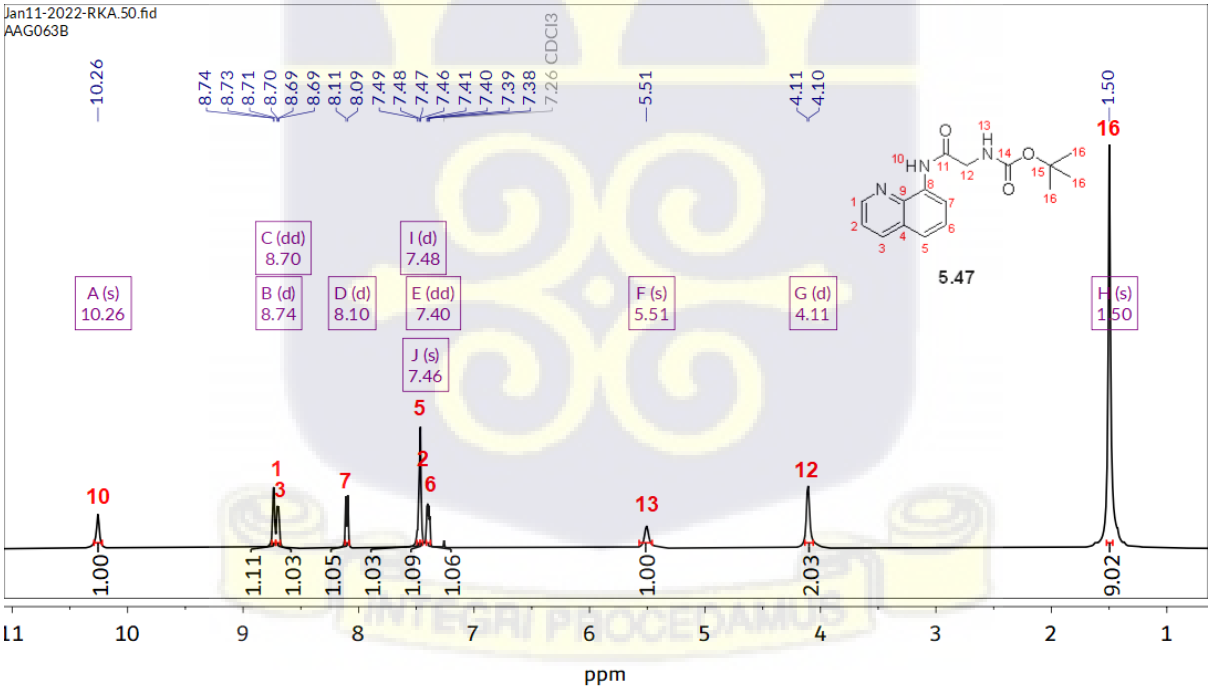

Appendix 1. 29: ^{1}H NMR spectrum (500 MHz, $CDCl_3$) of tert-butyl (2-oxo-2-(quinolin-8-ylamino)ethyl)carbamate **5.47.**

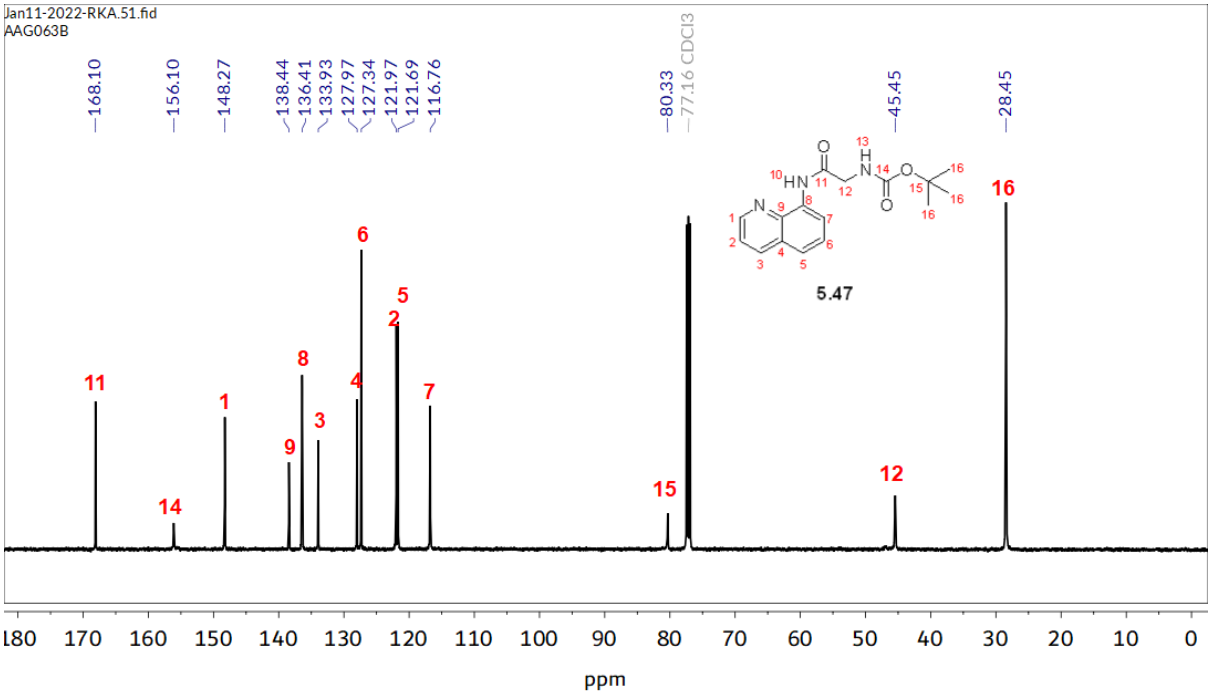

Appendix 1. 30: ^{13}C NMR spectrum (126 MHz, $CDCl_3$) of tert-butyl (2-oxo-2-(quinolin-8-ylamino)ethyl)carbamate **5.47.**

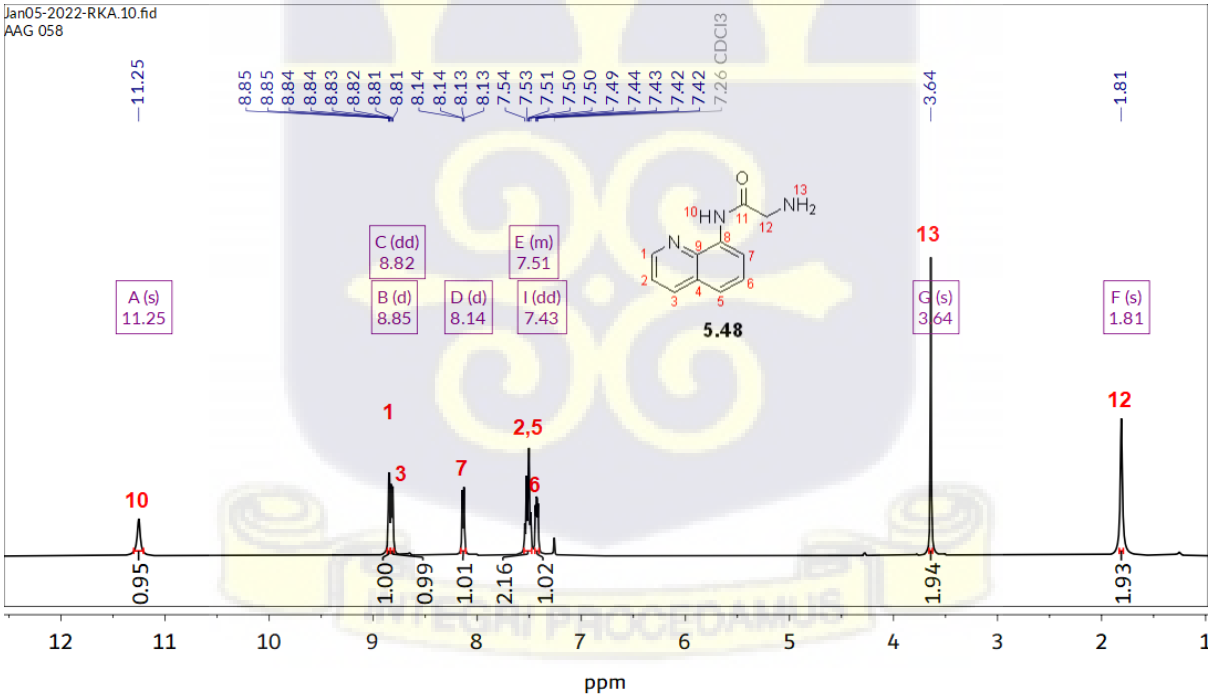

Appendix 1. 31: ^{1}H NMR spectrum (500 MHz, $CDCl_3$) of 2-amino-N-(quinolin-8-yl)acetamide **5.48.**

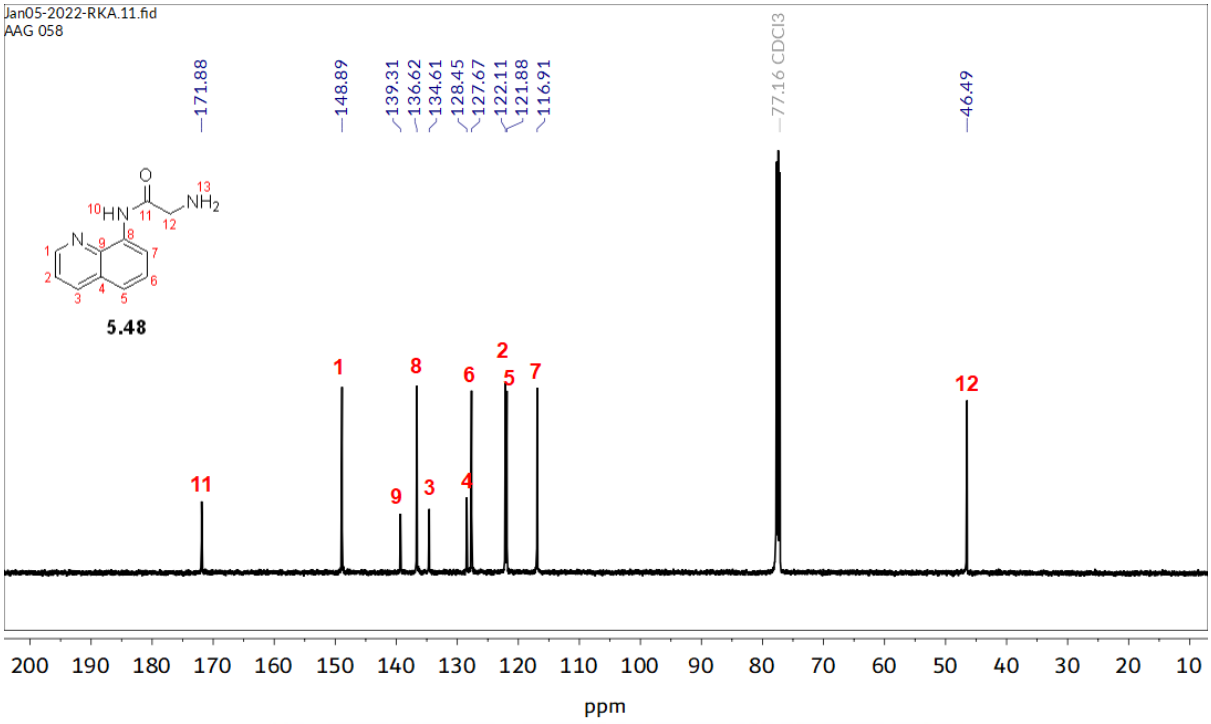

Appendix 1. 32: ^{13}C NMR spectrum (126 MHz, $CDCl_3$) of 2-amino-N-(quinolin-8-yl)acetamide **5.48.**

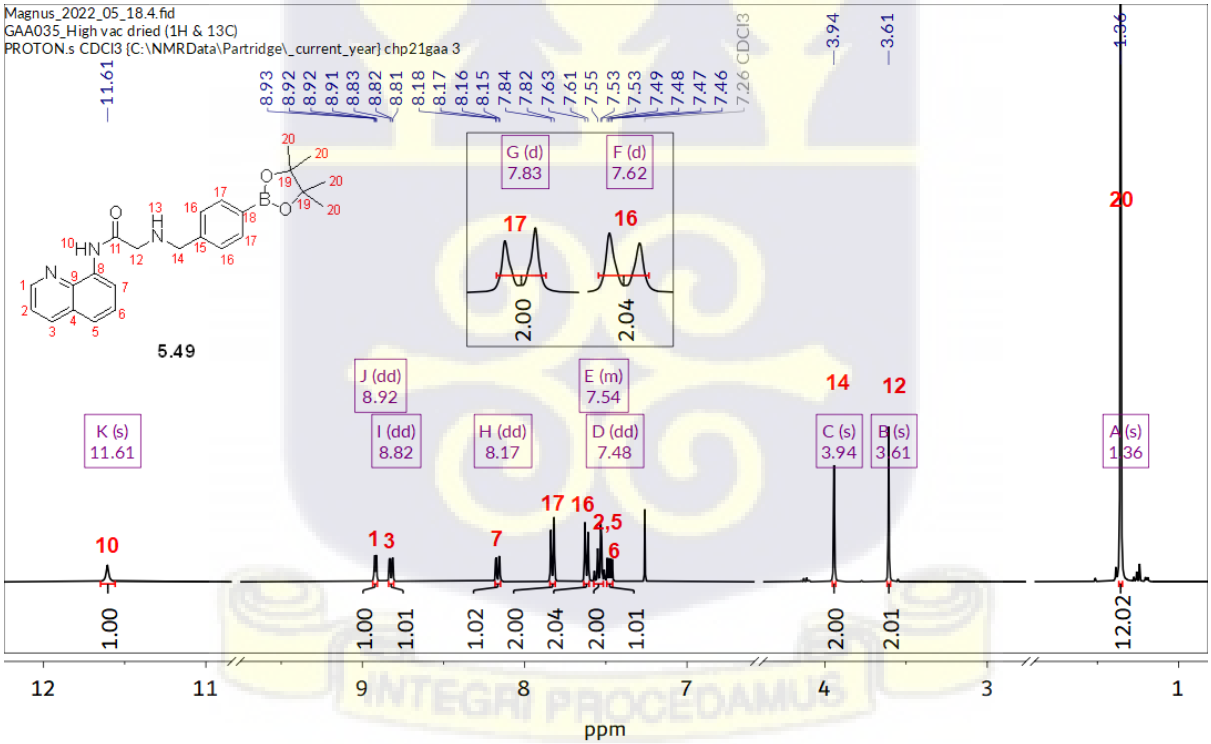

Appendix 1. 33: ^{1}H NMR spectrum (400 MHz, $CDCl_3$) of N-(quinolin-8-yl)-2-((4-(4,4,5,5-tetramethyl-1,3,2-dioxaborolan-2-yl)benzyl)amino)acetamide **5.49.**

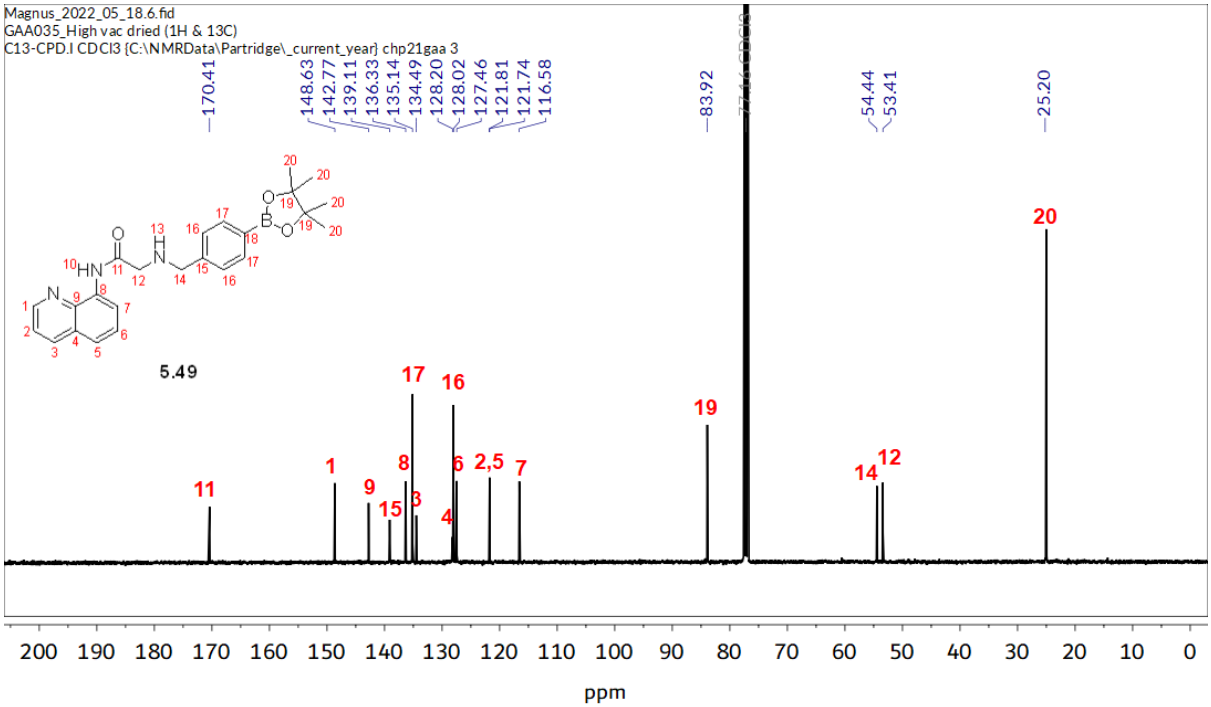

Appendix 1. 34: ^{13}C NMR spectrum (101 MHz, $CDCl_3$) of N-(quinolin-8-yl)-2-((4-(4,4,5,5-tetramethyl-1,3,2-dioxaborolan-2-yl)benzyl)amino)acetamide **5.49.**

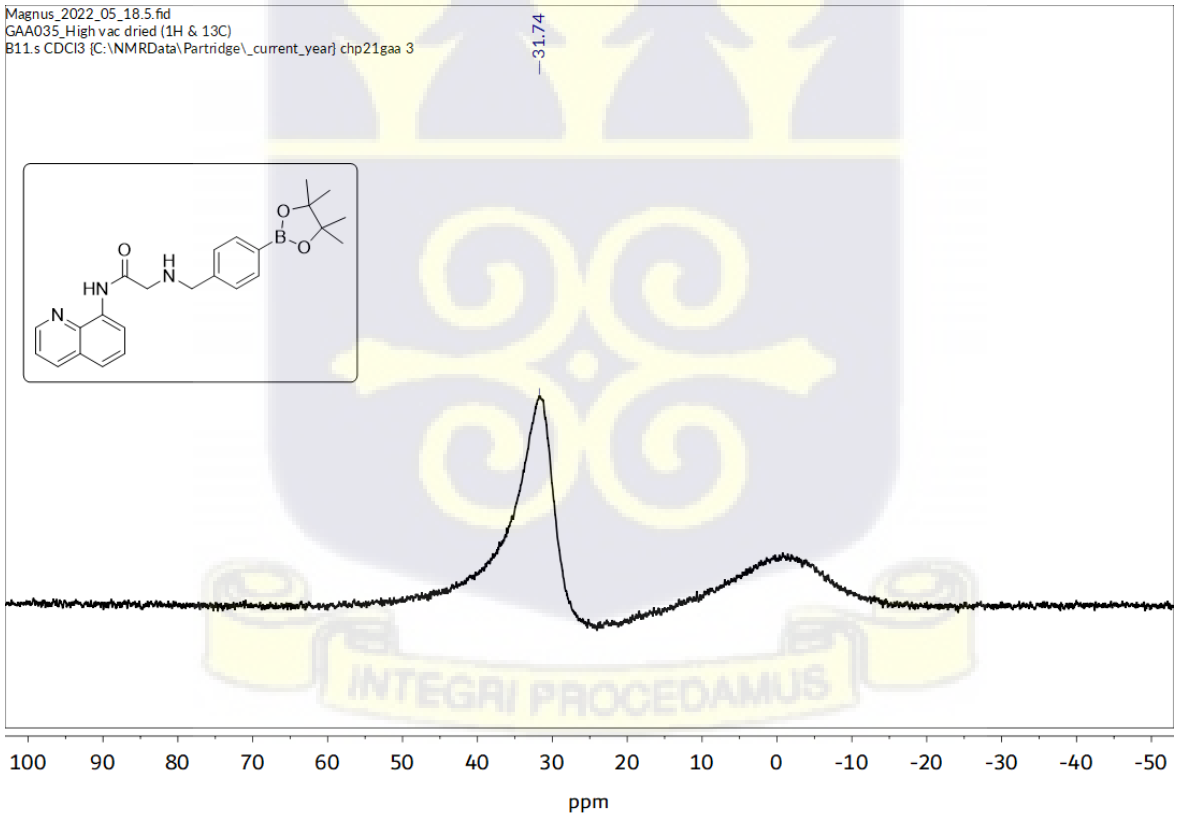

Appendix 1. 35: ^{11}B NMR (128 MHz, $CDCl_3$) of N-(quinolin-8-yl)-2-((4-(4,4,5,5-tetramethyl-1,3,2-dioxaborolan-2-yl)benzyl)amino)acetamide **5.49.**

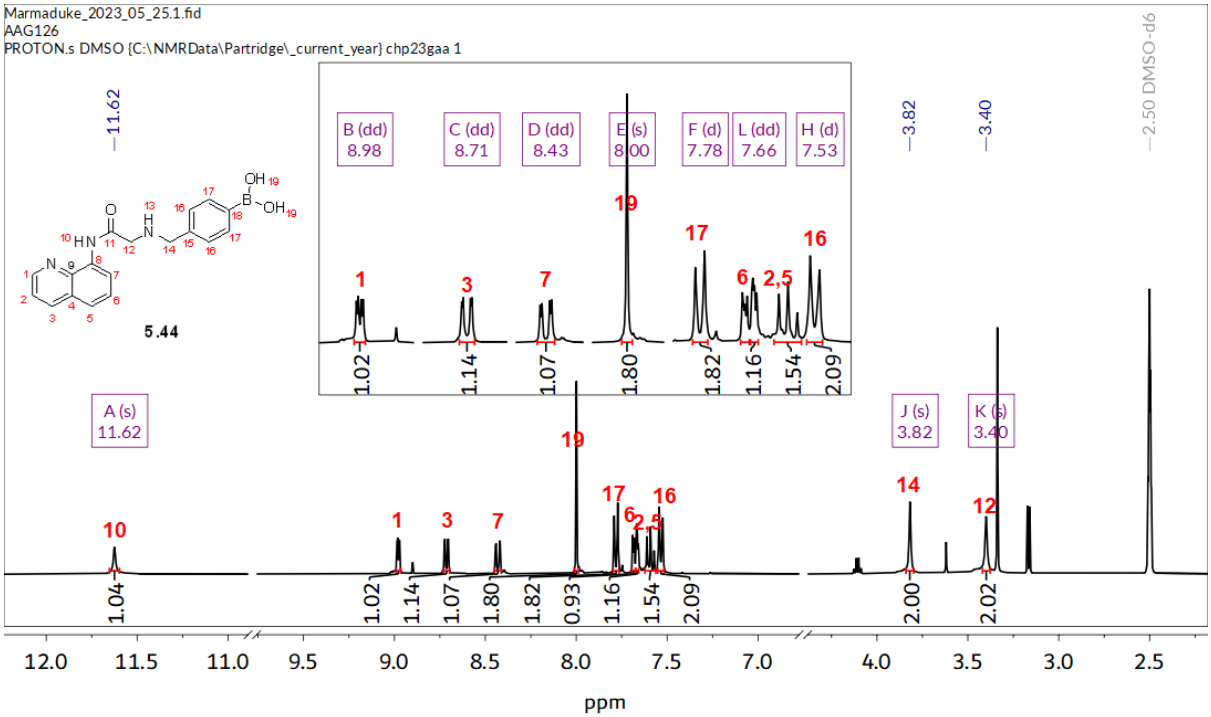

Appendix 1. 36: ^{1}H NMR spectrum (400 MHz, DMSO-*d*$_6$) of (4-(((2-oxo-2-(quinolin-8-ylamino)ethyl)amino)methyl)phenyl)boronic acid **5.44.**

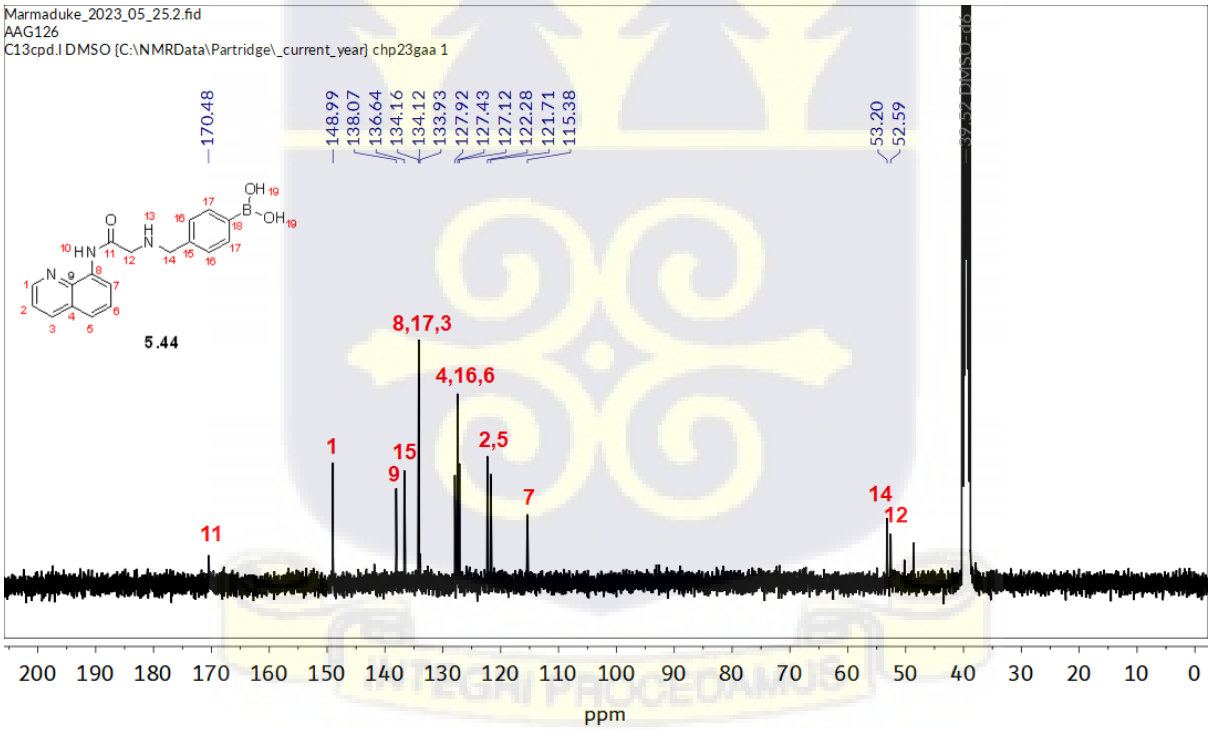

Appendix 1. 37: ^{13}C NMR spectrum (101 MHz, DMSO-*d*$_6$) of (4-(((2-oxo-2-(quinolin-8-ylamino)ethyl)amino)methyl)phenyl)boronic acid **5.44.**

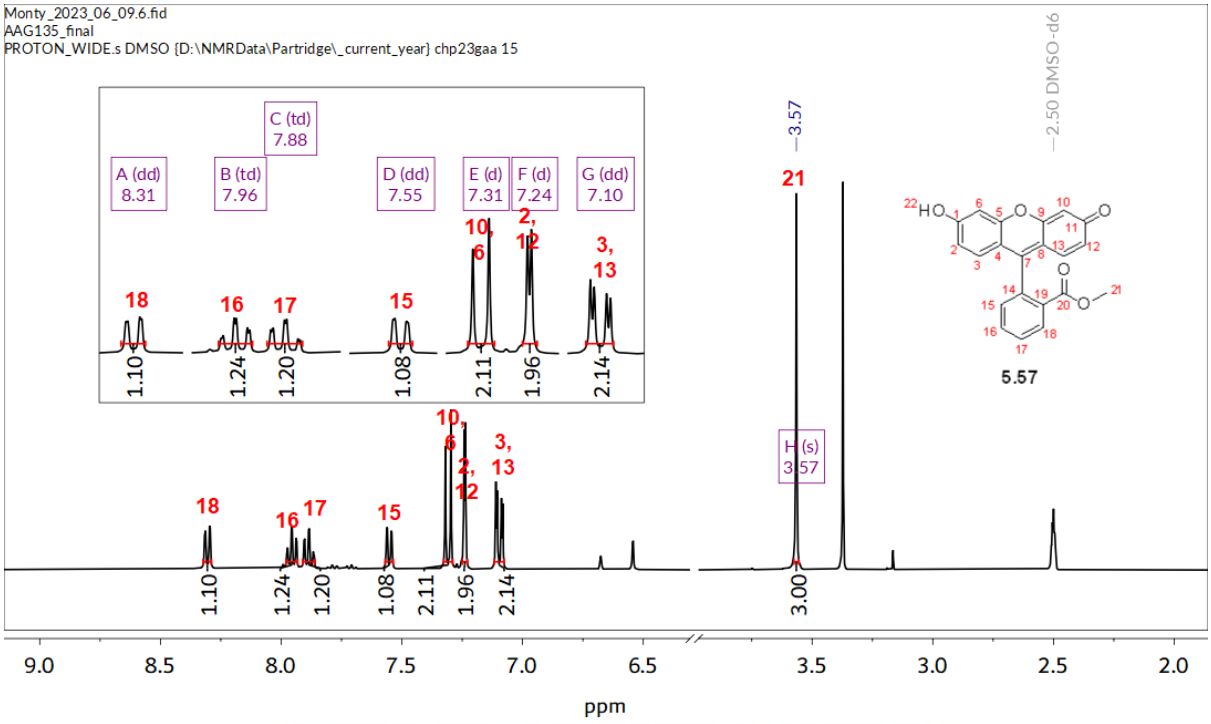

Appendix 1. 38: ^{1}H NMR spectrum (400 MHz, DMSO-d_6) of fluorescein methyl ester **5.57.**

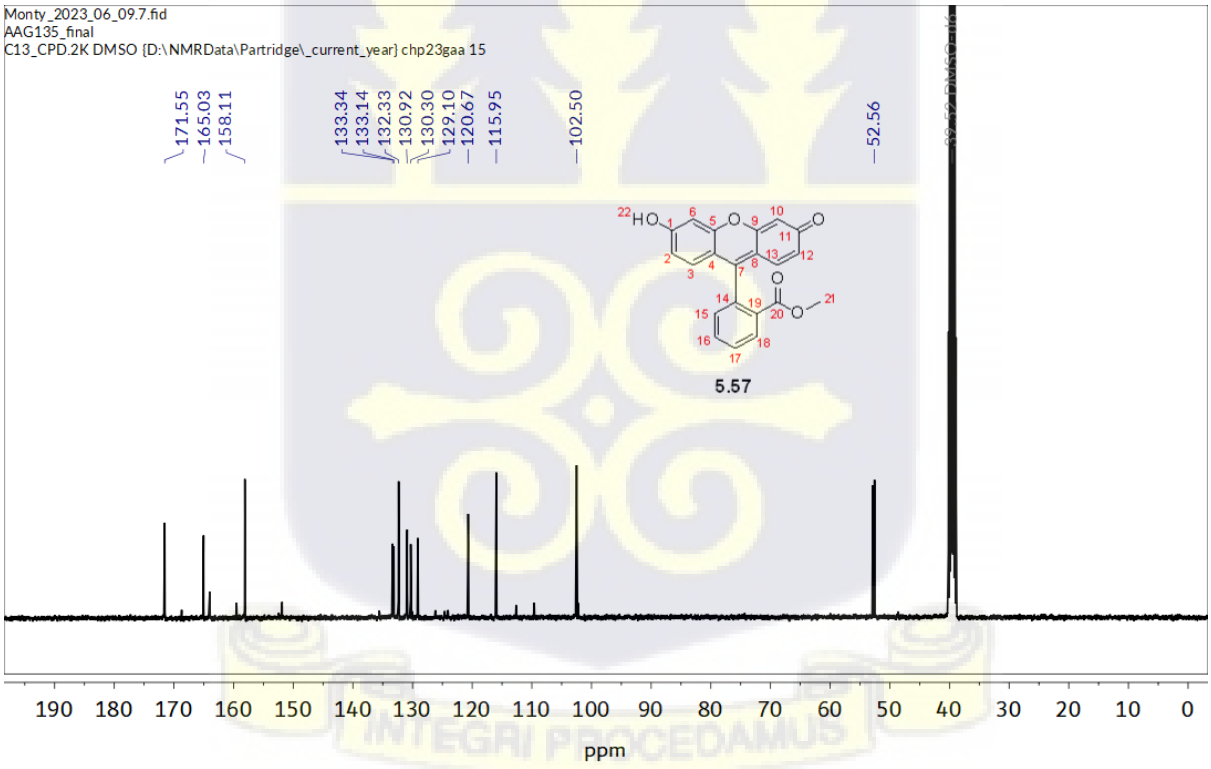

Appendix 1. 39: ^{13}C NMR spectrum (101 MHz, DMSO-d_6) of fluorescein methyl ester **5.57.**

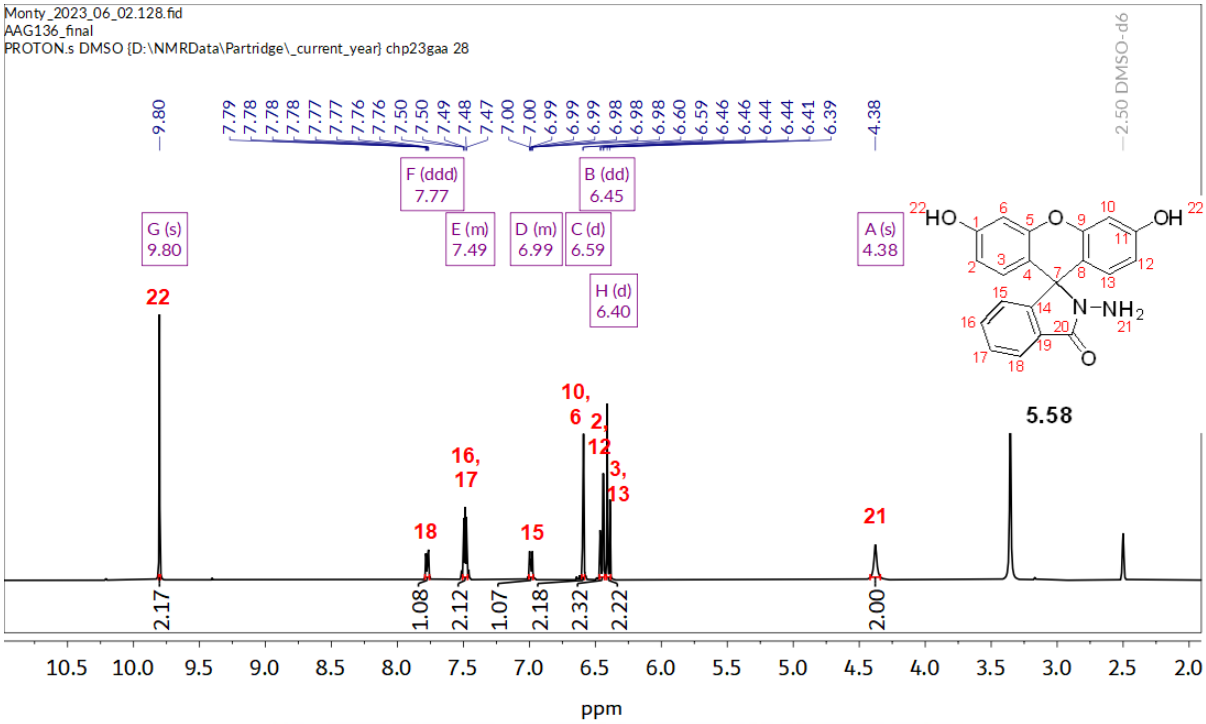

Appendix 1. 40: ^{1}H NMR spectrum (400 MHz, DMSO-d_6) of fluorescein hydrazide **5.58.**

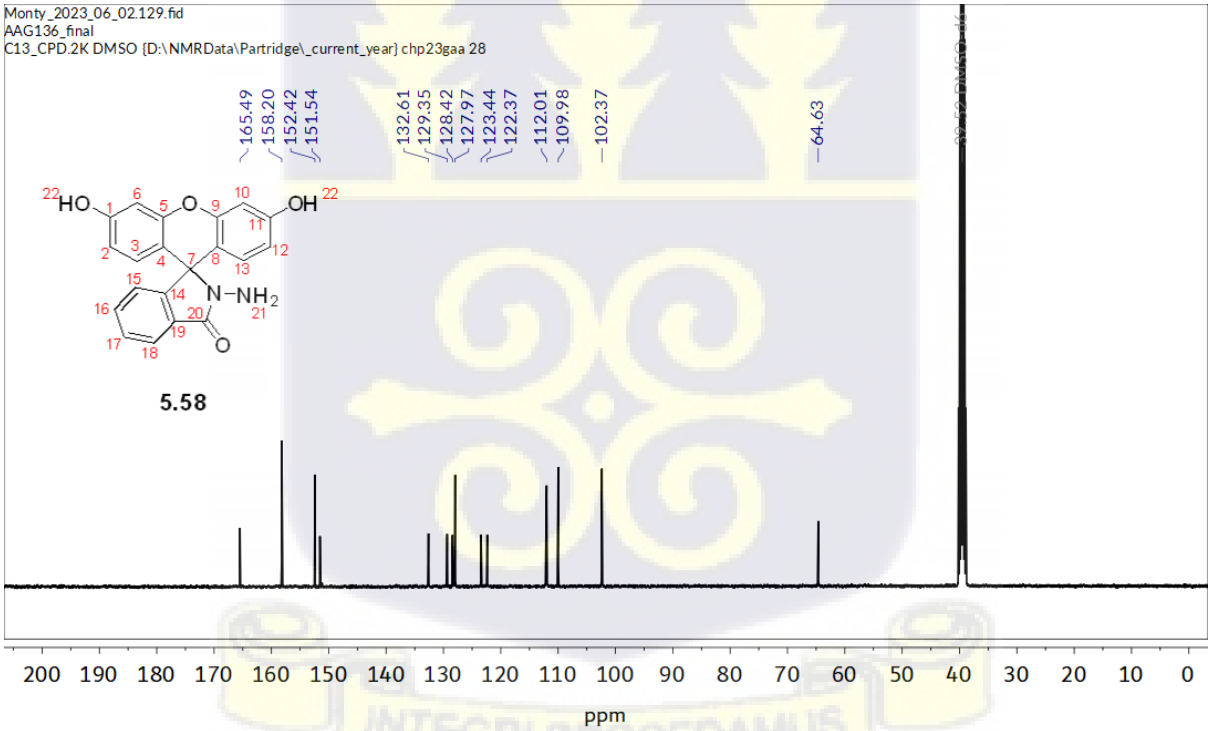

Appendix 1. 41: ^{13}C NMR spectrum (101 MHz, DMSO-d_6) of fluorescein hydrazide **5.58.**

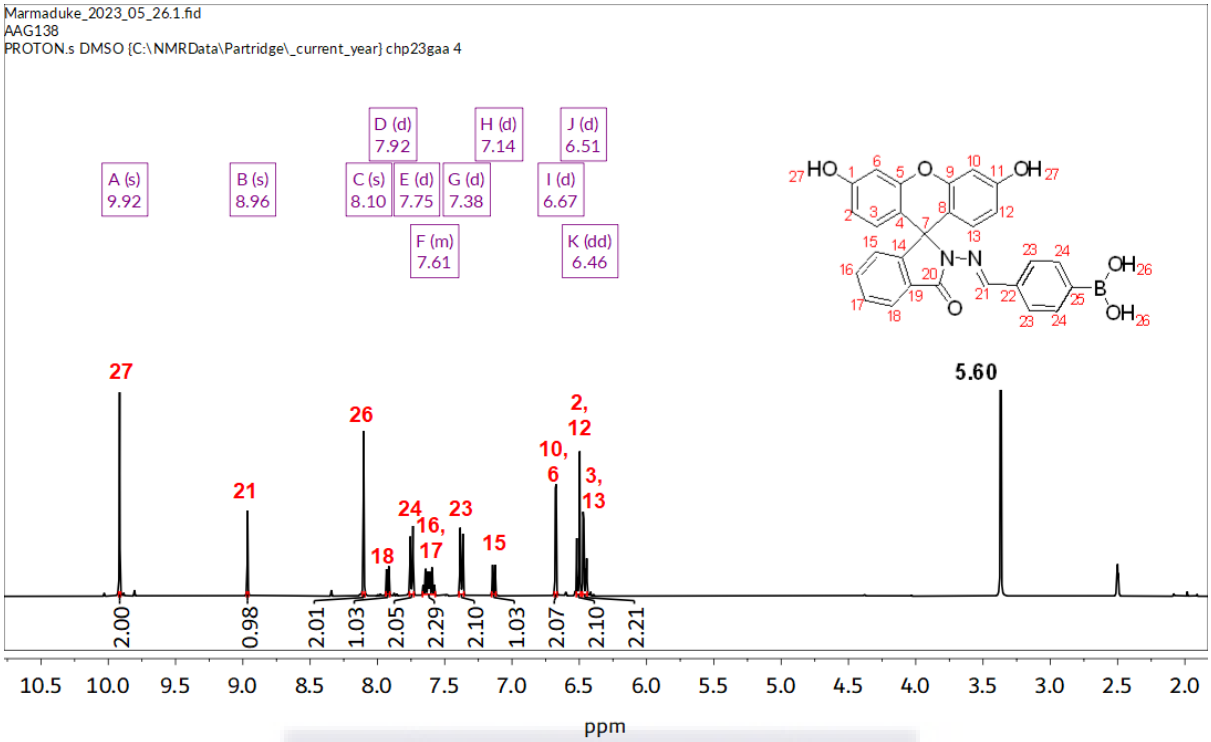

Appendix 1. 42: ^{1}H NMR spectrum (400 MHz, DMSO-d_6) of fluorescein-tagged arylboronic acid chemosensor **5.60 (AAG138).**

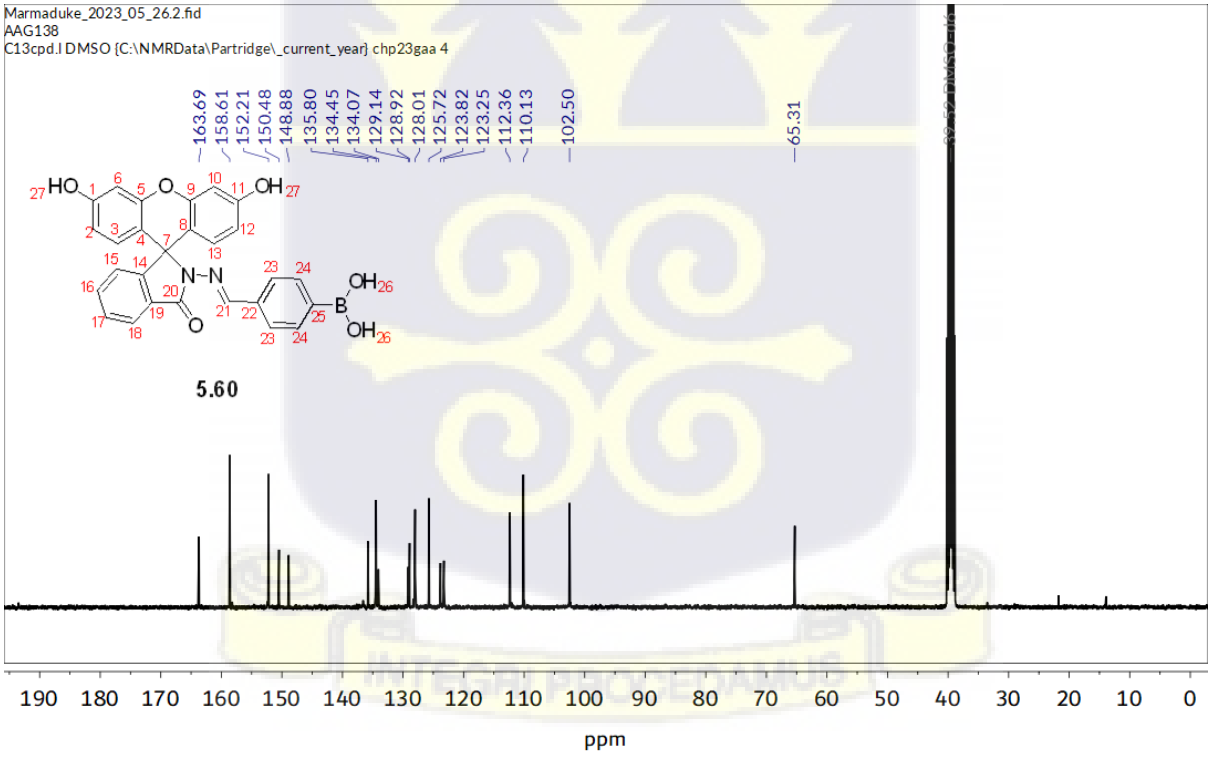

Appendix 1. 43: ^{13}C NMR spectrum (101 MHz, DMSO-d_6) of fluorescein-tagged arylboronic acid chemosensor **5.60 (AAG138).**

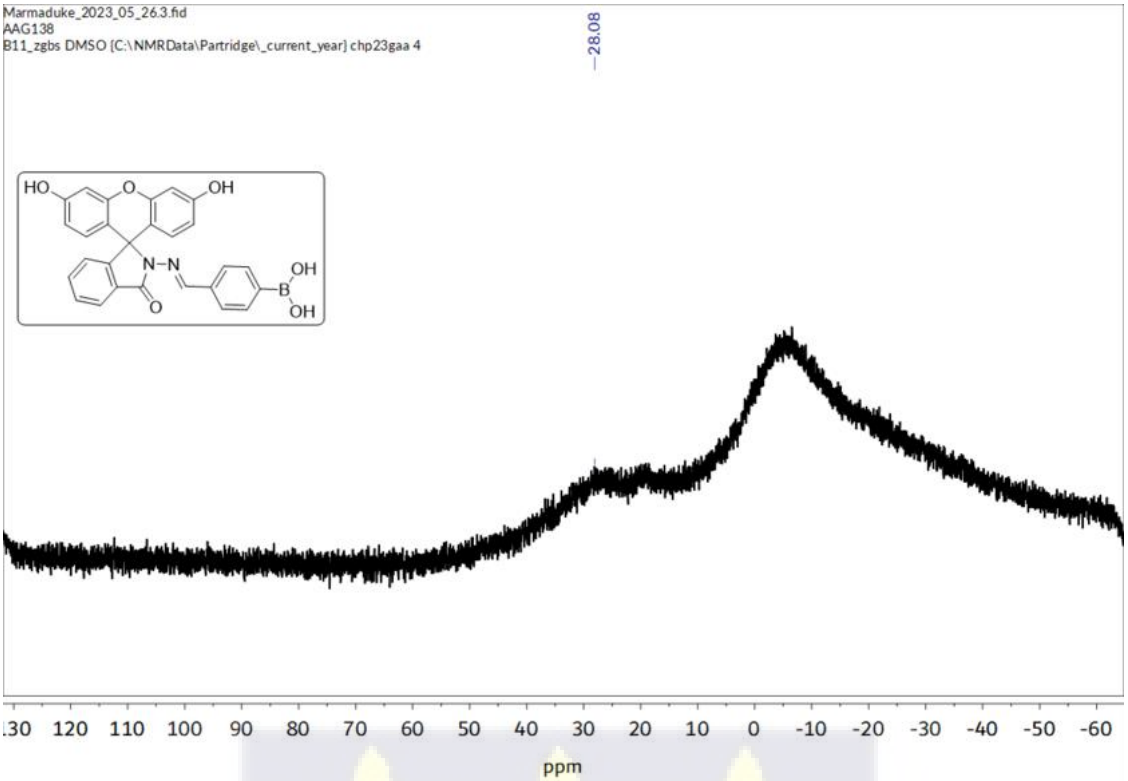

Appendix 1. 44: ^{11}B NMR (128 MHz, DMSO-d_6) of fluorescein-tagged arylboronic acid chemosensor **5.60 (AAG138).**

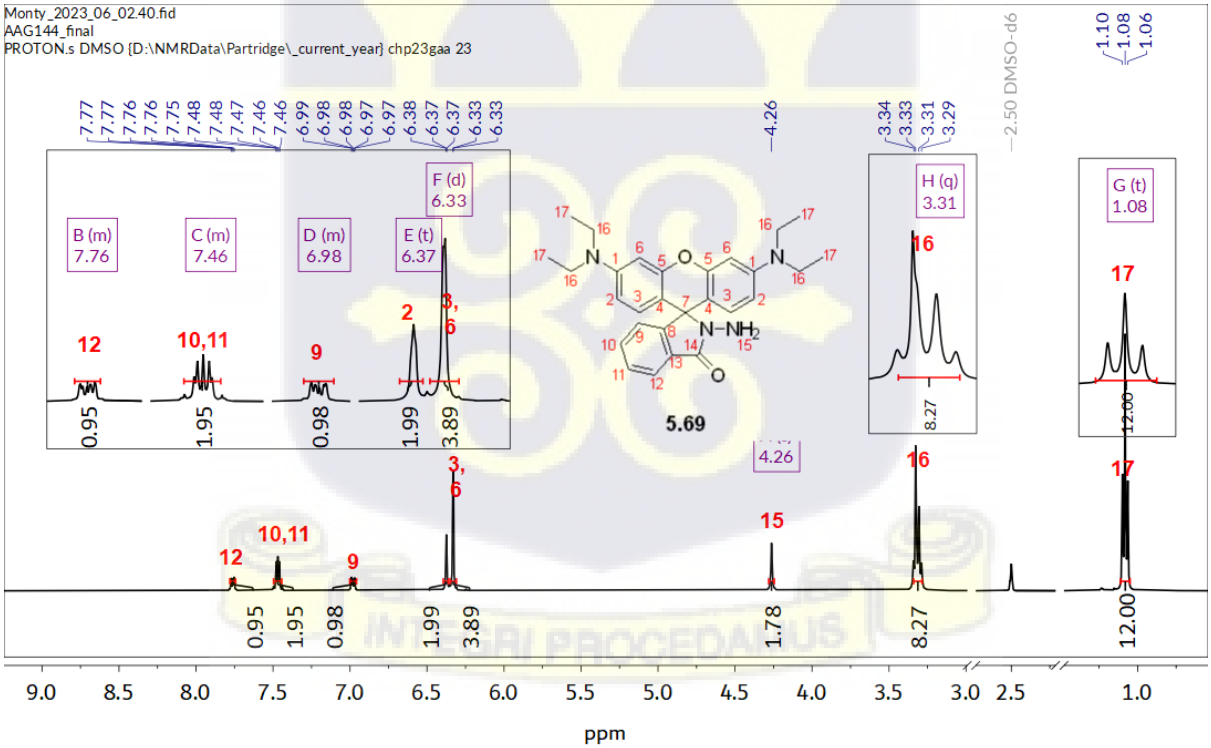

Appendix 1. 45: ^{1}H NMR spectrum (400 MHz, DMSO-d_6) of Rhodamine B hydrazide **5.69.**

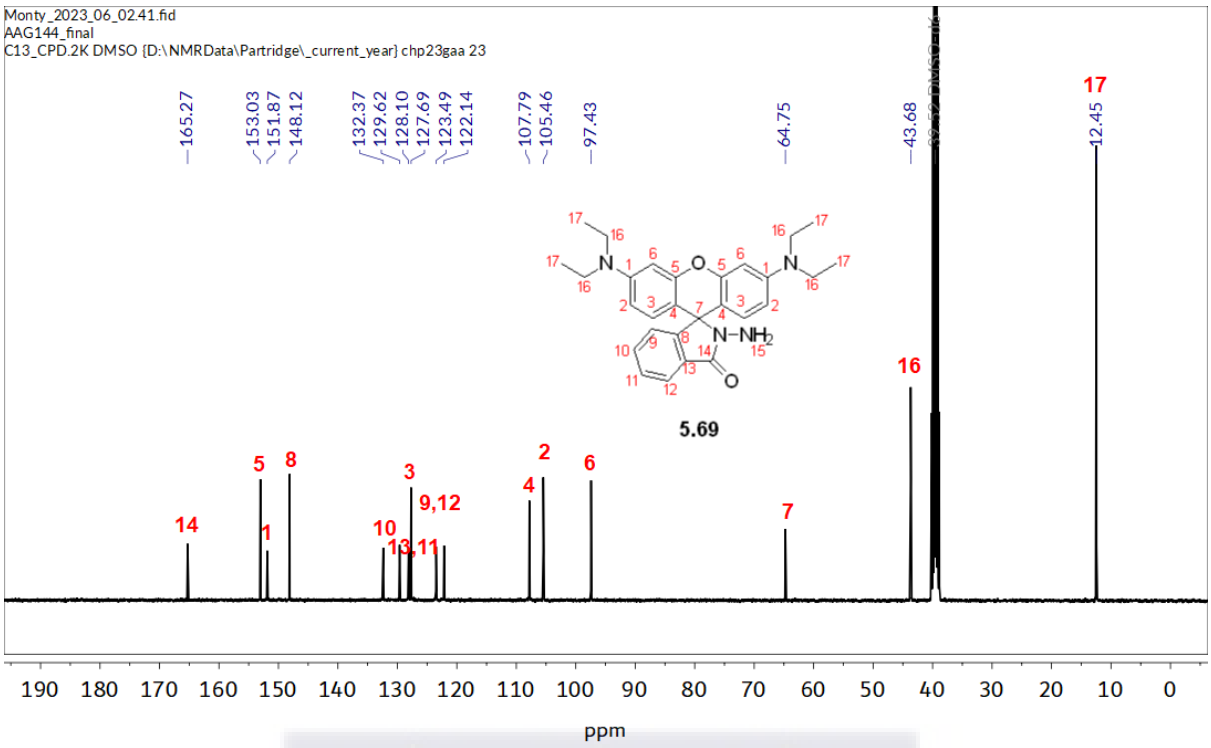

Appendix 1. 46: ^{13}C NMR spectrum (101 MHz, DMSO-d_6) of Rhodamine B hydrazide **5.69.**

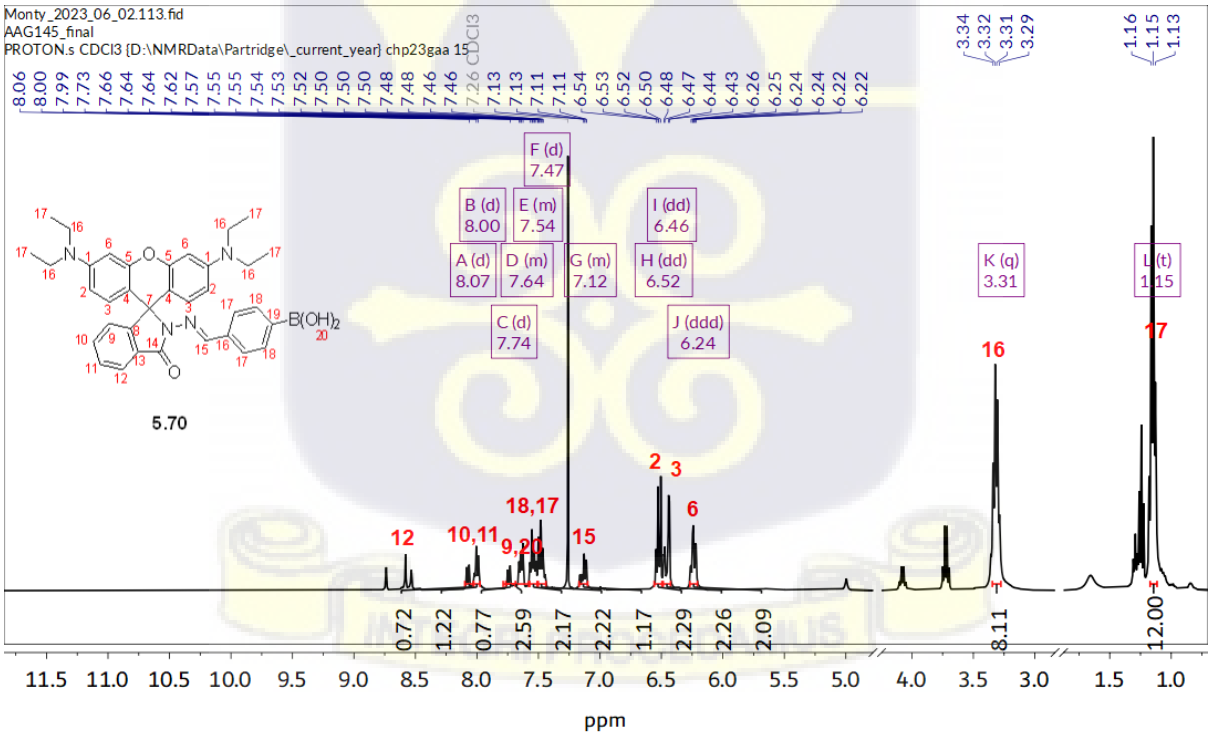

Appendix 1. 47: ^{1}H NMR spectrum (400 MHz, $CDCl_3$) of Rhodamine B boronic acid dye **5.70 (AAG145).**

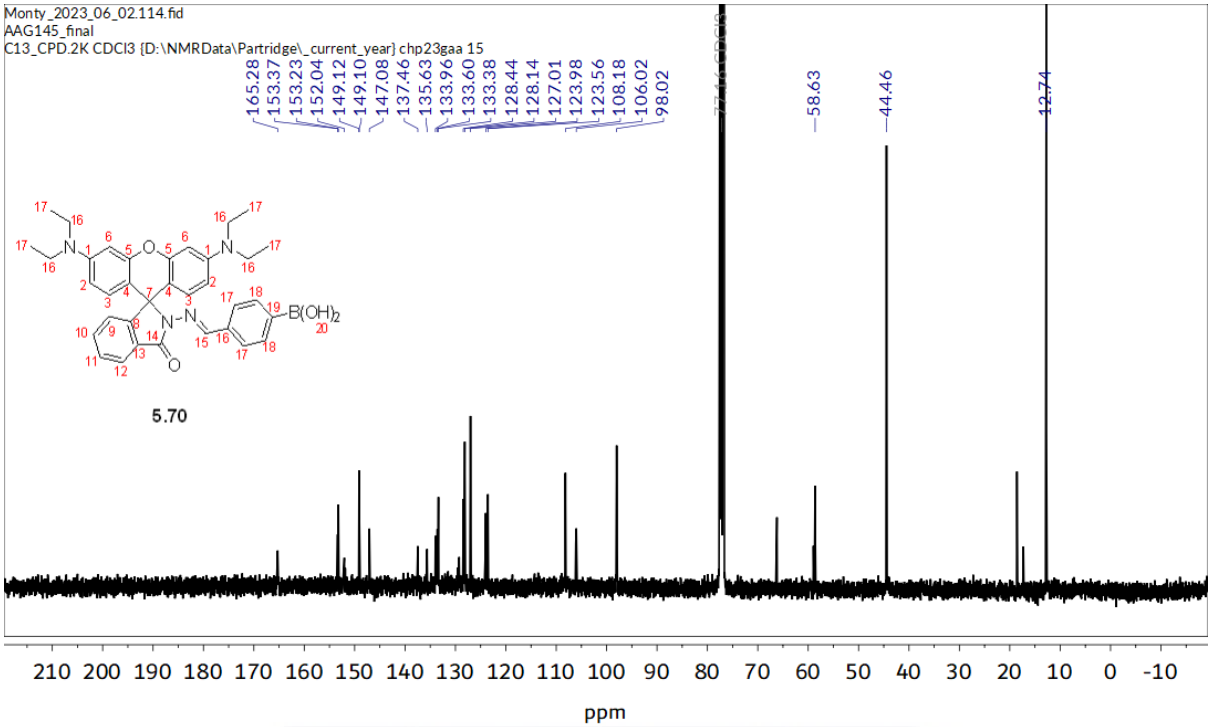

Appendix 1. 48: ^{13}C NMR spectrum (101 MHz, $CDCl_3$) of Rhodamine B boronic acid dye **5.70 (AAG145).**

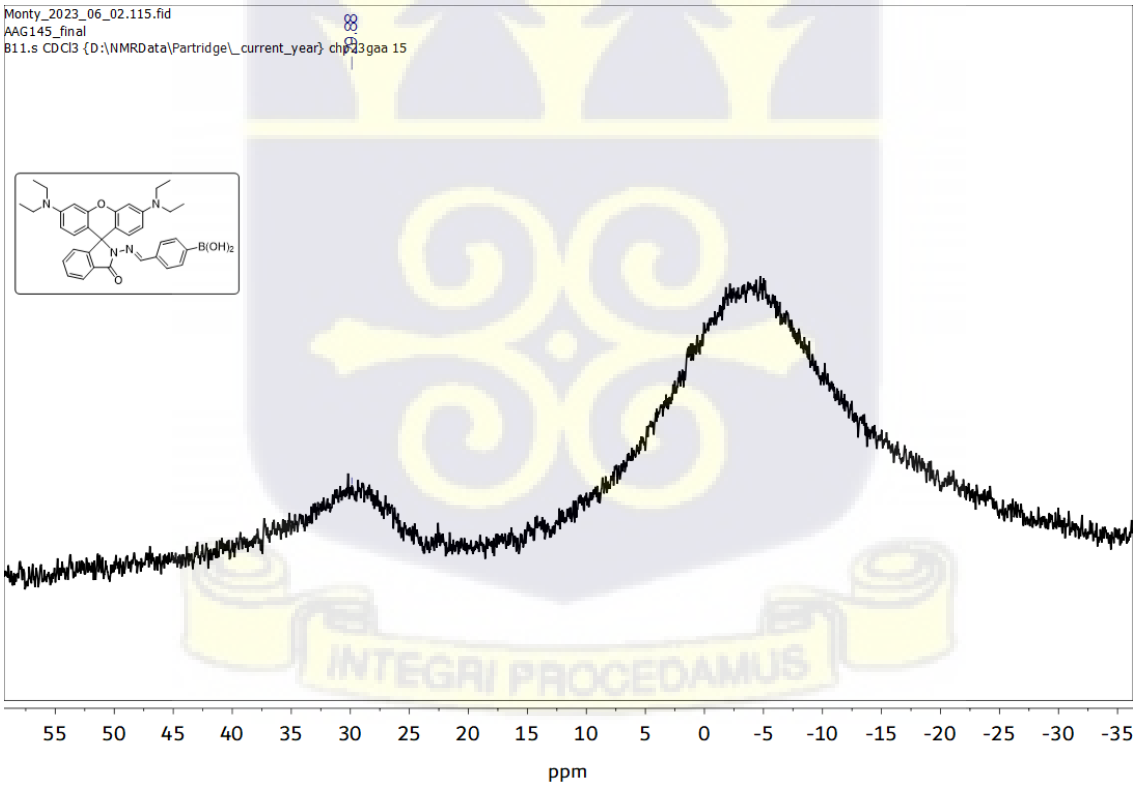

Appendix 1. 49: ^{11}B NMR (128 MHz, $CDCl_3$) of Rhodamine B boronic acid dye **5.70 (AAG145).**

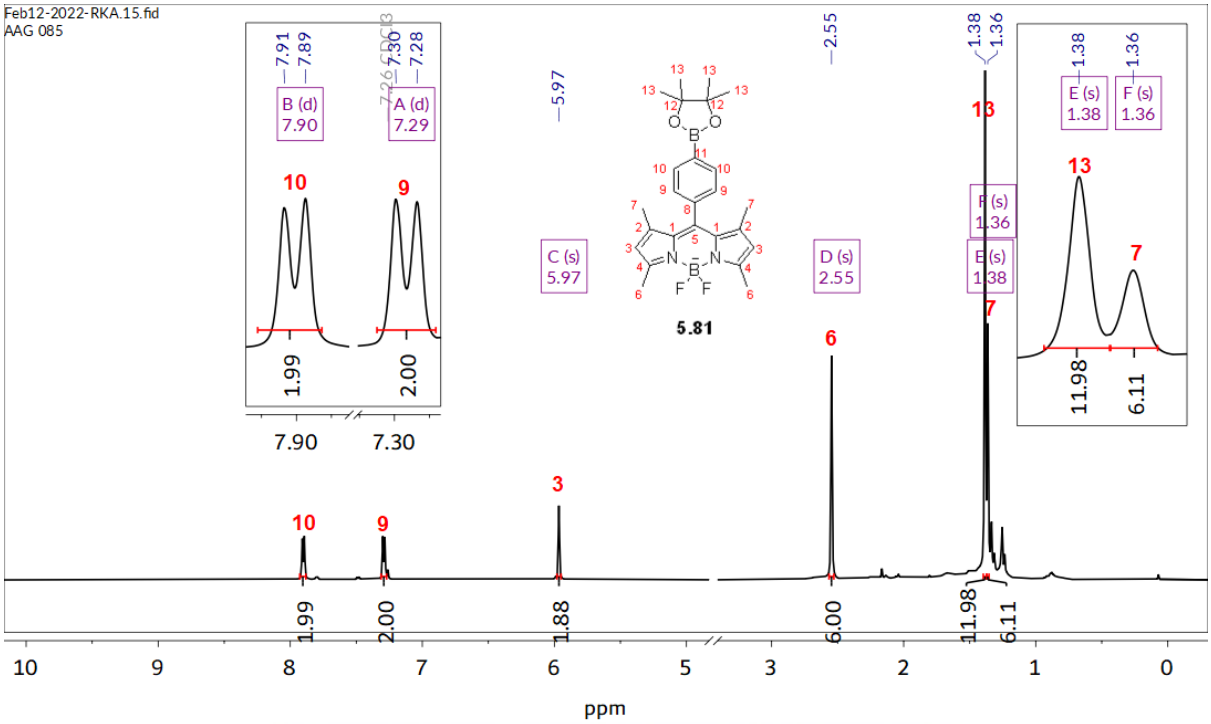

Appendix 1. 50: ^{1}H NMR spectrum (500 MHz, $CDCl_3$) of protected BODIPY dye **5.81.**

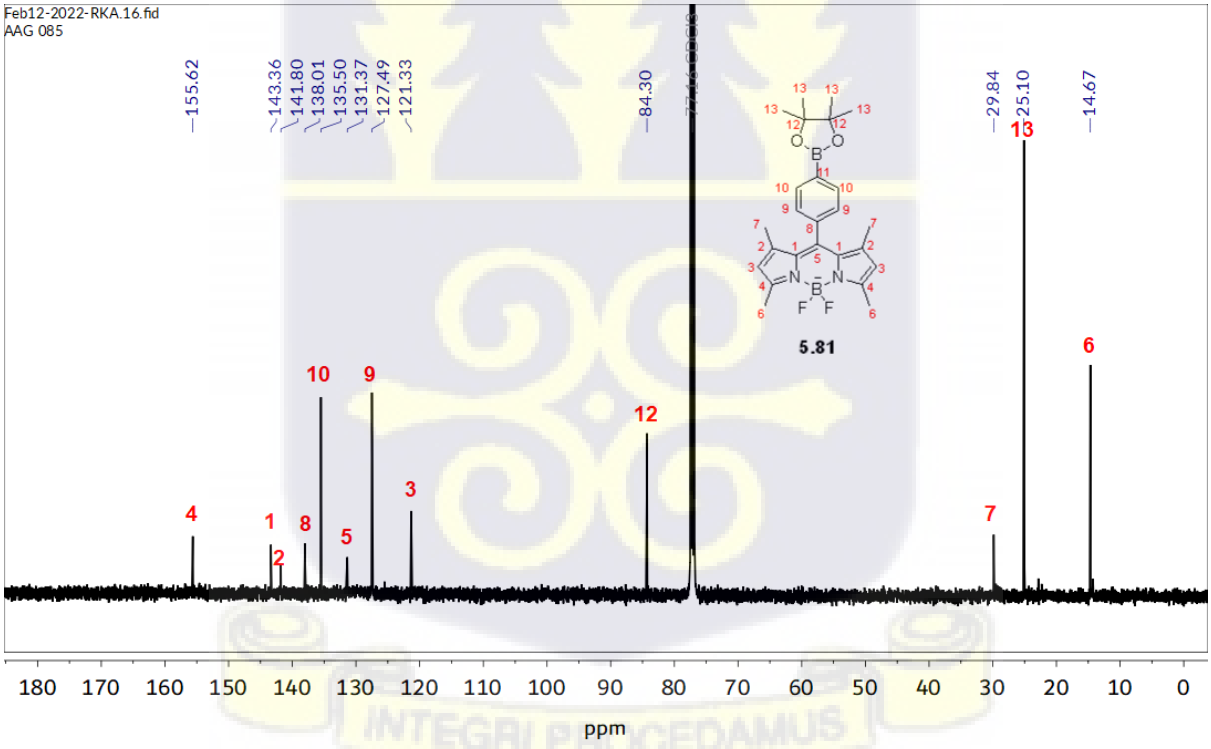

Appendix 1. 51: ^{13}C NMR spectrum (126 MHz, $CDCl_3$) of protected BODIPY dye **5.81.**

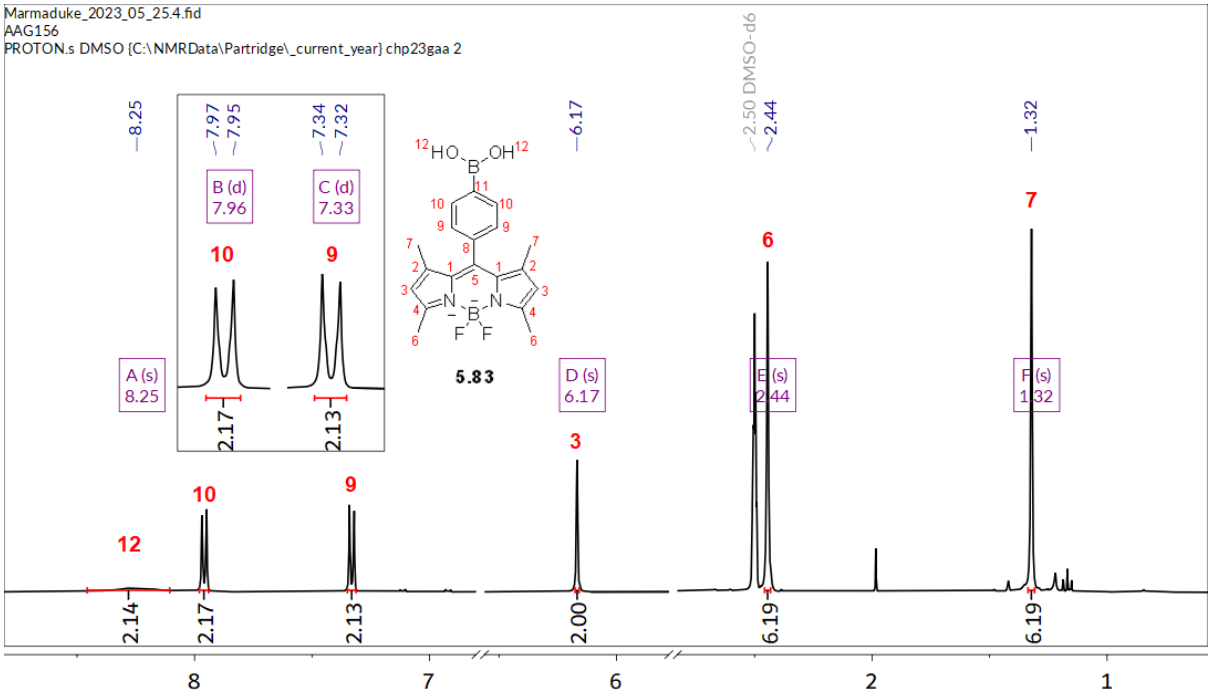

Appendix 1. 52: ^{1}H NMR spectrum (400 MHz, DMSO-d_6) of BODIPY dye **5.83.**

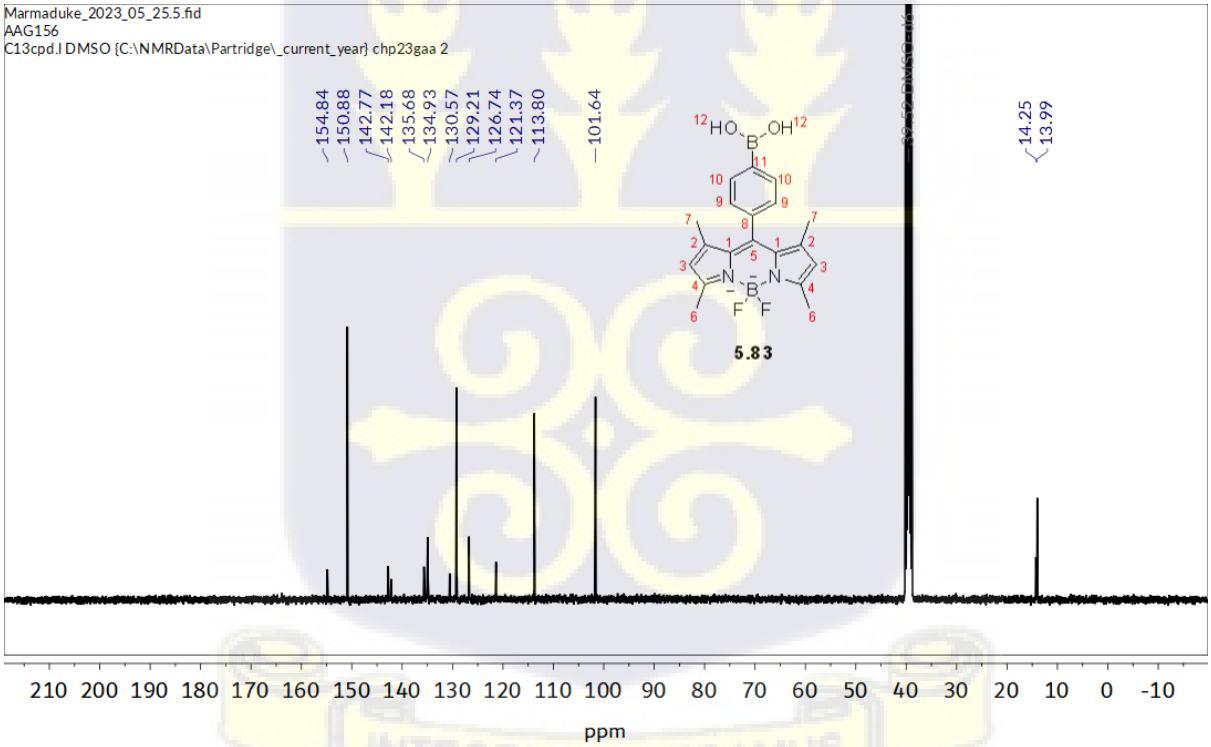

Appendix 1. 53: ^{13}C NMR spectrum (101 MHz, DMSO-d_6) of BODIPY dye **5.83.**

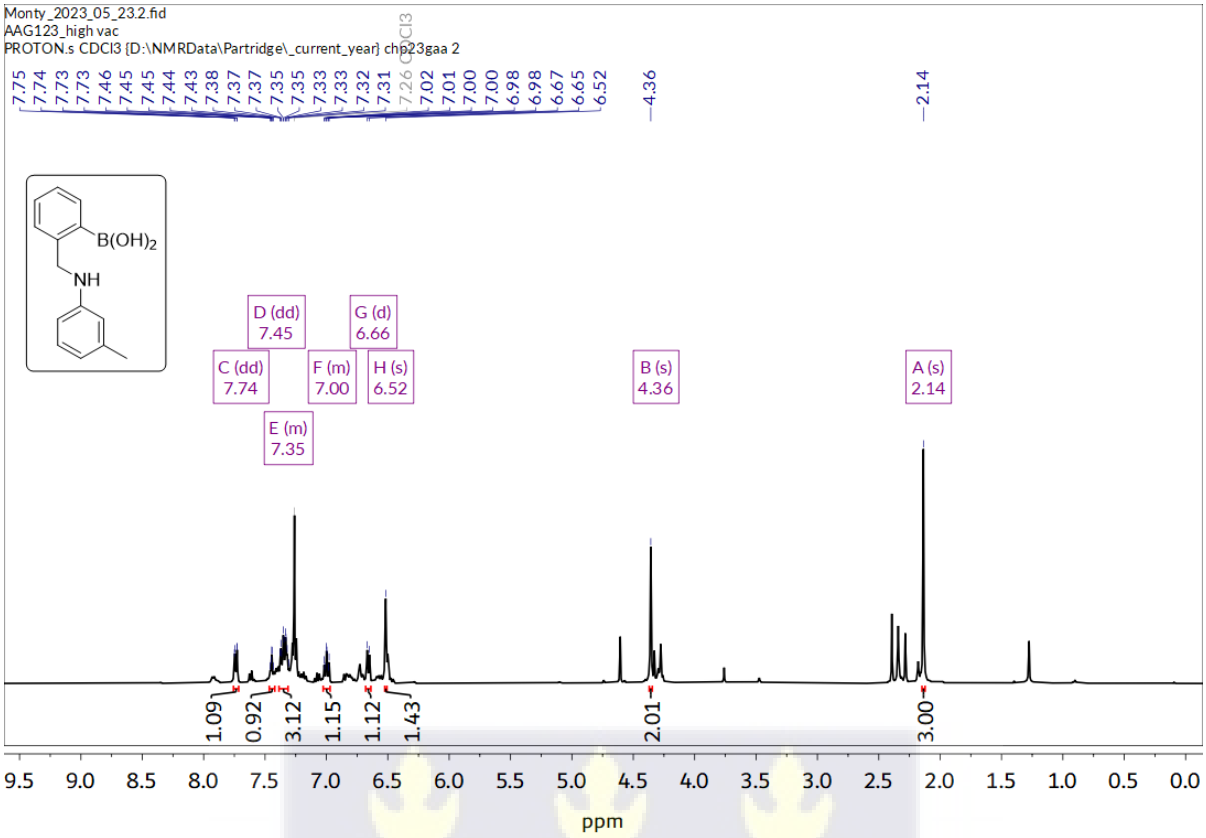

Appendix 1. 54: ^{1}H NMR spectrum (400 MHz, $CDCl_3$) of (2-((m-tolylamino)methyl)phenyl)boronic acid **5.86.**

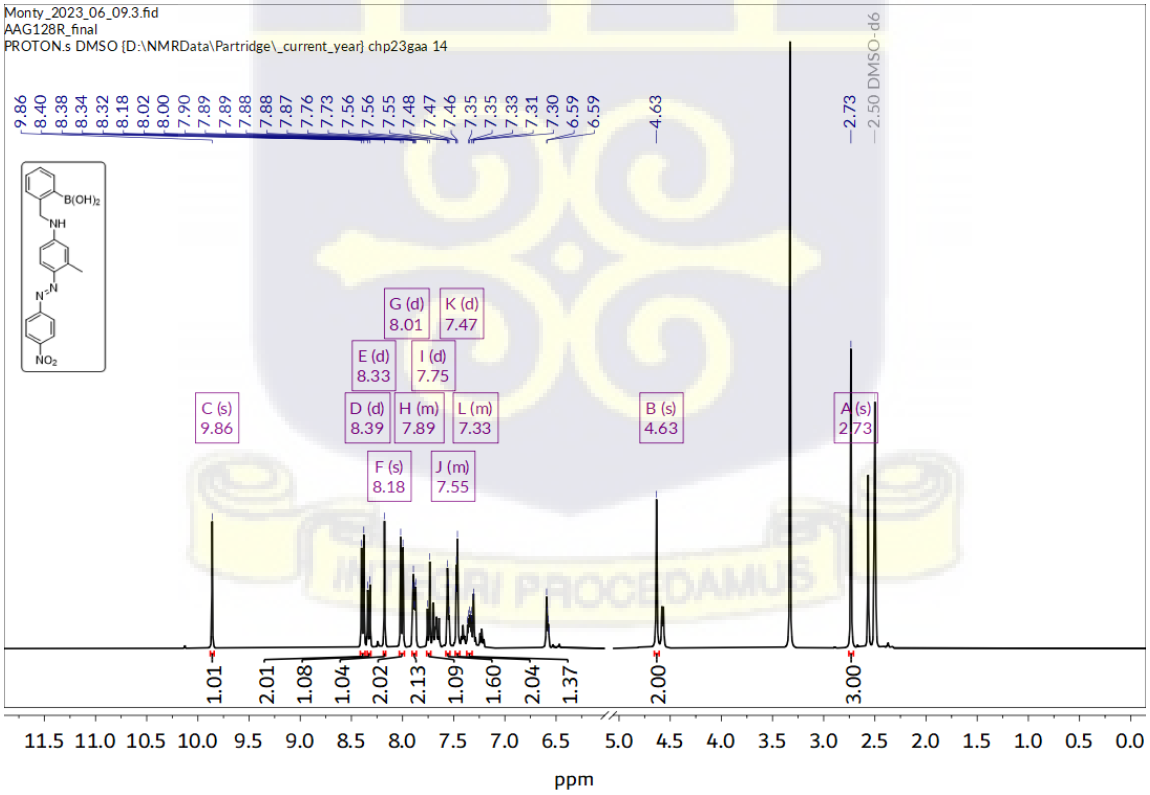

Appendix 1. 55: ^{1}H NMR spectrum (400 MHz, DMSO-d_6) of (E)-(2-(((3-methyl-4-((4-nitrophenyl)diazenyl)phenyl)amino)methyl)phenyl)boronic acid **5.87.**

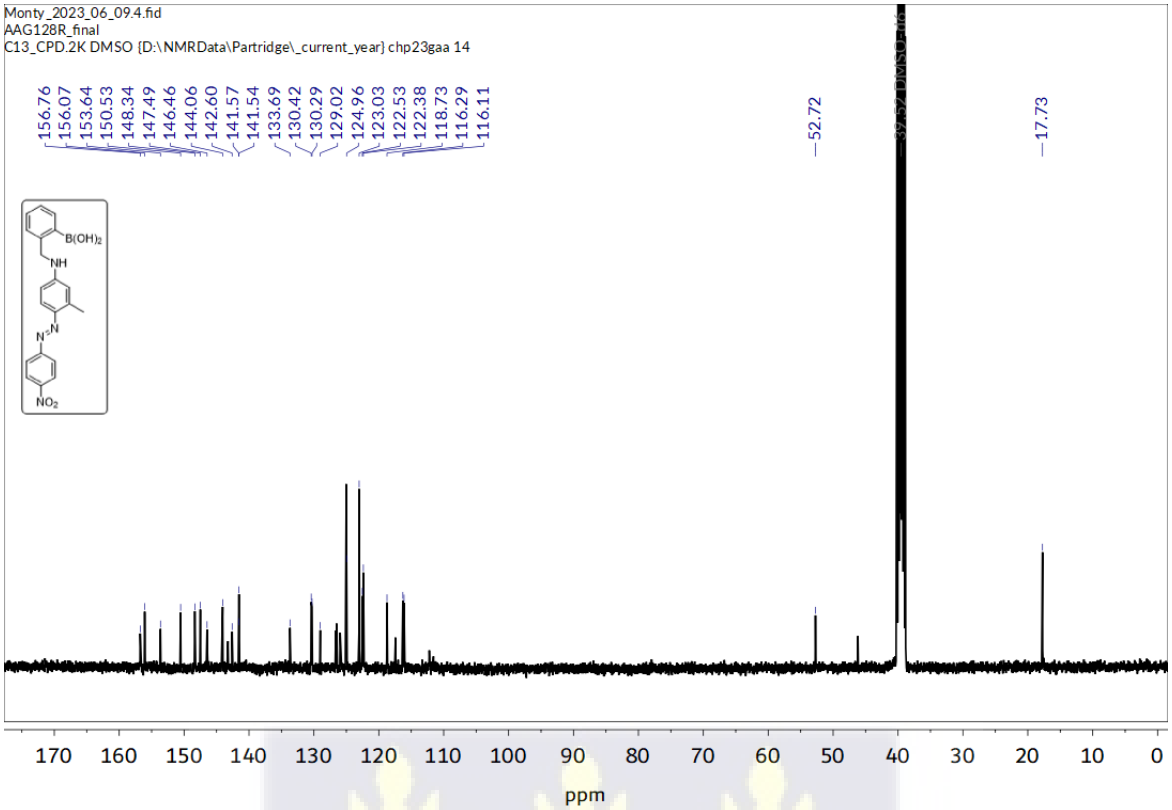

Appendix 1. 56: ^{13}C NMR spectrum (101 MHz, DMSO-d_6) of (E)-(2-(((3-methyl-4-((4-nitrophenyl)diazenyl)phenyl)amino)methyl)phenyl)boronic acid **5.87.**

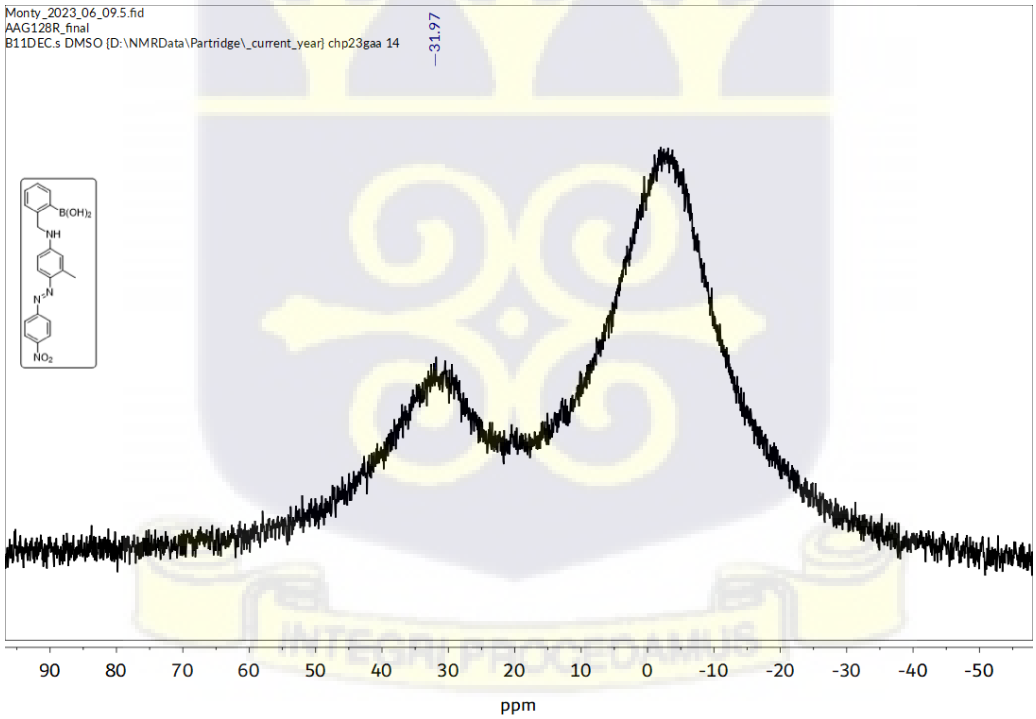

Appendix 1. 57: ^{11}B NMR (128 MHz, DMSO-d_6) of (E)-(2-(((3-methyl-4-((4-nitrophenyl)diazenyl)phenyl)amino)methyl)phenyl)boronic acid **5.87.**

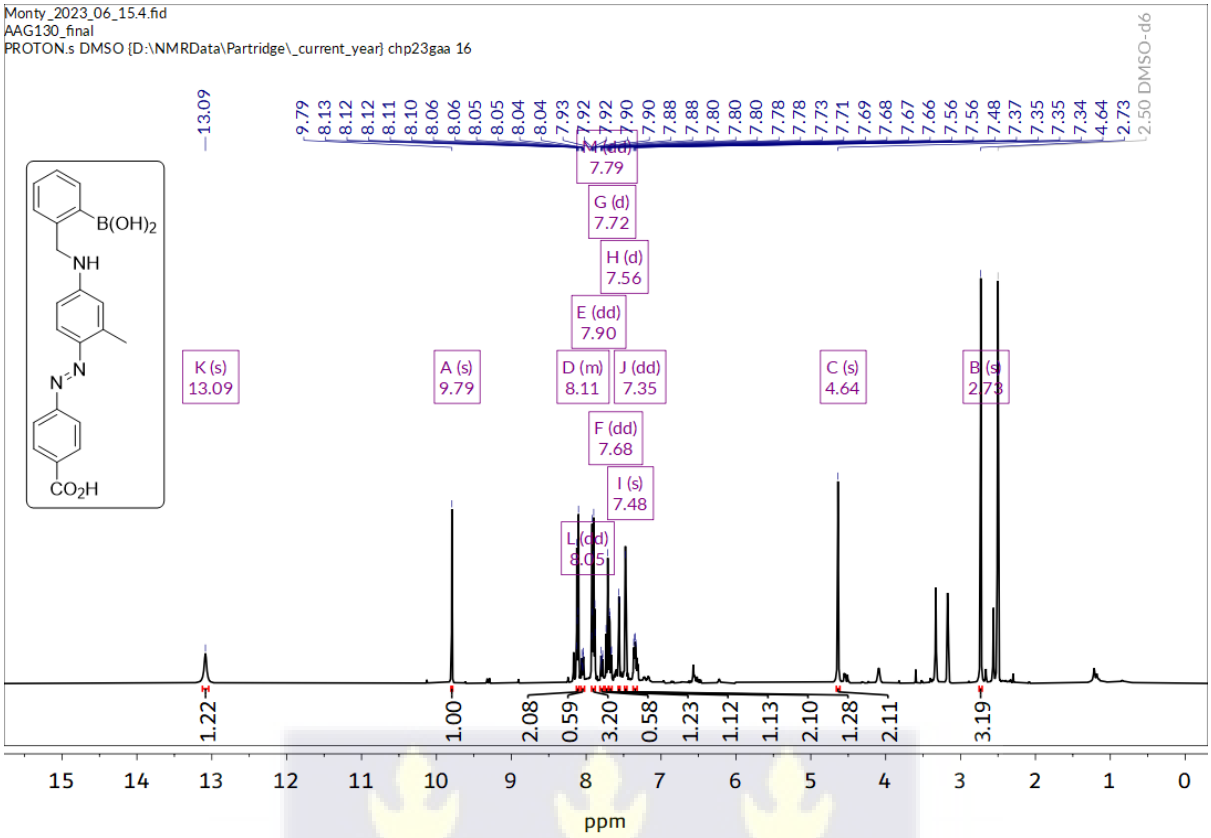

Appendix 1. 58: ^{1}H NMR spectrum (400 MHz, DMSO-d_6) of (E)-4-((4-((2-boronobenzyl)amino)-2-methylphenyl)diazenyl)benzoic acid **5.88.**

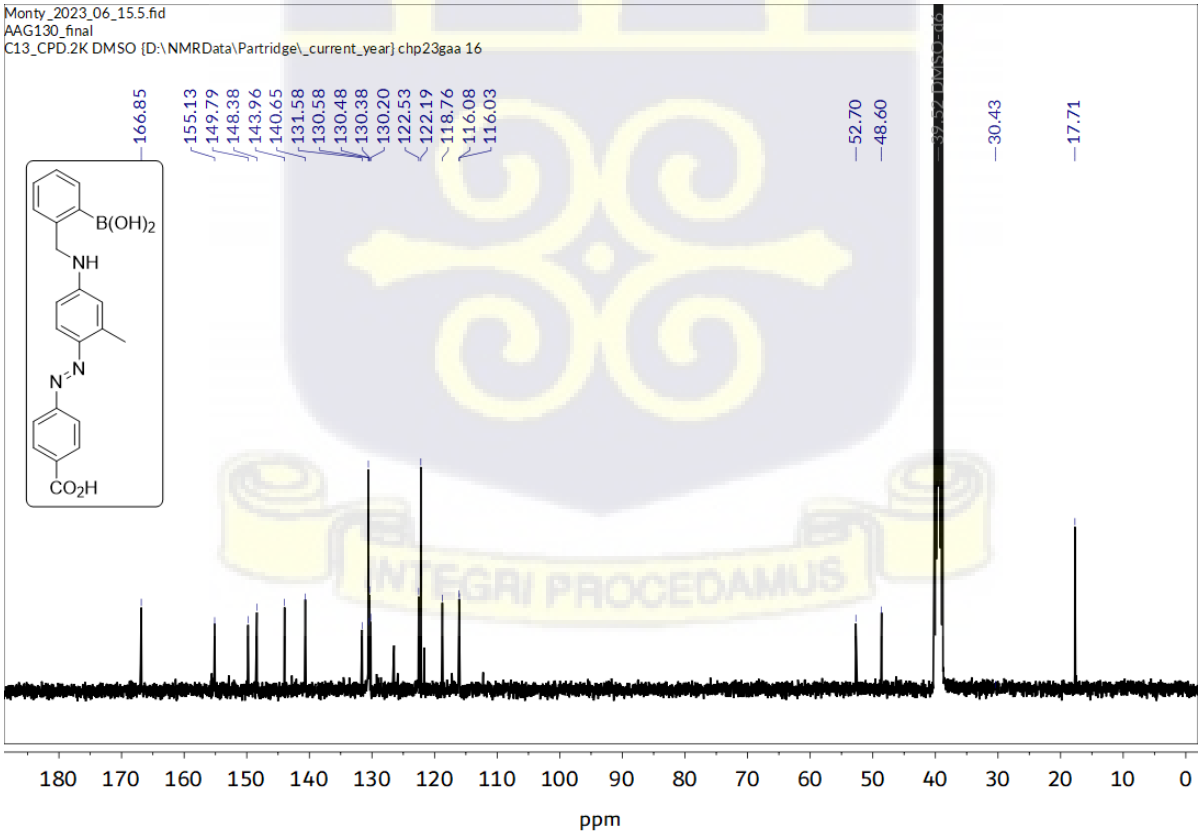

Appendix 1. 59: ^{13}C NMR spectrum (101 MHz, DMSO-*d*$_6$) of (E)-4-((4-((2-boronobenzyl)amino)-2-methylphenyl)diazenyl)benzoic acid **5.88.**

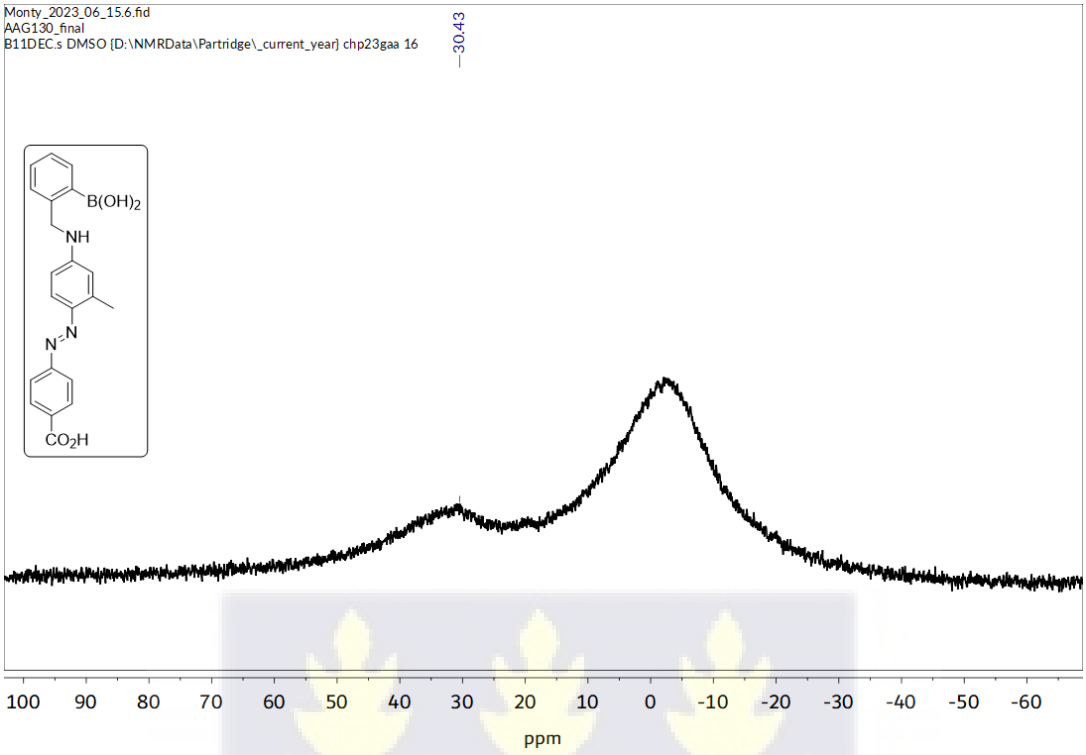

Appendix 1. 60: ^{11}B NMR (128 MHz, DMSO-*d*$_6$) of (E)-4-((4-((2-boronobenzyl)amino)-2-methylphenyl)diazenyl)benzoic acid **5.88.**

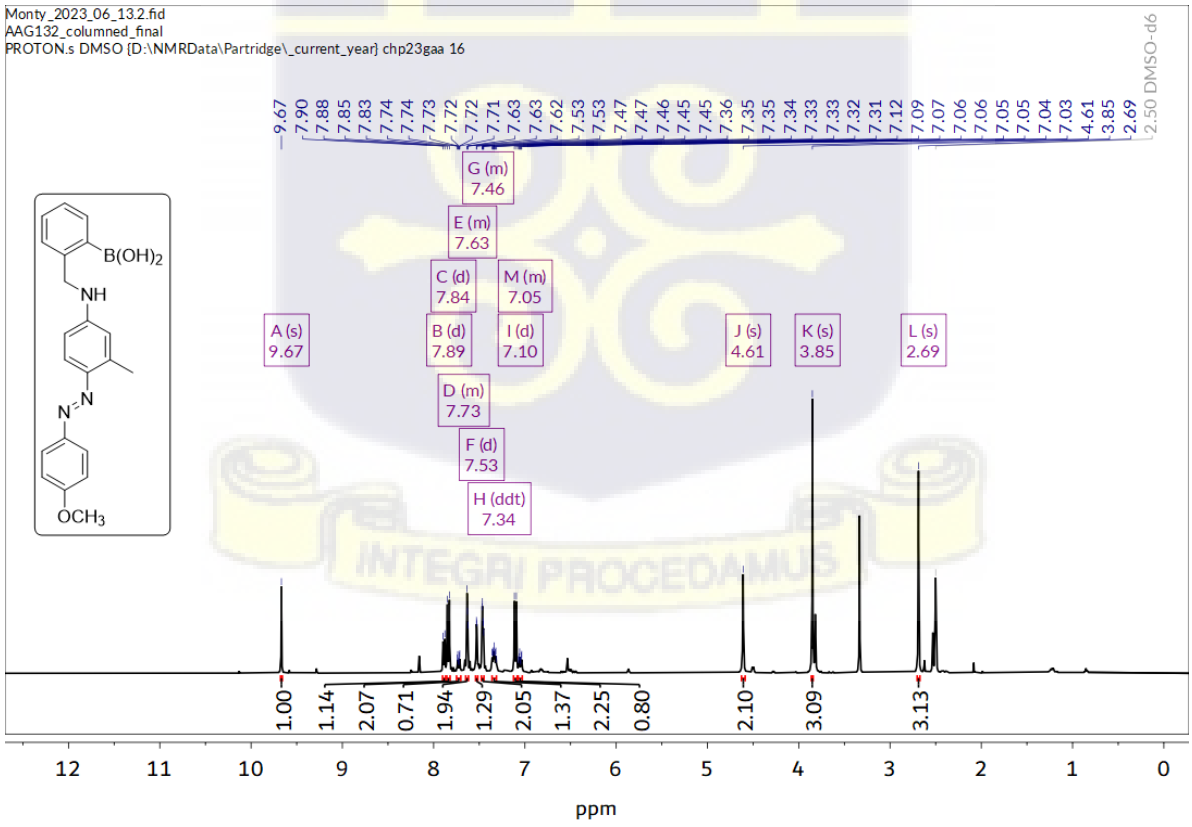

Appendix 1. 61: ^{1}H NMR spectrum (400 MHz, DMSO-*d*$_6$) of (E)-(2-(((4-((4-methoxyphenyl)diazenyl)-3-methylphenyl)amino)methyl)phenyl)boronic acid **5.89.**

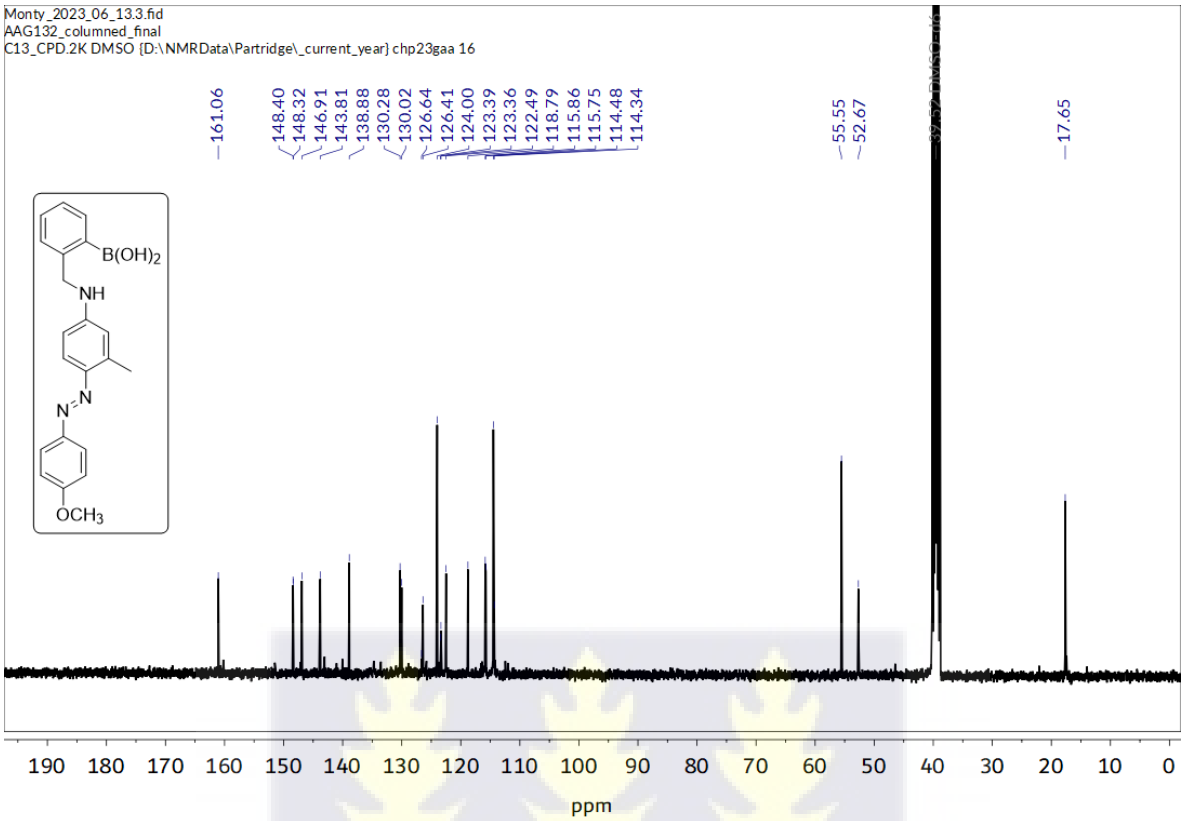

Appendix 1. 62: ^{13}C NMR spectrum (101 MHz, DMSO-*d*$_6$) of (E)-(2-(((4-((4-methoxyphenyl)diazenyl)-3-methylphenyl)amino)methyl)phenyl)boronic acid **5.89.**

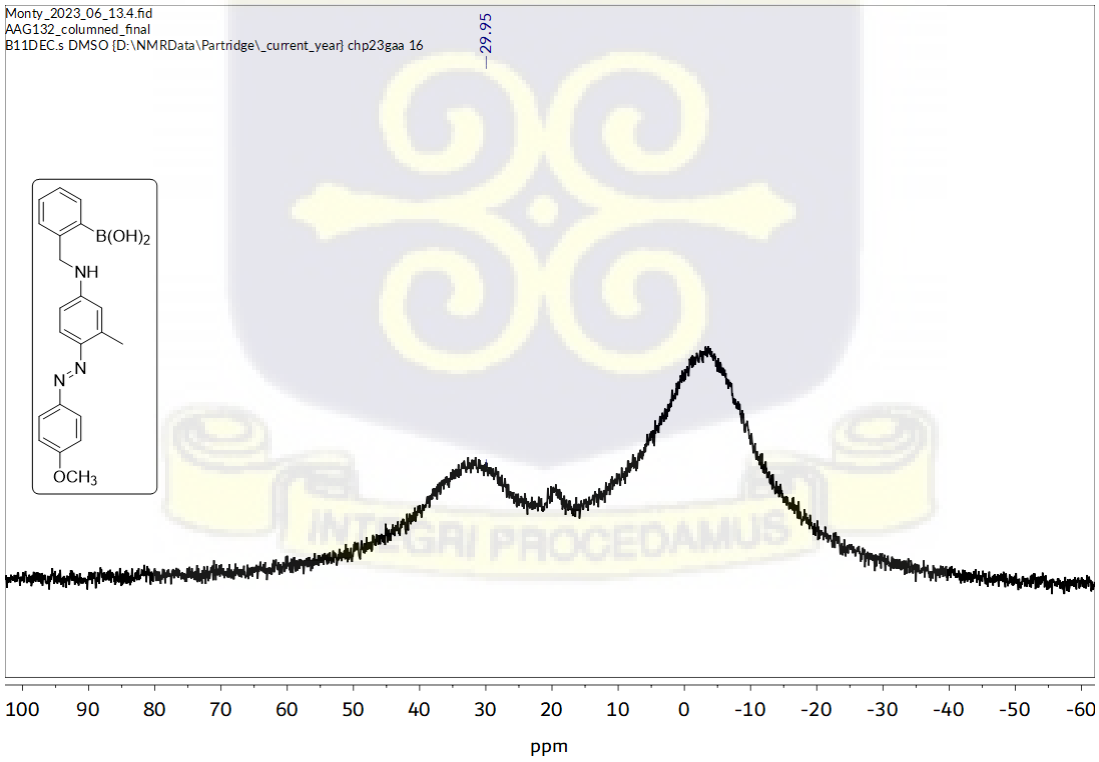

Appendix 1. 63: ^{11}B NMR (128 MHz, DMSO-*d*$_6$) of (E)-(2-(((4-((4-methoxyphenyl)diazenyl)-3-methylphenyl)amino)methyl)phenyl)boronic acid **5.89.**

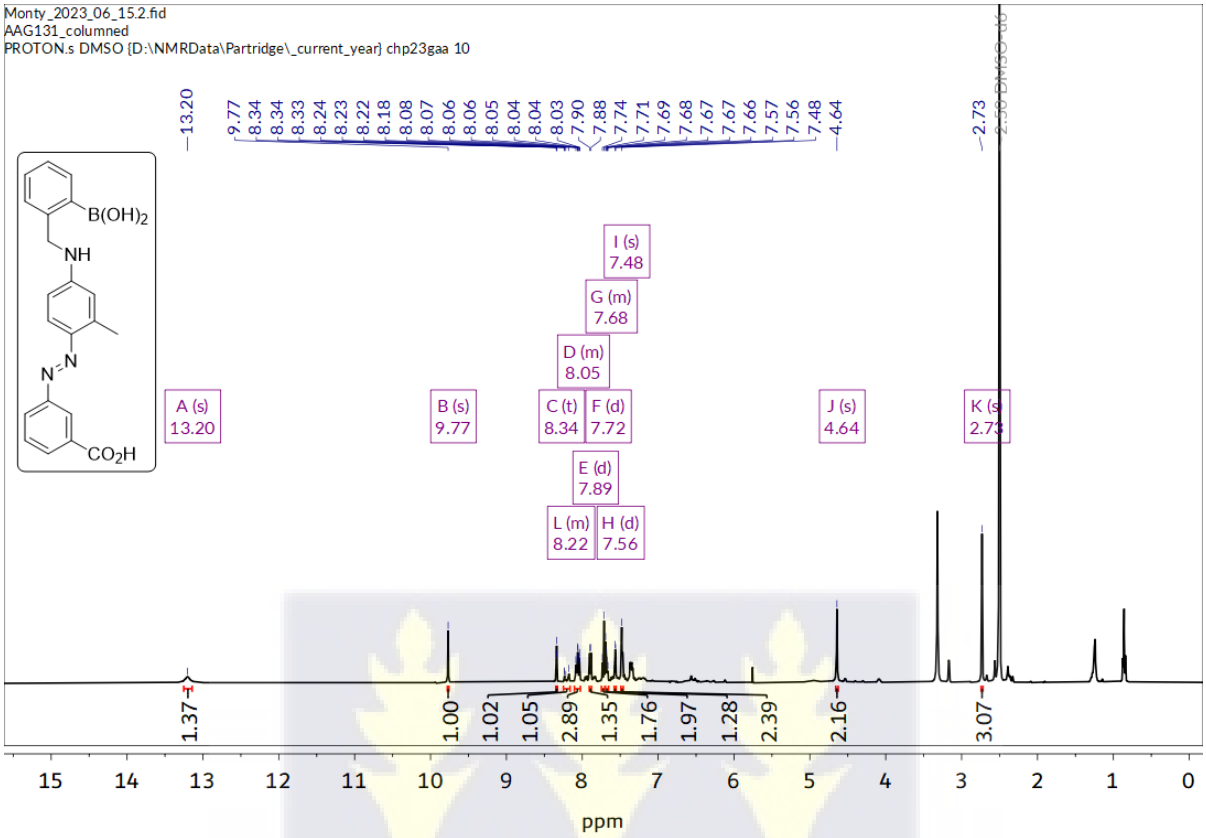

Appendix 1. 64: ^{1}H NMR spectrum (400 MHz, DMSO-*d*$_6$) of (E)-3-((4-((2-boronobenzyl)amino)-2-methylphenyl)diazenyl)benzoic acid **5.90.**

Appendix 2: LC-MS Data

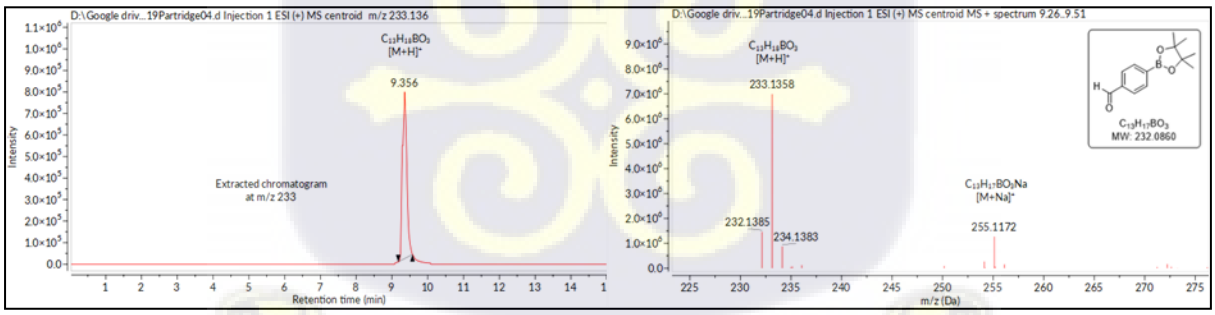

Appendix 2. 1: ESI-QTOF HRMS spectrum of 4-(4,4,5,5-tetramethyl-1,3,2-dioxaborolan-2-yl)benzaldehyde **5.4.**

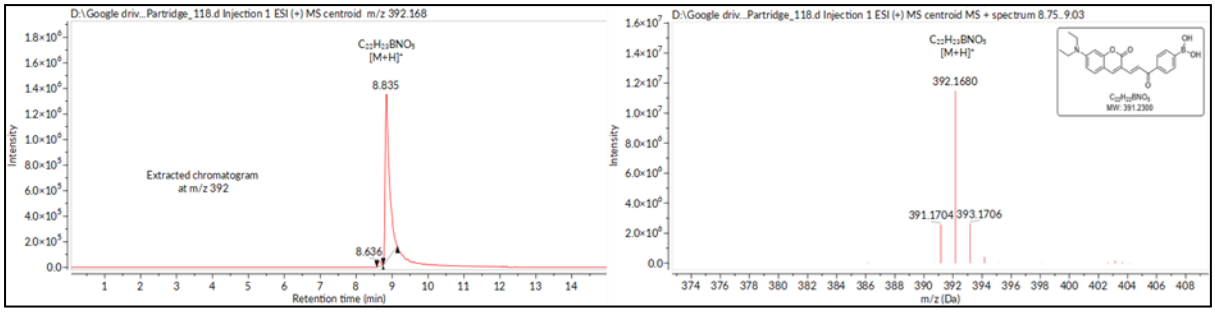

Appendix 2. 2: ESI-QTOF HRMS spectrum of (E)-(4-(3-(7-(diethylamino)-2-oxo-2H-chromen-3-yl)acryloyl)phenyl)boronic acid **AAG113.**

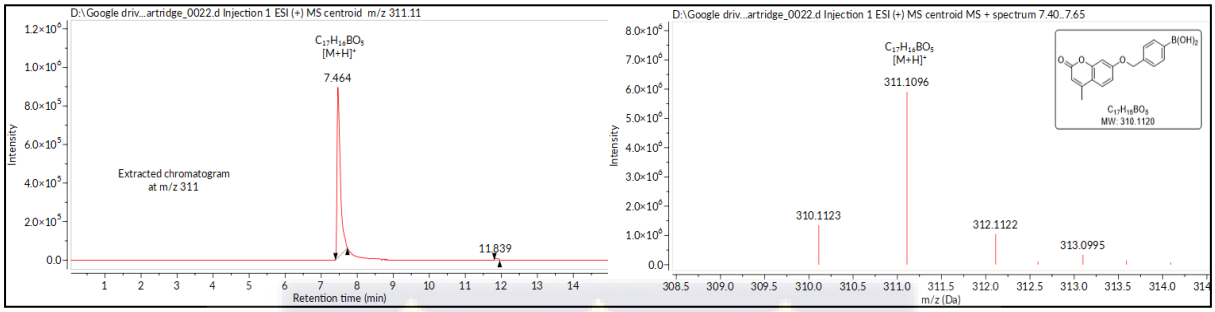

Appendix 2. 3: ESI-QTOF HRMS spectrum of (4-(((4-methyl-2-oxo-2H-chromen-7-yl)oxy)methyl)phenyl)boronic acid **5.28 (AAG143).**

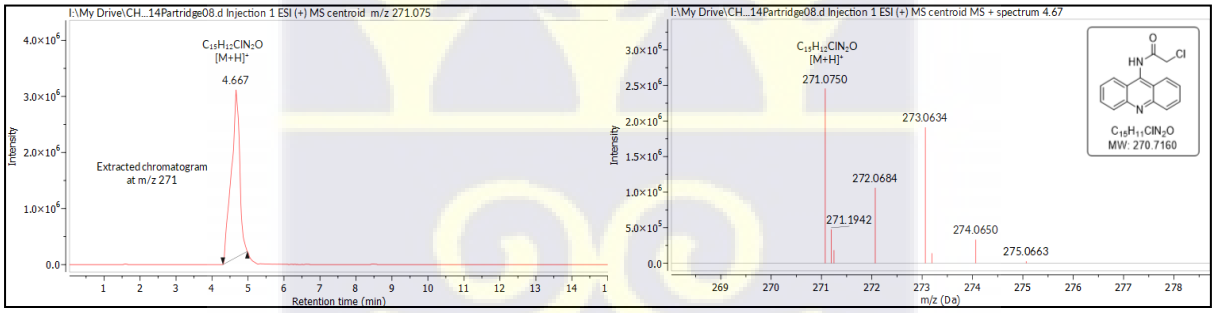

Appendix 2. 4: ESI-QTOF HRMS spectrum of N-(acridin-9-yl)-2-chloroacetamide **5.35.**

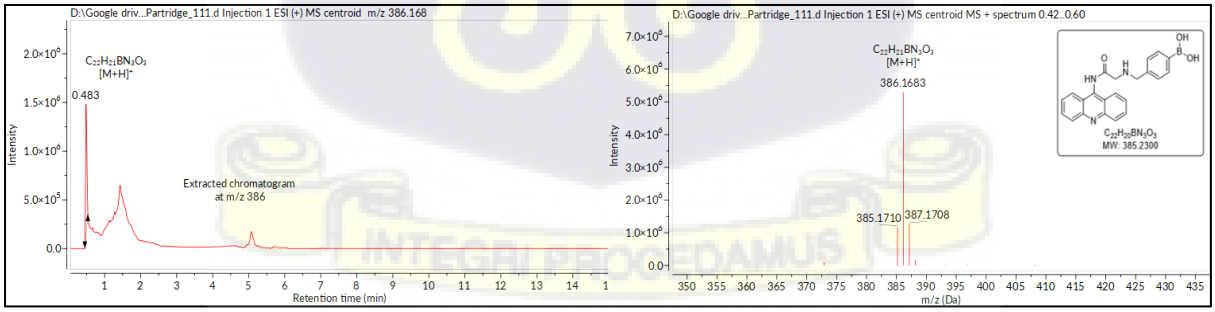

Appendix 2. 5: ESI-QTOF HRMS spectrum of (4-(((2-(acridin-9-ylamino)-2-oxoethyl)amino)methyl)phenyl)boronic acid **5.37 (AAG103).**

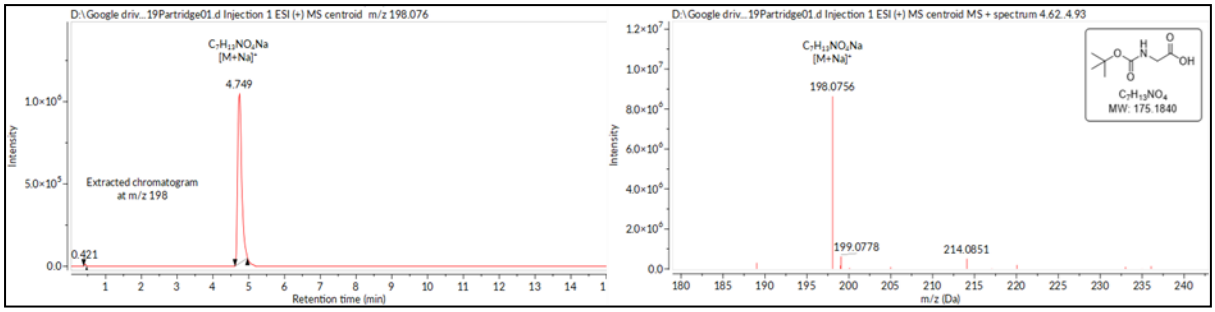

Appendix 2. 6: ESI-QTOF HRMS spectrum of 2-(tert-butoxycarbonylamino)acetic acid **5.45.**

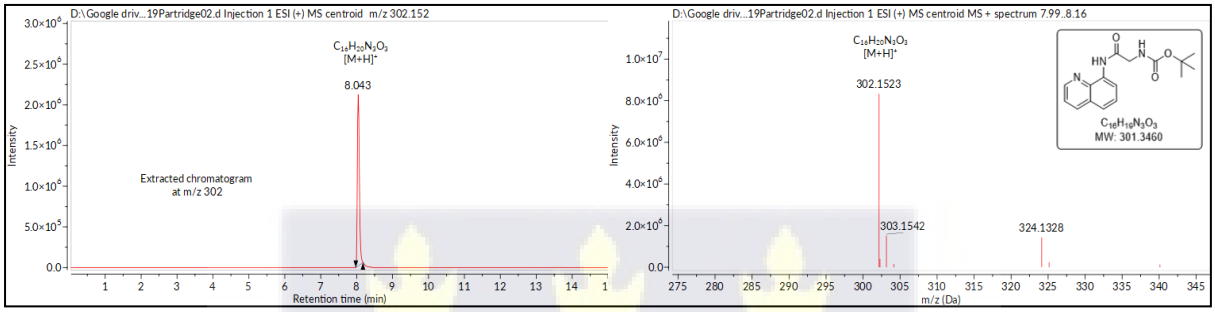

Appendix 2. 7: ESI-QTOF HRMS spectrum of tert-butyl (2-oxo-2-(quinolin-8-ylamino)ethyl)carbamate **5.47.**

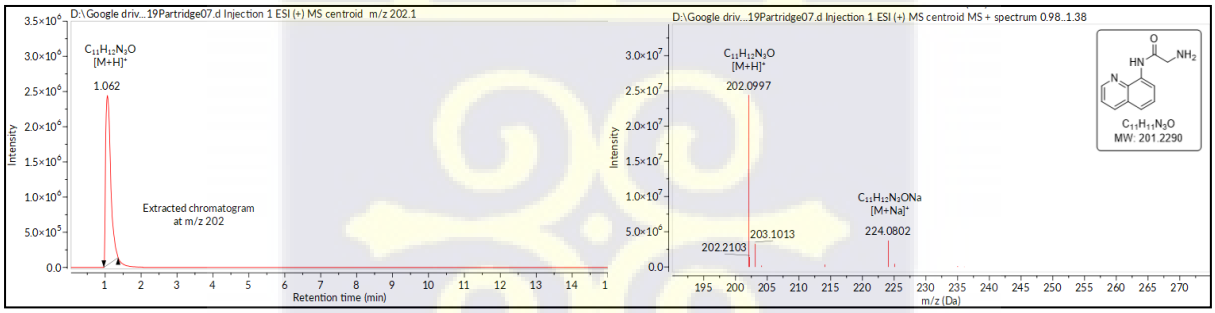

Appendix 2. 8: ESI-QTOF HRMS spectrum of 2-amino-N-(quinolin-8-yl)acetamide **5.48.**

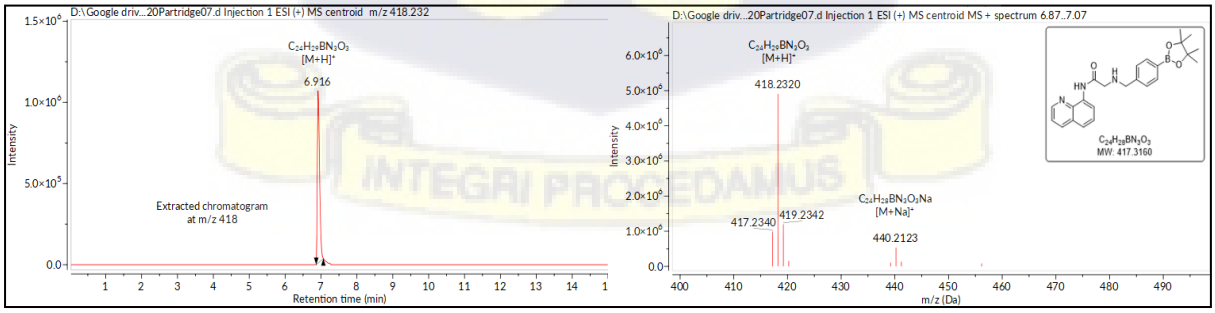

Appendix 2. 9: ESI-QTOF HRMS spectrum of N-(quinolin-8-yl)-2-((4-(4,4,5,5-tetramethyl-1,3,2-dioxaborolan-2-yl)benzyl)amino)acetamide **5.49.**

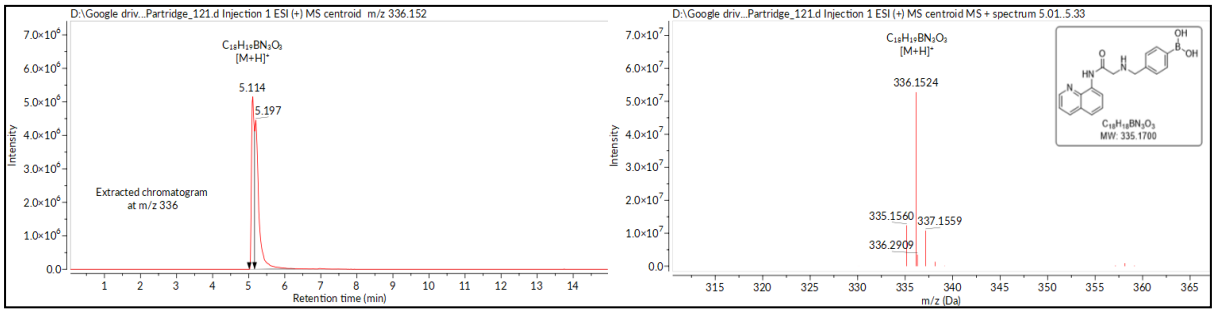

Appendix 2. 10: ESI-QTOF HRMS spectrum of 4-(((2-oxo-2-(quinolin-8-ylamino)ethyl)amino)methyl)phenyl)boronic acid **5.44.**

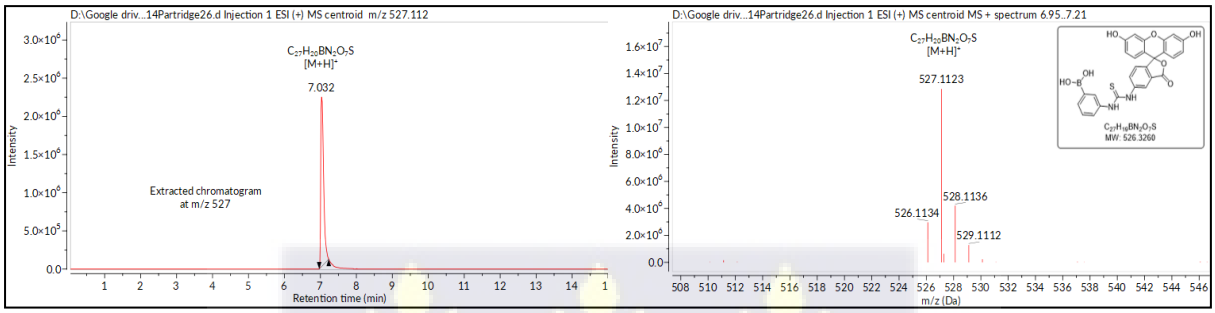

Appendix 2. 11: ESI-QTOF HRMS spectrum of **5.65.**

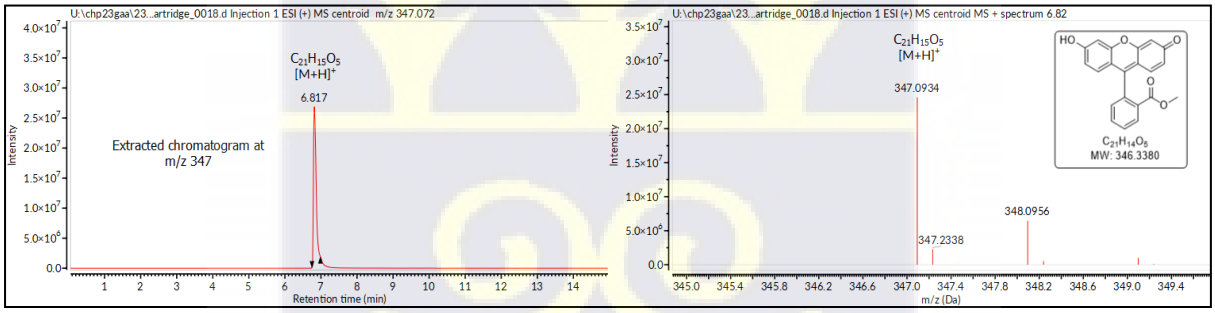

Appendix 2. 12: ESI-QTOF HRMS spectrum of fluorescein methyl ester **5.57.**

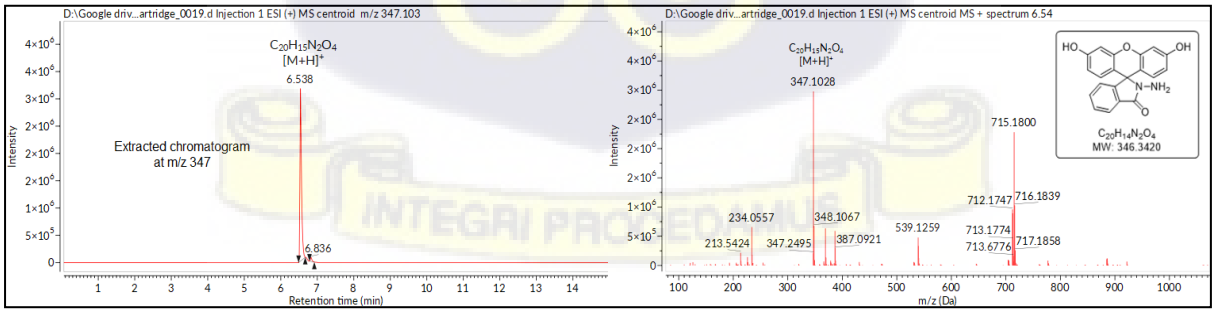

Appendix 2. 13: ESI-QTOF HRMS spectrum of fluorescein hydrazide **5.58.**

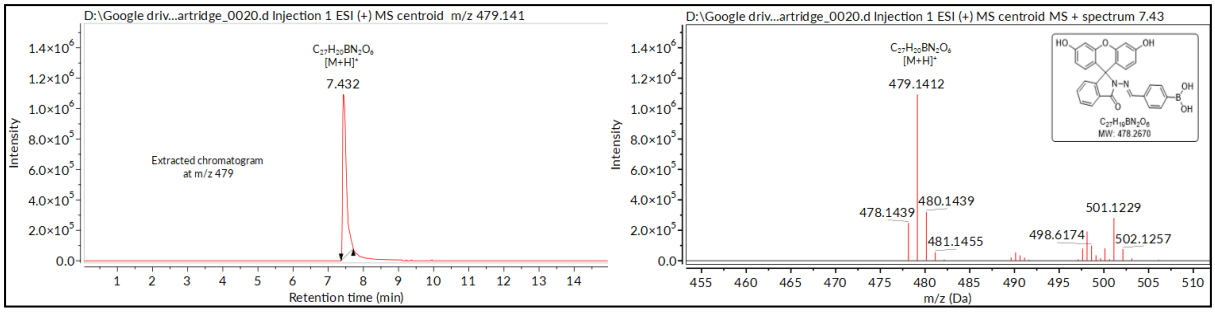

Appendix 2. 14: ESI-QTOF HRMS spectrum of fluorescein-tagged arylboronic acid chemosensor **5.60 (AAG138).**

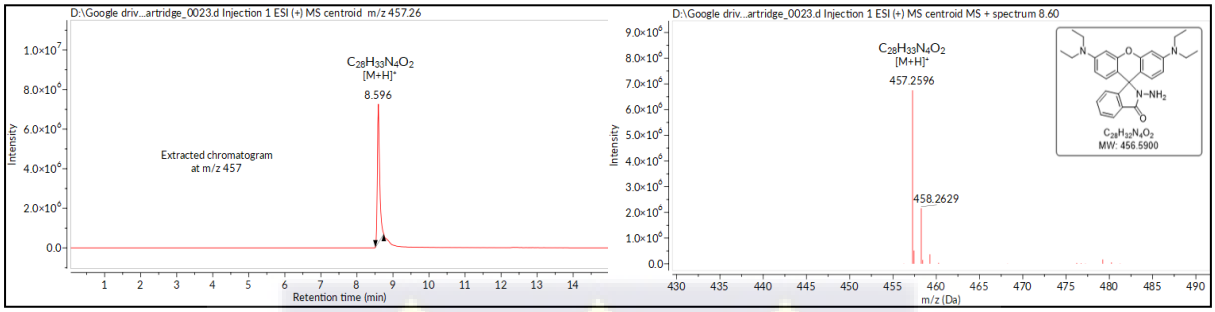

Appendix 2. 15: ESI-QTOF HRMS spectrum of Rhodamine B hydrazide **5.69.**

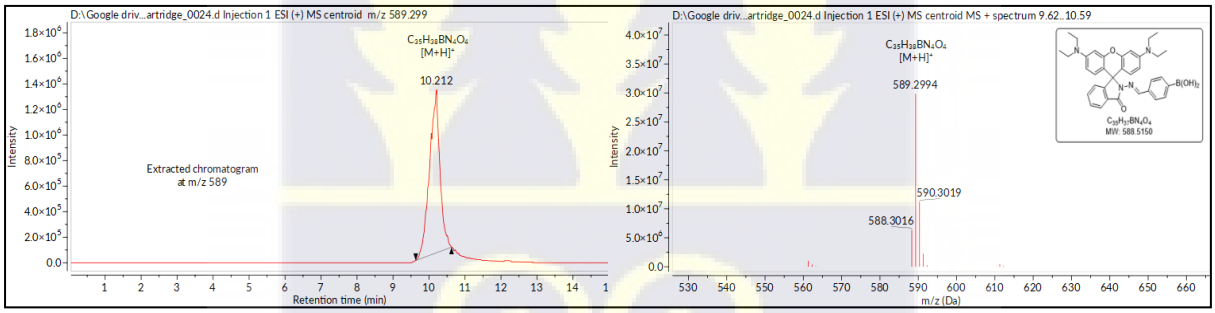

Appendix 2. 16: ESI-QTOF HRMS spectrum of Rhodamine B boronic acid dye **5.70 (AAG145).**

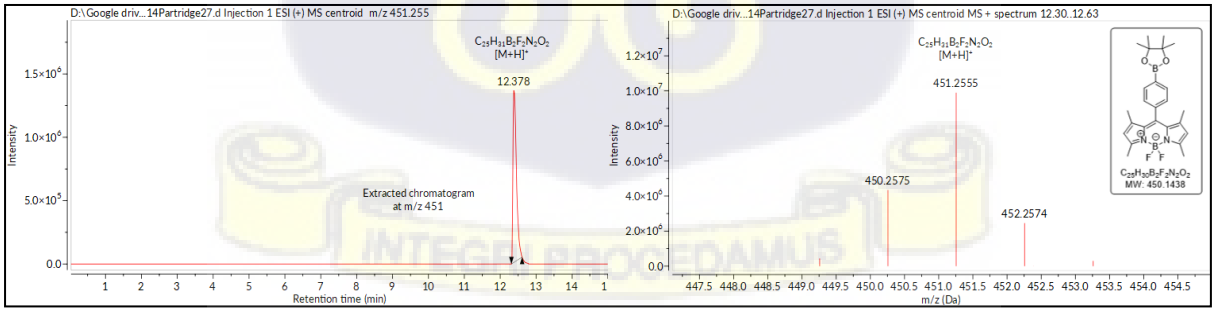

Appendix 2. 17: ESI-QTOF HRMS spectrum of protected BODIPY dye **5.81.**

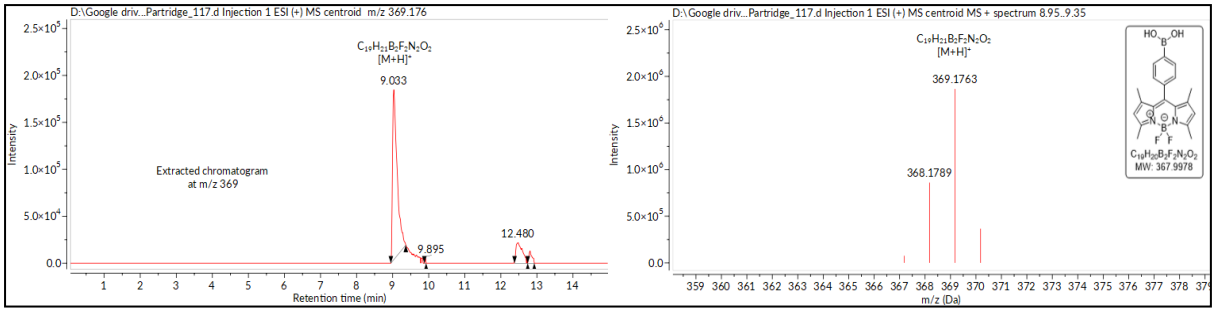

Appendix 2. 18: ESI-QTOF HRMS spectrum of BODIPY dye **5.83.**

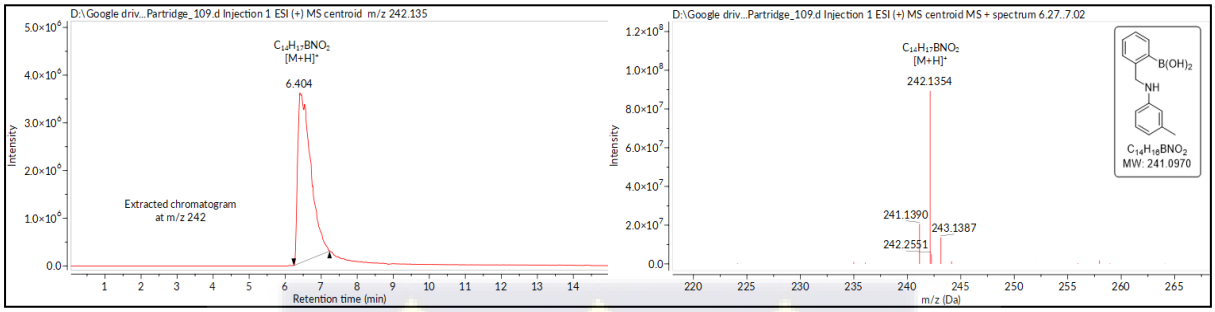

Appendix 2. 19: ESI-QTOF HRMS spectrum of (2-((m-tolylamino)methyl)phenyl)boronic acid **5.86.**

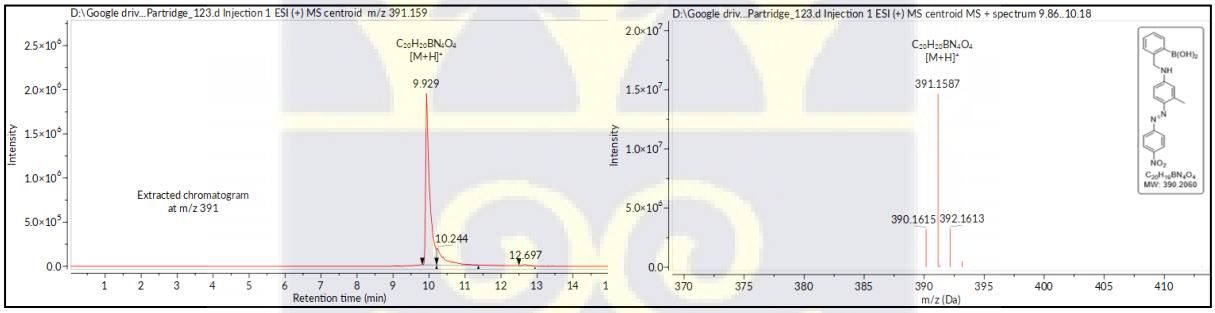

Appendix 2. 20: ESI-QTOF HRMS spectrum of (E)-(2-(((3-methyl-4-((4-nitrophenyl)diazenyl)phenyl)amino)methyl)phenyl)boronic acid **5.87.**

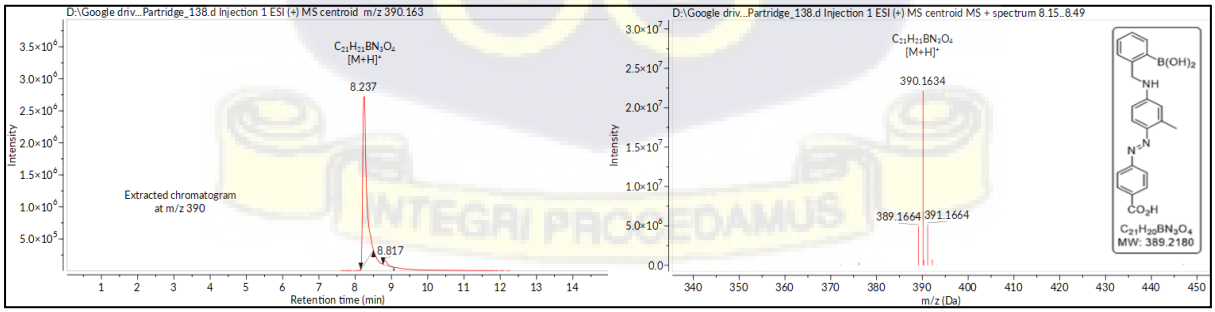

Appendix 2. 21: ESI-QTOF HRMS spectrum of (E)-4-((4-((2-boronobenzyl)amino)-2-methylphenyl)diazenyl)benzoic acid **5.88.**

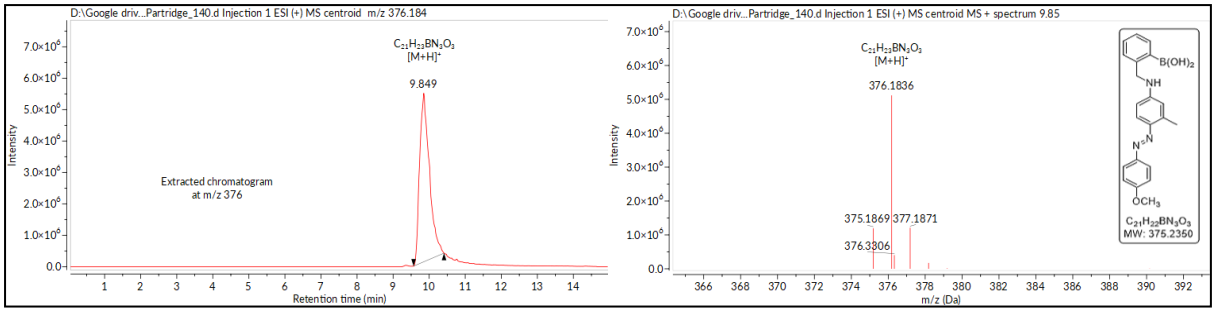

Appendix 2. 22: ESI-QTOF HRMS spectrum of (E)-(2-(((4-((4-methoxyphenyl)diazenyl)-3-methylphenyl)amino)methyl)phenyl)boronic acid **5.89.**

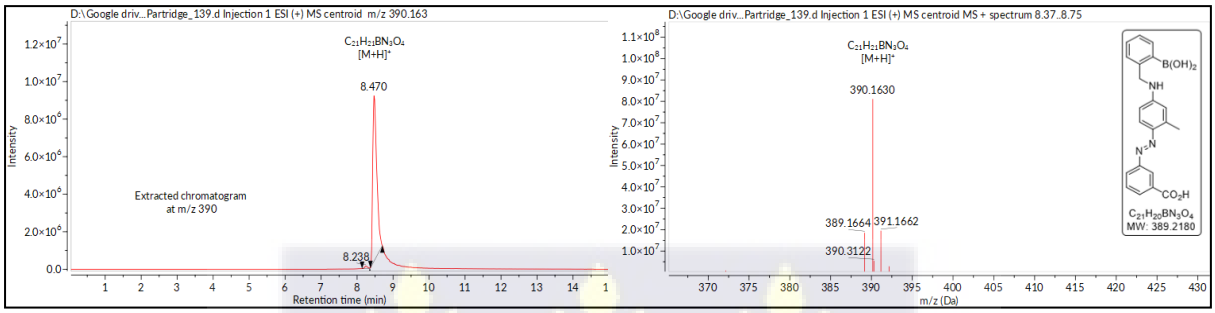

Appendix 2. 23: ESI-QTOF HRMS spectrum of (E)-3-((4-((2-boronobenzyl)amino)-2-methylphenyl)diazenyl)benzoic acid **5.90.**

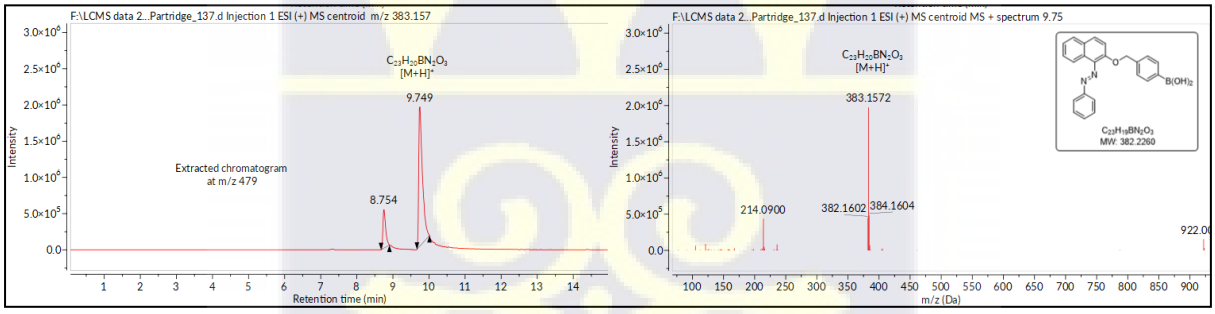

Appendix 2. 24: ESI-QTOF HRMS spectrum of (E)-3-((4-((2-boronobenzyl)amino)-2-methylphenyl)diazenyl)benzoic acid **AAG107R.**

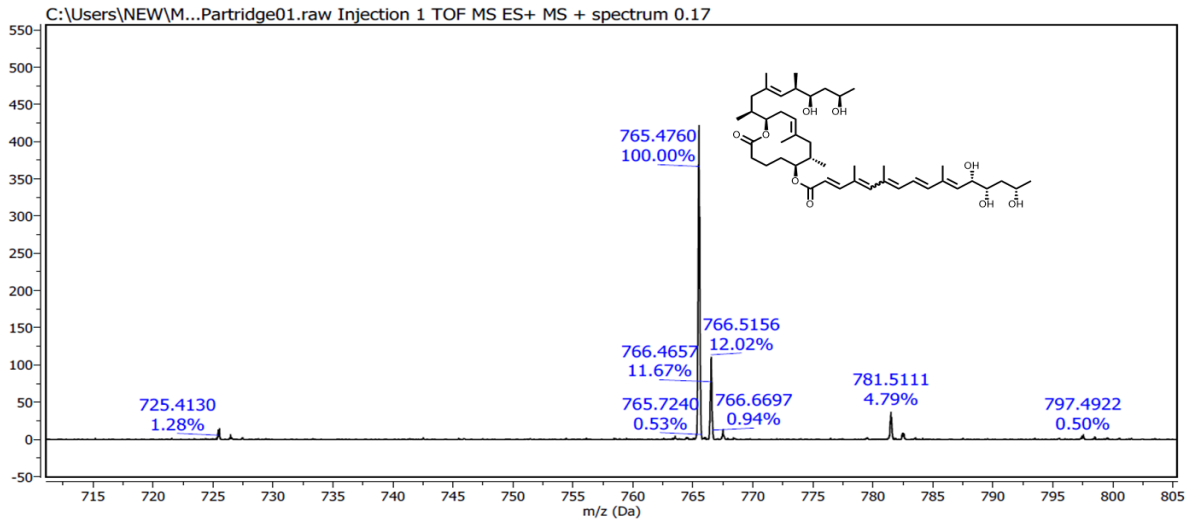

Appendix 2. 25: ESI LC-MS data for mycolactone A/B.

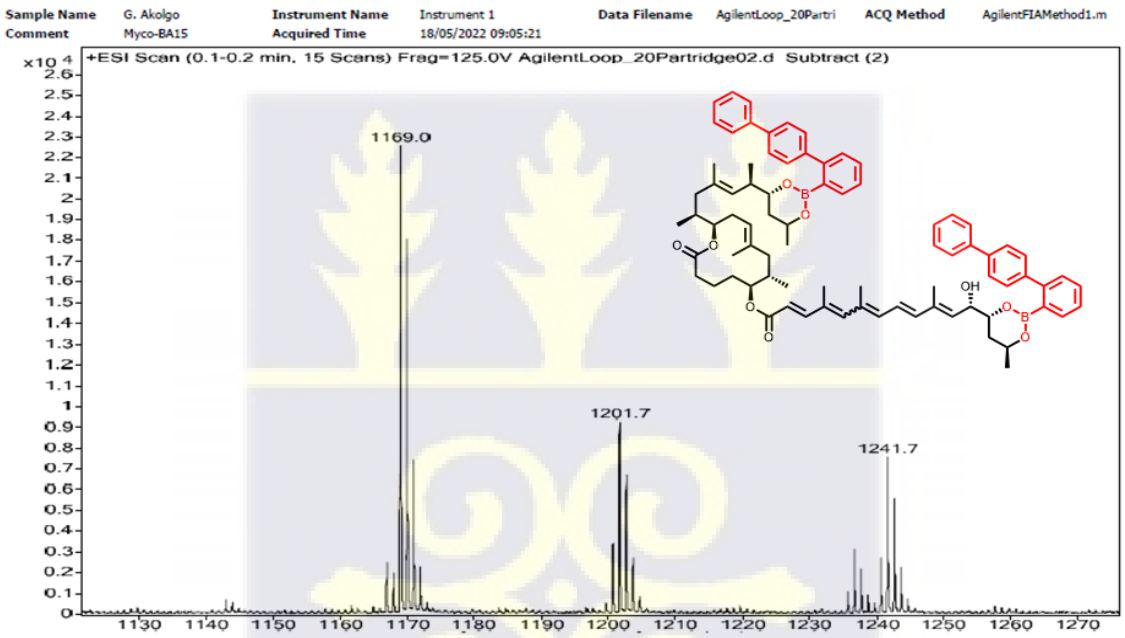

Appendix 2. 26: ESI LC-MS data for BA15-myco A/B adduct.

Appendix 3: FTIR spectra data

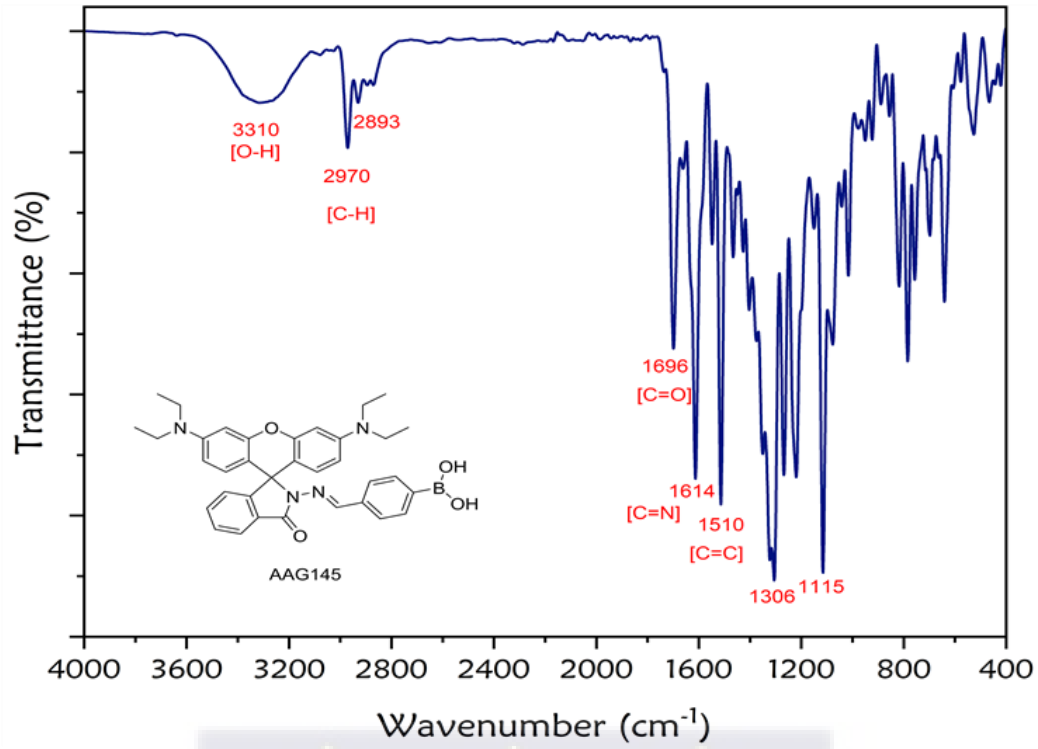

Appendix 3. 1: FTIR spectrum of **AAG145**

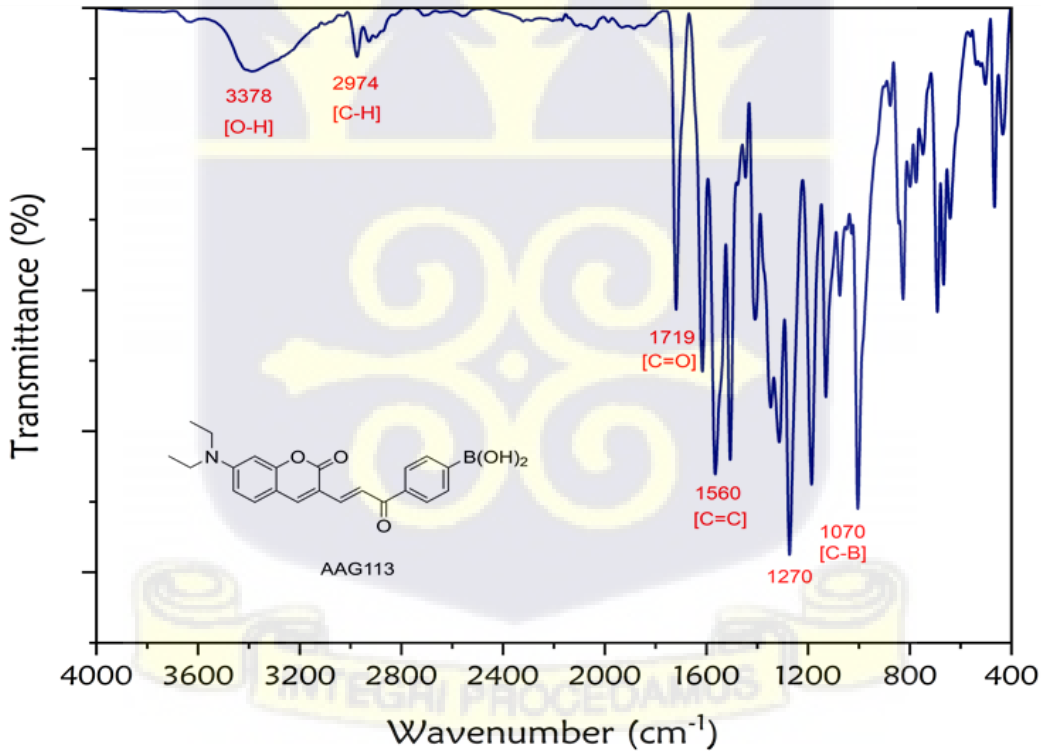

Appendix 3. 2: FTIR spectrum of **AAG113**

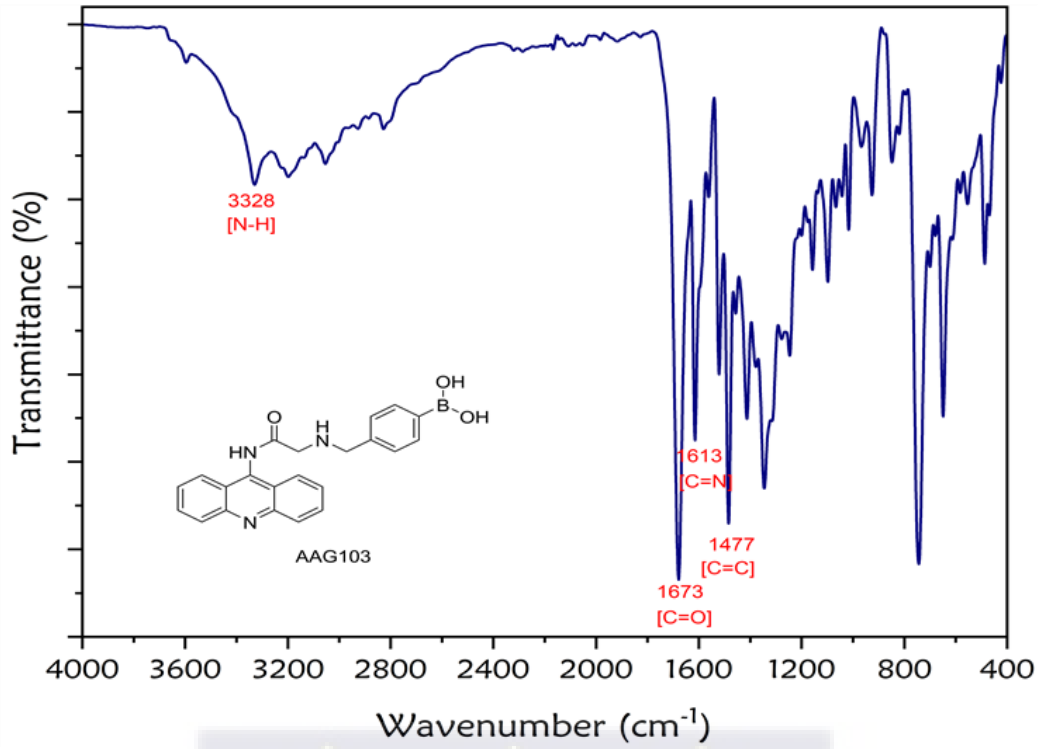

Appendix 3. 3: FTIR spectrum of **AAG103**

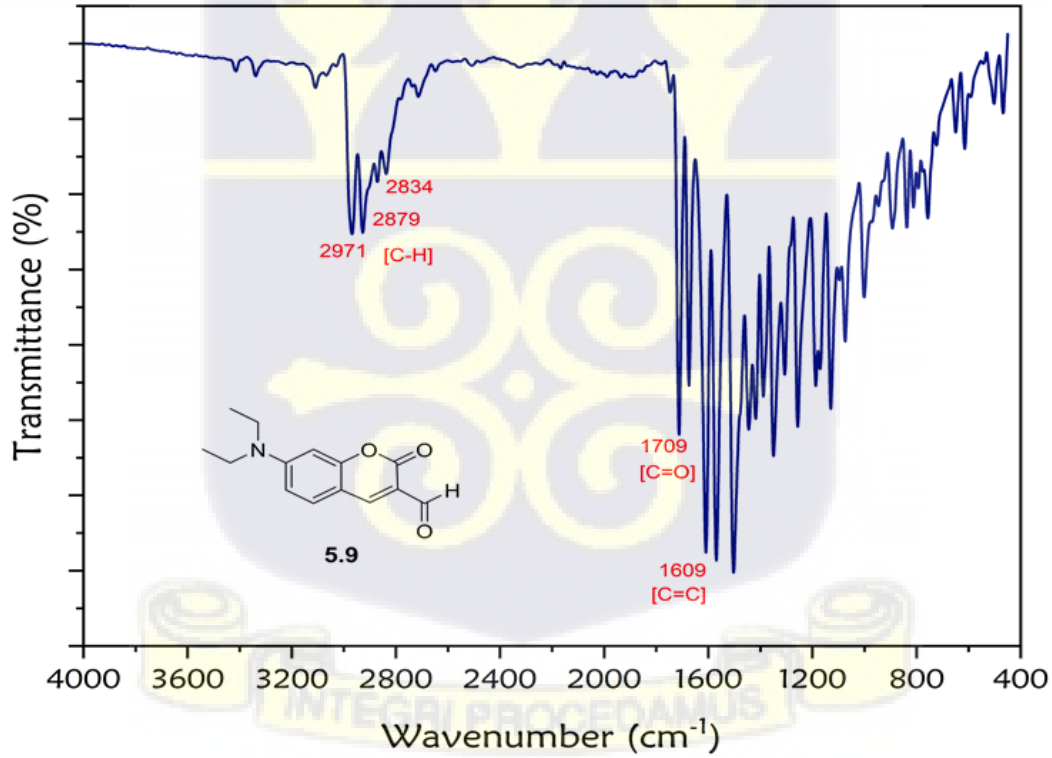

Appendix 3. 4: FTIR spectrum of 7-(diethylamino)-2-oxo-2H-chromene-3-carbaldehyde **5.9**

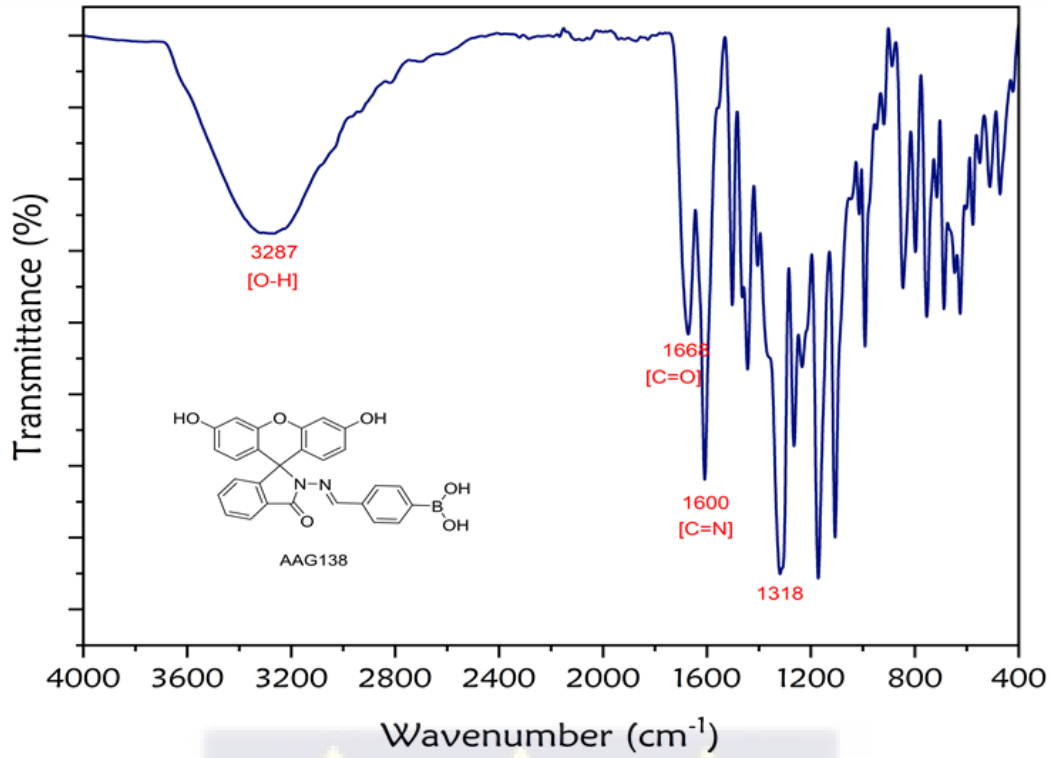

Appendix 3. 5: FTIR spectrum of **AAG138.**

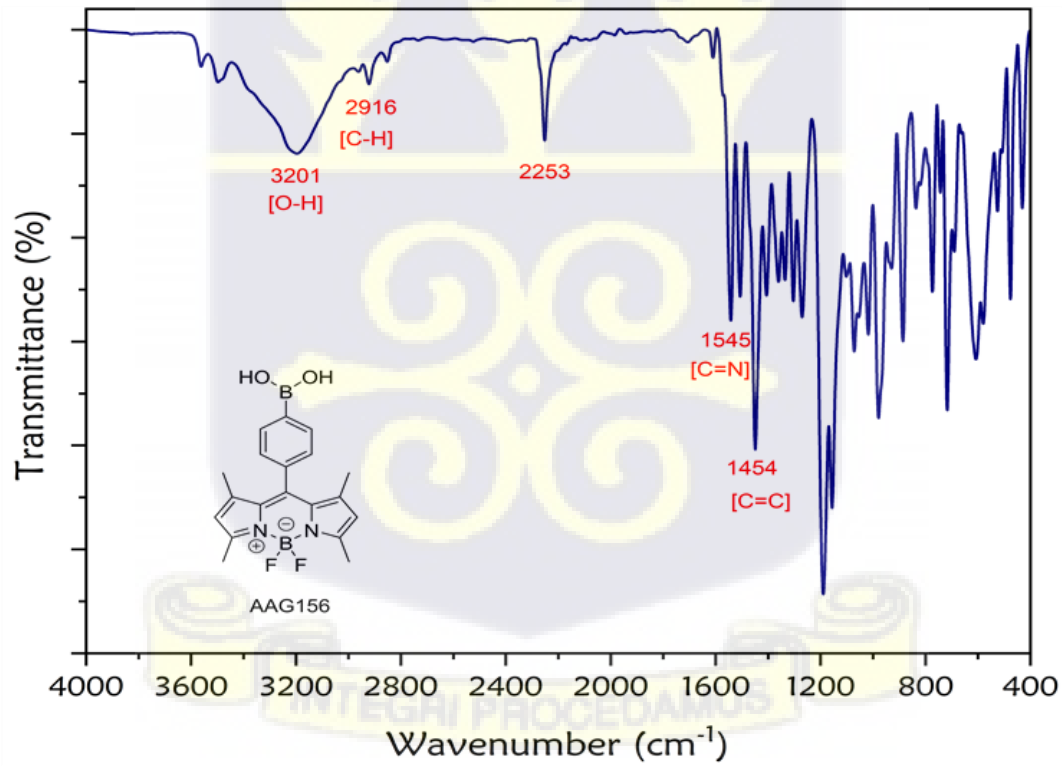

Appendix 3. 6: FTIR spectrum of **AAG156.**

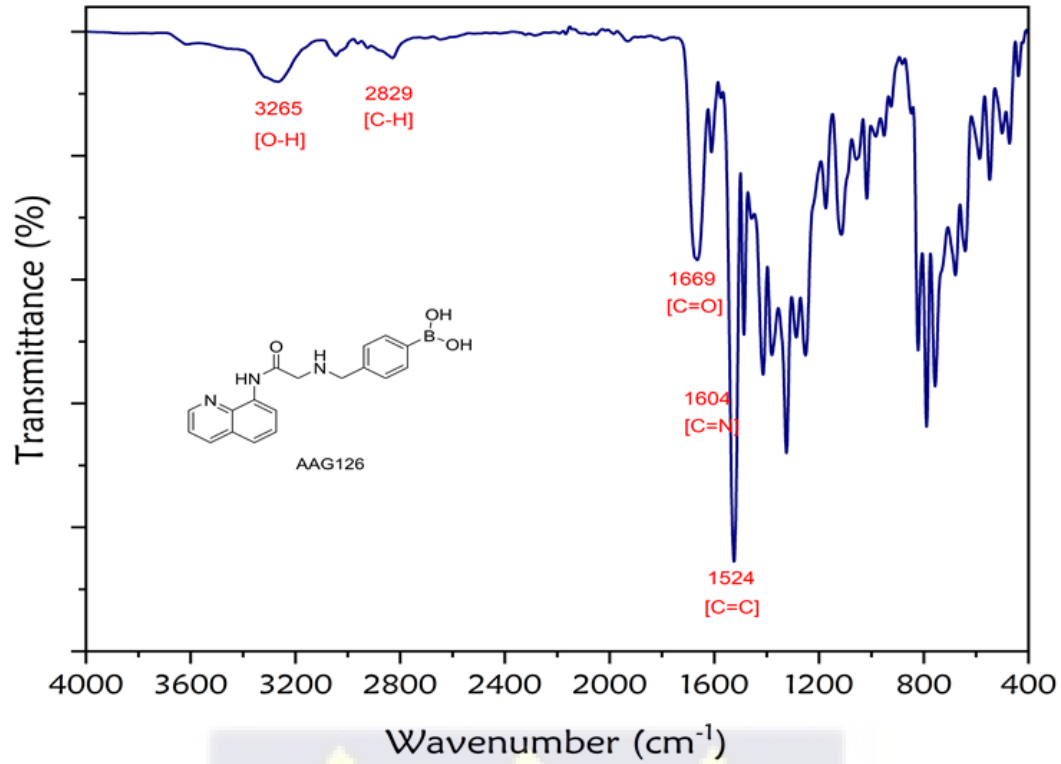

Appendix 3. 7: FTIR spectrum of **AAG126.**

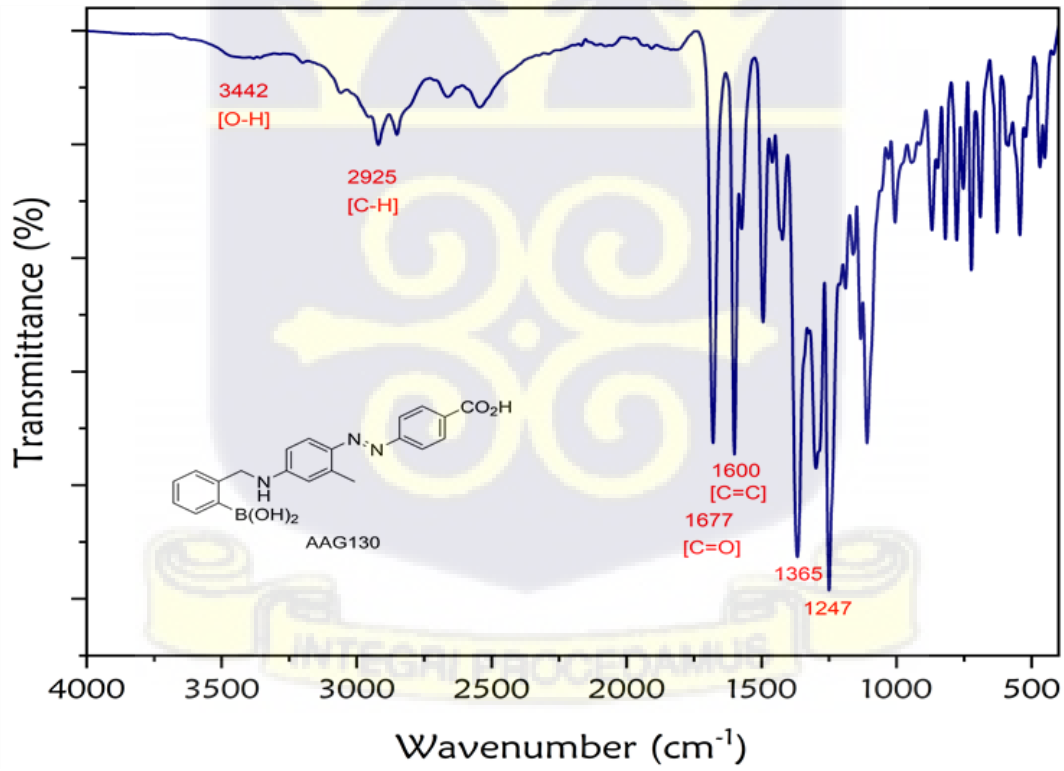

Appendix 3. 8: FTIR spectrum of **AAG130.**

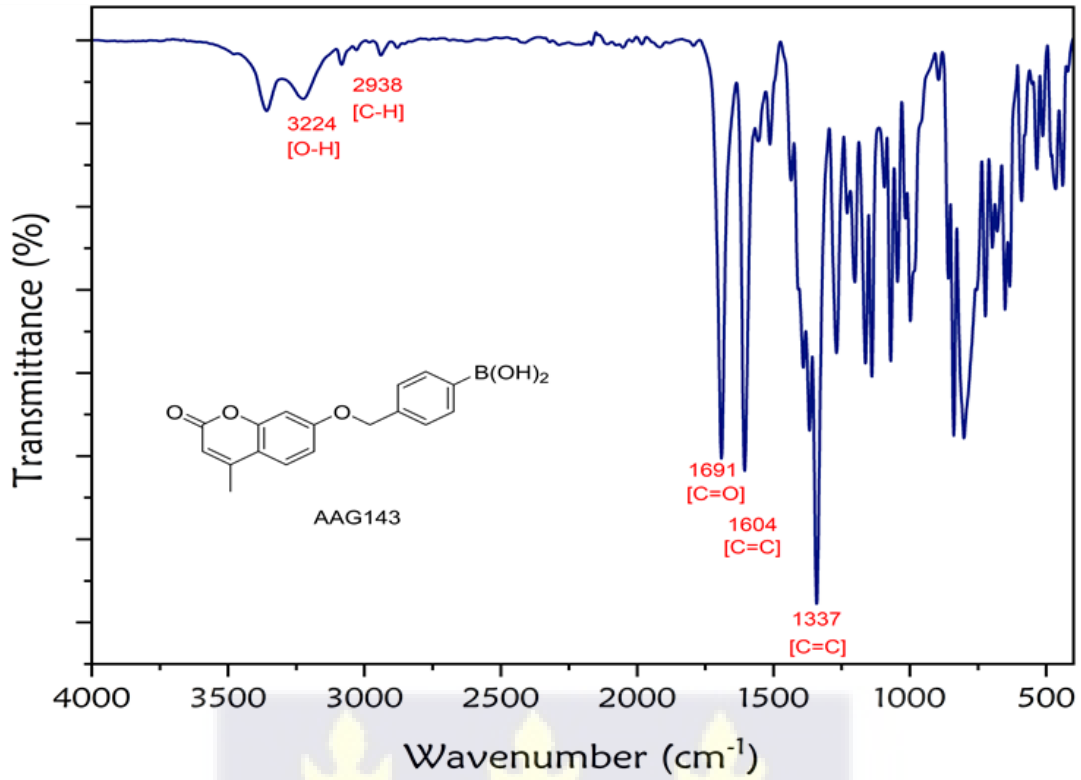

Appendix 3. 9: FTIR spectrum of **AAG143.**

Appendix 4: X-ray Crystallography Data

Appendix 4. 1: Crystal data and refinement details for the X-ray structure determinations of **AAG156.**

Compound	**AAG156**
Formula	$C_{19}H_{20}B_2F_2N_2O_2$
MW (g.mol^{-1})	367.99
T/K	100
Crystal system	triclinic
Space group	P-1
a/Å	9.0882(7)
b/Å	10.5364(8)
c/Å	10.7238(9)
α/°	92.199(2)
β/°	97.276(2)
γ/°	107.655(2)
Volume/Å^3	967.42(13)
Z	2
ρ_{calc}g/cm^3	1.263
μ/mm^{-1}	0.093
F(000)	384.0
Crystal size/mm^3	0.45 × 0.39 × 0.29
Radiation	MoKα (λ = 0.71073)
2Θ range for data collection/°	4.07 to 57.462
Index ranges	-12 ≤ h ≤ 12, -14 ≤ k ≤ 14, -14 ≤ l ≤ 14
Reflections collected	28108
Independent reflections	5006 [R_{int} = 0.0551, R_{sigma} = 0.0428]
Data/restraints/parameters	5006/0/250
Goodness-of-fit on F^2	1.035
Final R indexes [I>=2σ (I)]	R_1 = 0.0473, wR_2 = 0.1167
Final R indexes [all data]	R_1 = 0.0712, wR_2 = 0.1313
Largest diff. peak/hole / e Å^{-3}	0.34/-0.27

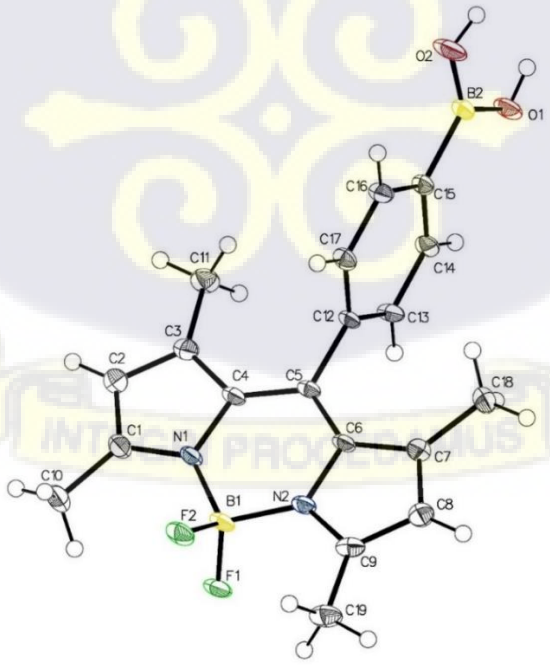

Appendix 4. 2: ORTEP representation of the molecular structure of compound **AAG156**

Appendix 5: Molar Absorptivity graphs

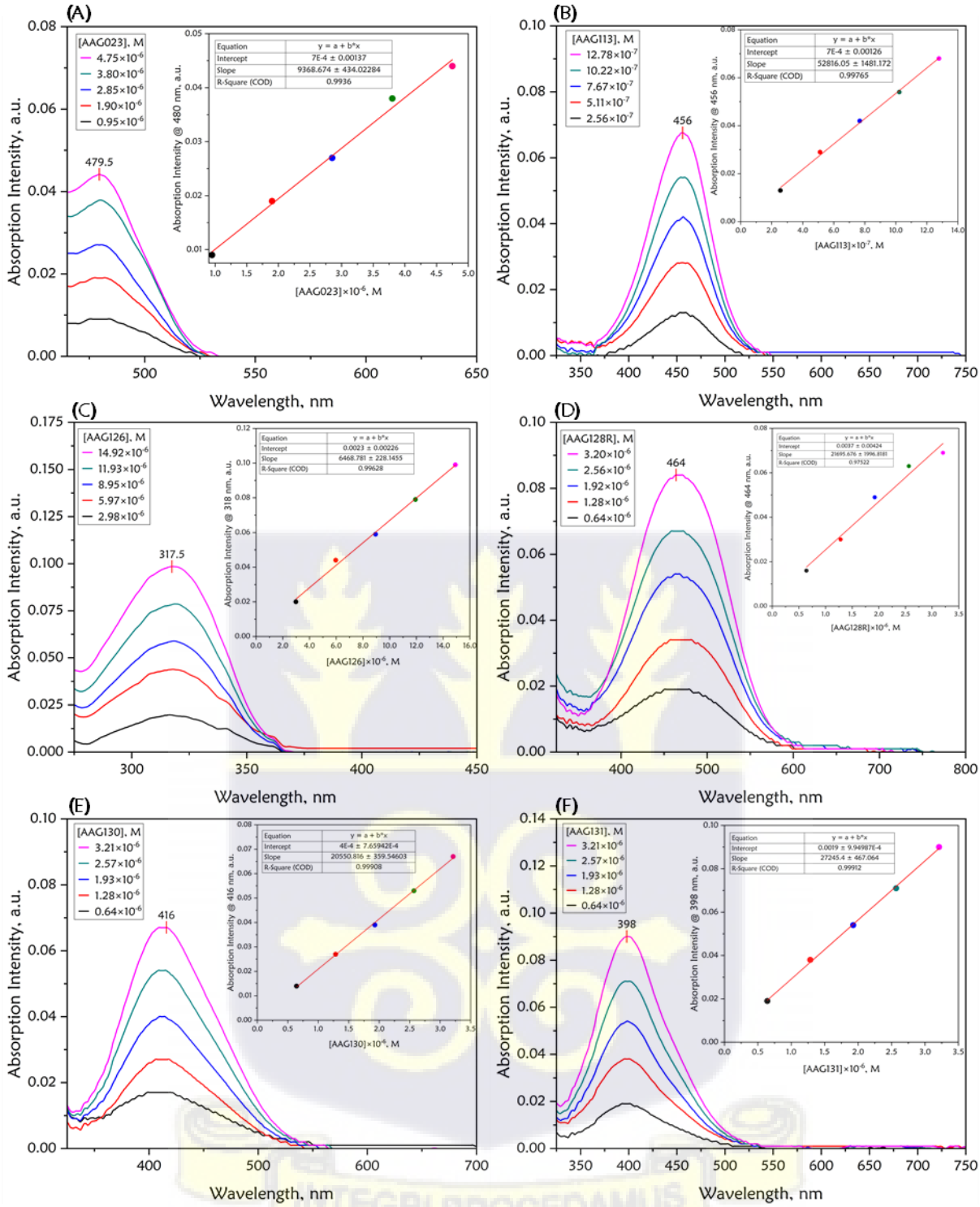

Absorbance spectra of various dyes in different organic solvents; Insets: respective linearity plots for the evaluation of molar extinction coefficients (ε) for the dyes at the absorption maxima.

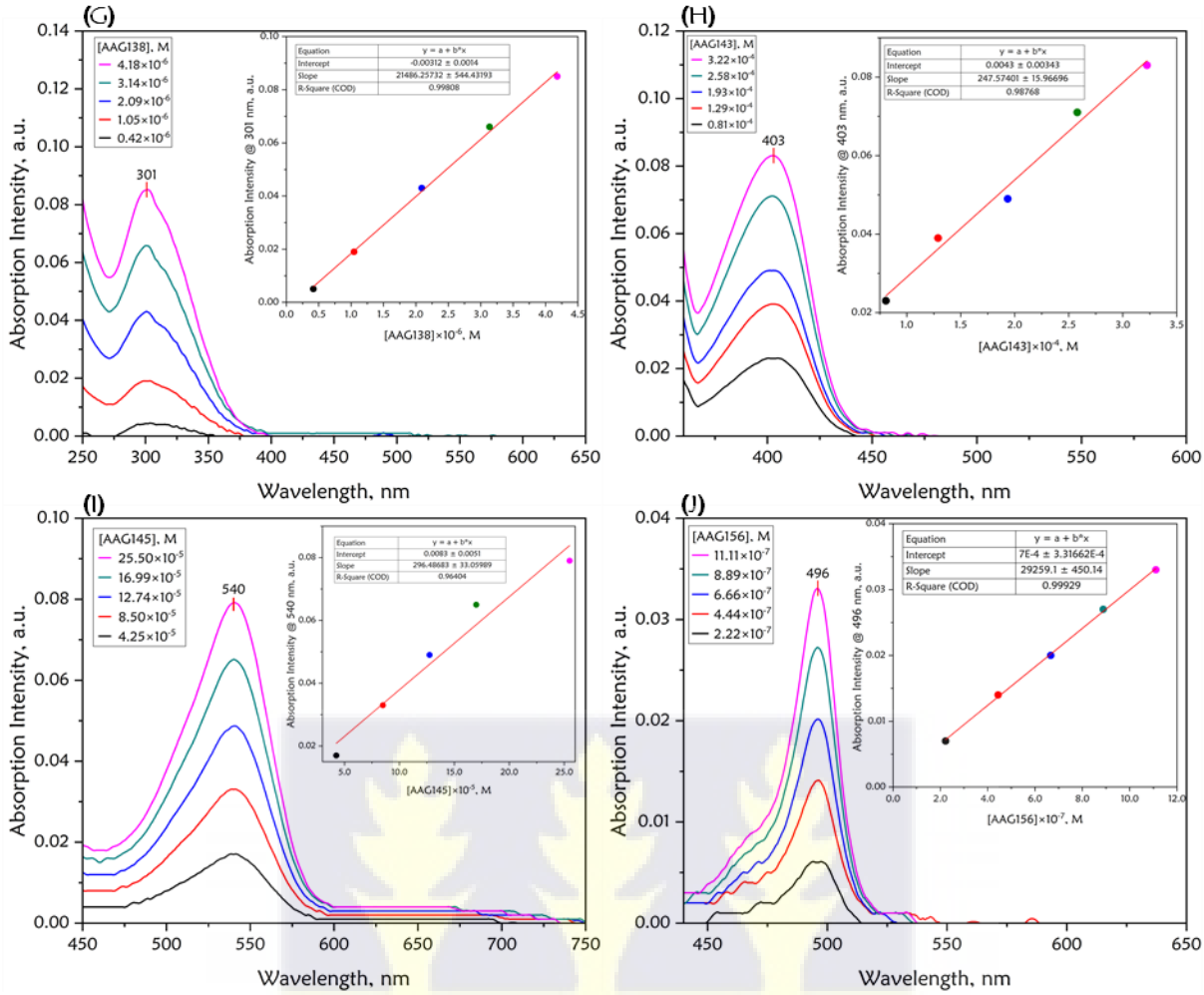

Appendix 5. 1: Absorbance spectra of various dyes in different organic solvents; Insets: respective linearity plots for the evaluation of molar extinction coefficients (ε) for the dyes at the absorption maxima.

Appendix 6: Fluorescence intensity and Quantum yield graphs

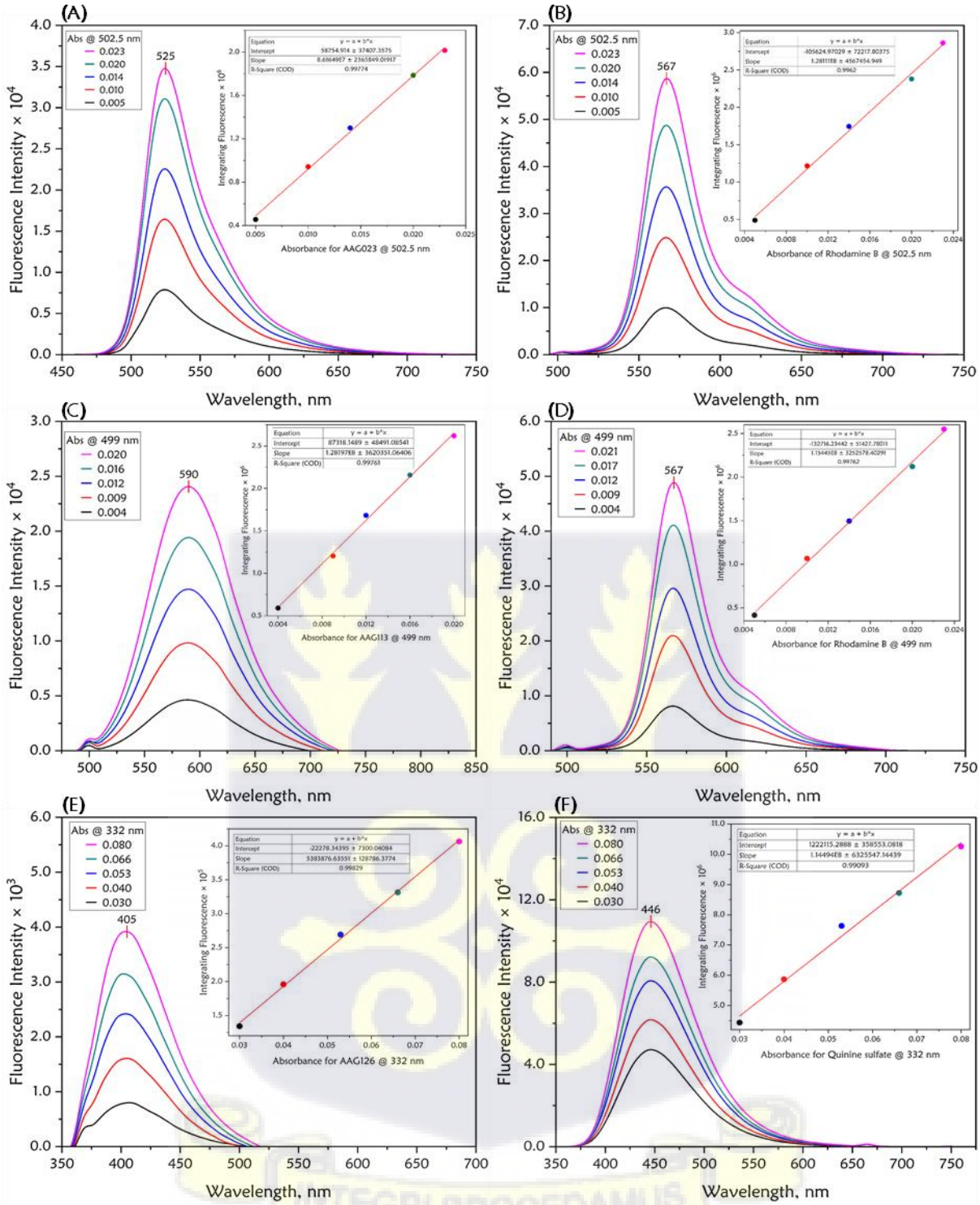

Fluorescence emission spectra of sample AAG023 (left) and reference Rhodamine B (right) with varying absorbance. Inset: Calibration curves of integrated fluorescence intensity (area under curve) against absorbance for sample respectively.

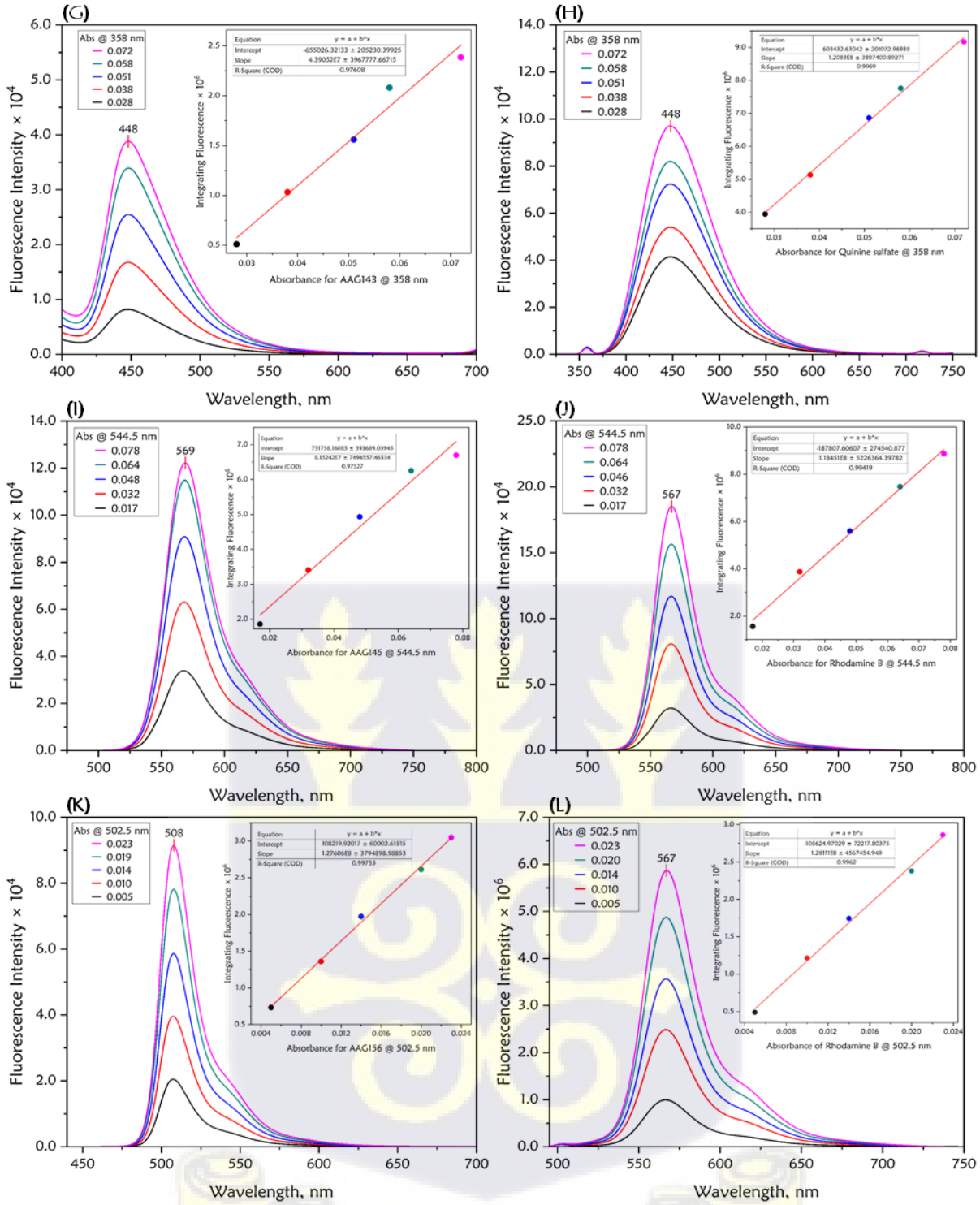

Appendix 6. 1: Fluorescence emission spectra of sample AAG023 (left) and reference Rhodamine B (right) with varying absorbance. Inset: Calibration curves of integrated fluorescence intensity (area under curve) against absorbance for sample respectively.

Appendix 7: f-TLC profiles of various boronic acids

Appendix 7. 1: List of attempted commercially screened arylboronic acids and their respective TLC profiles.

Entry	Boronic acid	Structure	TLC
BA	2-naphthylboronic acid	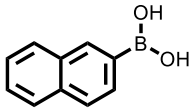	
BA1	Pyrene-1-boronic acid	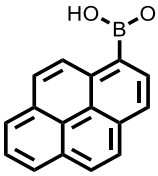	
BA2	4-Phenyl(napthalene-1-yl)boronic acid	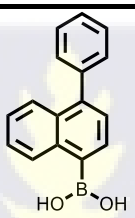	
BA3	4-Methyl-1-naphthaleneboronic acid	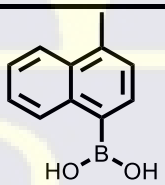	
BA4	6-Ethoxy-2-naphthaleneboronic acid	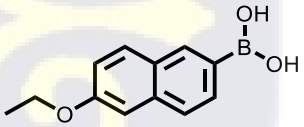	
BA5	9-phenanthreneboronic acid	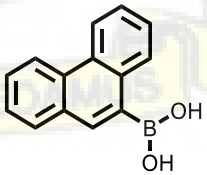	

BA6	4-(Naphthalen-2-yl)phenylboronic acid	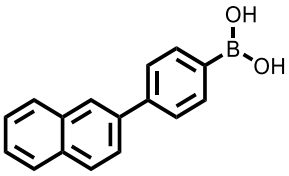	
BA7	Dibenzo[b,d]thiophen-2-ylboronic acid	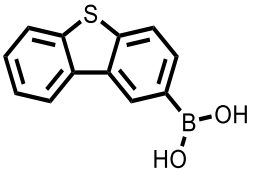	
BA8	(4-Bromonaphthalen-1-yl)boronic acid	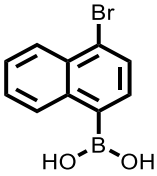	
BA9	4-aminomethylphenylboronic acid, hydrochloride	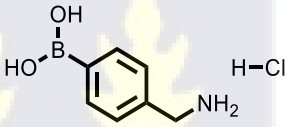	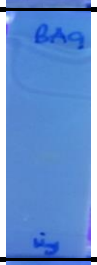
BA10	4-(Bromomethyl)phenylboronic acid	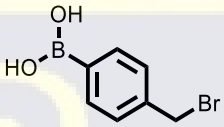	
BA11	4-Formylphenylboronic acid	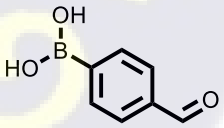	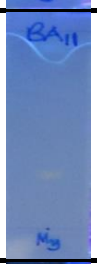
BA12	(4'-bromo-[1,1'-biphenyl]-4-yl)boronic acid	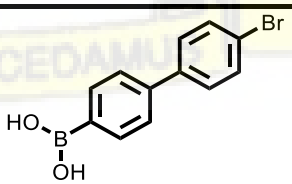	

BA13	(4-(9-Phenyl-9H-carbazol-3-yl)phenyl)boronic acid	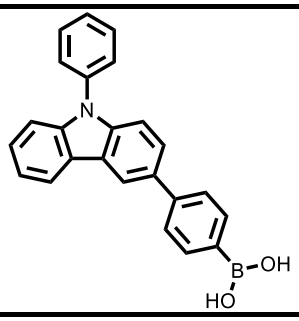	
BA14	10-(2-Naphthyl)anthracene-9-boronic acid	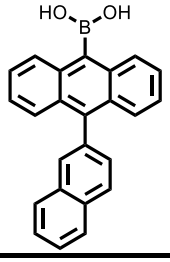	
BA15	[1,1':4',1''-terphenyl]-2-ylboronic acid	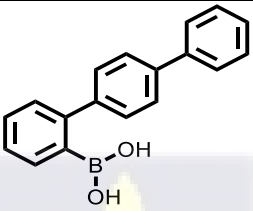	
BA16	4-Hydroxylphenylboronic acid	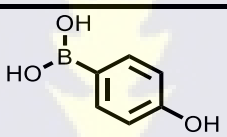	
BA26	4-(4-Biphenyl)phenyl boronic acid	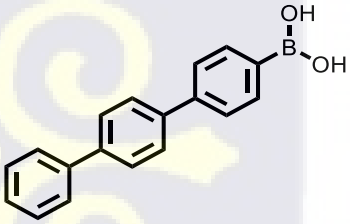	
BA18	(9,9-Diphenyl-9H-fluoren-4-yl)boronic acid	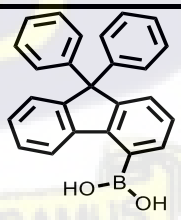	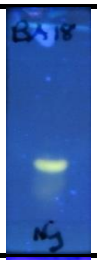
BA19	[1,1'-Binaphthalen]-4-ylboronic acid	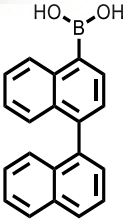	

BA20	(4'-Ethoxy-[1,1'-biphenyl]-4-yl)boronic acid	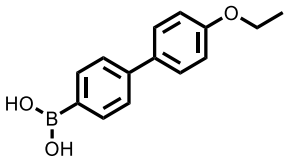	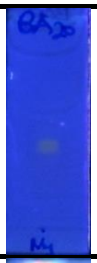
BA21	(3-(Naphthalen-1-yl)phenyl)boronic acid	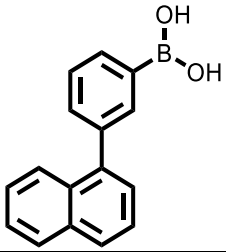	
BA22	3-(2-Naphthyl)phenylboronic acid	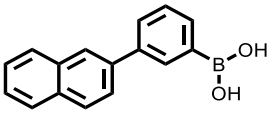	
BA23	2-Biphenylboronic acid	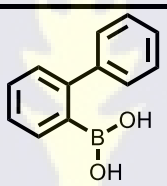	
BA24	3-Biphenylboronic acid	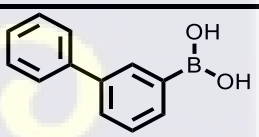	
BA25	9,9-Dimethyl-9H-fluoren-2-ylboronic acid